The Kiloparsec-Scale Structure and Kinematics of High-Redshift Star-Forming Galaxies

Thesis by
David R. Law

In Partial Fulfillment of the Requirements
for the Degree of
Doctor of Philosophy

California Institute of Technology
Pasadena, California

2009

(Defended July 30, 2008)

Acknowledgements

The thesis has been made possible by the aid of a large number of people who are deserving of my profound thanks. Dawn Erb, Naveen Reddy, Kurt Adelberger, and Alice Shapley always had a kind and helpful word for me as a beginning graduate student, and taught me many of the practical skills necessary to accomplish this work. I have been privileged to follow in their footsteps. Thank you also to Max Pettini for his eternally cheery correspondence, Milan Bogosavljević for countless 4AM discussions on the meaning of life, the universe, and everything while staring at fuzzy stars from Palomar, and James Larkin, Shelley Wright, and the rest of the OSIRIS team whose hard work made possible the observational backbone of this thesis. To Karín Menéndez-Delmestre and Thiago Gonçalves, whose friendship and help during the last 5 years has been a blessing. Kathy DeGioia-Eastwood, Kathryn Johnston, and Steve Majewski encouraged and supported me during my first forays into the world of research astronomy and are in large part responsible for convincing me to pursue graduate study, as is Mark Freeman who made me think that the physics of orbiting bodies was interesting in the first place. Thank you particularly to Chuck Steidel for advising and supporting me during the last 5 years. I appreciate equally his patience, scientifically sceptical nature, and uncannily accurate insights. To my parents, Clare and Richard Law, who taught me the value of rational inquiry (whether it be the nature of the heavens or of the Earth) and without whose unconditional support and encouragement none of this would have been possible. Finally, thank you to my wife, Sarah, for her patience, understanding, and indomitable spirit which provides an unfailing source of inspiration.

The Kiloparsec-Scale Structure and Kinematics of High-Redshift Star-Forming Galaxies

by

David R. Law

In Partial Fulfillment of the
Requirements for the Degree of
Doctor of Philosophy

Abstract

We study the spatially resolved properties of star-forming galaxies at redshift $z \sim 2-3$ on scales ~ 1 kpc using a combination of morphological and kinematic analyses in an effort to characterize the major mechanisms of galaxy formation in the young universe. Using a sample of 216 galaxies which have been spectroscopically confirmed to lie between redshifts $z = 1.8-3.4$ in the GOODS-N field we demonstrate that rest-UV morphology (as seen by the *Hubble Space Telescope*) is statistically uncorrelated with physical properties such as star formation rate and is therefore unable to support the hypothesis that the prevalence of irregular morphologies indicates a high major merger fraction. Further, we present a sample of 13 galaxies observed with the OSIRIS integral field spectrograph and the Keck laser-guide star adaptive optics system which demonstrate the prevalence of high velocity dispersions ~ 80 km s^{-1} and generally little in the way of spatially resolved velocity gradients, inconsistent with favored rotating disk models. We discuss the implications of these results for galaxy formation models, including gas accretion via cold flows and gravitational instability of early gas-rich galactic disks. There is some evidence for a trend towards stronger rotational signatures in galaxies with more massive stellar populations.

Contents

List of Figures

List of Tables

Chapter 1

Introduction

Galaxies are the discrete luminous building blocks of the visible universe, tracing the development of gravitational structures across cosmic ages. The earliest galaxies at redshift $z \sim 10$ (see, e.g., Stark et al. 2007) may have been simply glorified star-forming regions, composed of gas near the density peaks of the primordial power spectrum (e.g., Bardeen et al. 1986) which were able decouple from the cosmic expansion at early times and form a burst of stars. As time progressed, however, these chaotic proto-galaxies gradually evolved, merging with their neighbors in newly collapsing dark halos, accreting greater quantities of gaseous fuel from a filamentary intergalactic medium, and polluting their environments with the metallic detritus of their early stellar generations. It is not until comparatively recent times ($z \sim 1$) however that these early galaxies began to develop the orderly, regular morphological structures with which we are familiar in the local universe. Indeed, it is intermediate redshifts $z \sim 2 - 3$ (when the universe was roughly 16 – 25% of its present age) at which these morphologically irregular, juvenile galaxies are thought to have formed the majority of the stellar mass which we observe in modern-day galaxies (Dickinson et al. 2003, Reddy et al. 2008). Through a combination of galaxy-galaxy mergers, rapid star formation, and secular evolution, these galaxies experienced a strong morphological transformation into the coherent structures of the Hubble sequence which have predominated since redshift $z \sim 1$ (Giavalisco et al. 1996; Papovich et al. 2005).

Recent years have witnessed a veritable explosion of methods for locating such galaxies. These methods include optical ($U_nG\mathcal{R}$) color selection (e.g., Steidel et al. 2003, 2004), near-IR BzK (Daddi et al. 2004) and $J - K$ (Franx et al. 2003) color selection, and selection by sub-mm flux density (Smail et al. 1997). Of these samples, that arising from the optical

color selection is perhaps the most well studied. As described in detail by Adelberger et al. (2004), the $U_nG\mathcal{R}$ selection technique represents a generalized version of the Lyman-break technique employed by Steidel et al. (2003) to identify rapidly star-forming galaxies at redshift $z \sim 3$ on the basis of their strong 912 Å Lyman break as it is redshifted into the U_n bandpass. In this thesis, we focus primarily on this $U_nG\mathcal{R}$ sample, and particularly on those galaxies in the redshift ranges $z = 1.8-2.6$ (i.e., the "BX" galaxy sample of Steidel et al. 2004) and $z = 2.6-3.4$ (i.e., the "LBG" sample of Steidel et al. 2003). As detailed by Adelberger et al. (2004), these redshift ranges are dictated by the selection functions of the respective color selection criteria. While initial identification of these galaxies was based upon photometric preselection, extensive spectroscopic follow-up work has derived precise redshifts for all galaxies in our primary target sample.

The galaxies selected in this manner are typically bright and actively forming stars, with extinction-corrected star formation rates (SFR) $\gtrsim 30\ M_\odot\ \mathrm{yr}^{-1}$ (see discussion by Erb et al. 2006b), and SFR surface densities similar to those observed in local starburst galaxies (e.g., Kennicutt et al. 1998b). The resulting winds from supernovae and massive stars drive energetic (~ 500 km s^{-1}; Steidel et al. *in prep.*) large-scale outflows into the IGM surrounding these galaxies, creating the ubiquitous blueshifted interstellar absorption features observed in rest-frame UV spectra (e.g., Shapley et al. 2003). With the aid of deep near-IR (e.g., Erb et al. 2006c) and mid-IR (e.g., Papovich et al. 2006; Reddy et al. 2006b; and references therein) photometry, stellar population modelling suggests that galaxies at $z \sim 2-3$ span a broad range of stellar masses and evolutionary states.

Despite our growing knowledge of the broad global characteristics of $z \sim 2-3$ galaxies, however, our knowledge of their internal structure and dynamical evolution has been limited by their small angular size (typically $\lesssim 1$ arcsecond). Such objects are generally not well resolved in the ground-based imaging and spectroscopy which form the backbone of the observational data, precluding us from determining (for instance) the triggering and regulation mechanisms of these starbursts, whether this star formation occurs in nuclear or circum-nuclear regions of dynamically relaxed systems or as a result of tidal shocks induced by major mergers, and whether individual regions of star formation follow a global abundance pattern or exhibit strong variations in chemical enrichment. Each of these distinctions has appreciable implications for the evolution and development of structure and

stellar populations within a given galaxy. In this thesis, we capitalize on recent technological developments to explore what information can be gleaned from such spatially resolved information. We describe our specific goals in greater detail below.

1.1 MORPHOLOGY

One method of probing the small-scale structure and distribution of star formation is through deep wide-field imaging with space-based optical telescopes such as *HST* which are not subject to the atmospheric turbulence which limits ground-based facilities. In particular, the optical-wavelength Advanced Camera for Surveys (ACS) and the near-IR camera NICMOS provide high-quality imaging with spatial resolutions of 0.5 kpc and 1.6 kpc, respectively, at redshift $z \sim 2$. Such studies are particularly appealing given the wealth of information contained in the distribution of luminous matter (i.e., the morphology) within local Hubble-type galaxies, from which it is typically possible to deduce kinematics, rate and distribution of star formation, and the recent merger history. Unsurprisingly, numerous studies (e.g., Abraham et al. 2003; Conselice et al. 2003, 2006; Chapman et al. 2003; Lotz et al. 2004, 2006) have therefore sought to characterize the morphologies of $z \sim 2-3$ galaxies in order to derive information about their internal structure and interaction histories.

At redshifts $z \sim 2-3$ however, the majority of the galaxy population have highly irregular morphologies, frequently composed of multiple spatially separated components, which bear little similarity to the local Hubble-type population (Giavalisco et al. 1996; Papovich et al. 2005). This has commonly been assumed to indicate the wide-spread prevalence of major galaxy–galaxy mergers at this cosmic epoch, but it is uncertain whether these structures are predominantly caused by merger activity, patchy star formation, dust extinction, or some other physical process (and likely a combination of all of the above). Consequently, it is far from certain whether morphological information alone can reveal anything about the star formation history, mass, or kinematics of these galaxies. As a first step in understanding the resolved structure of the high-redshift galaxy sample, a comprehensive study of the physical interpretation of galaxy morphology at high redshift (i.e., how morphology relates to the derived stellar mass, star formation rate, outflow properties, etc.) is therefore warranted to ascertain whether morphological information alone can provide a meaningful characterization of the small-scale structure and mass assembly history of galaxies.

1.2 KINEMATICS

An approach which is both more time consuming and perhaps more promising is studying the ionized gaseous structure surrounding bright star-forming regions produced by the flood of energetic photons from these young stars. Excited atoms in this gas lose energy predominantly by emission of strong rest-frame optical nebular emission lines (redshifted into the near-IR for galaxies at $z \sim 2-3$) such as Hα, [O III], and [N II]. The relative strengths of these lines encodes information about the chemical composition of the gas and the shape of the ionizing spectrum, permitting deduction of the metallicity and star formation rates of the emission regions. These emission features are also intrinsically narrow, and the central wavelength and widths of the lines can therefore be used to derive precise relative velocities and kinematic dispersions among star-forming regions along a given line of sight.

Such information is critical for answering a number of outstanding questions, not least of which is the mechanism by which galaxy formation and gas accretion occurs in the young universe. According to basic theories of galaxy formation (e.g., White & Rees 1978) hot-mode accretion dominates the gas accretion history of galaxies. Once a sufficiently massive dark matter halo has virialized, gas can fall into its potential well, heating via shocks to the virial temperature of the host halo. As this gas cools over time it collapses to form a rotating disk supported by angular momentum which the cooled gas has been unable to shed. This gaseous disk is posited to be the home of the bulk of active star formation. The actual mechanism of dynamical support for galaxies at $z \sim 2-3$ is unknown, however, posing a crucial test for this theory.

Studies using slit (e.g., Erb et al. 2004, 2006b, 2006c; Weiner et al. 2006) spectroscopy have met with qualified success and demonstrated that the kinematics of these galaxies are frequently inconsistent with the gas-disk models (although c.f. Förster-Schreiber et al. 2006), often exhibiting kinematics that appear to be dominated by velocity dispersion rather than identifiable shear. However, these studies have been limited by the small angular size of typical galaxies relative to the atmospheric seeing. Not only may there typically be only 1–2 spatially uncorrelated samples across the face of a given galaxy, but additional uncertainty may be introduced by misalignment of the slit with the kinematic axis. It is therefore unclear whether the observed dispersion is *intrinsic* to the target galaxies, or caused by the smearing out of unresolved kinematic structure.

The recent advent of adaptive optics (AO) on 10 m class telescopes offers for the first time the opportunity to overcome the limitations previously imposed by atmospheric turbulence by rapidly correcting the distorted wavefront using deformable mirrors. While originally proposed over 50 years ago (Babcock et al. 1953), it is only in the last 10–15 years that advances in computer technology have made such an idea possible, albeit restricted to targets located near bright reference stars used to determine the wavefront corrections. The development of artificial laser-generated guide stars (LGSAO; see, e.g., discussion by Wizinowich et al. 2006) has greatly expanded the available sky coverage of this technique, permitting observation of the majority of deep-sky targets. Paired with integral-field spectroscopy, it is possible to obtain diagnostic spectra of spatial regions resolved on scales of order 100 milliarcseconds (corresponding to roughly 1 kpc at redshift $z \sim 2-3$). The data provide an empirical answer to whether the velocity fields of galaxies in the early universe are predominantly represented by virialized disk-like systems, major mergers, or some other dynamical structure, and whether the resulting star formation is uniform in its properties across a given galaxy or exhibits regional variation on scales of a kiloparsec.

The outline of this thesis is as follows: In Chapter 2 (Law et al. 2007b) we describe our morphological analysis of redshift $z \sim 2-3$ galaxies in the GOODS-N field. Using a variety of methods to characterize their irregular morphologies, we discuss the physical interpretation of galaxy morphology in light of photometric and spectroscopic measures of the galaxies' component stellar populations. We then proceed to explore the spatially resolved kinematics of these galaxies using the new OSIRIS (OH-Supressing InfraRed Imaging Spectrograph; Larkin et al. 2006) integral field spectrograph in conjunction with the Keck Observatory LGSAO system. In Chapter 3 (Law et al. 2006) we discuss the capabilities and limitations of this spectrograph prior to our observing program. Results for 3 galaxies obtained early in this program are presented in Chapter 4 (Law et al. 2007a). These early results are extended using observations of an additional 10 galaxies discussed in Chapter 5. In a separate article (included here as Chapter 6) we demonstrate the capability of these LGSAO data to determine the properties of galaxies which host luminous QSOs in addition to ordinary star-forming galaxies. Finally, in Chapter 7 we summarize our conclusions regarding the physical structure and formation history of $z \sim 2-3$ galaxies and describe the implications of these data for theoretical models of galaxy formation.

Chapter 2

The Physical Nature of Rest-UV Galaxy Morphology During the Peak Epoch of Galaxy Formation*

David R. Law[a], Charles C. Steidel[a], Dawn K. Erb[b], Max Pettini[c], Naveen A. Reddy[a], Alice E. Shapley[d], Kurt L. Adelberger[e], David J. Simenc[a]

[a]California Institute of Technology, MS 105–24, Pasadena, CA 91125

[b]Harvard-Smithsonian Center for Astrophysics, MS 20, 60 Garden St, Cambridge, MA 02138

[c]Institute of Astronomy, Madingley Road, Cambridge CB3 0HA, UK

[d]Department of Astrophysical Sciences, Princeton University, Peyton Hall, Ivy Lane, Princeton, NJ 08544

[e]McKinsey and Company, 1420 Fifth Avenue, Suite 3100, Seattle, WA 98101

Abstract

Motivated by the irregular and little-understood morphologies of $z \sim 2-3$ galaxies, we use non-parametric coefficents to quantify the morphologies of 216 galaxies which have been spectroscopically confirmed to lie at redshifts $z = 1.8$–3.4 in the GOODS-N field. Using measurements of ultraviolet (UV) and optical spectral lines, multi-band photometric

*A version of this chapter was published in *The Astrophysical Journal*, 2007, vol. 656, 1–26, and is reproduced by permission of the AAS.

data, and stellar population models we statistically assess possible correlations between galaxy morphology and physical observables such as stellar mass, star formation rate, and the strength of galaxy-scale outflows. We find evidence that dustier galaxies have more nebulous UV morphologies and that larger, more luminous galaxies may drive stronger outflows, but otherwise conclude that UV morphology is either statistically decoupled from the majority of physical observables or determined by too complex a combination of physical processes to provide characterizations with predictive power. Given the absence of strong correlations between UV morphology and physical parameters such as star formation rates, we are therefore unable to support the hypothesis that morphologically irregular galaxies predominantly represent major galaxy mergers. Comparing galaxy samples, we find that IR-selected BzK galaxies and radio-selected submillimeter galaxies (SMGs) have UV morphologies similar to the optically selected sample, while distant red galaxies (DRGs) are more nebulous.

2.1 INTRODUCTION

In the local universe the projected distribution of luminous matter within a galaxy, i.e., the morphology, often provides a wealth of information about that galaxy's kinematics, rate of star formation, and recent merger history. In the classical picture, late-type spiral galaxies harbor active star formation in the gas-rich arms of a flattened rotating disk, while early-type elliptical galaxies tend to be more massive, dispersion-supported, and quiescent systems. At high redshifts from $z \sim 2 - 3$, however, the morphologies of typical galaxies are highly irregular (Abraham et al. 1996; Kajisawa & Yamada 2001; Conselice et al. 2005), frequently composed of multiple spatially separated components, and appear to bear little similarity to the local Hubble-type population. It is uncertain whether these irregular morphologies are due to patchy star formation, prevalent merger activity, or some other physical process, and consequently unknown whether these morphologies can (analogously to local galaxies) tell us anything about the star formation rate, mass, or stellar kinematics of galaxies at high redshifts.

Since morphological studies are often performed at optical wavelengths which probe rest-frame ultraviolet (UV) radiation for galaxies at redshifts $z \gtrsim 1$, one might *expect* that the morphologies of such galaxies should appear irregular, since radiation at such wavelengths

predominantly traces emission from the brightest active star-forming regions rather than the redder bulk of the stellar population (Dickinson 2000). UV emission tends to be patchy and irregular even for local Hubble-type galaxies (e.g., Gordon et al. 2004), as in the case of the local galaxy merger VV 114 (whose broad rest-UV absorption line spectra suggest that it may be a local analog to $z \sim 2-3$ Lyman Break Galaxies; Grimes et al. 2006) whose near-infrared (NIR) morphology clearly shows a pair of interacting late-type galaxies while the rest-UV morphology shows only scattered clumps of emission (Goldader et al. 2002). However, high-redshift galaxies have irregular morphologies not only in the rest-UV, but often at rest-optical wavelengths as well (Dickinson 2000; Papovich et al. 2005), indicating that (in contrast to local galaxies) both wavelength regimes are dominated by emission from young starbursting components and therefore that there may be some fundamental difference between the two samples.

One popular explanation for these multi-component, irregular morphologies is that they represent major merger systems, and that their prevalence indicates that the rate of major mergers was much greater at high redshifts than in the local universe (e.g., Conselice et al. 2003). Such a conclusion fits well within the framework of cold dark matter (CDM) theory, and may additionally be supported by stellar population analyses (e.g., Dickinson et al. 2003) which suggest that many galaxies in the local universe accumulated a large fraction of their stellar mass at $z \sim 2-3$, as might be expected if star formation peaked in this epoch as a result of tidally induced collapse spurred by major mergers. However, the interpretation of a multi-component or otherwise irregular morphology is not always clear. In the case of VV 114, near-IR imaging (Goldader et al. 2002) indicates that all of the clumps of UV emission are associated with only one galaxy of the merger pair and that the multi-component UV morphology therefore directly reflects clumpy star formation rather than tracing tidally distorted features from each of the two galaxies.

Building on a body of literature characterizing the morphologies of galaxies at redshifts $z \sim 2-3$ (e.g., Abraham et al. 2003; Conselice et al. 2003; Lotz et al. 2004, 2006; Ravindranath et al. 2006) it is worthwhile to ask whether rest-UV morphologies correspond to any other physical observables such as UV/optical spectral line strengths (e.g., Shapley et al. 2003; Erb et al. 2006a), stellar population models (e.g., Shapley et al. 2005b; Erb et al. 2006a; Reddy et al. 2006a), or rest-optical to IR properties (e.g., Reddy et al. 2006a,

2006b). In this work, we use non-parametric coefficients to characterize the morphologies of 216 spectroscopically confirmed galaxies in the redshift range $z = 1.8 - 3.4$, assess the statistical significance of correlations with spectrophotometric observables, and discuss the resulting physical interpretation of galaxy morphology. In §2.2 we describe our galaxy sample and give a basic description of the sample population. In §2.3 we outline our morphological parameters, comparing our results to the recent studies of Conselice et al. (2003) and Lotz et al. (2004, 2006). Rest-frame UV spectra are introduced in §2.4, correlations between morphology and spectral line strength and kinematics are discussed in §2.5. In §2.6 and §2.7 we compare morphologies with stellar population models derived from UV to mid-IR photometric data, as well as discussing differences between different samples of high-redshift galaxies and AGN selected on the basis of various photometric criteria. Finally, we discuss the implications of our results for the physical interpretation of galaxy morphologies in §2.8. Our morphological statistics and ancillary data are made publically available in an electronic database located at http://www.astro.caltech.edu/∼drlaw/GOODS/ .

We assume a standard ΛCDM cosmology in which $H_0 = 71$ km s^{-1} Mpc^{-1}, $\Omega_{\rm m} = 0.27$, and $\Omega_\Lambda = 0.73$.

2.2 SAMPLE SELECTION

Our sample is drawn from rest-UV color-selected catalogs of $z \sim 2 - 3$ star-forming galaxy candidates (Steidel et al. 2003, 2004; Adelberger et al. 2004) in the GOODS-N field. These catalogs are based on deep ground-based imaging, and therefore select galaxies independent of morphology or surface brightness since even the largest galaxies are nearly unresolved in these seeing-limited images. We consider only those galaxies which have been spectroscopically confirmed to lie in the redshift intervals $z = 1.8 - 2.6$ or $z = 2.6 - 3.4$ (i.e., the peak redshift ranges defined by the selection functions of the color selection criteria, see Adelberger et al. 2004) and which exhibit no obvious spectroscopic signatures of active galactic nuclei.

The redshift distribution of galaxies in our sample is shown in Figure 2.1: the $z \sim 2$ sample contains 150 galaxies in the range $1.8 < z < 2.6$ with mean $\bar{z} = 2.17 \pm 0.21$, while the $z \sim 3$ sample contains 66 galaxies in the range $2.6 < z < 3.4$ with $\bar{z} = 3.02 \pm 0.19$.

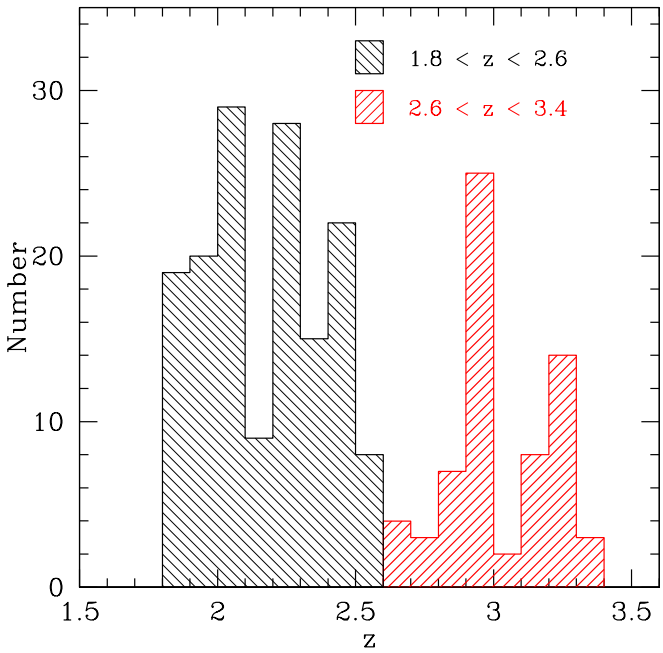

Figure 2.1 Distribution of galaxies with spectroscopic redshift z.

2.3 MORPHOLOGIES

Morphological parameters were determined from deep *HST*-ACS imaging obtained as part of the GOODS-N survey (Giavalisco et al. 2004) in F435W (B), F606W (V), F775W (I), and F850LP (z) bandpasses with drizzled pixel scale of 50 mas pixel^{-1} and 10σ limiting point source sensitivities of 27.8, 27.8, 27.1, and 26.6 mag (AB) respectively (Giavalisco et al. 2004). At redshifts $z \sim 2$ and $z \sim 3$ these bandpasses collectively probe rest-frame UV emission in the wavelength intervals $\sim 1500 - 3000$ Å and $\sim 1000 - 2000$ Å, respectively.

The observed morphology is qualitatively similar throughout this range of wavelengths (see §2.3.6), and we therefore improve our signal-to-noise ratios per pixel by creating a single rest-frame UV image from a weighted sum of the four individual bandpasses. Weights for this sum are determined proportionally to the inverse variance of the overall sky noise relative to the average number of counts from the $z \sim 2 - 3$ galaxies. The UV composite morphologies of our 216 galaxies are shown in Figure 2.2 in order of increasing redshift, and demonstrate a variety of morphological types ranging from single nucleated[1] sources

[1]We adopt the term "nucleation" to qualitatively describe a concentrated region of flux which might naively be described as the "nucleus" of a given galaxy. This contrasts with the term "nebulosity" which we

to extremely asymmetric sources with multiple nucleations and/or nebulous components. The "typical" galaxy has a morphology comprising one or more spatially distinct clumps with some degree of diffuse nebulosity, reminiscent of the HST-*STIS* UV morphology of the local interacting galaxy VV 114 (Goldader et al. 2002) which is dominated by a patchy distribution of star formation regions. Our initial morphological classification groups galaxies by visual inspection on the basis of the apparent nucleation of their light profiles and the presence and number of multiple nucleated emission components. Galaxies fall within five general classes:

1. Single strongly nucleated sources (11 sources at $z \sim 2$, 9 sources at $z \sim 3$).

2. Multiple strongly nucleated sources (6 sources at $z \sim 2$, 2 sources at $z \sim 3$).

3. Single nucleated source accompanied by nebulosity (61 sources at $z \sim 2$, 27 sources at $z \sim 3$).

4. Multiple nucleated sources accompanied by nebulosity (35 sources at $z \sim 2$, 12 sources at $z \sim 3$).

5. Nebulous emission with no strong nucleation (37 sources at $z \sim 2$, 16 sources at $z \sim 3$).

We seek a set of numerical parameters which will allow us to effectively reproduce these intuitive divisions, while providing a more rigorous mathematical basis for the classification. The "CAS" system of parameters has recently been a popular choice, characterizing galaxies on the basis of their concentration (C; Kent 1985, Bershady et al. 2000), asymmetry (A, Schade et al. 1995), and clumpiness (S, Conselice et al. 2003). However, the first two of these quantities are explicitly defined with regard to circular or elliptical apertures measured about a central point, which is only well defined for galaxies with morphologies similar to traditional elliptical or spiral galaxies, while the third quantity relies upon suitable choice of a smoothing scale on which clumpiness is defined. In the case of the $z \sim 2-3$ galaxy sample, morphologies are generally so irregular (see Fig. 2.2) that they do not have a well-defined "center", and the measured values of the CAS parameters can depend strongly

use to describe diffuse flux which is spread fairly uniformly over a number of pixels.

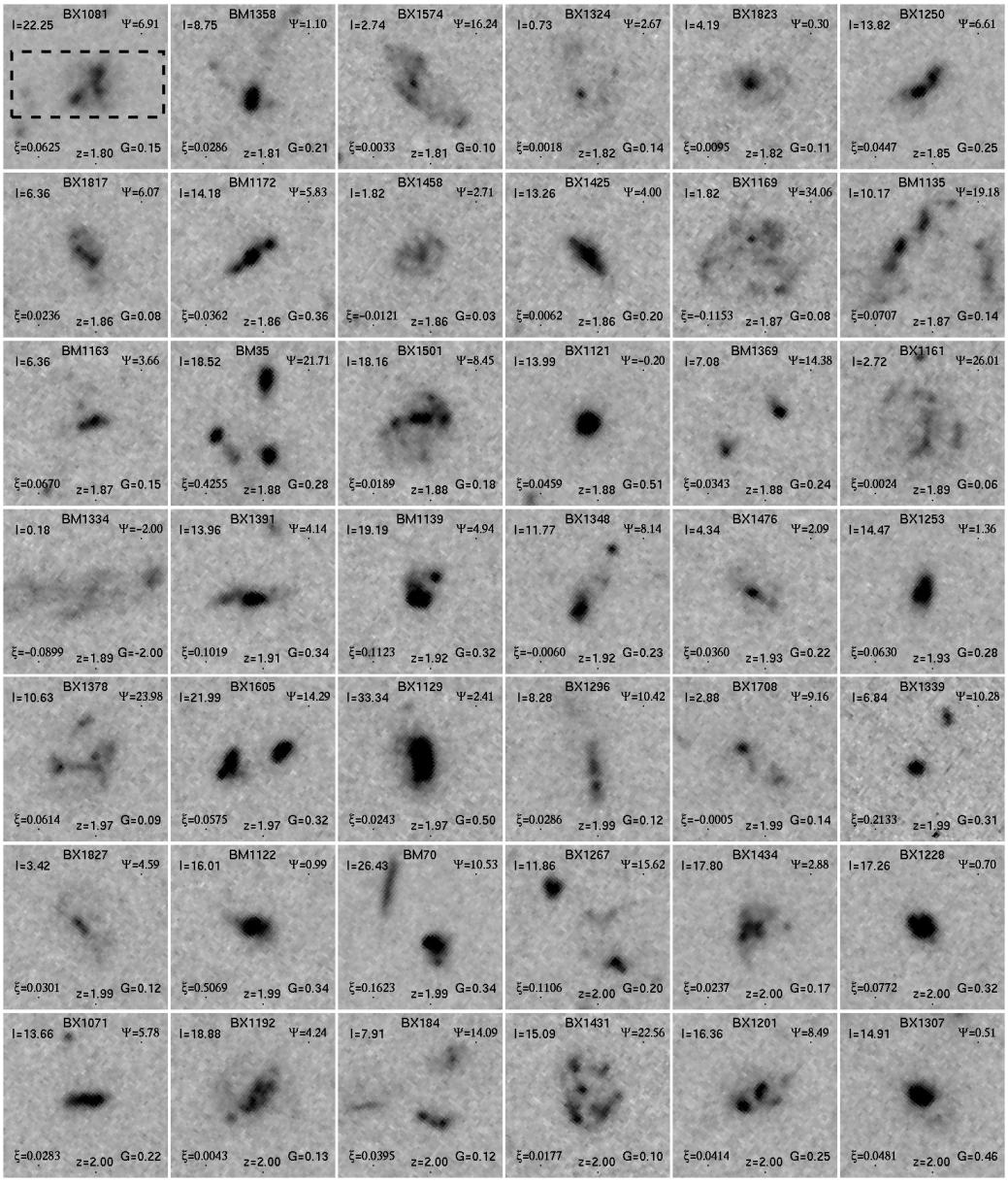

Figure 2.2 *HST*-ACS rest-UV morphologies of the $z \sim 2-3$ galaxy sample, sorted in order of increasing redshift. All panels include the galaxy name, redshift z, and morphological parameters size (I), gini (G), multiplicity (Ψ), and color dispersion (ξ). Images are 3 arcseconds on a side, oriented with North up and East to the left. Values of -2.00 for a particular morphological parameter indicate that a galaxy had too few pixels of suitably high surface brightness to define the parameter. Greyscale is logarithmic and chosen to emphasize the visibility of fainter nebulous regions, the details of high surface brightness features are thus suppressed. The $1\farcs2$ width of the LRIS slit is indicated by a dashed box in the top left panel.

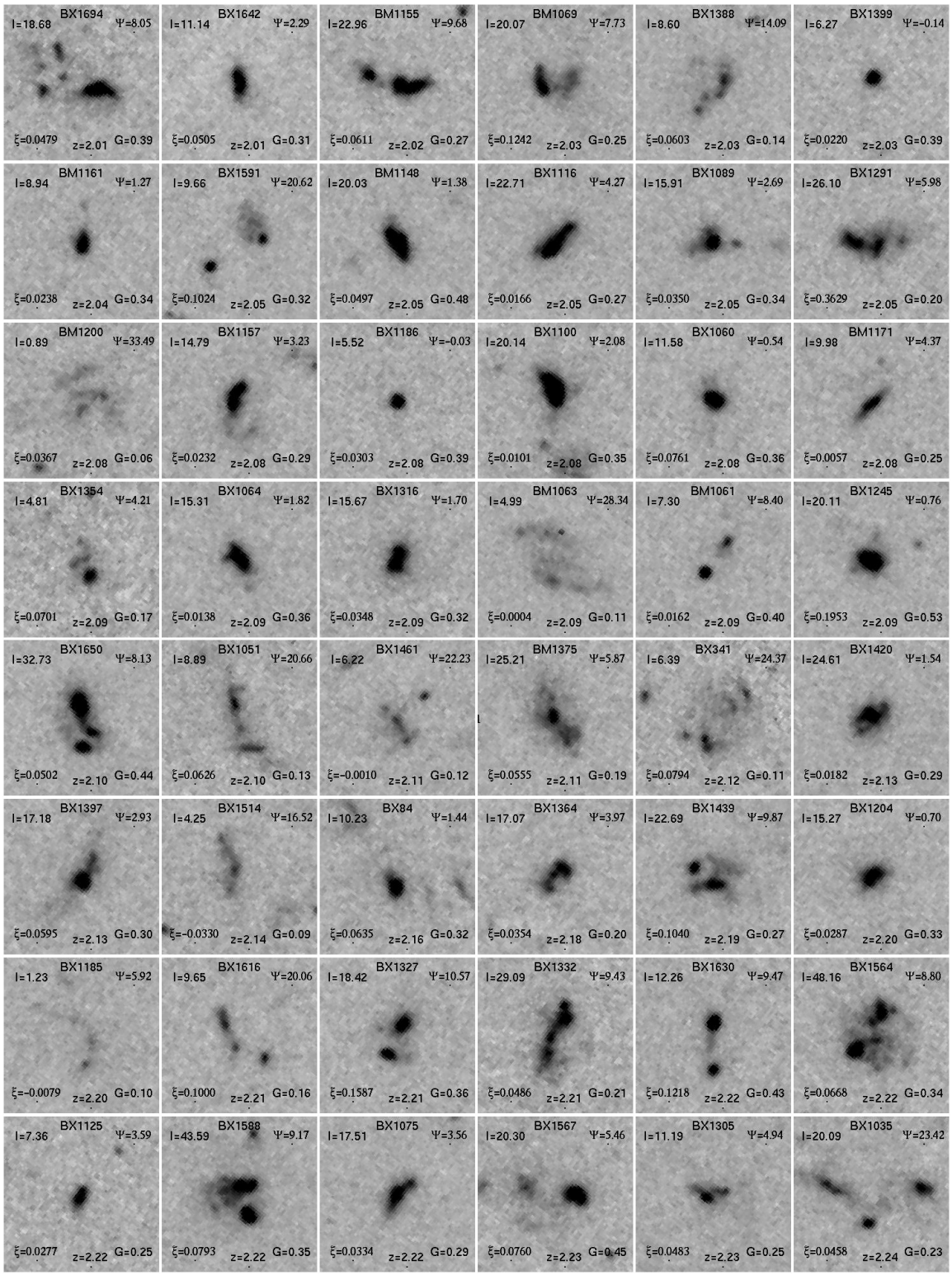

Figure 2.2 (continued)

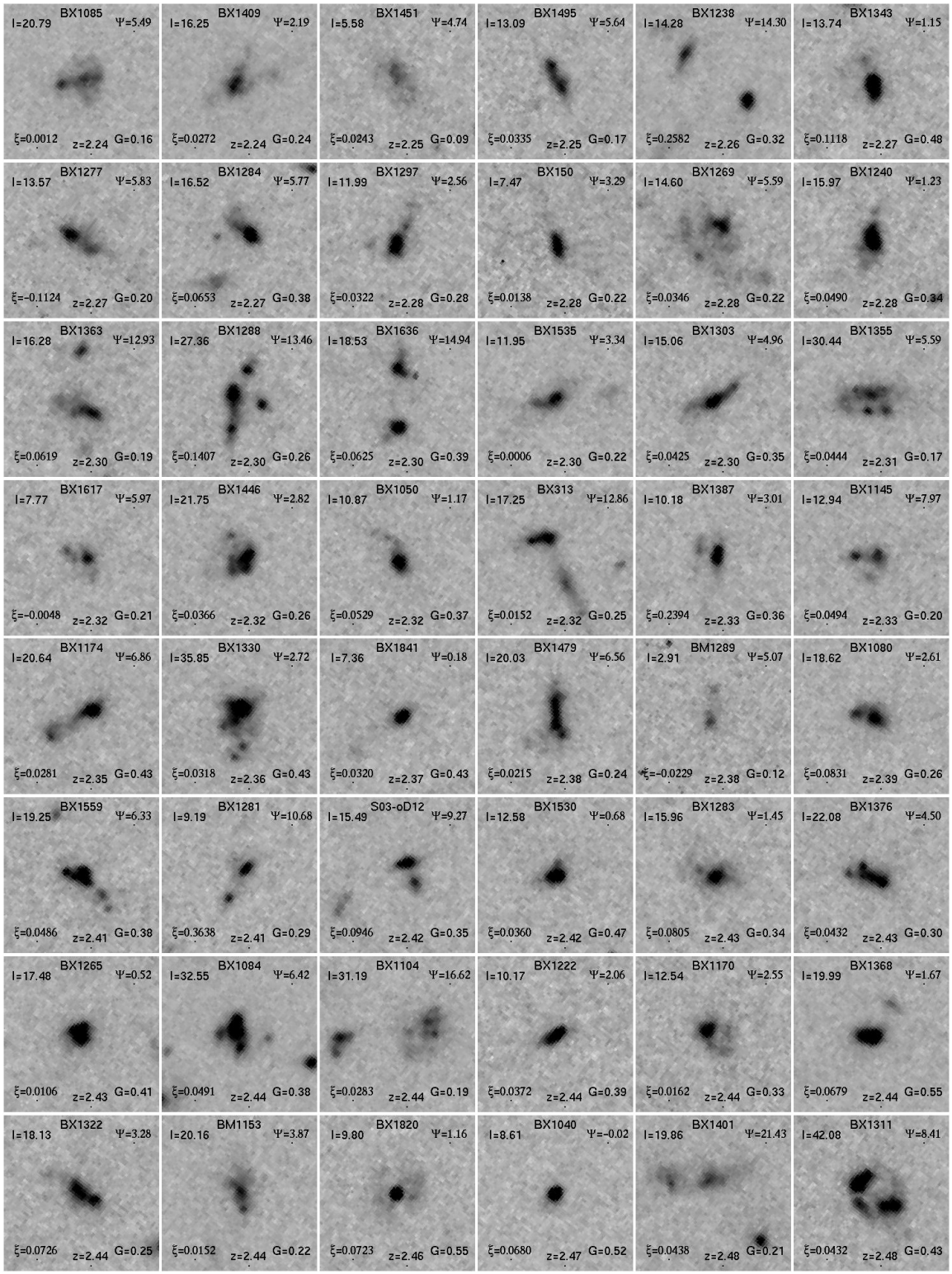

Figure 2.2 (continued)

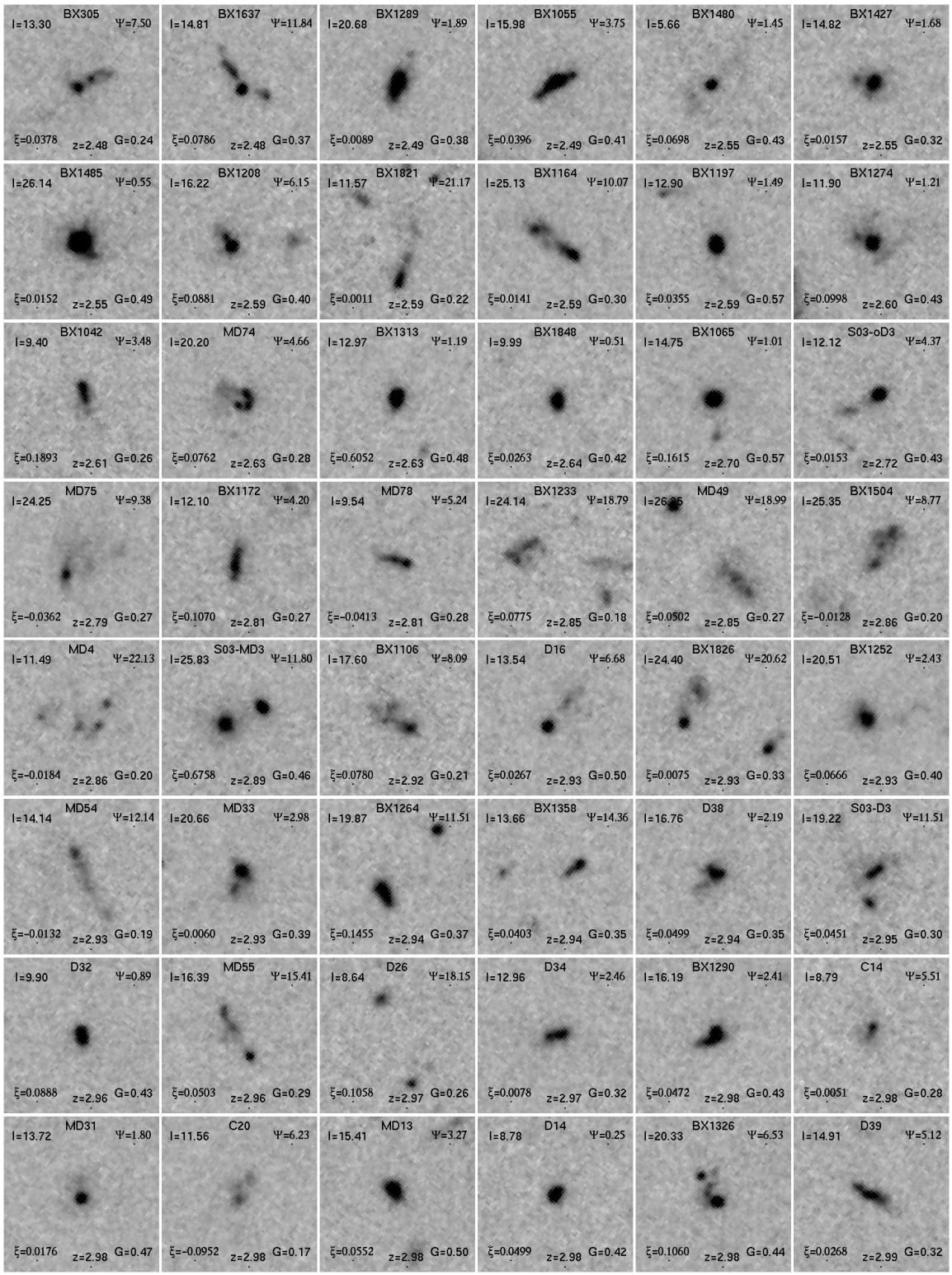

Figure 2.2 (continued)

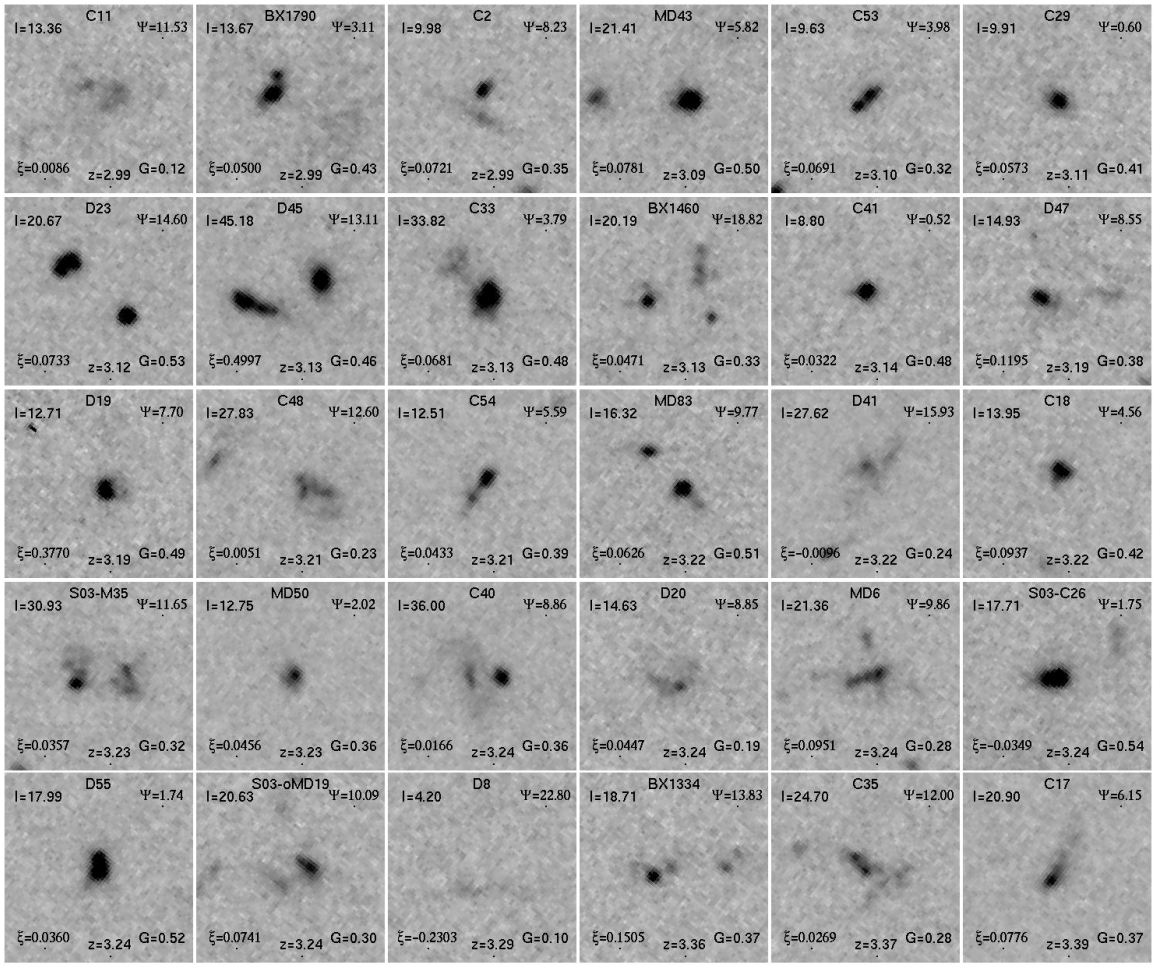

Figure 2.2 (continued)

upon the particular choice of center[2] and smoothing length (see Lotz, Primack, & Madau 2004, hereafter LPM04, for a detailed discussion).

We therefore favor a non-parametric approach to classification similar to that discussed by Abraham et al. (2003), LPM04, and Lotz et al. (2006) who define the gini coefficient G as a measure of the uniformity of the flux distribution within a source. In the following sections, we describe this and three additional non-parametric coefficients which we find effectively characterize the irregular morphologies of these $z \sim 2-3$ galaxies. We note that although we considered a host of additional parameters in our analyses (including the Petrosian radius and a non-parametric "Petrosian area"), we found that they provided no additional information and therefore omit them from further discussion.

2.3.1 Pixel Selection

It is of critical importance when measuring the morphologies of faint and highly irregular galaxies to apply uniform selection criteria by which to assign pixels to a galaxy as opposed to the surrounding sky (i.e., defining the "segmentation map" of the source). A variety of criteria have been adopted in previous studies, ranging from complex methods based upon curve-of-growth analysis (e.g., LPM04) to basic surface brightness selection (e.g., Abraham et al. 2003).

The first of these methods, while robust to cosmological surface brightness dimming, can be non-trivial to implement in a manner consistent with non-parametric analysis. As outlined by LPM04, the curve-of-growth method calculates the elliptical Petrosian radius of a source (i.e., the radius from the center of the source at which the average flux falls to a fixed fraction of the total inscribed flux; Petrosian 1976), and assigns to the segmentation map all pixels within a suitably large radius of this center whose fluxes are greater than the value at the Petrosian radius. Unfortunately, such a segmentation map enforces elliptical Petrosian radii about a particular center and introduces biases similar to that of the CAS system into the resulting morphological coefficients. While such a segmentation map is useful for sources with approximately elliptical isophotes, we find that it tends to fail for

[2]The asymmetry parameter A is strictly found by numerically searching through the image for the choice of center which minimizes the value of A (see discussion by Conselice, Bershady, & Jangren 2000). While this relaxation technique partially mitigates bias arising from poor centering, it does not address the underlying bias present in the assumption of circular symmetry for galaxies as irregular as those depicted in Figure 2.2.

galaxies with multiple components or extremely irregular shapes, since pixels at a particular "Petrosian" radius from an artificial center tend to include a large number of sky pixels, decreasing the threshhold for surface brightness selection and resulting in some fraction of sky pixels being allocated to the galaxy in the final segmentation map. While the most noticeable cases may be fixed by hand, this nonetheless introduces a bias as a function of morphological irregularity. We explore the effect of this bias on the measured gini coefficient in further detail in §2.3.3.

In contrast, the second of these methods (basic surface brightness selection) takes no account of surface brightness dimming but is more amenable to non-parametric analysis. However, with the aid of our confirmed spectroscopic redshifts for each galaxy in the optically selected sample, we adapt this morphology-independent surface brightness selection technique to utilize a variable threshhold tuned to select pixels in an identical range of intrinsic surface brightnesses at each redshift.

Our segmentation map is calculated as follows: For each galaxy, we use our initial estimates of the position (based on seeing-limited $U_nG\mathcal{R}$ imaging) to calculate the first-order moment of the *HST*-ACS UV flux distribution within a 1.5 arcsecond (30 pixel) radius. A revised value for the center is calculated using this first-order moment, and all pixels within a 1.5 arcsecond radius (i.e., slightly larger than the size of the largest galaxy in our sample, so the exact position of the "center" is unimportant) of this new center are considered as possible candidates for assignment to the segmentation map. While the ACS data product images have already been sky subtracted, we find that this subtraction is sometimes imperfect and therefore subtract off residual sky flux measured in an annulus of radius 1.5–2 arcseconds around the revised center (using a 3σ rejection algorithm to eliminate possible contaminating flux from sources which are nearby in projection). Generally, these residual sky fluxes were small compared to the calculated object flux.

Once this pre-processing is complete, we assign to the segmentation map all pixels whose flux is at least $n\sigma$, where σ is the standard deviation of pixel values in the sky annulus, and where n varies with redshift as

$$n = 3\left(\frac{1+z}{1+z_{\max}}\right)^{-3}. \tag{2.1}$$

This variable surface brightness selection compensates for the effects of cosmological dim-

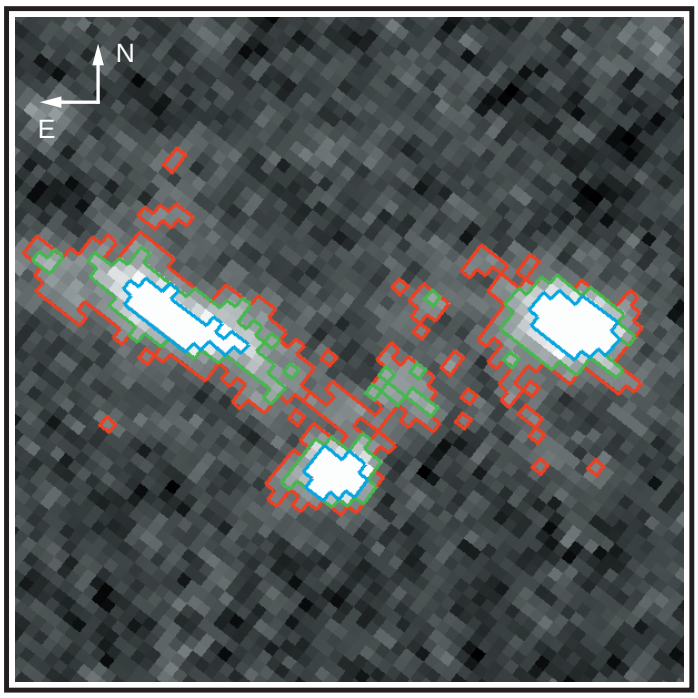

Figure 2.3 Stacked ACS rest-UV image of HDF-BX1035 ($z = 2.238$), overplotted with outlines of the 3, 5, and 10σ segmentation maps (red, green, and cyan outlines, respectively). The greyscale is linear in flux with the whitepoint set to 10σ, the field of view is 3×3 arcseconds (corresponding to a physical region 25×25 kpc at the redshift of the source).

ming throughout our range of sample redshifts since (for a fixed observed bandpass) surface brightness scales as $(1+z)^{-3}$ and our selection criteria therefore include pixels of the same intrinsic surface brightness at all redshifts (we make the assumption that there is no intrinsic evolution of surface brightness with redshift, although see discussion in §2.3.2). We set $z_{\rm max} = 3.4$ (i.e., the upper end of our redshift distribution), so the value of the selection threshhold varies by a factor of about four across our redshift interval from 3σ at redshift $z = 3.4$ to $\sim 12\sigma$ at $z = 1.8$. We neglect the change in angular size with redshift since the angular diameter distance changes by only ~ 13 % over $z \sim 1.8 - 3.4$ for our assumed cosmology. The physical interpretation of our adopted segmentation map is illustrated in Figure 2.3, which shows the pixels selected for a typical source according to 3, 5, and 10σ criteria.

We note that by considering only flux within a 1.5 arcsecond radius we effectively restrict our sensitivity to morphology on distance scales $\lesssim 13$ kpc at the redshift of our sample, sim-

ilar to previous analyses (Conselice et al. 2003a; LPM04; Lotz et al. 2006) whose selection radii range up to about 10 kpc. Based on visual analysis of ACS and ground-based color maps, this appears to be the optimal choice of distance scale to include the majority of likely components for a particular galaxy whilst almost entirely excluding probable contaminants which appear nearby in projection. While it is likely that some gravitationally interacting systems extend considerably beyond 13 kpc, we neglect these distant components in our characterization of the system morphology since 1) our photometric and spectroscopic data is sensitive only to light at radii $\lesssim 1.5$ arcseconds, and 2) close interactions are more likely than distant to produce observable changes in the physical state of a galaxy.

2.3.2 The Size Parameter: *I*

The simplest morphological parameter to define is the projected physical size of the source (I) seen above our surface brightness threshhold (we use I instead of the more intuitive S to avoid confusion with the "clumpiness" parameter of Conselice et al. 2003). Since the radius of a galaxy is not meaningful for multi-component systems, we use our spectroscopic redshifts to define I as the total projected galaxy area in square physical kpc[3]. That is,

$$I = N(0.05\,\frac{\mathrm{arcsec}}{\mathrm{pixel}})^2\,(2.4\times10^{-11}\frac{\mathrm{ster}}{\mathrm{arcsec}^2})\,D_A^2, \tag{2.2}$$

where N is the total number of 50 mas $\times$ 50 mas pixels in the segmentation map, and D_A is the angular diameter distance (in kiloparsecs) to redshift z for the assumed cosmology. This parameter makes no attempt to discriminate between sources on the basis of the total amount or relative distribution of flux within the segmentation map, and may therefore classify similarly both small strongly nucleated sources (which have a low number of high flux pixels) and large yet extremely faint and nebulous sources (which have a low number of low flux pixels barely satisfying the surface brightness selection criteria).

In Figure 2.4 we plot the distribution of I for the $z\sim2$ and $z\sim3$ samples (upper left panel, black and red histograms, respectively). I typically ranges in value from less than 5 kpc^2 for faint and nebulous sources to around 10 kpc^2 for the most strongly nucleated single sources, and up to as much as 48 kpc^2 for the brightest extended sources. In the

[3]Given the small change in angular diameter distance across the redshift range of the sample there is little practical difference between using physical and angular sizes in our analyses.

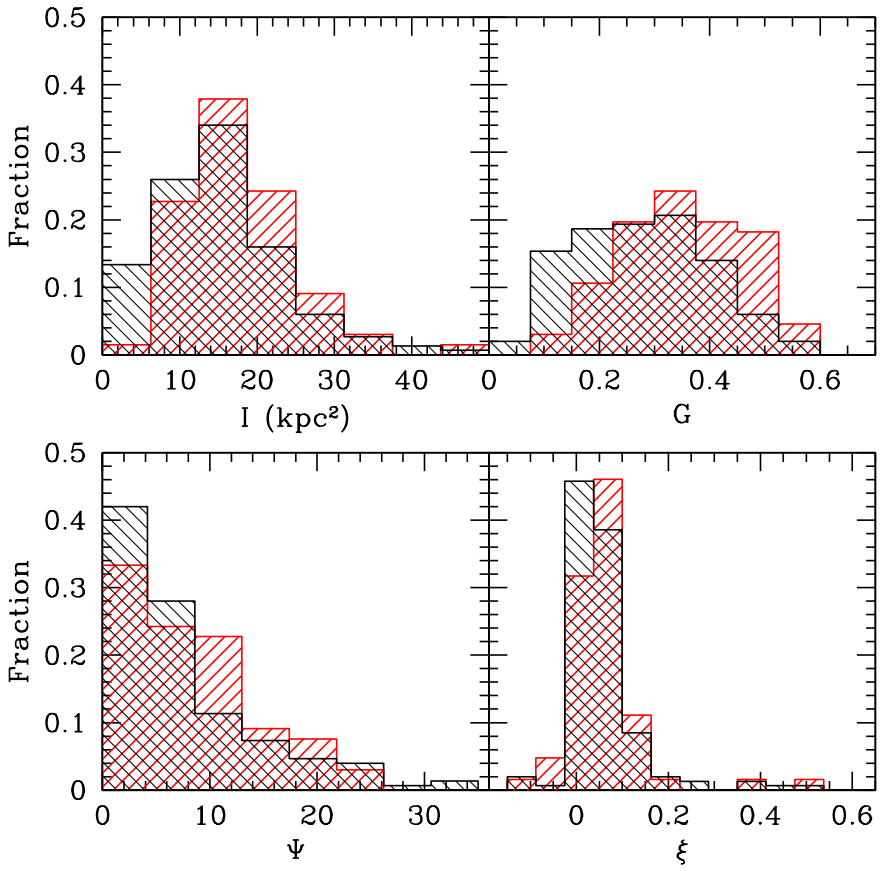

Figure 2.4 Relative distribution of the morphological parameters I (size), G (gini), Ψ (multiplicity), and ξ (color dispersion) for the redshift $z \sim 2$ and $z \sim 3$ samples (black and red histograms respectively). Counts are normalized by the total number of galaxies in each sample.

$z \sim 2$ and $z \sim 3$ samples the mean projected size is $\bar{I} = 15.0 \pm 0.7$ kpc^2 and $\bar{I} = 17.4 \pm 0.9$ kpc^2, respectively[4]. This small ($\sim 3\sigma$) apparent increase in average size from $z \sim 2$ to $z \sim 3$ arises because the $z \sim 3$ sample does not extend as far down the luminosity function as the $z \sim 2$ and small faint sources are therefore underrepresented in the $z \sim 3$ sample. If we compare only the fraction of the $z \sim 2$ sample that overlaps the $z \sim 3$ in rest-frame UV luminosity ($L_{1600} > 2 \times 10^{10} L_{\odot}$; Reddy et al. 2006a)[5] the average value of I at $z \sim 2$ rises to $\bar{I} = 16.7 \pm 1.0$ kpc^2, which is within 1σ of the $z \sim 3$ result. Indeed, we note that in a recent analysis designed to more precisely measure the size evolution of galaxies (as determined from their SExtractor half-light radii) Ferguson et al. (2004) found that the angular size of single-component galaxies decreases with increasing redshift above $z \sim 1$.

2.3.3 The Gini Parameter: *G*

The gini coefficient (G, originally attributed to Corrado Gini [1912] and first introduced into the astronomical literature by Abraham et al. 2003) measures the cumulative distribution function of a population and may be used to distinguish between the cases for which flux is strongly nucleated versus uniformly nebulous (see LPM04 for a detailed introduction). Mathematically, G may be calculated as (Glasser 1962):

$$G = \frac{1}{\bar{X} N(N-1)} \sum_{i=1}^{N} (2i - N - 1) X_i \tag{2.3}$$

where $\bar{X}$ is the average flux and the X_i pixel fluxes are sorted in increasing order before the summation over all N pixels in the segmentation map. The normalization prefactor multiplying the summation ensures that G takes values from zero to one inclusive, where low values indicate a uniform flux distribution and high values a concentration of flux in a few pixels.

Practically, we find that G differentiates clearly between galaxy morphologies based on the degree of nucleation of their UV emission—sources which appear very nebulous generally have $G \lesssim 0.2$, while sources with strongly nucleated emission have $G \gtrsim 0.5$ (see Fig. 2.2). The wide range of galaxies with some combination of nucleated and nebulous emission

[4]Uncertainties quoted henceforth are uncertainties in the mean unless otherwise specified.

[5]62% of the $z \sim 2$ sample have well determined measurements of L_{1600}, compared with 41% of the $z \sim 3$ sample. 84% of the $z \sim 2$ sample with measured L_{1600} have $L_{1600} > 2 \times 10^{10} L_{\odot}$.

components fall in a continuous distribution between these values. We note that this range of values ($0 < G \lesssim 0.6$) is substantially different from that calculated for $z \sim 2-4$ HDF-N Lyman Break galaxies (LBGs) by Lotz et al. (2004, 2006), who found $0.4 < G < 0.7$. While some discrepancy is to be expected with the LPM04 results since these authors used rest-optical data from HST-NICMOS (although this difference should be minimal in light of the similarity between rest-UV and rest-optical morphologies), we should expect greater similarity to the findings of Lotz et al. (2006) who used HST-ACS rest-UV data similar to our own. This difference in results appears to arise primarily from the adopted pixel selection method; we find that elliptical Petrosian selection methods similar to that of LPM04 tend to include more sky pixels at the "Petrosian" radius for highly irregular and nebulous objects (i.e., low G in our sample), which lowers the threshhold for assignment to the galaxy and includes more sky pixels in the resulting segmentation map. Including extra sky pixels in the map makes the genuine galaxy pixels appear to be comparatively more rich in flux, artificially increasing the value of G calculated for the sources. Applying a segmentation map similar to that of LPM04, we find that the gini coefficient calculated for our highest G sources remains relatively unchanged, while our low gini sources increase their values of G considerably, artificially compressing the range of values to $0.4 \lesssim G \lesssim 0.6$, closely mimicking the range of values presented by LPM04. We conclude that while the LPM04 values are accurate in the sense that a $G = 0.4$ (in their calculation) galaxy is more nebulous than a $G = 0.6$, the noise introduced by this compression in dynamic range severely hampers the discriminating power of the gini coefficient.

A histogram of values of G is plotted in Figure 2.4, and suggests that the mean value of the gini coefficient appears to change from $\bar{G} = 0.27 \pm 0.02$ at $z \sim 2$ to $\bar{G} = 0.35 \pm 0.01$ at $z \sim 3$. To some extent this may be due to the underrepresentation of faint, nebulous objects in the $z \sim 3$ sample (see §2.3.2), but even when restricting the sample to the same range in intrinsic UV luminosity the difference between the two samples is of order 3σ. This suggests that the UV emission from objects at $z \sim 3$ is genuinely slightly more nucleated than at $z \sim 2$, consistent with the finding of Ferguson et al. (2004) who demonstrated that apparent galaxy size at constant luminosity decreases with increasing redshift.

We note that to first order, G does not distinguish between sources based upon their number of nucleated components— i.e., a galaxy with two or more apparent nucleations

has a value of G nearly identical to a galaxy with only one, so long as the cumulative distribution of light is similar. That is, the exact *spatial* distribution of flux is irrelevant to G, which is instead sensitive to the overall *curve of growth* of the total flux.

2.3.4 The Multiplicity Parameter: Ψ

Our third classification parameter (Ψ) is designed to discriminate between sources based on how many apparent components the light distribution is broken into, i.e., how "multiple" the source appears. This parameter is similar to both the asymmetry parameter A (Schade et al. 1995) and the second-order moment of the 20% brightest pixels (M_{20}, LPM04) in that it is sensitive to the presence and distribution of multiple clumps of flux. However, both A and M_{20} have their limitations: A depends strongly on the assumption of overall circular symmetry about some central point for each galaxy, while M_{20} is normalized by the moment of the segmentation map to remove the effect of overall galaxy size, which unfortunately results in a limited dynamic range since the segmentation map and the 20% brightest pixels often have a similar spatial distribution. In contrast, Ψ is defined in a manner that requires neither a center of symmetry nor a conventional normalization.

Using the observed flux distribution as a proxy for "mass", we calculate the "potential energy" of the light distribution projected into our line of sight as

$$\psi_{\rm actual} = \sum_{i=1}^{N} \sum_{j=1, j\neq i}^{N} \frac{X_i X_j}{r_{ij}}, \tag{2.4}$$

where the summation of the pixel fluxes X_i and X_j runs over all N pixels in the segmentation map, and r_{ij} is the distance (in pixels) between pixels i and j. This value is normalized by that which would be achieved with the most compact possible re-arrangement of the flux pixels, i.e., the configuration which would require the most "work" to pull apart. We re-arrange the physical positions of the N pixels of the segmentation map in a circular configuration with the brightest pixel in the center and with pixel flux decreasing outwards with radius. Calling the distance between pixels i and j in this re-arranged map r'_{ij}, the projected potential energy of this compact light distribution is

$$\psi_{\rm compact} = \sum_{i=1}^{N} \sum_{j=1, j\neq i}^{N} \frac{X_i X_j}{r'_{ij}}. \tag{2.5}$$

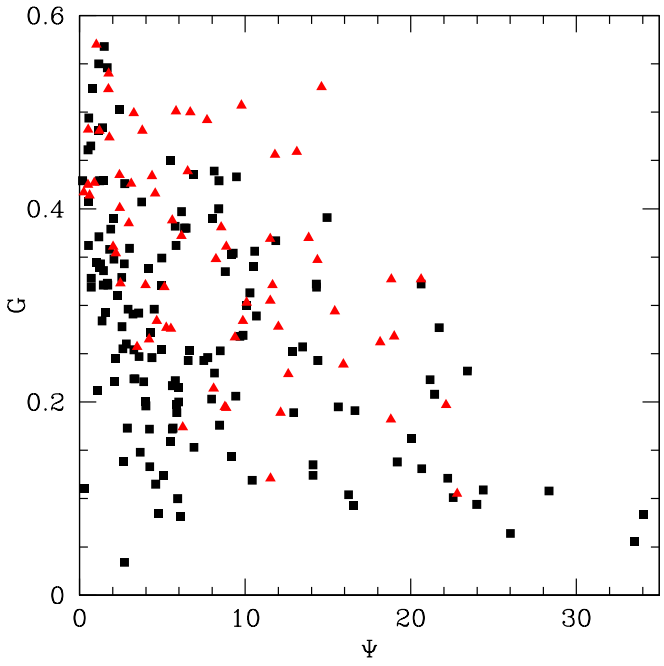

Figure 2.5 Distribution of G (gini) versus Ψ (multiplicity) for galaxies in the $z \sim 2$ (black squares) and $z \sim 3$ (red triangles) samples. Values are correlated in the sense that faint, nebulous galaxies tend to be broken into a greater number of non-contiguous components.

The multiplicity coefficient is then defined logarithmically as the ratio of these two quantities:

$$\Psi = 100 \times \log_{10}\left(\frac{\psi_{\rm compact}}{\psi_{\rm actual}}\right). \tag{2.6}$$

As shown in Figure 2.4, Ψ ranges from 0 up to about 30. Typically, $\Psi = 0-2$ for single well-nucleated sources, $\Psi \sim 5$ for sources which are beginning to show a second component in addition to the main nucleation, and $\Psi \sim 10$ for strong double-nucleation systems. At values of $\Psi > 10$, Ψ increases as the number and separation distance of nucleations increase, but numerical distinctions become less obvious until at $\Psi \gtrsim 25$ the majority of sources are low G nebulous sources for which Ψ breaks down as a useful statistic (see §2.3.6). There is therefore some degree of correlation between Ψ and the gini coefficient G (Fig. 2.5) since sources with very nebulous emission (i.e., small G) tend to have very spread out flux distributions (i.e., large Ψ). However, this is of secondary importance to the largely orthogonal classification permitted by these two parameters; while G is most sensitive to

the overall curve of growth of the flux distribution and fairly insensitive to the number of nucleated components, Ψ is sensitive to the number of bright components and comparatively insensitive to the overall curve of growth. We note that since Ψ is a flux-weighted statistic it is more sensitive to bright pixels, and therefore a bright central source with an extremely faint secondary source will tend to have low Ψ, while the same central source with a bright secondary source will tend to have higher Ψ.

2.3.5 The Color Dispersion: ξ

Finally, we capitalize on the available multi-wavelength *HST*-ACS data by defining the color dispersion parameter ξ (Papovich et al. 2003), which quantifies the degree of morphological difference between two bandpasses. Applied between rest-optical and UV wavelengths, ξ can measure the difference in spatial distribution between stellar populations of differing ages, convolved with variations in the dust distribution and resulting extinction (Papovich et al. 2003). Using rest-UV data alone ξ is a less powerful statistic, but nevertheless potentially informative.

We calculate ξ as

$$\xi(I_V, I_z) = \frac{\sum(I_z - \alpha I_V - \beta)^2 - \sum(B_z - \alpha B_V)^2}{\sum(I_z - \beta)^2 - \sum(B_z - \alpha B_V)^2}, \tag{2.7}$$

where I_V, I_z are the object pixel fluxes in V and z bandpasses, respectively[6]; B_V, B_z the background sky flux in the bandpasses; α is the flux ratio between the two bands; and β represents the difference in background levels between the two bands. In brief, the first term in the numerator represents the summed square difference in pixel fluxes between the bands, the first term in the denominator the summed square total object flux (for normalization), and the second terms in both numerator and denominator represent corrections to statistically eliminate contributions to ξ from the natural background sky variance. Further details regarding the definition of this statistic are given by Papovich et al. (2003).

As shown in Figure 2.4, typical values range from $\xi \sim 0.0$ to 0.15, with $\bar{\xi} = 0.057 \pm 0.006$ at $z \sim 2$ and $\bar{\xi} = 0.061 \pm 0.011$ at $z \sim 3$ (i.e., consistent with a constant value to well within

[6]While use of the B and z bands would provide a greater wavlength baseline for morphological differences, we use V instead since B is blanketed by absorption from the Lyman α forest for galaxies in the upper end of our redshift range.

the uncertainty). We note that this range of values is larger than that of $\xi \sim 0.0 - 0.05$ found by Papovich et al. (2005) for a sample of $z \sim 2.3$ galaxies measured between rest-UV and optical bandpasses. The origin of this discrepancy is uncertain, although it is likely that different galaxy samples, segmentation maps, and bandpasses all contribute. By and large, it appears that our calculated ξ is dominated mainly by scatter rather than by genuine differences between the apparent morphology in V and z bands. Figure 2.6 shows that for two galaxies with $\xi = 0.023$ and $\xi = 0.112$ the most obvious trend from V to z bands is an overall decrease in the signal-to-noise ratio. Given the similarity of the effect in both cases, it is not readily apparent why the two galaxies should have such different color dispersions.

Curiously, while ξ has no obvious correlation with a visible difference in morphology between bands, it does correlate with the Gini coefficient G of a source (as shown in Fig. 2.7) in the sense that ξ is (on average) slightly larger in the most nucleated sources. This is likely a consequence of the flux-weighting of ξ— high flux pixels have greater absolute variation between bandpasses and tend to dominate the sum in Equation 2.7, increasing ξ for high G sources where ξ is dominated by variation from a few bright pixels rather than averaging over a larger number of lower-variation pixels for low G sources. In conclusion, we caution that while ξ is ideally a useful statistic, in the present case it may be too erratic to provide a great deal of information.

2.3.6 Robustness of the Parameters

We test the robustness of these parameters to cosmological distance by selecting one representative galaxy for each of the five general morphological categories (defined previously in this section), artificially redshifting them through the range $z = 1.8 - 3.4$, and measuring the resulting morphologies using our variable threshhold pixel selection technique. As illustrated by Figure 2.8, in most cases we would measure consistent values for the morphological parameters for a given galaxy if it were located at any redshift throughout our sample. This constancy fails however for the most faint and nebulous of objects ($G \lesssim 0.15$, green dot-dashed line in Figure 2.8), for which the multiplicity Ψ and the color dispersion ξ can vary substantially because the number of pixels in the segmentation map is small and random variations in noise can drastically affect both the locations of selected pixels (to which Ψ is particularly sensitive) and the residual color (to which ξ is sensitive). Such

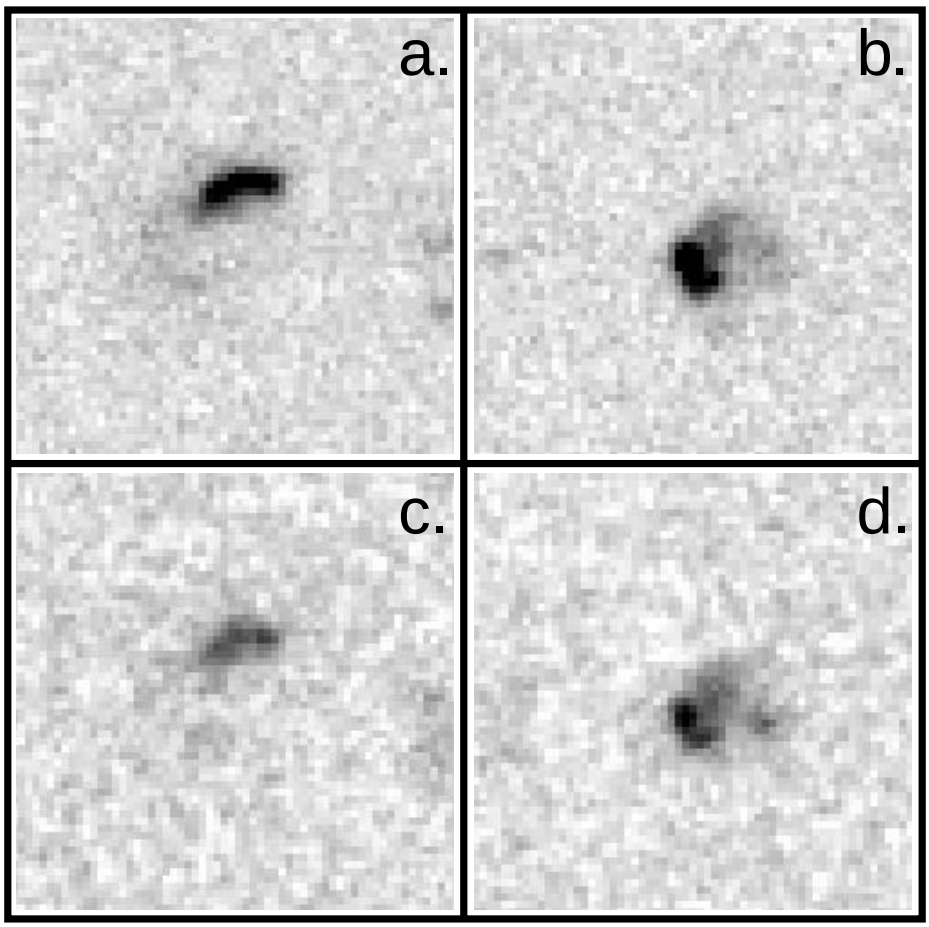

Figure 2.6 HST-ACS images of HDF-BX1157 and HDF-BM1139 in F606W (Panels a and b, respectively) and in F850LP (Panels c and d). Both galaxies have comparable redshifts (z = 2.08 and 1.92), gini (G = 0.291, 0.321), and multiplicity (Ψ = 3.23, 4.94) in the summed rest-UV image. Both galaxies show similar decrease in signal-to-noise ratio from F606W to F850LP, but have widely variant color dispersions ($\xi = 0.023, 0.112$). Image size and orientation are the same as in Figure 2.2.

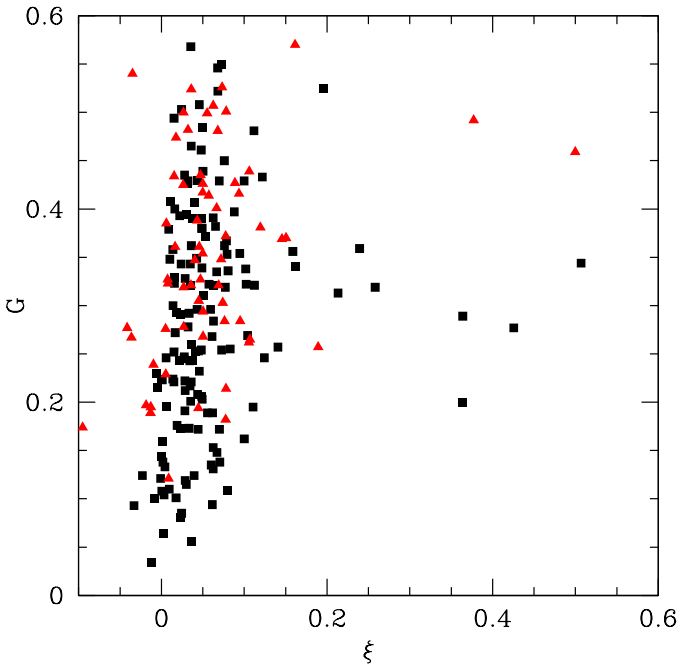

Figure 2.7 Distribution of G (gini) versus ξ (color dispersion) for galaxies in the $z \sim 2$ (black squares) and $z \sim 3$ (red triangles) samples. Note that a few extreme outliers from this trend lie outside the visible region of this plot to better illustrate the main correlation.

objects represent less than 20% of the sample however, and the importance of this effect on Ψ may be mitigated by noting that Ψ is only well-defined up to $\Psi \sim 25$. We also note a slight decrease in I with redshift to $z = 3$, followed by a smaller upturn at $z > 3.3$. The first of these effects is consistent with our neglect of the change in angular size with redshift, and the second with the inclusion of a small number of sky pixels in the segmentation map when the selection threshhold is pushed down to 3σ. Neither effect is large enough to noticeably impact our analysis.

Having demonstrated the uniformity of the selection technique, we consider what (if any) information is lost for galaxies in the lower end of the redshift range by effectively restricting our analysis to those pixels brighter than about 10σ above the background sky noise. In Figure 2.9 we plot morphological parameters calculated for the same five galaxies as before for a range of surface brightness selection threshholds. Most obviously, I decreases rapidly with increasing brightness threshhold, since correspondingly fewer pixels are included in the segmentation map. In addition, G declines noticeably as the lower-flux population is gradually omitted from the map. In contrast, Ψ and ξ remain relatively constant throughout the range of selection threshholds considered, with the exception of purely nebulous sources (dot-dashed green line) for which we have previously noted the instability of these two parameters. Most importantly however, if we neglect purely nebulous sources we note that the same *relative* information is preserved at all brightness threshholds—no matter what the threshhold it is equally possible to distinguish between the galaxy types despite the overall trends. That is, since the lines do not cross (again with the exception of the green dot-dashed line and ξ at very low threshholds) we may be confident that we are not discarding information by using a $\sim 10\sigma$ segmentation map at lower redshifts.

We now note a few caveats to this analysis which should be borne in mind. First, by using a fixed bandpass we have measured the morphologies of $z \sim 2$ and $z \sim 3$ galaxies at slightly different rest wavelengths. However, this effect should be negligible since our morphological parameters do not change substantially using data from the B, V, or I bandpasses (although they can change somewhat in the z bandpass due to the lower signal-to-noise ratio for all detections at near-IR wavelengths). Parameters calculated in each of these bands correlate very strongly with one another, differences being dominated by the limiting surface brightness reached in each band. Given that our sample consists of

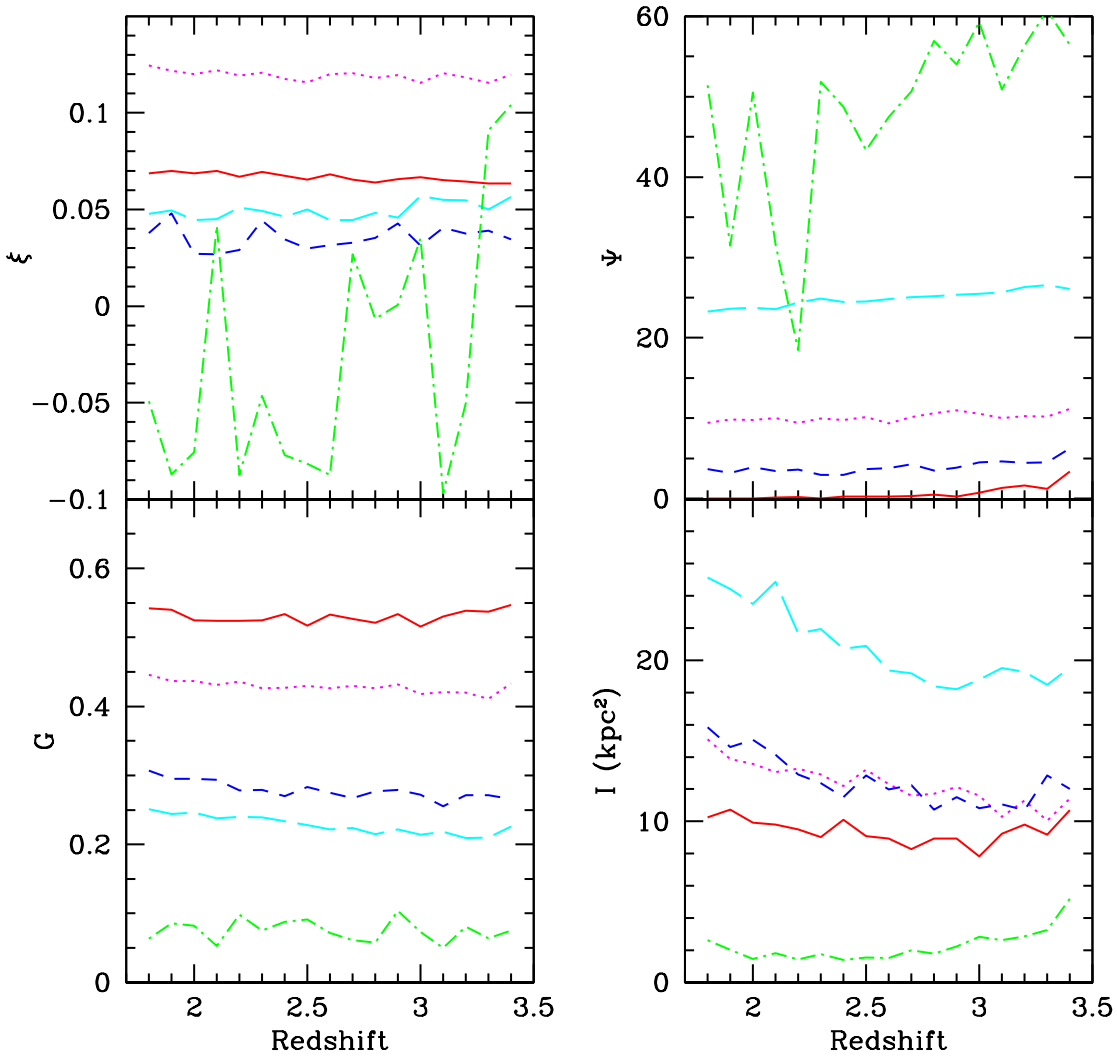

Figure 2.8 Figure illustrates the robustness of morphological parameters to redshift when using the variable surface brightness method to define the segmentation map. Colored lines indicate the trends found by artificially redshifting one representative galaxy from each of the five general morphological classes through the range $z = 1.8 - 3.4$ before performing morphological analysis. These five classes (defined in §2.3) and their representative galaxies are: single nucleated source (BX 1040: solid red line), multiple nucleated source (BX 1630: dotted magenta line), single nucleated source with nebulosity (BX 1297: short-dashed dark blue line), multiple nucleated source with nebulosity (BX 1035: long-dashed cyan line), and purely nebulous source (BX 1169: dot-dashed green line).

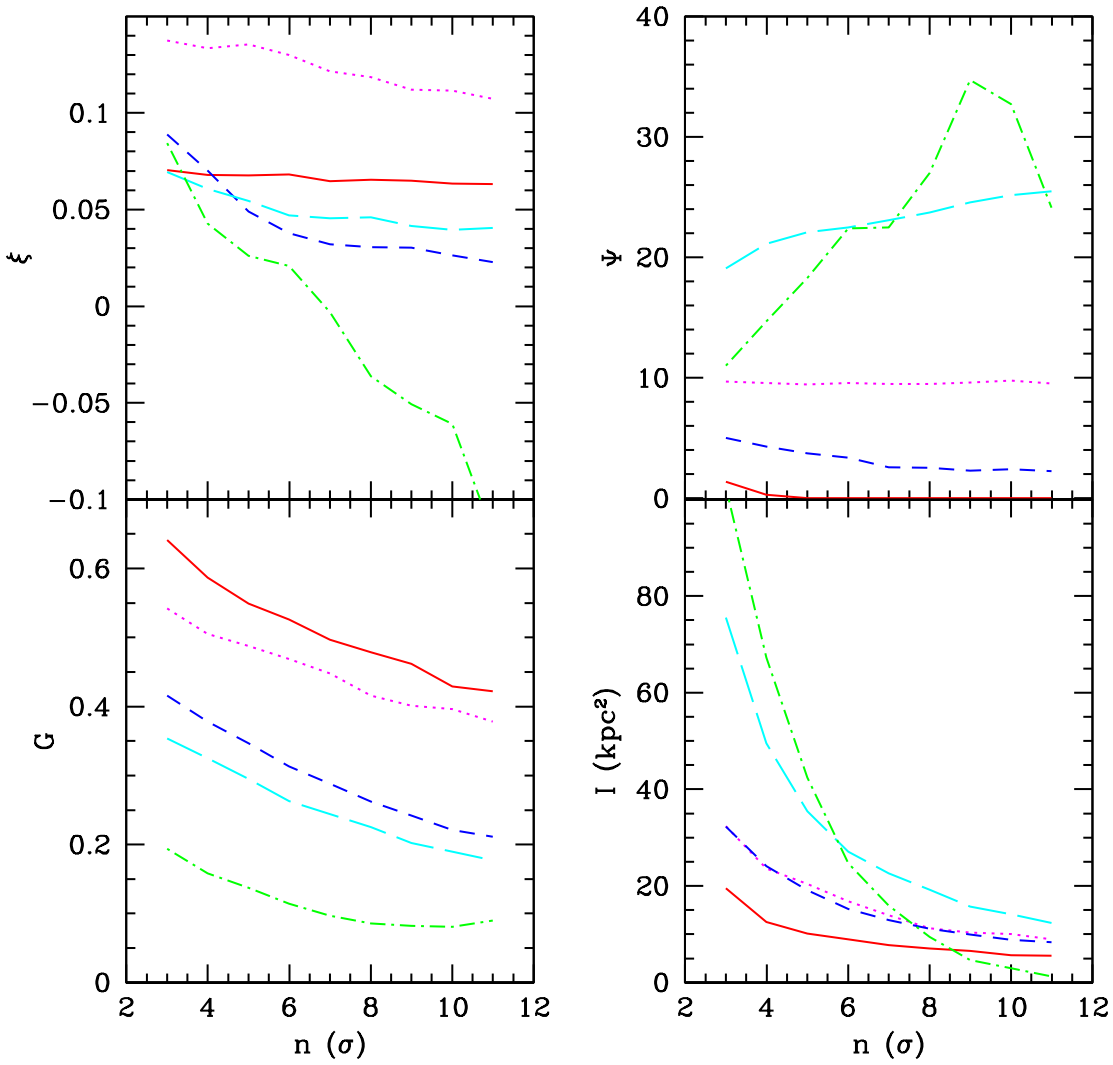

Figure 2.9 As Figure 2.8, but plots the calculated values of morphological parameters for the five classes of galaxies as a function of the adopted surface brightness selection threshhold in multiples of the background sky noise σ. Note for comparison that segmentation maps corresponding to the 3, 5, and 10σ selection regions for BX1035 (i.e., long-dashed cyan line) are shown in Figure 2.3.

actively star-forming galaxies, this is perhaps not surprising since young massive stars tend to dominate the SED out to at least rest-frame blue wavelengths. Second, we have neglected surface brightness evolution throughout our sample. Since our primary goal is to investigate the physical meaning of morphology rather than providing a detailed comparison between samples at different redshifts we choose not to introduce uncertain corrections for such effects into our analysis. Third, it is possible that some regions of flux included in our segmentation maps are due to chance alignments of some object at a very different redshift than the target galaxy. However, we judge this to be an unlikely major source of contamination to our sample since 1) the various pieces of the galaxies have consistent colors, and 2) the total number density of optically selected $z \sim 2-3$ galaxies is ~ 10 arcmin^{-2} to $\mathcal{R} = 25.5$ (Steidel et al. 2004), giving a low probability for chance supposition of two unrelated galaxies within 1.5 arcseconds. Finally, we have made no correction for the effects of galaxy inclination to the line of sight. While it is conceivable, and indeed likely, that some of the variance in apparent morphology may be due simply to different orientations relative to the line of sight, our knowledge of these galaxies is at present insufficient to allow us to compensate for such effects in any meaningful way.

Of the four parameters which we have introduced, the G–Ψ classification scheme best reproduces the morphological trends apparent to the eye. This system is illustrated in Figure 2.10, which shows a representative set of galaxies from our sample and demonstrates how these two parameters serve to distinguish galaxies based on their degree of nucleation and number of components. Since surface brightness dimming and bandshifting make it difficult to associate the morphologies of $z \sim 2-3$ sources with galaxies in the local universe, we avoid such direct, and potentially misleading comparisons. We describe the *sense* of our classification parameters by noting, however, that early-type galaxies typically are larger (i.e., larger I), more concentrated (larger G), less multiple (lower Ψ), and have lower color dispersion (ξ) than their late-type counterparts, which are instead dominated by emission from multiple scattered knots of star formation. A more thorough overview of the relation between local and high-redshift galaxies is given by LPM04.

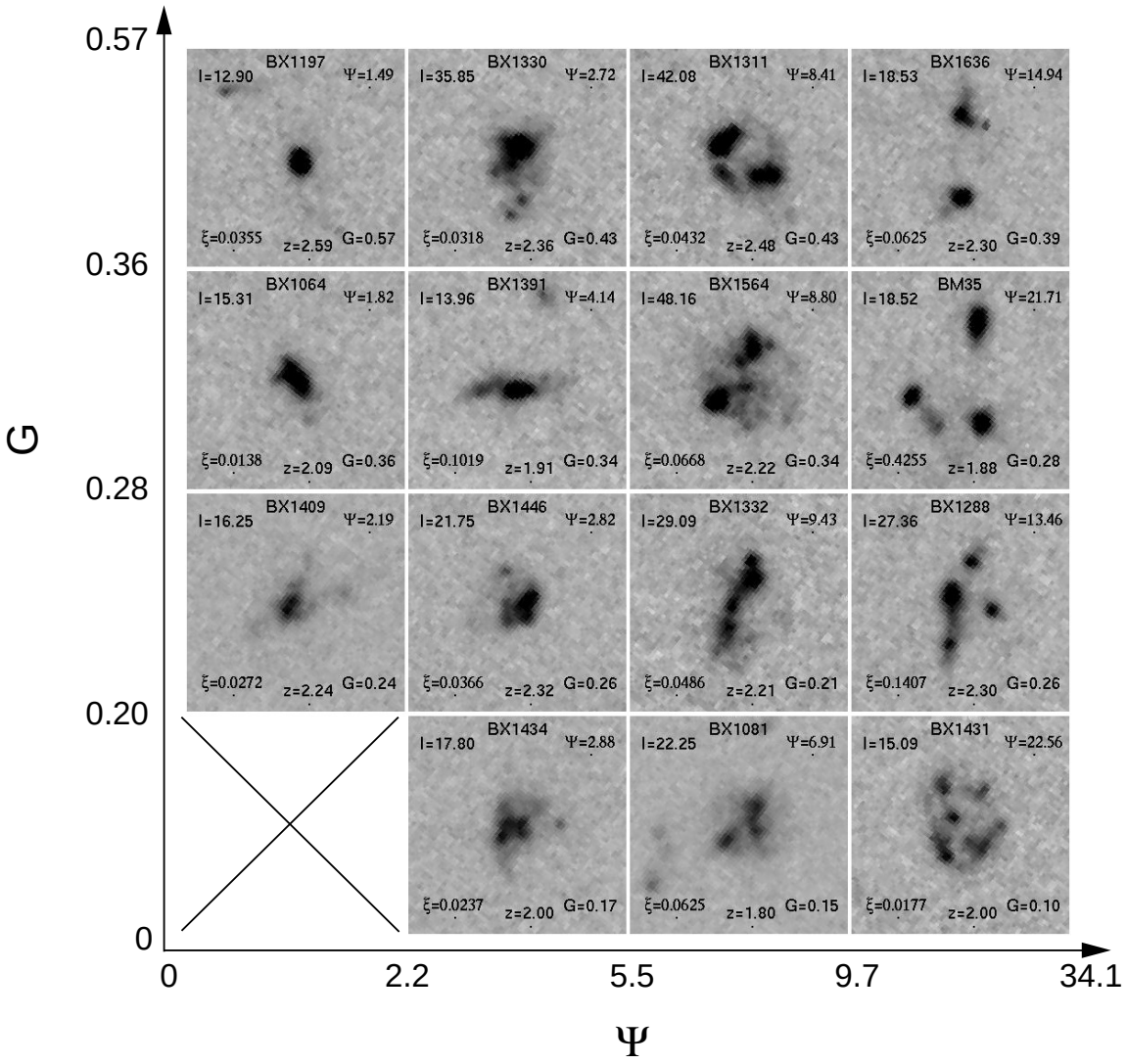

Figure 2.10 As Figure 2.2: *HST*-ACS rest-UV morphologies of redshift $z \sim 2$ galaxies classified according to gini (G) and multiplicity (Ψ) parameters. Horizontal and vertical bin ranges are chosen to divide the sample into quartiles. Increasing values of G correspond to increasing nucleation of source emission, and increasing values of Ψ correspond to increasing number of components.

2.4 OVERVIEW OF REST-UV SPECTRA

2.4.1 Spectral Processing

As part of an ongoing Keck LRIS-B spectroscopic survey (Steidel et al. 2004) we have compiled UV spectra of our 216 target galaxies in the GOODS-N field, and here explore how these spectra correspond to the morphology of their host galaxies. Unfortunately, spectra of individual galaxies are rarely of sufficient quality to accurately measure the strengths of their emission/absorption components, and we therefore divide the spectra into five bins according to each of our four morphological parameters and measure the strengths of features in stacks of the spectra within these bins. We find that five bins gives a suitably large number of bins across which spectroscopic trends may be assessed while still producing reasonable quality stacked spectra (each comprised of 30 galaxies at $z \sim 2$ and 13 galaxies at $z \sim 3$).

Our spectroscopic combination method is similar to that described by Shapley et al. (2003). Before stacking, individual sky-subtracted spectra were flux-calibrated and shifted to the systemic rest frame using the prescriptions given by Adelberger et al. (2005a), then resampled to a common dispersion of 1 Å pixel^{-1} and rescaled to a common mode in the range $\lambda\lambda 1250 - 1500$ Å. Spectra were manually cropped to eliminate overly noisy segments due to falloff of the LRIS-B blue-side efficiency and of the red-side dichroic transmission. The resulting spectra were averaged using a min/max rejection of hot pixels, cosmic rays, and bad sky subtraction events; three high and low values were rejected at each dispersion coordinate (corresponding to a rejection of the high/low 10% for the $z \sim 2$ sample). Continuum normalization was performed by iteratively fitting a spline function to the stacked spectrum using wavelength intervals selected to be free of strong interstellar features, giving results consistent with the normalization method described by Rix et al. (2004).

2.4.2 Key Spectral Features.

The rest-frame ultraviolet ($\lambda\lambda 1000 - 1800$ Å) spectra of rest-UV color selected galaxies are typified (Fig. 2.11) by redshifted Lyman α (Lyα) emission superposed on a broad blueshifted resonant absorption trough, and by strong velocity-broadened absorption lines due to energetic galaxy-scale outflows (Shapley et al. 2003). The strength of Lyα emis-

sion is originally governed by the rate of star formation and initial mass function (IMF) in galactic H II regions, although this raw flux is significantly modified by resonant scattering from interstellar H I, generally culminating in its eventual absorption by interstellar dust and subsequent reradiation in the infrared. The observed Lyα emission strength is therefore a complex function of neutral hydrogen column density, dust fraction, and geometric/kinematic projection of the outflowing ISM on the line of sight. Typically, observed Lyα emission is redshifted by roughly 400 km s^{-1} relative to the systemic velocity (Shapley et al. 2003; Steidel et al. 2004), corresponding to scattering from the back side of outflowing ISM, from which the Doppler shift is suitable to take the photon off of resonance and permit it to escape the galaxy.

Other notable features include strong, optically thick absorption lines from low-ionization species (e.g., Si II λ1192, Si II λ1260, O I+S II λ1303, C II λ1334, Si II λ1526, Fe II λ1608, and Al II λ1671) arising from outflowing neutral ISM. As shown in Figure 2.11, these absorption lines are blueshifted from the systemic redshift, corresponding to absorption from outflowing gas seen from the nearby side of a galaxy-wide outflow — their full widths can reach $\sim 1000\,\mathrm{km\ s^{-1}}$ (Pettini et al. 2002; Shapley et al. 2003). We note that while O I+Si II λ1303 (a blend of the low ionization species O I λ1302 and Si II λ1304) appears to be blended with a third component around λ1297 (resulting in a shallower blue-side slope for the composite line) it is generally possible to deblend this additional component to measure O I+Si II λ1303 alone. This broad λ1297 Å feature is likely itself a blend of the stellar photospheric lines C III λ1296.33, Si III λ1294.54, Si III λ1296.73, and Si III λ1298.93 (Tremonti et al. 2007), variations in the relative strengths of which can shift the apparent centroid of the λ1297 Å blend from $\lambda = 1295$ to 1298 Å.

Also apparent are absorption lines due to higher-ionization species, including the Si IV $\lambda\lambda 1393, 1402$ doublet and C IV absorption around λ1549 Å. Although all of these lines are blended with stellar features, C IV is a particularly complex blend of interstellar absorption lines at λ1548 Å and 1550 Å, combined with a P-Cygni component from the winds of the most luminous O and B stars. We neglect the numerous additional features due to nebular, fine-structure, and stellar atmosphere transitions (e.g., C III λ1176; see Shapley et al. 2003 for a further list), since they are not generally detected to high statistical significance after the sample has been divided amongst five morphological bins. We refer the reader to Shapley

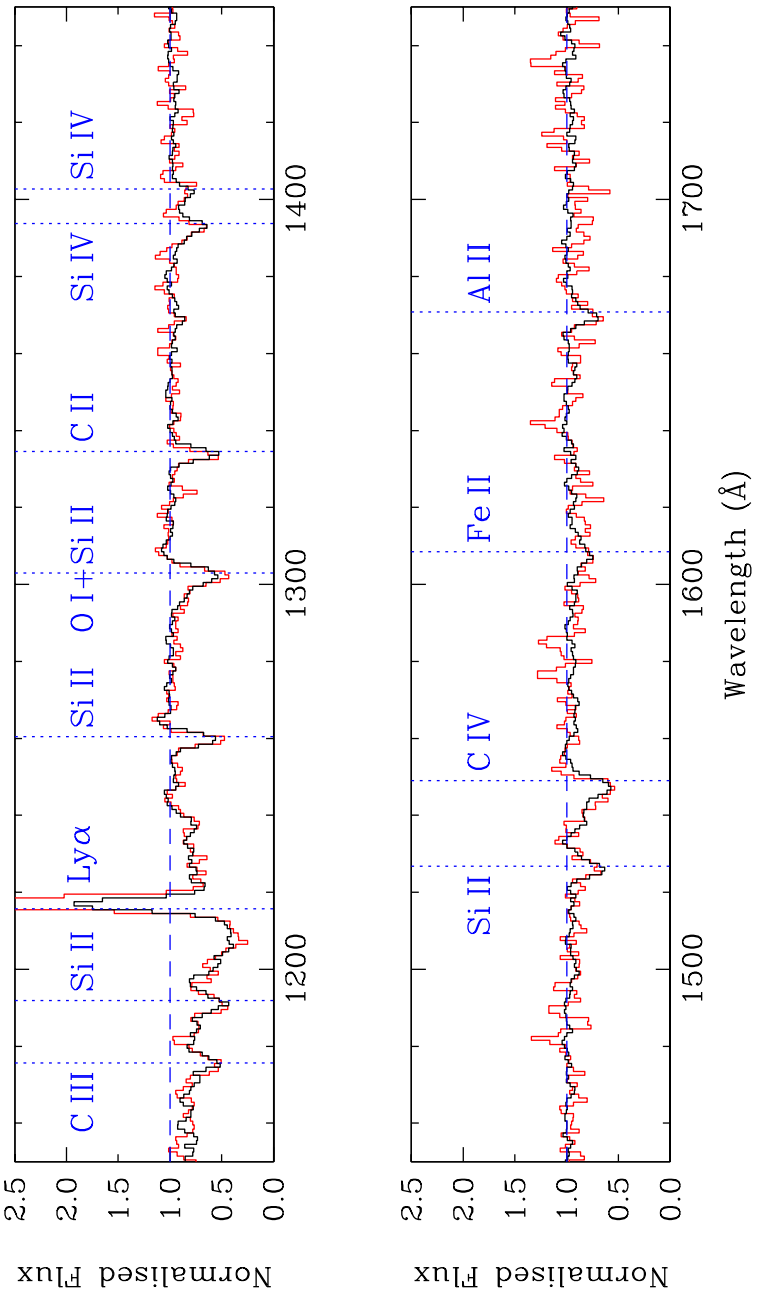

Figure 2.11 Stacked continuum-normalized spectra are plotted for all 150 $z \sim 2$ and 66 $z \sim 3$ galaxies (black/red lines respectively). Labels and dotted lines indicate the fiducial locations of atomic transitions corresponding to major spectroscopic features. Note that Lyα emission is considerably stronger in the $z \sim 3$ sample than the $z \sim 2$, and peaks at a relative normalized flux of 3.95 (not shown for clarity).

et al. (2003) and references therein for further discussion of the physical interpretation of the rest-UV spectra.

2.4.3 Equivalent Widths and Uncertainties

The equivalent widths of all absorption features were integrated non-parametrically relative to the normalized continuum. Generally, features shortward of Lyα and longward of λ1500 Å are considerably noisier than those between these wavelengths, and we therefore define average "low-ionization" and "high-ionization" absorption line strengths ($W_{\rm LIS}$ and $W_{\rm HIS}$, respectively) as the weighted means of the shorter wavelength transitions Si II λ1260, O I+Si II λ1303, and C II λ1334 (for $W_{\rm LIS}$) and Si IV λ1393 Å and λ1402 Å (for $W_{\rm HIS}$).

The total equivalent width of the Lyα feature (i.e., absorption plus emission) tends to be strongly affected by the noisiness of the absorption trough, so we characterize the strength of the emission component alone. The equivalent width of emission ($W_{\rm Ly\alpha}$) is determined by dividing the total flux in the emission component by the continuum level which would be present in the absence of any absorption trough.

It is possible to assess the statistical significance of possible deviations from a constant value by using the χ^2 statistic

$$\chi^2 = \sum_i \left(\frac{x_i - \bar{x}}{\sigma_{\rm sample}} \right)^2 , \tag{2.8}$$

where x_i is the measured equivalent width for a given bin, $\bar{x}$ is the mean equivalent width among all five bins, and $\sigma_{\rm sample}$ is the square root of the natural variance among samples of randomly binned spectra.[7] We find that $\sigma_{\rm sample}$ is considerably larger than the uncertainty in the mean equivalent width for a given stack (which belies the actual variance observed between randomly drawn samples), and therefore adopt it as a conservative means of ensuring that any possible trends are more significant than would be likely to occur randomly. As such, the significance of a particular value of χ^2 is evaluated using $5 - 1 = 4$ degrees of freedom to give the likelihood P that deviations of the five measurements from a constant average value (whether in the form of a monotonic trend or a single bin whose equivalent width varies greatly from the average with respect to the expected variance) are greater

[7] Thirty samples were sufficient to converge $\sigma_{\rm sample}$ to within 5%.

than that expected from a random binning of the sample. Applying this method to our measurements from randomly selected quintiles of galaxies, we determine that a threshhold of $P > 90\%$ suffices to cull apparent associations due to random variance.

2.5 THE RELATION OF REST-UV MORPHOLOGIES TO SPECTRA

As described in §2.4.1, we bin the galaxy sample separately into quintiles according to each of the morphological parameters I, G, Ψ, and ξ. Bin divisions are determined so that each bin contains an identical number of galaxies (i.e., 30 each for the $z \sim 2$ sample, and 13 each for the $z \sim 3$ sample); precise ranges are given in Table 2.1. In all cases our spectra are broadly consistent with the diffuse light spectrum of local starburst galaxies (e.g., Chandar et al. 2005) indicating that largely similar processes likely dominate the UV light output of all morphological types in our sample. Despite this general similarity the spectra show some variation with morphology as demonstrated in Figure 2.12, which we proceed to discuss in detail.

We first note however the caveat that the position angles of the slits used to obtain our UV spectra have not been chosen to correspond to the major axis of each of the galaxies, and it is therefore possible for a few of the most widely separated sources with multiple components that the UV spectra may represent only one of the components. Given the seeing-limited nature of the spectroscopic observations and the fact that the typical size of our targets (~ 1 arcsecond) is less than the width of the LRIS-B slit ($1\farcs2$) we doubt that this has a considerable effect. More likely perhaps is the probability that spectra are dominated by light from the bright nucleated regions of our sources and may not be expected to show any difference between nucleated and nucleated + nebulous sources if the spectrum of the nucleated regions are similar in each case.

2.5.1 Interstellar Absorption Lines

As illustrated in Figure 2.12 (middle rows), we find that the strength of interstellar absorption lines ($W_{\rm LIS}$ and $W_{\rm HIS}$) is largely uncorrelated with UV morphology, although there appears to be a statistically significant ($P = 92\%$) association of the strength of low-

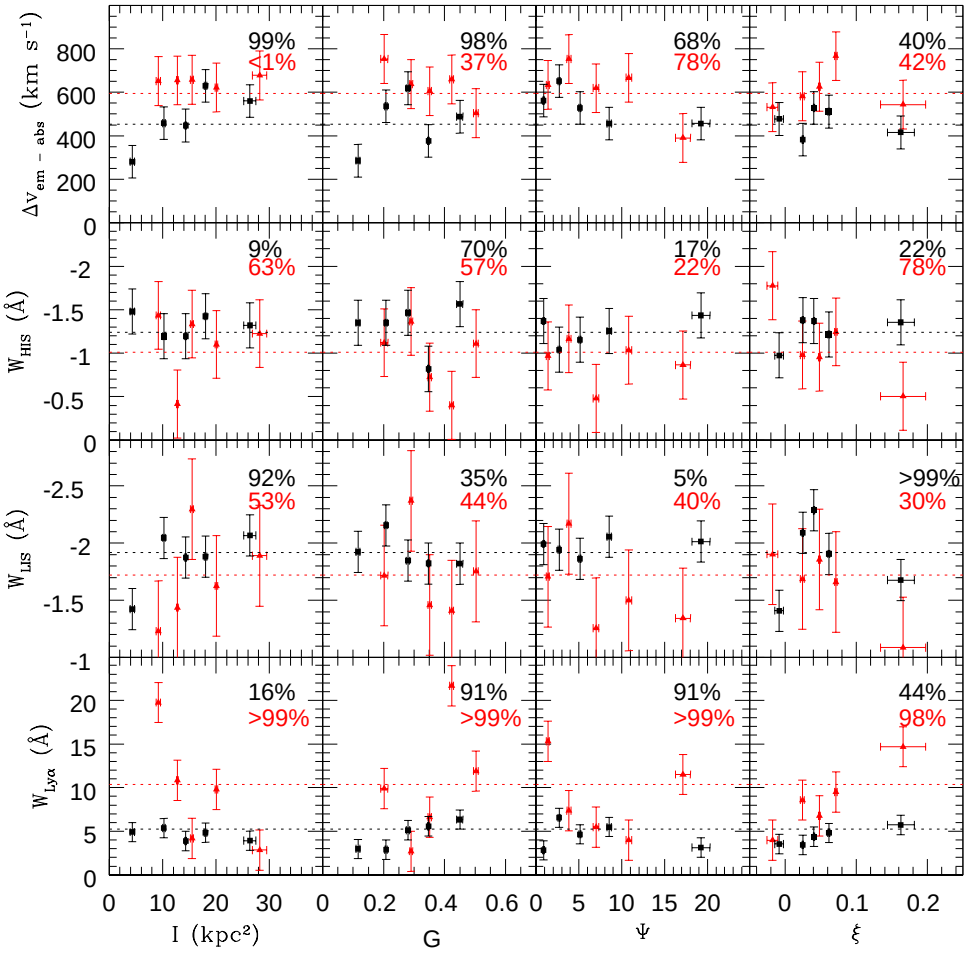

Figure 2.12 Lyα emission ($W_{\mathrm{Ly}\alpha}$) equivalent width, low- and high-ionization interstellar absorption equivalent width (W_{LIS} and W_{HIS}, respectively), and the kinematic offsets between emission and absorption lines ($\Delta v_{\mathrm{em-abs}}$) are shown measured from quintiles in the morphological parameters I (size), G (nucleation), Ψ (multiplicity), and ξ (color dispersion). Black and red points represent data from the $z \sim 2$ and $z \sim 3$ samples, respectively, shown with error bars representing the standard deviation among measurements made from randomly binned samples. Red and black dotted lines indicate the values measured for the complete $z \sim 2$ and $z \sim 3$ stacks, respectively, while the black and red percentages given in each panel indicate the χ^2 probability P that the data points shown are statistically inconsistent with a constant value. Generally, values of $P > 90\%$ are indicative of significant deviation—note particularly the linear trends of Lyα emission increasing for more nucleated sources (i.e., those with higher G) and low-ionization absorption strength increasing for larger sources (i.e., those with greater I).

ionization species with galaxy size I. Indeed, the data may be consistent with a trend that larger galaxies tend to have stronger interstellar absorption lines. Such a trend is most apparent for the $z \sim 2$ sample; while the $z \sim 3$ sample suggests a similar trend, the greater statistical uncertainties mitigate its significance.

We explore this possible trend in greater detail for the $z \sim 2$ sample by stacking our spectra in two dimensions to explore the variation of line strengths across a plane of two parameters smoothed by a variable-width kernel. We stack the spectrum of each galaxy with that of its 10 nearest neighbors in the $I-G$ plane to distinguish large nebulous objects from large yet nucleated objects, with inter-point "distances" along each axis normalized by the dynamic range of values along the axis. In Figure 2.13 we plot I versus G for $z \sim 2$ galaxies, with point size corresponding to the strength of $W_{\rm LIS}$. On the whole, the distribution of galaxies with strong and weak low ionization lines (i.e., large and small points) is quite similar, except for the lower left corner representing the faintest and most nebulous galaxies, for which there is an overabundance of small points (i.e., sources with weak $W_{\rm LIS}$). Given the similar overall distribution of line strengths, we conclude that the association between I and low-ionization absorption strength is due to the over-representation of weaker-line sources among the faint and nebulous galaxy sample rather than to an overall trend. Although this may indicate a genuine physical characteristic, we note that it is this class of low surface-brightness galaxies for which spectra are typically of the poorest quality and absorption line measurements least reliable. It is interesting, however, to note that the high ionization absorption lines do not likewise appear weaker in this class of galaxies (see Fig. 2.12), as might be expected were the apparent decline in low-ionization line strength due to spectrum quality alone.

Figure 2.13 also introduces another curiosity, namely the overabundance of weak-line objects in a line running through the plot from $G, I = 0.2, 30$ kpc^2 to $G, I = 0.6, 10$ kpc^2. This band does not correspond to an obviously distinct class of galaxies, or have any obvious reason for occupying the region of this plot which it does. We suggest the possibility that there could be a population of galaxies which have relatively weak outflowing components which are somehow distinguishable in this plot, but caution that random variation combined with the kernel smoothing technique might also be responsible for this enigmatic feature.

There is one additional significant deviation from uniformity for the color dispersion ξ

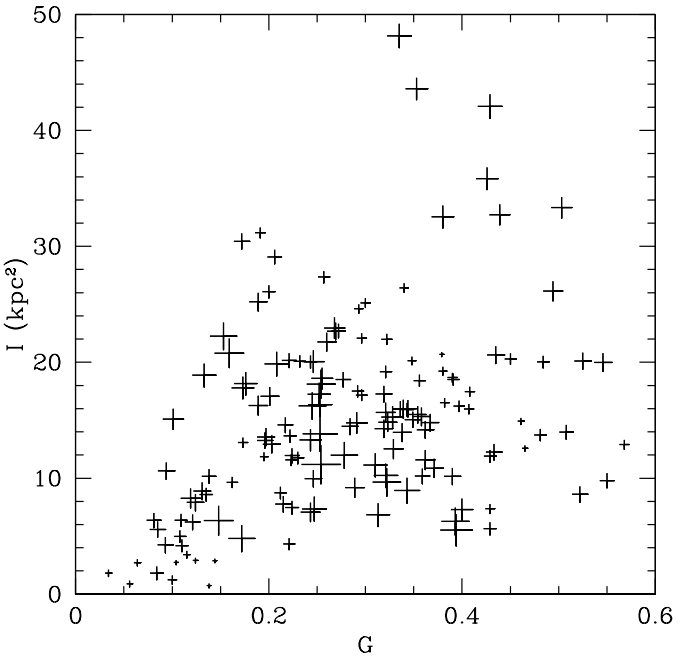

Figure 2.13 Low-ionization absorption line strengths for $z \sim 2$ galaxies are plotted (plusses) according to their location in the size – gini $(I - G)$ plane; spectra of each galaxy have been stacked with those of their ten nearest neighbors in this plane. Point sizes correspond linearly to the value of $W_{\rm LIS}$. Note the overabundance of weak-absorption sources (smaller symbols) in the lower left corner of the plot, and in the strip running from $G, I = 0.2$, 30 kpc^2 to 0.6, 10 kpc^2.

and the low-ionization absorption line strength (at a significance level of $> 99\%$ for the $z \sim 2$ sample). However, inspection of Figure 2.12 offers no clear explanation of the nature of this association: objects in both the smallest and largest bins of ξ have weaker absorption lines than objects in the intermediate three bins, and there hence appears to be no particular *linear* correlation between the variables. While this deviation may be a genuine product of physical phenomena its interpretation is unclear, particularly given the uncertain meaning of ξ.

2.5.2 Lyα Emission

As indicated by Figure 2.12 (bottom row) there are relatively many possible associations between Lyα emission strength and galaxy morphology, the simplest of which to interpret is the positive correlation between Lyα and the gini coefficient G. These two parameters show a clear linear trend of increasing emission strength with increasing nucleation; for the $z \sim 2$ sample the most strongly nucleated sources show roughly twice the emission seen in the most nebulous (see also Fig. 2.14), and for the $z \sim 3$ sample an even stronger trend is possible (although less well defined). It is unlikely that this trend is due to substantial variation of the composition or velocity of interstellar gas since such variations should also affect the strengths of absorption lines, which remain statistically constant across all values of G (see Figs. 2.12 and 2.14). A more plausible explanation may be that dust might be present in greater quantities in nebulous low-G sources, causing greater attenuation of Lyα photons. Under this hypothesis, it may be simply the presence of more or less dust which determines both the observed degree of UV nucleation and the strength of resonant Lyα emission. We explore this hypothesis further in §2.6.

We map the Lyα trend in greater detail in Figure 2.15, which compares the strength of the association between Lyα and G with the previously known association between Lyα and stellar mass $M_\star$ (i.e., that galaxies with higher stellar masses have lower average Lyα emission strength, Erb et al. 2006c).[8] Figure 2.15 suggests that the overall association between G and Lyα is genuine, but that emission strength in fact peaks for galaxies with $G \sim 0.4$ rather than for the few galaxies with $G > 0.5$. Since the galaxies with $G > 0.5$ represent

[8] We caution that despite the fact that G is correlated with $W_{\mathrm{Ly}\alpha}$ and $W_{\mathrm{Ly}\alpha}$ with $M_\star$, G itself is *not* correlated with $M_\star$ (see §2.6), indicating that correlations are not necessarily commutative.

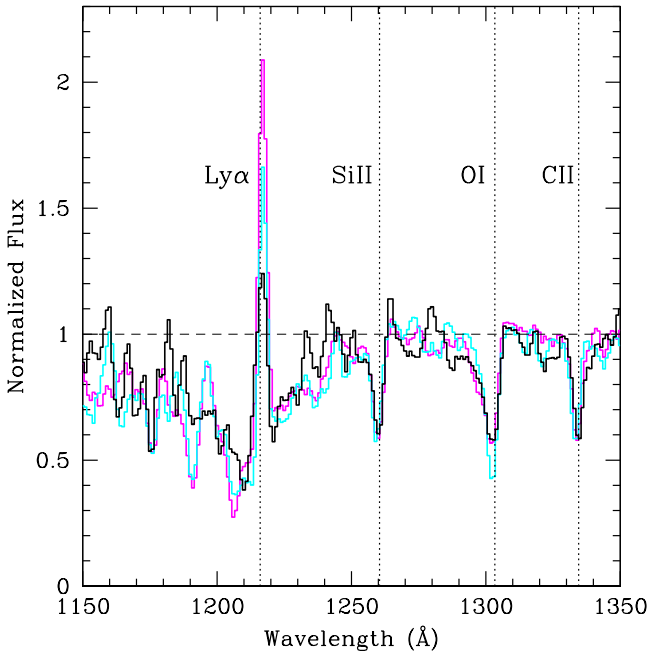

Figure 2.14 Stacked, continuum-normalized spectra for $z \sim 2$ galaxies representing three bins in the morphological nucleation parameter G. The low G nebulous galaxy bin is represented by the black line, the intermediate bin by the cyan line, and strongly nucleated sample by the magenta line. Spectra have been smoothed by a three pixel boxcar filter and normalized consistent with the prescriptions of Rix et al. (2004). Labels and dotted lines indicate the fiducial locations of major spectral features.

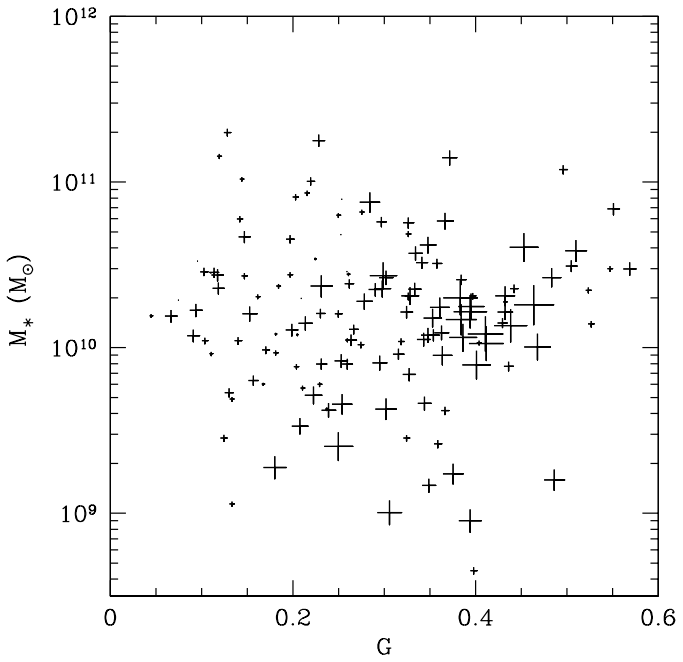

Figure 2.15 Lyα emission line strengths for $z \sim 2$ galaxies are plotted (plusses) according to their location in the stellar mass – gini ($M_\star - G$) plane; spectra have been stacked with their ten nearest neighbors in this plane as described in §2.5.1. Point sizes correspond linearly to the value of $W_{\mathrm{Ly}\alpha}$. Note the concentration of sources with strongest Lyα emission around $G \sim 0.4$ and $M_\star \sim 1.5 \times 10^{10} M_\odot$.

the extreme of nucleation and have much weaker Lyα emission than expected based on the majority of the galaxy sample we posit that these few galaxies may be somewhow distinct from the rest of the sample. Alternatively, the $G \sim 0.4$ galaxies may represent a particularly dust-free population from which it is possible to see both star-forming regions and their surrounding material.

We also observe also that $W_{\mathrm{Ly}\alpha}$ deviates from statistical uniformity when binned according to multiplicity Ψ (for both $z \sim 2$ and $z \sim 3$ samples), apparent size I (for the $z \sim 3$ sample), and color dispersion ξ (for the $z \sim 3$ sample). In the first case, there is less of an obvious trend in Figure 2.12 than an apparently random scatter of points, with particularly discrepant points found in both the highest and lowest bins in Ψ. In the latter two cases, $W_{\mathrm{Ly}\alpha}$ possibly declines with I and increases with ξ for the $z \sim 3$ sample, but these trends are absent from the $z \sim 2$ spectra. It is possible that these apparent deviations are due to the residual correlation between our morphological parameters (in which case the sense of a trend would be a complicated projection of the G–$W_{\mathrm{Ly}\alpha}$ correlation onto the density distribution in morphology space), or simply that these deviations are telling us of some trend or population of galaxies which is not well distinguished using our chosen morphological parameters (or indeed any of the many others which we have explored). However, we are inclined (despite our conservative estimates of the uncertainty) to ascribe at least those deviations only visible in the $z \sim 3$ spectra to statistical variance, since similar trends do not appear in the much higher-quality composite spectra from the $z \sim 2$ galaxy sample.

2.5.3 Kinematic Offsets

Since our stacked spectra have all been shifted to the systemic rest frame (i.e., that of the stars and [H II] regions), it is possible to calculate the kinematic offset $\Delta v_{\mathrm{em-abs}}$ in each stack between Lyα emission and the average of the low-ionization absorption lines Si II λ1260, O I+Si II λ1303, and C II λ1334. For the $z \sim 2$ and $z \sim 3$ samples, respectively, we find that $\Delta v_{\mathrm{em-abs}} = 453$ and 594 km s^{-1}, roughly similar to the Shapley et al. (2003) value of $\Delta v_{\mathrm{em-abs}} = 510$ km s^{-1} found for a large stack of 794 $z \sim 3$ LBG spectra [9]. While our relatively small sample of 66 spectra at $z \sim 3$ is too noisy to distinguish any significant

[9] We note that the average velocity offset in *individual* $z \sim 3$ LBG spectra with both emission and absorption components is typically ~ 650 km s^{-1}— see Shapley et al. (2003) for details.

trends with morphology, for the $z \sim 2$ sample $\Delta v_{\rm em-abs}$ is convincingly correlated with both the size parameter I and the gini coefficient G (see Fig. 2.12, top panels).

In particular, the offset velocity increases nearly linearly from $\sim$ 300 km s^{-1} for the smallest galaxies with $I \sim 5$ kpc^2 to near 600 km s^{-1} for the largest with $I \sim 20$ kpc^2. The differences are similarly pronounced with respect to the gini parameter G, but instead of increasing linearly through the sample, Figure 2.12 suggests that $\Delta v_{\rm em-abs}$ is lowest for galaxies with $G \lesssim 0.2$, peaks for intermediate values of $G \sim 0.3$, and possibly declines slightly at the most nucleated values of $G \gtrsim 0.5$. This high $\Delta v_{\rm em-abs}$ sample of high I and moderate – high G corresponds reasonably well to a particular morphological sample- the Type 4 galaxies (as identified in §2.3) which occupy a large angular area and tend to have bright nebulous emission paired with one or more distinct nucleations.

These data suggest that larger, more UV luminous (I correlates well with UV luminosity—see §2.6) galaxies on average may have stronger outflows than the rest of the population, as might be expected if these galaxies have particularly energetic input to their interstellar media and are therefore capable of blowing the most energetic outflows. We caution however that the major discrepant point in both of these trends is for the most nebulous sample (i.e., that with both small I and small G) whose UV spectra are fainter and typically of slightly lower quality.

Pairing this with the most significant understandable trend discovered in §2.5.1 and 2.5.2, namely the positive correlation between G and Lyα emission strength, we might be led to conclude that Lyα and $\Delta v_{\rm em-abs}$ are positively correlated, in constrast to the results of Shapley et al. (2003) who found that outflow velocities are slightly weaker for $z \sim 3$ LBGs with strong Lyα emission. This discrepancy illustrates the important point that, given the large scatter in all of our correlations, *correlation is not commutative.* That is, while there is a general trend that Lyα emission strength increases for more nucleated objects, this nucleated population is not the same as that moderately nucleated, large I population for which $\Delta v_{\rm em-abs}$ peaks.

2.5.4 Rest-Optical Spectroscopic Features

As part of an ongoing near-IR spectroscopic survey (Erb et al. 2006a) we have obtained rest-frame optical spectra in the wavelength regime of Hα and [N II] for 19 of the 150 galaxies

in the $z \sim 2$ galaxy sample, and use these spectra to explore whether there is any apparent relation between morphology and Hα flux and/or the oxygen abundance as measured by the [N II]/Hα ratio (Pettini & Pagel 2004). Given the extremely small sample of galaxies with near-IR spectra, we divide these 19 galaxies into only three bins according to our morphological parameters and analyze the resulting stacked spectra (shown in Figure 2.16) with a method similar to that adopted for the rest-UV spectra.

As indicated by the general similarity of all of the composites shown in Figure 2.16, and plotted more precisely in Figure 2.17, we find no significant variation in the strength of Hα emission with rest-UV morphology. [N II] is only marginally detected in many of the composite spectra, and all variations are well within the uncertainty expected based on the noise of the composite spectra. We conclude therefore that to within the accuracy permitted by our small (and hence not fully representative of the large distribution of UV morphologies) spectroscopic sample, the UV morphology of $z \sim 2$ galaxies is uncorrelated with rest-frame optical spectroscopic features and the degree of metal enrichment as parametrized by the [N II]/Hα oxygen abundance estimate.

2.6 THE ASSOCIATION OF REST-UV MORPHOLOGIES WITH PHOTOMETRICALLY DERIVED PROPERTIES

Using ground-based $U_nG\mathcal{R}$ and *Spitzer*-MIPS photometry it is possible to calculate the rest-frame, k-corrected luminosities of each of our target galaxies in the UV (L_{1600}) and mid-IR ($L_{5-8\mu}$),[10] in addition to estimating the total bolometric luminosity ($L_{\rm BOL}$) and the ratio of IR/UV luminosities ($L_{\rm FIR}/L_{1600}$). The resulting spectral energy distribution from these and additional JK and *Spitzer*-IRAC data may then be fit with stellar population models to determine the best-fit stellar mass ($M_\star$), age, and optical extinction ($E(B-V)$) for a given galaxy. Although the risk of confusion is greater in stellar population models based on such seeing-limited imaging, in almost all cases (except of those of the few most widely separated clumps) we find that the isophotes of the target galaxies reliably trace the ACS morphology, and all components are blurred together into a single object with minimal contamination

[10] L_{1600} typically ranges from $\sim 10^{10} L_\odot - 1.2 \times 10^{11} L_\odot$, $L_{5-8\mu}$ from $\sim 5 \times 10^9 L_\odot - 1.3 \times 10^{11} L_\odot$; see Reddy et al. 2006a for further details

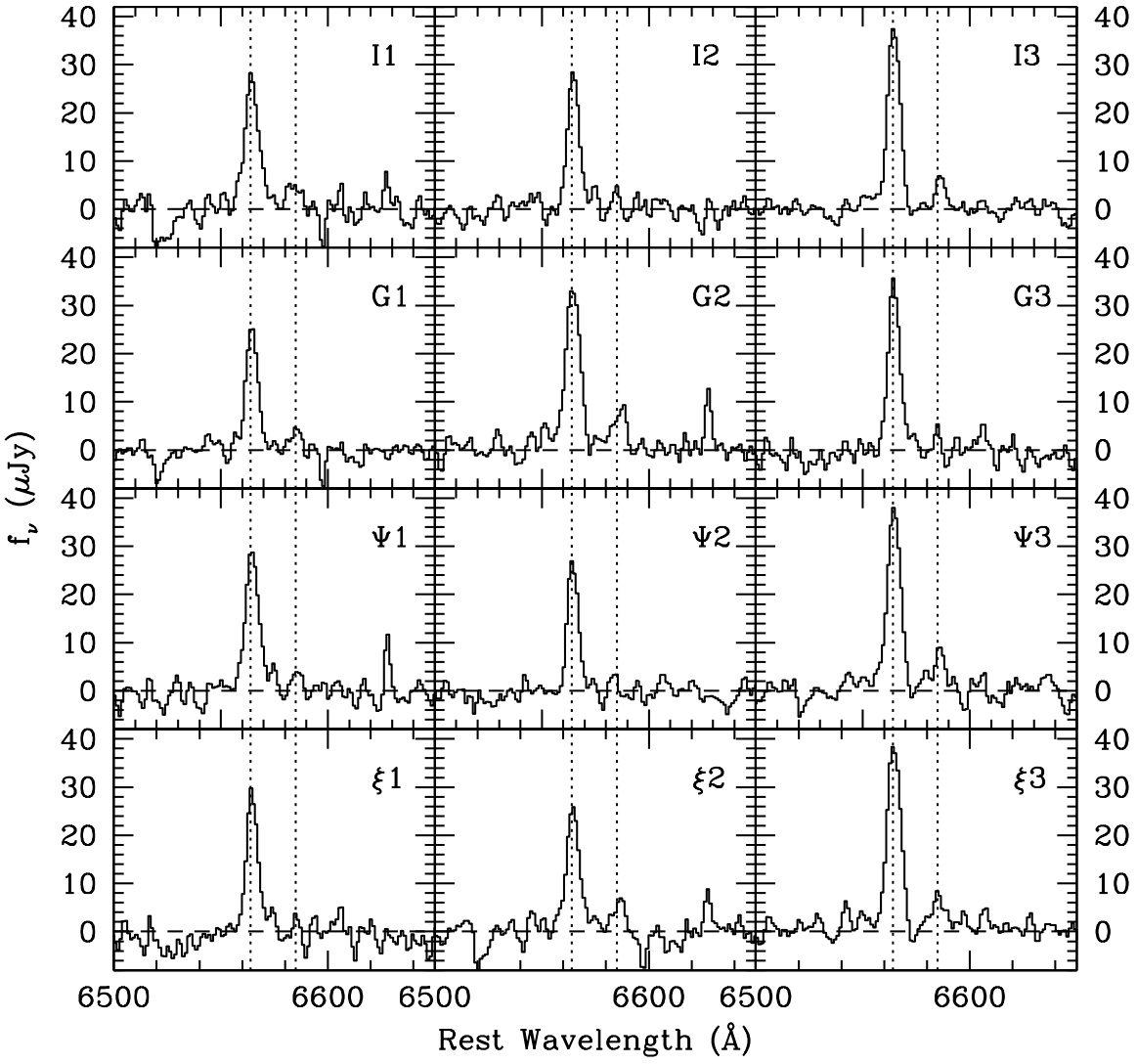

Figure 2.16 Flux-calibrated, composite Hα spectra are plotted for each of three bins in the morphological parameters I (size), G (gini), Ψ (multiplicity), and ξ (color dispersion). Spectra are numbered according to increasing values of the morphological parameter (e.g., $G3$ is composed of more nucleated sources than $G1$). The fiducial wavelength of Hα and [N II] λ6583 Å are indicated by dotted lines. Note that the strength of Hα and [N II] is not significantly different in any of these panels.

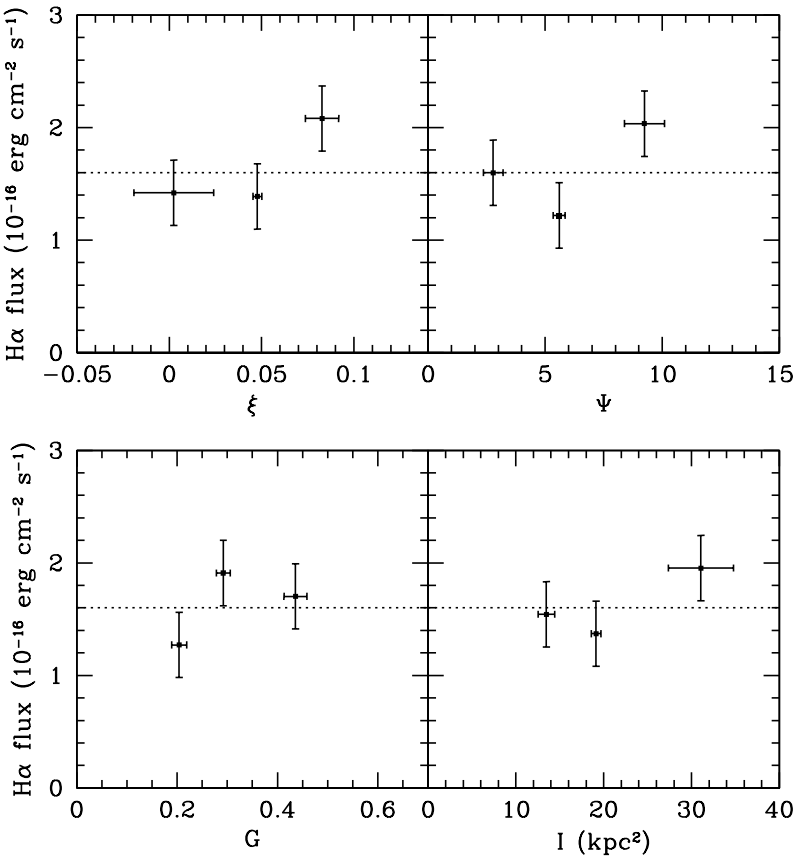

Figure 2.17 Hα fluxes measured for the composite stacks in each of the morphological parameters I (size), G (gini), Ψ (multiplicity), and ξ (color dispersion). Horizontal errorbars represent uncertainty in the mean value of a morphological quantity within each bin, vertical errorbars represent 1σ uncertainties on the flux based on random-draw tests. The dotted line in each panel represents the mean Hα flux of the entire sample.

from nearby sources. The comprehensive results of such efforts have been summarized by Reddy et al. (2006a); in the present contribution we test the degree of association between morphology and such photometrically derived parameters. In this section we consider only the 62% of the $z \sim 2$ sample of galaxies for which *Spitzer*-MIPS 24 μm detections directly measure the strength of rest-frame mid-IR emission (see further discussion in Reddy et al. 2006b).

We quantify the degree of association using the Spearman non-parametric rank correlation coefficient r_s, values of which are assessed in terms of their two-sided significance t. This significance gauges the probability that the null hypothesis (i.e., that there is no correlation between the two parameters) is true and that any apparent correlation is due to random chance alone. In Table 2.2 we calculate t_σ [11] for a grid of photometric versus morphological parameters (adopting the convention that positive t_σ indicates a positive correlation, and negative t_σ a negative), highlighting in bold typeface those for which the null hypothesis is less than 10% probable (i.e., $|t| < 0.1$, $|t_\sigma| > 1.65$). We note from Table 2.2 that the null hypothesis is rejected in very few cases, indicating that in general morphology is largely decoupled from photometrically derived parameters.

The most significant correlations relate galaxy size (I), nucleation (G), and rest-frame ultraviolet luminosity (L_{1600}) in the sense that larger and more strongly nucleated galaxies tend to have brighter UV continua. In general, these correlations are unsurprising since I effectively measures the number of UV bright pixels in a galaxy (and a galaxy with large I is hence likely to have a large total UV luminosity), and high values of G are produced by relatively high concentrations of flux in a small percentage of the total number of UV bright pixels (which occurs more commonly in galaxies with a high total UV luminosity to distribute). However, we note that the positive correlation between G and L_{1600} may also (at least in part) have a more physical explanation; if indeed nebulous low G sources are dustier, then UV radiation from these galaxies would be more strongly attenuated than from less-dusty high G galaxies, contributing to the observed trend.

The next most significant correlations relate I, G, $E(B-V)$ (the estimated reddening based on stellar population models and the far-UV spectral slope) and the ratio of IR to

[11] Since t is an awkward statistic to print for extremely small values, we instead give results in terms of t_σ corresponding to the number of sigma that t lies out along the wings of a Gaussian probability distribution.

UV luminosity ($L_{\rm FIR}/L_{1600}$, a proxy for UV attenuation). As quoted in Table 2.2, I and G are both negatively correlated with $E(B-V)$ and $L_{\rm FIR}/L_{1600}$ (at levels of significance ranging from about $2-3\sigma$) in the sense that the most attenuated galaxies tend to have smaller UV luminous areas (low I) with weaker nucleation in the flux distribution (low G). Although this correlation contains a great deal of scatter and does not hold precisely for every galaxy (i.e., not all "small and nebulous" galaxies are highly extinguished), it nonetheless appears that *statistically* the most extinguished galaxies tend to be smaller and more nebulous than the general population. As previously hypothesized on the basis of Lyα emission strength, it may therefore be the case that galaxy morphology is dictated in part by the presence and location of dust which partially extinguishes the UV continuum radiation and causes galaxies to appear slightly smaller (to a fixed limiting surface brightness) and more nebulous.

The color dispersion ξ appears to follow the trends found for I and G with UV luminosity and extinction (although at lower significance), possibly due to its known positive correlation with G. The multiplicity parameter Ψ however (also loosely correlated with G) exhibits no statistically significant associations with any of the photometrically derived quantities presented in Table 2.2. In addition, we note that— contrary to possible expectations (e.g., that galaxies with higher stellar mass might, analagously to local elliptical galaxies, appear morphologically more evolved and distinct from those with low stellar mass)— there is no evidence for a relationship between stellar mass and UV morphology, implying that through a combination of physical processes galaxies ranging over two decades in stellar mass from $M_\star \sim 10^9 - 10^{11} M_\odot$ somehow appear visually indistinguishable. However, while no significant *overall* correlation was found by the Spearman test, almost all (20/22) of the most strongly nucleated sources ($G > 0.4$) have masses greater than $10^{10} M_\odot$ in contrast to those with $G < 0.4$ which span a full two decades in stellar mass.

In Table 2.3 we compare rest-UV morphologies to star formation rate (SFR) estimates based on SED fitting, and UV and IR continuum emission. Although these estimates tend to be loosely correlated with each other, there is considerable scatter in individual estimates of the SFR for a particular source using different methods. The least reliable of our estimates are the SFR estimated from normalization of stellar population models (Shapley et al. 2005b; Erb et al. 2006a; Reddy et al. 2006a), for which we find no significant correlations

with morphological parameters (due either to the intrinsic lack of such a correlation, or to the uncertainty inherent in the SFR estimate given by this method). The next most reliable estimate is that based on UV continuum flux, for which we calculate the uncorrected star formation rate based on $U_nG\mathcal{R}$ photometry and the conversion factor given by Kennicutt (1998a). As shown in Table 2.3, the uncorrected UV SFR is strongly correlated with all morphological parameters save the multiplicity Ψ. However, this is not surprising given the strong association between total UV luminosity and morphology shown in Table 2.2. While it is likely that large (high I), nucleated (high G) objects have a higher than average rate of *uncorrected* star formation it is not necessarily true that the same holds for the total star formation rate. Indeed, in the majority of cases *obscured* star formation comprises the bulk of the total. Rather than assuming an average extinction factor to estimate this from the UV luminosity, we estimate the obscured SFR from the IR luminosity $L_{\rm IR}$ calculated by Reddy et al. (2006b), adopting the $L_{\rm IR}-$ SFR conversion factor given by Kennicutt (1998a). As shown in Table 2.3, obscured star formation has far less compelling associations with UV morphology— none are found to have statistical significance.

The most accurate estimate of the total star formation rate may be found by summing the rates determined from UV and IR luminosities. We break this comparison into two cases— galaxies for which the IR-derived SFR has been directly measured using *Spitzer*-MIPS detections at 24 μm, and galaxies which are undetected at 24 μm and an estimate of the IR-derived SFR has been computed based upon the average bolometric luminosity of MIPS-undetected sources[12] ($L_{\rm BOL} = 6 \times 10^{10} L_{\odot}$, Reddy et al. 2006b). For the first of these cases, no significant correlations are found with either the total or specific (stellar mass-normalized) star formation rate. We note however that the specific star formation rate is on the threshhold of statistical significance for a positive correlation with G. If the eleven galaxies with stellar populations younger than 40 Myr (i.e., for which stellar population fits are the most uncertain) are neglected in our analysis, this correlation becomes statistically significant, deviating from the null hypothesis by approximately 2.1σ. While therefore there is mild evidence for a positive correlation between UV nucleation and net star formation for galaxies directly detected at 24 μm, this association is not at present statistically compelling. In contrast, for the 24 μm undetected sources all of the associations between morphology

[12] $L_{\rm IR}$ effectively scales with $L_{\rm BOL}$.

and uncorrected UV SFR are recovered for the total estimated SFR (although this trend is smeared out by the division by mass for the specific SFR), largely because the obscured SFR extrapolated from total bolometric luminosity contributes only marginally to the total in these cases.

2.7 A COMPARISON OF MORPHOLOGIES WITH OTHER GALAXY SAMPLES

2.7.1 AGN/QSO

As given in the table of AGN/QSO in GOODS-N presented by Reddy et al. (2006a, their Table 3), there are a total of nine spectroscopically confirmed AGN/QSO in our sample in the redshift range $z = 1.8-3.4$, six of which are directly detected in X-ray emission (although one very weakly) and three of which have no X-ray counterpart to a depth of 2 Ms (based on the catalog of Alexander et al. 2003) but are confirmed AGN based upon high-ionization optical emission lines and/or power-law mid-IR SEDs. As noted by Reddy et al. (2006a), the morphologies of the X-ray undetected sample are more disturbed than their directly detected counterparts. As we show in Figure 2.18, all three X-ray undetected sources have $G < 0.4$, while the the five detected sources all have strongly nucleated values $G > 0.38$ (four with $G > 0.47$) and the two QSO in the sample (BMZ 1083 and MD 39) have the highest values of any object considered in this contribution at $G = 0.63$ and 0.88, respectively (close to the stellarity limit of $G \sim 0.90$). This suggests a possible correlation between X-ray luminosity and UV nucleation, in the sense that AGN which produce obvious X-ray radiation also contribute sufficiently to the total UV output of their host galaxies such that the centralized AGN radiation visibly affects the apparent nucleation of the UV light profile. Given the extremely small size of our sample, it is difficult to assess the global applicability of this correlation, although we note for comparison that in a larger sample of 31 AGN in the redshift range $z \sim 2 - 4$ Akiyama (2005; their Fig. 3) found that AGN with the most centrally concentrated light distributions tended to be X-ray bright ($L_{2-10\mathrm{keV}} > 10^{44}$ erg s^{-1}) broad-line sources, while the population of X-ray bright narrow-line sources and X-ray faint sources tended to be slightly less centrally concentrated. Likewise, recent studies of AGN at lower redshifts ($z \lesssim 1.3$) by Pierce et al. (2007) and Grogin et al. (2005) also found

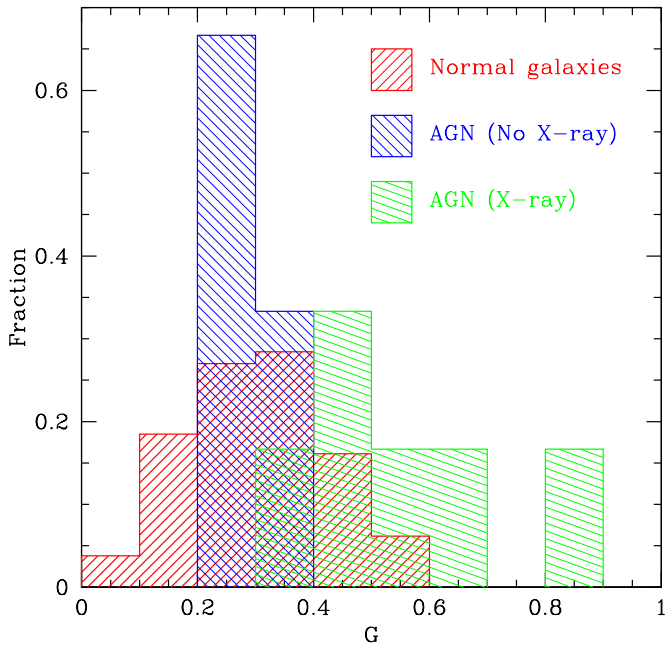

Figure 2.18 Histogram showing the relative UV nucleation for the $z = 1.8-3.4$ galaxy sample (red histogram) versus X-ray detected (green histogram) and X-ray undetected AGN/QSO (blue histogram). The nucleation of the X-ray undetected sample is broadly consistent with the median nucleation of the overall $z = 1.8 - 3.4$ population, while X-ray detected galaxies are more strongly nucleated.

the rest-frame optical morphologies of X-ray luminous AGN to be more compact than those of IR-selected AGN or ordinary field galaxies.

Not only are the X-ray undetected AGN more nebulous than their X-ray bright counterparts, we find that they also appear to have a greater number of components to their UV light, exhibiting a range of multiplicities $\Psi = 4.6 - 11.8$ as compared to the $\Psi < 1.8$ found for all directly detected X-ray sources. These irregular morphologies, coupled with a power-law SED longward of $3\,\mu$m (indicating the presence of warm dust), yet a UV SED well fit by a simple stellar population, suggest (Reddy et al. 2006b) that these sources may be obscured AGN whose UV emission is dominated by spatially extended star formation rather than a central active nucleus.

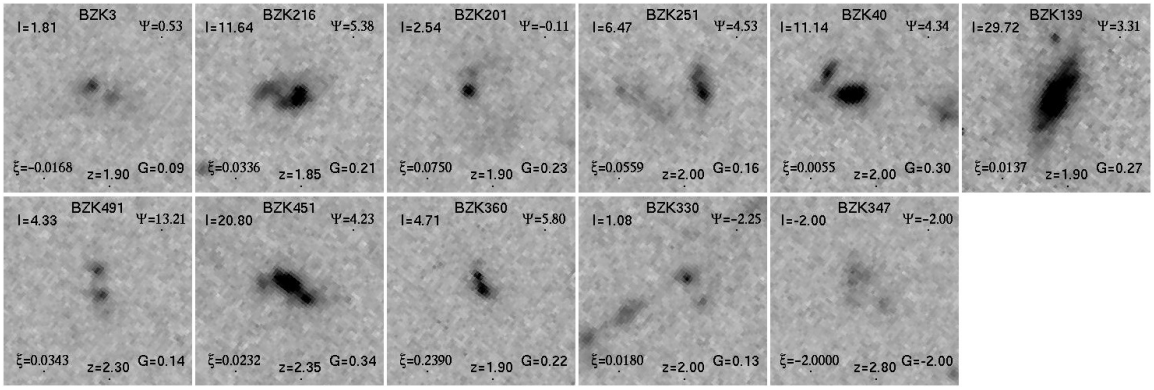

Figure 2.19 As Figure 2.2, but for IR-selected BzK sources brighter than $K = 21$ which are not selected by the rest-UV color selection criteria. Redshifts given are photometric.

2.7.2 IR-Selected *BzK* Galaxies

One well-studied near-IR color-selected galaxy sample is the BzK-selected catalog (Daddi et al. 2004), for which many sources (fifty-two sources brighter than $K = 21$ in the redshift range $z = 1.8 - 2.6$) simultaneously satisfy both the BzK selection criteria and our optical $U_nG\mathcal{R}$ color selection criteria. In Figure 2.19 we show the morphologies of those GOODS-N BzK galaxies which are comparably bright in K band and and have well-determined photometric redshifts, yet fail to meet the optical selection criteria. Qualitatively, we note that the BzK galaxies not in the optically selected sample appear morphologically very similar to those in Figure 2.2, as might be expected given the large general overlap between the two samples, and suggesting that these few galaxies may fall just outside of the optical selection criteria.

We quantify these morphological differences in Figure 2.20, using photometric redshift estimates to scale the surface brightness selection algorithm. As expected based on Figure 2.19, the average morphology of BzK sources which are also $U_nG\mathcal{R}$ sources (filled triangles) is identical to that of the overall $U_nG\mathcal{R}$ sample (filled squares) to within the uncertainties in the mean. The sample of eleven BzK sources which do *not* meet the $U_nG\mathcal{R}$ criteria (empty triangles) has slightly fewer high-surface brightness pixels (lower I) and is slightly less nucleated (lower G) than the other two samples, but at a confidence level of only $1-2\sigma$. The apparent multiplicity Ψ and color dispersion ξ remain approximately constant among all of these samples to within the uncertainty.

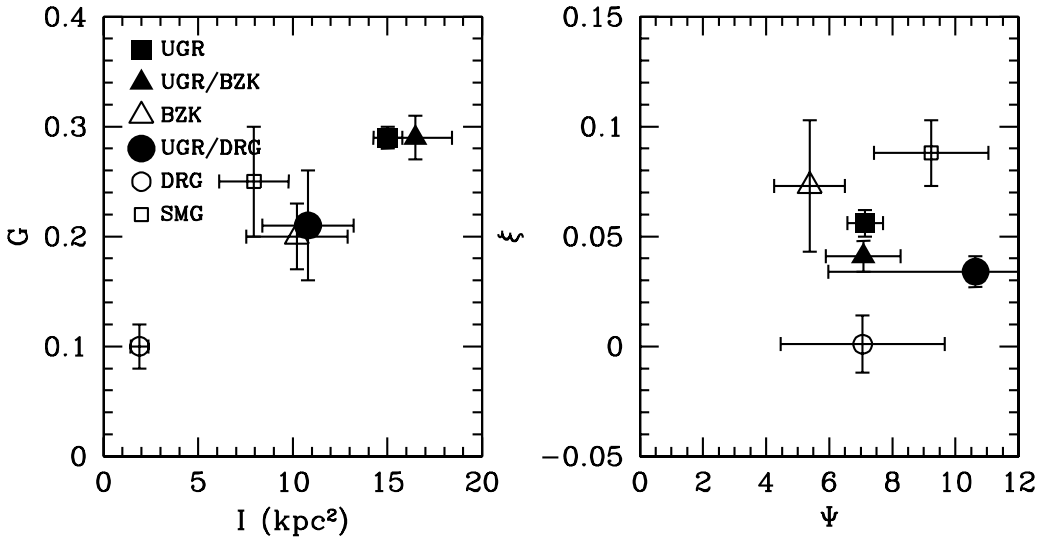

Figure 2.20 Comparative average size (I), nucleation (G), multiplicity (Ψ), and color dispersion (ξ) for optically selected $U_nG\mathcal{R}$, BzK, DRG, and SMG galaxy samples. Filled squares represent all $z \sim 2$ $U_nG\mathcal{R}$-selected galaxies, filled triangles and circles the respective subsets which also fulfill BzK and DRG criteria, open triangles and circles galaxies which fulfill the BzK and DRG criteria (respectively) which do not meet the $U_nG\mathcal{R}$ selection criteria, and open squares all galaxies which fulfill the SMG critera. All galaxies are limited to the redshift range $z = 1.8 - 2.6$ (using photometric redshifts where spectroscopic are unavailable), and the BzK and DRG galaxy samples are limited those with no X-ray counterparts to 2 Ms and K magnitudes $K < 21$. Errorbars indicate the 1σ uncertainty in the mean values for each population.

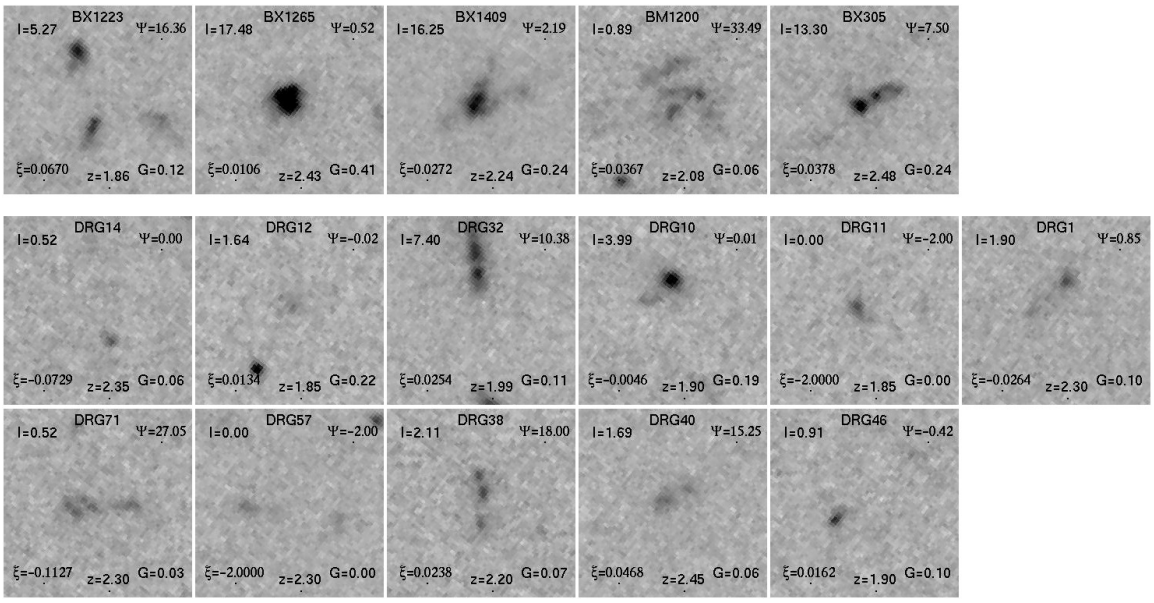

Figure 2.21 As Figure 2.2, but for IR-selected DRG sources brighter than $K = 21$. Top row: DRG which are also selected by rest-UV color selection criteria. Bottom rows: DRG which are not selected by rest-UV color selection criteria. Redshifts given for galaxies not selected by the rest-UV criteria are photometric.

2.7.3 IR-Selected Distant Red Galaxies

Distant red galaxies (DRGs, Franx et al. 2003) constitute another major IR-selected sample of high redshift galaxies for which there are five sources brighter than $K = 21$ in the redshift range $z = 1.8 - 2.6$ which meet the $U_nG\mathcal{R}$ selection criteria and have secure spectroscopic redshifts, and eleven sources which do not but for which we measure reliable photometric redshifts. As illustrated by Figure 2.21, the DRG population is fainter and more nebulous in UV emission than any of the other galaxy samples considered, consistent with what may be expected for particularly dusty IR-bright galaxies given the apparent correlation between UV nucleation and dust extinction.

As for the BzK sample, the overlapping sample of $U_nG\mathcal{R}$-selected DRGs has morphological coefficients similar to the bulk of the $U_nG\mathcal{R}$ population to within $1 - 2\sigma$ (although it is on average slightly slightly smaller and more nebulous, see Fig. 2.20). It is those DRG *not* selected by $U_nG\mathcal{R}$ criteria however which particularly stand out— these galaxies (Fig. 2.20, open circles) have much smaller I and G to a high level of confidence and in some cases

(e.g., DRG 14) are barely detected in our *HST*-ACS imaging data. Largely, this difference is a reflection of the much fainter UV luminosity of the DRG sample— typical DRG which do not meet the optical selection criteria have UV luminosities $L_{1600} < 10^{10} L_{\odot}$ (and commonly $L_{1600} < 10^{9} L_{\odot}$), as compared to the median luminosity for the optically selected sample $L_{1600} \sim 5 \times 10^{10} L_{\odot}$. Similarly to the BzK sample, the apparent multiplicity Ψ for DRGs is again consistent with the $U_n G\mathcal{R}$ sample, although the color dispersion ξ is roughly 2σ lower and is consistent with zero (the value expected for a pure measurement of the background sky).

2.7.4 Submillimeter Galaxies

The submillimeter galaxy (SMG) population offers the opportunity to compare the rest-UV morphologies of optically selected galaxies with those in a similar redshift range ($z \sim 2-3$) which are selected on the basis of submillimeter flux. Using the catalog of SMG coordinates and spectroscopic redshifts compiled by Chapman et al. (2005), we apply our morphological analysis to a sample of these galaxies in the GOODS-N field. The wide range of morphological types covered by the SMG selection criteria are shown in Figure 2.22 and range from single, nucleated sources to extremely faint and nebulous, and include one strong high-redshift spiral galaxy candidate (BZK 294, see Dawson et al. 2003). On average however, the SMG population has a morphology similar to that of the $U_n G\mathcal{R}$-selected sample (Fig. 2.20) with values of Ψ and ξ consistent to within the uncertainty and apparent sizes I and nucleations G only slightly smaller and more nebulous than the $U_n G\mathcal{R}$-selected sample. These results are consistent (since our size parameter I is closely related to surface brightness) with the findings of Chapman et al. (2003) and Conselice et al. (2003b), whose *HST*-STIS imaging led them to conclude that the SMG sample had lower surface brightness than typical $z \sim 3$ LBGs, yet was slightly larger *for the reduced surface brightness*.

Additionally, Conselice et al. (2003b) also find that the asymmetry index A of their sample of eleven SMGs is slightly greater on average than that of optically selected $z \sim 3$ LBGs, which these authors conclude implies a greater major merger fraction for the submillimeter-bright sample. However, we find no statistically significant change in our multiplitiy parameter Ψ (which most closely measures the morphological irregularity of a

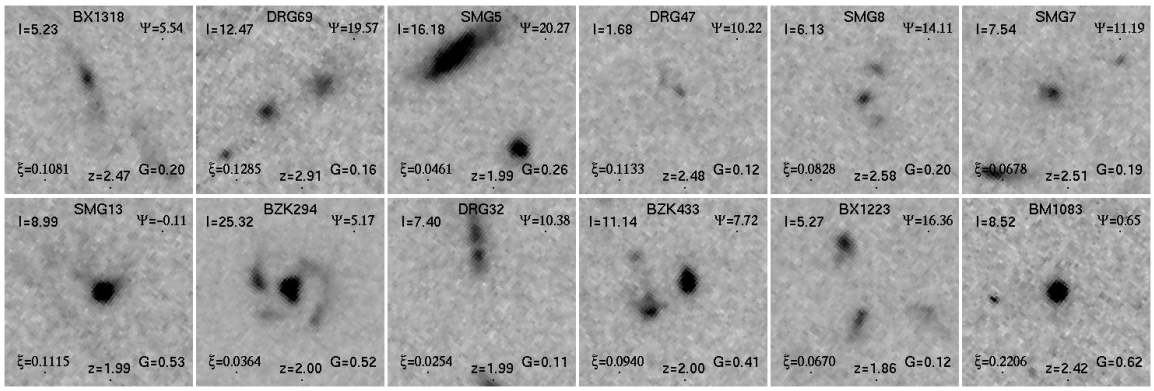

Figure 2.22 As Figure 2.2, but for all SMGs on the HST-ACS image frame of the GOODS-N field in the redshift range $z = 1.8 - 2.6$ (plus one source at $z = 2.91$). Positions and spectroscopic redshifts are drawn from the catalog of Chapman et al. (2005). Galaxies which also fulfill $U_nG\mathcal{R}$, BzK, or DRG selection criteria are labelled accordingly. Note that the lower-right object in this figure (BM 1083) is a known QSO.

source). If the morphologies of the SMG sample are governed by the same physical processes as the optically selected galaxies (as seems likely given the two samples appear to fall on the same trend of dustiness versus bolometric luminosity for star-forming galaxies at $z \sim 2$; Reddy et al. 2006b) then when considered non-parametrically we conclude that the SMG sample may be no more likely to be dominated by major mergers than other $z \sim 2 - 3$ galaxy samples.

2.8 DISCUSSION

Through a comprehensive statistical analysis, we have found two key trends with morphology. First, the degree of nucleation/nebulosity is related to the UV/optical extinction of the source (as parametrized through both the value of $E(B-V)$ calculated from stellar population models and the ratio of IR to UV luminosity), suggesting that more nebulous sources may appear as such since their greater quantities of dust obscure a great quantity of the UV light. Second, physically larger, more UV luminous sources have rest-UV emission and absorption lines seperated by a greater velocity, indicating that they may drive more energetic outflows than their lower luminosity counterparts. However, we note that these trends are typically on the order of $3-4\sigma$ significance, and are far from being unambiguously

convincing morphological differences. Indeed, given the relatively large sample of galaxies and volume of spectrophotometric data compiled to date, the overall *lack* of correlation between morphology and fundamental galactic properties such as stellar mass, SFR, and outflows is more remarkable. To some degree this may be due to the unknown distribution of viewing angles, but whether as a result of this complication or a more fundamental process the rest-UV morphologies of high redshift galaxies generally do not appear to contain a great deal of separable information. If morphologies truly mean so little, this may help explain the lack of correlation seen between elongated morphologies and major axis velocity shear by Erb et al. (2004), who found that morphologically elongated galaxies are no more likely than compact galaxies to exhibit kinematic signatures of rotation.

It is interesting to note the implications of these findings for the major-merger hypothesis which posits that, similarly to luminous and ultraluminous infrared galaxies (LIRGs and ULIRGs) in the local universe, particularly irregular morphologies correspond to major galaxy mergers (e.g., Conselice et al. 2003; Chapman et al. 2003; LPM04; Lotz et al. 2006). In particular, Conselice et al. (2003a) adopt the asymmetry selection criterion $A > 0.35$ to identify major mergers, and interpret the increase in galaxy irregularity with redshift out to $z \sim 3$ to indicate a higher merger fraction in the early universe and evidence for hierarchical formation. If the most irregular galaxies truly represent such major events however, we might reasonably expect these galaxies to differ significantly from their non-merging counterparts in some additional way, perhaps by displaying tidally enhanced rates of star formation or broadened interstellar absorption lines due to the juxtaposition of the ISM of two or more galaxies with relative velocity differences of order a few hundred km s^{-1}. However, we find no evidence for such a distinction between any of a variety of morphological samples, suggesting that either major mergers at $z \sim 2-3$ are largely indistinguishable from the non-merging sample, that *all* $z \sim 2-3$ galaxies are experiencing major merger induced starbursts, or simply that irregular morphology (at least to within $\sim$ 13 kpc at rest-UV wavelengths) is not a reliable indicator of a major merger. While it is possible that major mergers may be distinguishable on the basis of multiple components beyond our 13 kpc detection threshhold, it seems unlikely that such systems would produce changes as profound as may be found on closer passes.

Supposing then that irregular, multi-component morphologies do *not* represent bursts

of star formation in the orbiting galaxies and satellite galaxies of a major merger, another possibility is that these systems may instead represent patchy star formation occuring from the collapse of local instabilities within galactic molecular clouds. Combined with the complicating effects of dust and viewing angle, such an explanation may fit the local LBG-analog VV 114, based on the UV and near-IR imaging of Goldader et al. (2002). It is also possible that, in some small number of cases, multi-component morphologies may reflect objects which are nearby in projection, but unrelated due to large differences in redshift. While individual components of multi-component objects have not been spectroscopically confirmed to be associated, however, the angular distribution of sources suggests that such projection effects should contribute minimally to the total population.

Finally, we note that while the rest-UV and rest-optical morphologies of $z \sim 2-3$ galaxies are similar in the majority of cases (as shown by Dickinson 2000) and appear to contain little separable information, there is a small sub-sample of these galaxies for which the optical morphologies appear considerably more regular and "evolved" than their UV counterparts (Toft et al. 2005). It may be the case that this small population of galaxies has rest-optical morphologies which are easier to interpret than the majority of the galaxy sample, and may have useful correlations between rest-optical morphology and spectrophotometric or kinematic indices. In particular, such galaxies are intriguing possible targets for future kinematic study with the aid of AO-assisted integral-field spectroscopy (e.g., Forster-Schreiber et al. 2006; Law et al. 2006), which could demonstrate whether these galaxies are any more likely than the rest of the galaxy sample to contain tractable meaning in their luminous spatial structures.

DRL and CCS have been supported by grant AST03-07263 from the US National Science Foundation, and archival grant HST-AR 10311 from the Space Telescope Science Institute. The authors thank Rupali Chandar and Christy Tremonti for helpful communications.

Table 2.1. Quintile Bins for Morphological Parameters

Parameter	x_1[a]	x_2	x_3	x_4	x_5	x_6
I ($z \sim 2$)	0.181	7.473	12.540	15.977	20.108	48.163
I ($z \sim 3$)	4.200	11.559	13.952	17.991	21.407	45.181
G ($z \sim 2$)	0.034	0.172	0.245	0.321	0.382	0.568
G ($z \sim 3$)	0.105	0.265	0.321	0.385	0.459	0.570
Ψ ($z \sim 2$)	-0.199	1.667	3.871	6.151	10.677	34.062
Ψ ($z \sim 3$)	0.249	2.426	5.236	8.849	12.599	22.795
ξ ($z \sim 2$)	-0.115	0.015	0.033	0.049	0.076	0.507
ξ ($z \sim 3$)	-0.095	0.008	0.040	0.057	0.078	0.500

[a]Successive values of x_i denote boundary divisions between galaxies binned into equal-size quintiles according to each of the morphological parameters (without regard to the other three parameters).

Table 2.2. Standard Deviations from the Null Hypothesis for Independence between Morphological and Photometric Parameters

Quantity	I	G	Ψ	ξ
L_{1600}[a]	**+6.39**	**+4.57**	−0.32	**+3.10**
$L_{5-8\mu}$[b]	+0.92	−0.10	+0.68	−0.30
$L_{5-8\mu}$[c]	+0.21	+0.59	+0.02	+0.68
$L_{\rm FIR}/L_{1600}$[d]	**−3.33**	**−1.85**	−0.22	−1.22
$L_{\rm BOL}$[e]	+0.71	+0.90	+0.03	+0.73
$M_\star$[f]	+0.98	−0.05	−0.99	+0.07
Age[g]	−0.83	−0.02	−0.16	+1.12
$E(B-V)$[h]	**−3.29**	**−2.35**	−0.68	**−1.84**

[a]Rest-frame ultraviolet luminosity.

[b]Rest-frame mid-IR luminosity (all sources).

[c]Rest-frame mid-IR luminosity (MIPS sources only).

[d]Ratio of far-IR to ultraviolet luminosities.

[e]Bolometric luminosity.

[f]Stellar mass.

[g]Age of stellar population.

[h]Estimated reddening based on far-UV spectral slope.

Note. — '+' denotes positive correlation, '-' denotes negative. Bold typeface indicates correlations of greater than 90% confidence.

Table 2.3. Standard Deviations from the Null Hypothesis for Independence of Morphological Parameters and Star Formation

Quantity	I	G	Ψ	ξ
SFR_{SED}[a]	-0.32	$+0.59$	-0.15	$+0.30$
SFR_{UV}[b]	**+8.04**	**+4.77**	$+0.46$	**+3.15**
SFR_{IR}[c]	$+0.21$	$+0.59$	$+0.02$	$+0.47$
SFR_{UV+IR}[d]	$+0.92$	$+1.05$	$+0.03$	$+0.87$
SFR_{UV+IR}[e]	**+5.67**	**+2.17**	$+0.80$	**+1.76**
ϕ[f]	$+1.24$	$+1.62$	$+0.88$	$+1.01$
ϕ[g]	-1.12	-0.43	-0.04	-0.70

[a]Star formation rate estimated from SED fitting.
[b]Star formation rate estimated from UV photometry.
[c]Star formation rate estimated from IR photometry.
[d]Star formation rate estimated from UV+IR photometry (MIPS detected sources only).
[e]Star formation rate estimated from UV+IR photometry (MIPS undetected sources only).
[f]Specific star formation rate, $\phi = SFR_{UV+IR}/M_\star$ (MIPS detected sources only).
[g]Specific star formation rate, $\phi = SFR_{UV+IR}/M_\star$ (MIPS undetected sources only).

Note. — '+' denotes positive correlation, '-' denotes negative. Bold typeface indicates correlations of greater than 90% confidence.

Chapter 3

Predictions and Strategies for Integral-Field Spectroscopy of High-Redshift Galaxies*

David R. Law, Charles C. Steidel, Dawn K. Erb

California Institute of Technology, Department of Astronomy, MS 105-24, Pasadena, CA 91125

Abstract

We investigate the ability of infrared integral-field spectrographs to map the velocity fields of high redshift galaxies, presenting a formalism which may be applied to any telescope and imaging spectrograph system. We discuss the 5σ limiting line fluxes which current integral-field spectrographs will reach, and extend this discussion to consider future large aperture telescopes with cryogenically cooled adaptive reimaging optics. In particular, we simulate observations of spectral line emission from star-forming regions at redshifts $z = 0.5$ to 2.5 using a variety of spatial sampling scales and give predictions for the signal-to-noise ratio expected as a function of redshift. Using values characteristic of the W.M. Keck II telescope and the new OH-Suppressing InfraRed Imaging Spectrograph (OSIRIS) we calculate integral-field signal-to-noise ratio maps for a sample of $U_nG\mathcal{R}$ color-selected star-forming galaxies at redshift $z \sim 2 - 2.6$ and demonstrate that OSIRIS will be able to reconstruct the two-dimensional projected velocity fields of these galaxies on scales of 100 mas ($\sim$ 1 kpc at redshift $z \sim 2$). With signal-to-noise ratios per spatial sample up to $\sim$

*A version of this chapter was published in *The Astronomical Journal*, 2006, vol. 131, 70–83, and is reproduced by permission of the AAS.

20, OSIRIS will in some cases be able to distinguish between merger activity and ordered disk rotation. Structures on scales smaller than 1 kpc may be detected by OSIRIS for particularly bright sources, and will be easy targets for future 30 m class telescopes.

3.1 INTRODUCTION

As the available instrumentation on large telescopes has pushed observations into the near-infrared (NIR), the denizens of the so-called "redshift desert" from $z \sim 1.4 - 2.5$ have increasingly become targets of concerted study. Observations suggest that the morphological chaos of the $z \sim 3$ universe evolves into the familiar modern-day Hubble sequence by redshift $z \sim 1$ (e.g., Giavalisco et al. 1996; Papovich et al. 2005), and the redshift $z \sim 2$ population is likely to contain a wide assortment of galactic types as protogalactic merging activitity transitions to kinematically ordered evolution. It often proves difficult however to distinguish starbursting galaxies with an ordered disk morphology from those actively experiencing protogalactic assembly, since the relevant angular scales are barely resolved under typical ground-based seeing conditions, and the rest-frame UV light (e.g., as observed in the optical by the Hubble Space Telescope) is dominated by emission from bright, clumpy star-forming regions.

Long-slit nebular emission line spectroscopy has enabled velocity curves to be derived for a sample of high-redshift galaxies (e.g., Pettini et al. 2001; Lemoine-Busserolle et al. 2003; Moorwood et al. 2003; Erb et al. 2003, 2004), giving some insight into the kinematic properties of these sources and suggesting that massive disk systems may be present out to at least redshift 2.5. However, ground-based long-slit spectroscopy suffers from severe atmospheric seeing problems (as demonstrated by Erb et al. 2004), and recovered velocity curves for morphologically selected potentially disk-like galaxies at redshift $z \sim 2$ often show little-to-no spatially resolved velocity shear (Erb et al. 2004). One possible explanation for this lack of velocity shear may be that these sources are composed of proto-galactic fragments of angular size below the typical seeing limit ($\sim 0\farcs5$ in the K-band).

Given the small apparent angular size of these sources (radius $r \lesssim 1\farcs0$) compared to that of the seeing disk ($\Theta_{\rm seeing} \approx 0\farcs5$), high spatial resolution data from ground-based telescopes has only recently become available through the aid of adaptive-optics (AO) technology. The advent of integral-field spectrographs (IFS) on 10 m class telescopes equipped with laser-

guide star adaptive optics systems offers the new possibility of mapping the kinematics of galaxies at $z \sim 2$ on the scale of tenths of an arcsecond or less. Not only can such AO-fed spectrographs mitigate the seeing-induced uncertainties inherent in velocity curves derived from long-slit spectra, but their integral-field capability will provide two-dimensional velocity maps from which it may be possible to reconstruct the kinematic profiles of these galaxies on scales of a few hundred parsecs.

Recent years have seen a rapid increase in the number of optical/NIR integral-field spectrographs capable of studying the velocity fields of high redshift galaxies (Table 3.1), and these instruments are starting to yield kinematic maps of large galaxies from redshifts $z = 0.1$ (Swinbank et al. 2005a) and 0.5 (Flores et al. 2004) up to $z = 2.4$ (Swinbank et al. 2005b). In this contribution, we outline an observing strategy for integral-field IR spectroscopy of high redshift galaxies, treating the case of a general telescope + IFS system in §3.2. In §3.3 we narrow our discussion to concentrate on simulating the capabilities of the OSIRIS spectrograph on the W.M. Keck II telescope, and predict the signal-to-noise (S/N) ratios expected for observations of nebular line emission from star-forming regions with redshifts from $z \sim 0.5 - 2.5$. We explore the relative merits of available lenslet scales and observable spectral emission lines, and assess the ability of OSIRIS to obtain spatially resolved velocity information from $U_n G\mathcal{R}$ color-selected galaxies at redshift $z \sim 2$ – 2.5 in the Hubble Deep Field North (i.e., the "BX" sample defined by Steidel et al. 2004 and Adelberger et al. 2004). Finally, in §3.4 we use characteristics typical of the OSIRIS spectrograph to investigate the limiting line fluxes detectable from an arbitrary source using current generation spectrographs, extending this discussion to consider next-generation telescopes and cryogenically cooled optical systems.

We assume a cosmology in which $h = 0.7$, $\Omega_m = 0.3$, $\Omega_\Lambda = 0.7$.

3.2 METHOD

Integral-field (or multi-object) spectrographs may have optical designs ranging from a simple objective prism to a more complex fiber-fed, lenslet-based, or image-slicing configuration. We tailor our discussion specifically to the case of an imaging lenslet array, in which each of a closely spaced array of lenslets disperses a spectrum in a staggered pattern onto a detector (a good introduction to this technique is given by Bacon et al. 1995). Our formalism is

presented with such a lenslet-type spectrograph in mind, but may be easily modified for both image-slicing and fiber-type spectrographs.

3.2.1 Signal Estimation

3.2.1.1 Estimating Background Count Rates

We adopt the Gemini Observatory model for the Mauna Kea near-IR sky brightness spectrum[1] (spectral resolution $\mathcal{R} \sim 2000$) which incorporates zodiacal emission (from a 5800 K blackbody), atmospheric emission (from a 250 K blackbody), and radiation from atmospheric OH molecules. In addition to these components we introduce models of the thermal blackbody emission from warm reflective surfaces in the light path. The telescope mirrors and the adaptive reimaging optics are modelled as 270 K blackbodies with net emissivities $\epsilon = 1 - \eta$ (where η is the transmission coefficient of the component).

Using the Planck blackbody function, the photon flux due to thermal emission from these components is

$$f_\lambda = \epsilon\,\alpha^2\,\frac{2\,c}{\lambda^4}\frac{1}{e^{hc/\lambda kT}\,-\,1}\,\text{photons}\,\text{s}^{-1}\,\text{cm}^{-2}\,\text{cm}^{-1}\,\text{arcsec}^{-2}, \tag{3.1}$$

where f_λ is the spectral flux at wavelength λ, $\alpha = 4.85 \times 10^{-6}$ is a scale factor representing the number of steradians per square arcsecond, T is the temperature of the component in degrees Kelvin, and the remaining symbols c, h, and k are standard physical constants.

The corresponding total electron count rate per detector pixel per lenslet (R_{BG}, electrons s^{-1} lenslet^{-1} pixel^{-1}) from these three background sources (Gemini sky brightness model, telescope emissivity, and AO system emissivity) is given by

$$R_{\text{BG}}(\lambda) = \left(f_{\lambda,\text{sky}}\,\eta_{\text{tel}}\,\eta_{\text{AO}} + f_{\lambda,\text{tel}}\eta_{\text{AO}} + f_{\lambda,\text{AO}}\right)\eta_{\text{spec}}(\lambda) A\,a^2\frac{P}{\mathcal{N}_1}, \tag{3.2}$$

where $f_{\lambda,\text{sky/tel/AO}}$ represents the photon flux from the sky/telescope/AO system respectively in photons s^{-1} cm^{-2} cm^{-1} as^{-2}, η_{tel} is the throughput of the telescope optics, η_{AO} is the throughput of the AO system, $\eta_{\text{spec}}(\lambda)$ is the throughput of the spectrograph (a complicated function of λ including the throughput of the spectrograph blaze function, filter

[1] Available at http://www.gemini.edu/sciops/ObsProcess/obsConstraints/atm-models/nearIR_skybg_16_15.dat

transmission, detector response, and optical throughput additional components), A is the telescope collecting area, a is the angular lenslet size (in arcseconds), P is the pixel scale (wavelength coverage per pixel), and $\mathcal{N}_1$ is the spatial width of each spectrum in detector pixels.

3.2.1.2 Estimating Source Count Rates

The source count rate in a given emission line may be estimated by scaling a finely sampled (i.e., with spatial resolution at least as fine as the desired lenslet scale) map of the source morphology by the total emission line flux of the source. While Hα maps of high redshift galaxies are generally unavailable, Hα emission often correlates well with the FUV (1500 Å) morphology — as demonstrated for late-type local galaxies by Gordon et al. (2004), Kennicutt et al. (2004), and Lee et al. (2004) — and it is often a reasonable approximation to use a FUV flux map to represent the Hα flux distribution (although cf. Conselice et al. 2000). The FUV flux can readily be observed by the Hubble Space Telescope's Advanced Camera for Surveys (HST-ACS) since rest-frame FUV emission is redshifted into the B-band for sources at redshift $z \sim 2 - 2.6$, and we therefore use images of our target galaxies in the GOODS-N field which are publically available from the HST-ACS data archives[2]. These images are ideal for studying the morphology of the target galaxies on angular scales of less than an arcsecond since the point-spread function of the ACS data is about 125 mas (Giavalisco et al. 2004).

These FUV flux maps are resampled into pixel maps with a pixel size corresponding to the desired lenslet scale, and the sum of the pixel values is rescaled by the total line flux of the source divided by the average photon energy to obtain a grid of line fluxes $f_{\lambda,\mathrm{source}}$ (photons s^{-1} cm^{-2} lenslet^{-1}) for each lenslet. Since the adopted ACS flux maps have already been sky-subtracted we assume that all pixels within a given region with fluxes above zero-threshold represent source emission, and find the total FUV source flux by simply summing all such pixels. The average electron count rate per detector pixel (electrons s^{-1}

[2]Based on observations made with the NASA/ESA Hubble Space Telescope, obtained from the data archive at the Space Telescope Science Institute. STScI is operated by the Association of Universities for Research in Astronomy, Inc., under NASA contract NAS 5-26555.

lenslet^{-1} pixel^{-1}) is then calculated in analogy to Equation 3.2 as

$$R = f_{\lambda,\mathrm{source}}\,\eta_{\mathrm{atm}}(\lambda)\,\eta_{\mathrm{tel}}\,\eta_{\mathrm{AO}}\,\eta_{\mathrm{spec}}(\lambda)\,\frac{A}{\Delta\lambda}\,\frac{P}{\mathcal{N}_1}, \tag{3.3}$$

where $\Delta\lambda$ is the full width at half maximum (FWHM) of the spectral line (computed as the quadrature sum of the line width due to source velocity dispersion σ_{v} and from the finite spectrograph resolution) and $\eta_{\mathrm{atm}}(\lambda)$ is the atmospheric transmission as a function of wavelength, for which we adopt the Mauna Kea transmission spectra generated by Lord (1992).[3]

3.2.1.3 Adaptive-Optics and Seeing Corrections to Count Rates

We now take into account the effects of realistic AO performance and losses to the atmospheric seeing halo (the net throughput of the AO system was already taken into account in §3.2.1.1 and 3.2.1.2). The flux in each lenslet is resampled uniformly into a grid of $x \times x$ squares,[4] and the approximation made that the flux in each grid square (before incidence upon the Earth's atmosphere) may be described as a point source. After traversing both the atmosphere and the AO system, the light from this point source is divided between a diffraction-limited core and a seeing-limited halo, the fluxes of which are given by

$$f_{\mathrm{diffraction}} = \mathcal{S} \times f_{\mathrm{total}} \tag{3.4}$$

$$f_{\mathrm{seeing}} = (1 - \mathcal{S}) \times f_{\mathrm{total}} \tag{3.5}$$

[3] Both the Mauna Kea transmission spectra and sky brightness profiles assume 1.6 mm H_2O and sec(z) = 1.5 at local midnight.

[4] x is chosen to be suitably large that the results of this method converge, but small enough that computational efficiency is reasonably high. We find that $x = 5$ gives a good convergence of the PSF integration with a reasonable efficiency for all except the finest sampling scales of $a = 20$ mas, for which we employ $x = 2$. Note that the efficiency will depend also on the total size of the field covered by the lenslet array.

where $\mathcal{S}$ is the strehl of the AO correction. Assuming that the net wavefront error of the adaptive optics system $\sigma_{\rm wfe}$ is constant, strehl[5] as a function of wavelength is given by

$$\mathcal{S} = e^{-(2\pi\sigma_{\rm wfe}/\lambda)^2}. \tag{3.6}$$

Both the seeing-limited halo and diffraction-limited core may be approximately represented by two-dimensional Gaussian profiles with $\sigma_{\rm halo} = \frac{\theta_{\rm seeing}}{2.4}$ and $\sigma_{\rm core} = \frac{1.22\,\lambda/D}{2.95}$ (where D is the diameter of the telescope's primary mirror).[6] The core and halo light profiles from each grid square may be integrated over each lenslet to generate an observed flux distribution which incorporates both *losses to* the seeing halo from a given lenslet and *gains from* the seeing halos of neighboring lenslets.

Since this procedure assumes that light lost to the seeing halo of one lenslet is recovered by surrounding lenslets, it is possible that all losses to the seeing halo from a given lenslet may be regained from spill-over flux from the halos of neighboring lenslets if the intrinsic flux in these neighbors is suitably high. However, this flux will generally be a source of additional background noise — if the flux is spilled from a region of the source with a very different line-of-sight velocity it will contribute this flux at the corresponding wavelength and hinder precise measurement of the spectral peak of flux originating from a given lenslet. Modeling this complex effect in detail requires *a priori* knowledge of the velocity substructure of the source, and we therefore generally assume that all such spilled flux adds to the noise of the observation rather than the signal. In §3.2.2 and §3.3.4 where we adopt specific velocity models, however, spilled light is treated comprehensively as a function of both angular position and wavelength.

[5]The strehl actually achieved in laser-guide star operation for a given source will also depend on the proximity of the source to a suitably bright (magnitude $R < 18$) reference star for tip-tilt correction of the wavefront.

[6]The point spread function (PSF) of the diffraction-limited core is best described by a two-dimensional Airy function, which has a central peak narrower than that of a standard Gaussian with the same peak value. However, the 2D Airy function profile is closely approximated by a 2D Gaussian whose FWHM has been reduced by a factor of $2.4/2.95 = 0.81$. Since the exponential form of the Gaussian lends itself more readily to analytic integration than the Airy function, in the interests of efficiency we adopt this Gaussian approximation.

3.2.1.4 Estimating Signal-to-Noise Ratios

Using the quantities derived it is possible to calculate the S/N ratio expected for detection of a particular spectral line in each lenslet. We use the standard equation

$$\frac{S}{N} = \frac{R \mathcal{N}_1 \mathcal{N}_{\rm spec} t}{\sqrt{(R + R_{\rm BG} + R_{\rm DK}) \mathcal{N}_1 \mathcal{N}_{\rm spec} t + N_{\rm RD}^2 (t/t_0) \mathcal{N}_1 \mathcal{N}_{\rm spec}}}, \tag{3.7}$$

where $\mathcal{N}_{\rm spec}$ is the number of spectral pixels summed (i.e., the FWHM of the spectral line in pixels), $R_{\rm DK}$ is the dark current count rate in e^- s^{-1} pixel^{-1}, $N_{\rm RD}$ is the detector read noise in e^- pixel^{-1}, t and t_0 are the total and individual exposure times, respectively, and all other quantities have been previously defined.

3.2.2 Spectral Synthesis

Simply *detecting* an emission line with some confidence does not guarantee that its *centroid* can be measured with great accuracy, and we therefore generate artificial spectra and attempt to measure their centroids using techniques which will be applied to observational data to effectively simulate the recovery of velocity substructure.

Defining a spectral vector with one element for each spectral pixel (i.e., summing over the $\mathcal{N}_1$ detector pixels to create a 1-dimensional spectrum), it is easy to generate a simulated spectrum from the counts as a function of wavelength by introducing noise according to Poisson statistics. Using this simulated spectrum (or an observed spectrum which has been precisely wavelength calibrated using the bright OH spectral features), the background signal $N_{BG} = (R + R_{\rm BG} + R_{\rm DK}) \mathcal{N}_1 \mathcal{N}_{\rm spec} t + N_{\rm RD}^2 (t/t_0) \mathcal{N}_1 \mathcal{N}_{\rm spec}$ due to read noise, dark current, and the sky background may be subtracted off[7] to determine the sky-subtracted counts as a function of wavelength for the source. This spectrum may be further processed to obtain velocity centroids using standard routines. Hand-processing by an experienced individual appears to be the most reliable method of measuring velocity centroids, although such a method is impractically time-consuming for extensive simulations with hundreds of spectra apiece. Instead, we adopt an automated routine which fits a Gaussian profile to the background-subtracted spectra using a Levenberg-Marquardt fitting algorithm (a non-linear

[7]Generally this background signal will be well-determined for all except the smallest fields of view. We explore this for the case of the OSIRIS spectrograph in §3.3.1.

least-squares regression algorithm similar to that used in the standard IRAF routine *splot*) and measures the velocity shift of the peak flux from the systemic redshift. This method is found to perform reliably for most spectral features with S/N ratios > 3, although some particularly faint features which are not handled well by this automated method may still yield useful information when individually hand-processed.

We note that for the case of spectrographs whose output is in the form of data cubes, one-dimensional observational spectra may be extracted for each spatial element, and may then be processed in entirely the same manner as these simulated spectra.

3.3 SIMULATED OBSERVATIONS WITH OSIRIS

The simulation method described in the previous section has been outlined in a general manner so that it may be applied to any telescope and integral-field spectrograph system. We now proceed to adopt characteristics typical of the W.M. Keck II telescope and OSIRIS spectrograph in order to quantify the performance capability expected from this system for the study of high-redshift galaxies. In §3.3.1 we describe the site, telescope, and spectrograph characteristics, and in §3.3.2 we explore the expected detection limits of OSIRIS for observations of nebular line emission from typical star-forming regions at redshifts $z = 0.5-2.5$. In §3.3.3 we present integral-field S/N ratio maps for selected $z \sim 2-2.6$ star-forming galaxies in the GOODS-N field and explore the integration times and lenslet scales required to achieve significant detections. Finally, in §3.3.4 we explore the ability of OSIRIS to recover the velocity substructure of these sources assuming disparate kinematic models. We note that the assumed characteristics of the OSIRIS spectrograph are preliminary results based upon commissioning data, and the results of our analysis should therefore be scaled accordingly to reflect the final well-determined specifics of the instrument once such information is available.

3.3.1 The OSIRIS Spectrograph

3.3.1.1 Mechanical Overview

OSIRIS (OH-Suppressing InfraRed Imaging Spectrograph) is an integral-field spectrograph designed and built at UCLA for the Keck II telescope (Larkin et al. 2003), and is presently

in the initial stages of commissioning during the 2005 observing season. The spectrograph employs reimaging optics to select between lenslet scales of 20, 35, 50, and 100 mas and uses a low dark-current Hawaii-2 HgCdTe 2048 $\times$ 2048 IR detector array. OSIRIS is designed to work in conjunction with the Keck-II laser guide star (LGS) AO system, since the vast majority of targets (about $\sim 99\%$ of the sky) are too distant from a suitably bright star to permit natural guide star (NGS) observations. Characteristic parameters for the Keck II telescope, LGS AO system, and OSIRIS spectrograph are summarized in Table 3.2. The spectrograph parameters given are based upon values provided in the OSIRIS pre-ship report (J. Larkin, private communication).

OSIRIS uses broad- and narrow-band order-sorting filters to select the wavelength range imaged on the detector; the available four broadband IR filters (outlined in Table 3.3) are chosen to correspond to the regions of high throughput in orders $n = 3 - 6$ of the spectrograph grating (blazed at 6.5 μm). Operating in broad-band mode, OSIRIS is capable of producing spectra from 16 x 64 lenslets for a total of 1024 spectra with 1600 spectral pixels each. OSIRIS is also capable of operating in narrow-band mode using 19 narrow-band filters which together span the same range of wavelengths as the broadband filter set. This narrow-band mode will generally be more useful for targeted velocity studies of high-redshift galaxies, for which velocity-shifted nebular emission lines are expected to fall within a few angstroms of the systemic value. In this mode, spectra from 48 x 64 lenslets can fit on the detector for a total of 3072 spectra comprised of 400 spectral pixels each. The resulting fields of view for broad-band and narrow-band operation at each of the four available lenslet scales are given in Table 3.4.

In the interests of integration time, a suitably large field of view must be chosen so that a reasonable number of lenslets are imaging both the science target and the off-source background sky (for calibration purposes) simultaneously. In narrow-band mode, this means that at least 5% of the lenslets must have negligible flux from the science target in order to calculate a background signal with an uncertainty of less than 10% of the Poisson shot noise. Most redshift $z \sim 2$ star-forming galaxies have radial size ~ 1 arcsecond or less, resulting in a source area of

$$A_{\text{source}} \lesssim \pi \left(\frac{1\,\text{arcsecond}}{a} \right)^2 \text{ lenslets} \tag{3.8}$$

where a is again the lenslet scale in arcseconds. Operating at all except the finest sampling scales of $a = 20$ mas, these sources cover considerably less than the total number of lenslets available over the field of view, indicating that accurate estimation of the background flux will be possible with no additional pointings. Studies using lenslet scales of $a = 20$ mas will require greater caution in the placement of their fields of view to ensure reasonable background coverage, although, as will be demonstrated in §3.3.3, these small sampling scales are unlikely to be of great utility for OSIRIS observations of $z \sim 2$ galaxies anyway.

3.3.1.2 Mauna Kea/OSIRIS Noise Characteristics

The model background sky brightness as a function of wavelength is calculated as outlined in §3.2.1.1 for typical Keck II and AO system characteristics and is plotted in Figure 3.1. Note that for sake of clarity we suppress individual OH emission lines which are visibly separated from neighboring lines by a region of inter-line background, since it will in general be possible to work around these emission features. Effective sky surface brightnesses corresponding to this background spectrum are given in Table 3.3.

It is informative to compute the relative contribution of detector read noise, dark current, and background radiation in determining the total noise in an exposure. As given in Table 3.2, the read noise for the Hawaii-2 infrared detector array is $N_{\rm RD} \sim 3$ electrons pixel^{-1} (after multiple correlated double samples), with a dark current of $R_{\rm DK} = 0.03$ electrons s^{-1} pixel^{-1}. Using the model background spectrum (Fig. 3.1), it is possible to calculate the minimum exposure time $t_{\rm min}$ required for read noise to become a negligible contributor to the total noise budget,

$$t_{\rm min} = \frac{N_{\rm RD}}{R_{\rm DK} + R_{\rm BG}}. \tag{3.9}$$

Figure 3.2 plots the minimum exposure time as a function of wavelength for lenslet scales of 20, 35, 50, and 100 mas. Note that for wavelengths where background radiation is negligible compared to the dark current $t_{\rm min}$ approaches 100 seconds (since $N_{\rm RD}/R_{\rm DK} =$ 100 seconds), while at wavelengths for which $t_{\rm min} < 50$ seconds the background radiation dominates over the dark current. In order to minimize the contribution of detector read noise to our simulations we fix invidual exposure times at $t_0 = 900$ seconds, although we note that shorter times could be chosen on the basis of Figure 3.2 if long observations prove problematic due to technical difficulties such as LGS-shuttering from beam collisions with

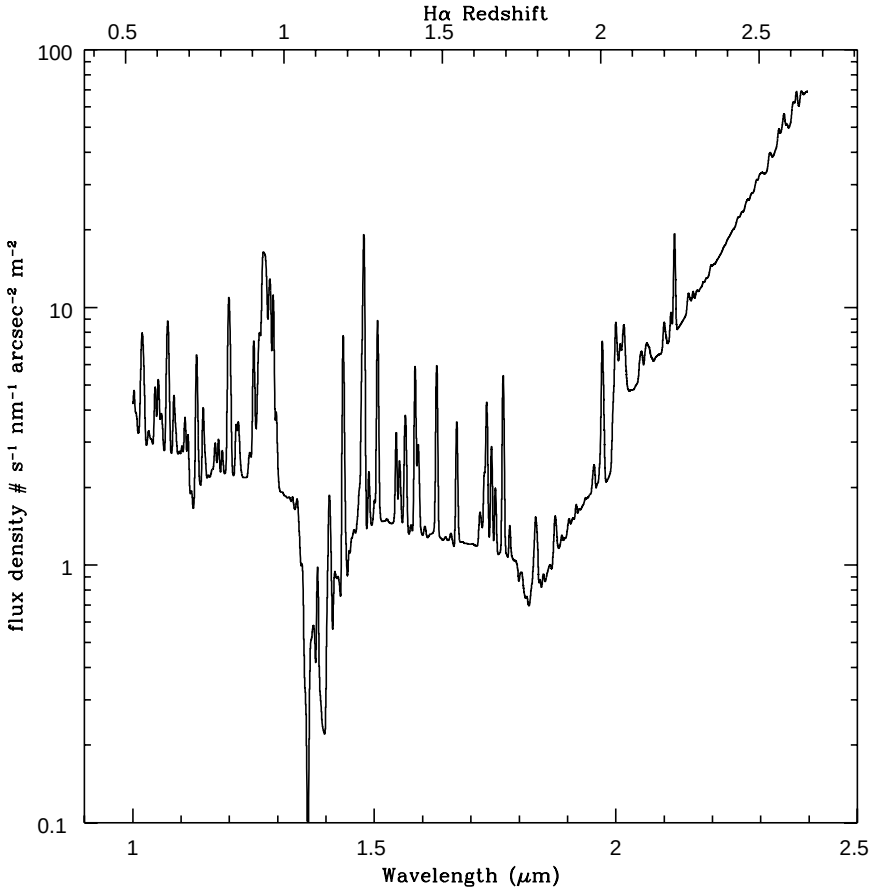

Figure 3.1 Model effective background sky spectrum for Keck II incorporating the Gemini model for zodiacal light and atmospheric emission ($\mathcal{R} \sim 2000$), a 35% emissivity in the AO system, and a 20% emissivity in the telescope optics (90% throughput for both the primary and secondary mirrors) at temperature $T = 270$ K. Spectrally dense OH emission line regions appear as spikes since a spectrograph with resolution $\mathcal{R} = 2000$ will not be able to reach inter-line background levels in these regions of severe contamination. The dip around 1.4 μm is due to high atmospheric opacity. Redshifts for which Hα emission falls at a particular wavelength are indicated along the top axis of the plot.

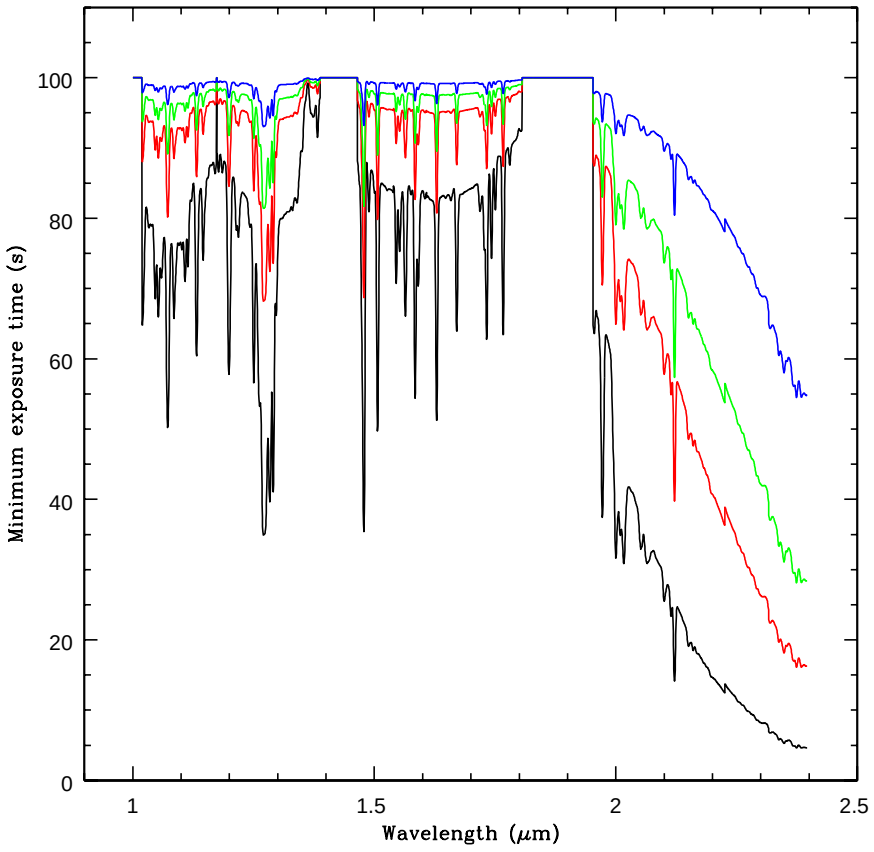

Figure 3.2 Minimum integration time required for detector dark current + background counts to equal the detector read noise for lenslet scales of 100 (black line), 50 (red line), 35 (green line), and 20 mas (blue line).

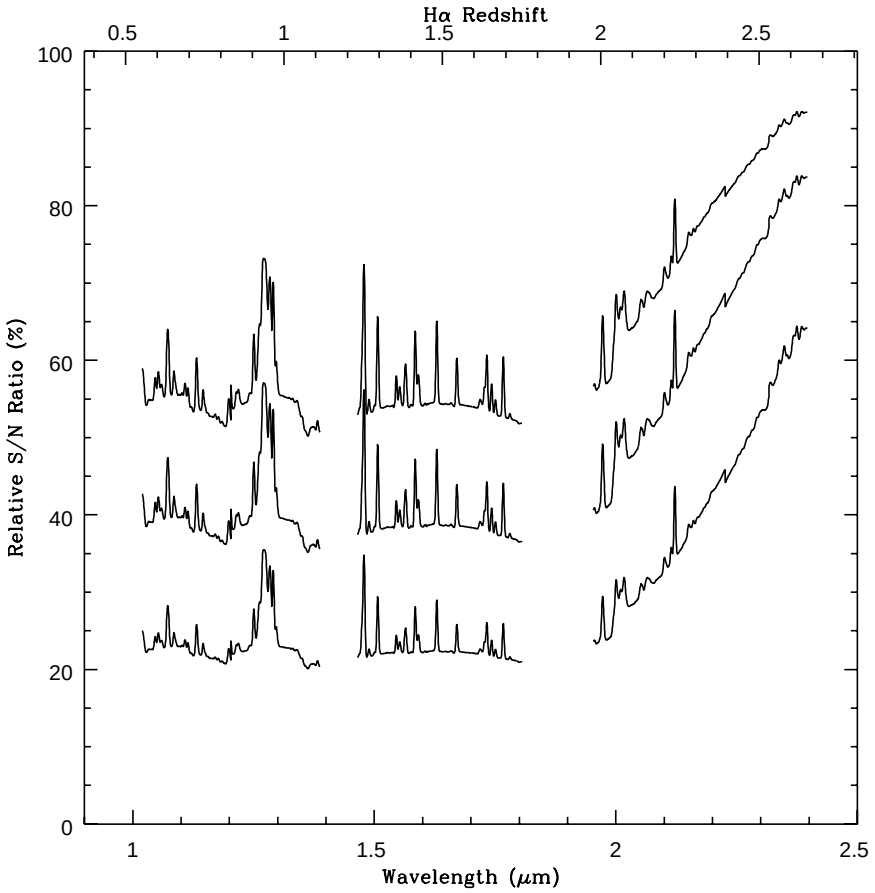

Figure 3.3 Relative S/N ratios achieved binning data from 50, 35, and 20 mas lenslets (solid curves, top to bottom, respectively) to 100 mas, as compared to data taken using 100 mas lenslets. Redshifts for which Hα emission falls at a particular wavelength are indicated along the top axis of the plot.

other Mauna Kea observatories (S. Kulkarni, private communication).

Ideally, observations could be conducted using the finest available lenslet scale for which the field of view covers the entire target, since (even if the signal is too low to usefully measure on such a fine scale) the results may be spatially binned to coarser scales. In practice, however, detector noise often imposes severe penalties on fine sampling scales, introducing noise into the binned sample. Using our characterization of the Keck/OSIRIS noise budget, we assess the utility of such binning as a function of wavelength by plotting the fractional change in the S/N ratio obtained by binning data from the three smaller lenslet scales to 100 mas (Fig. 3.3). These calculations adopt an individual exposure time of 900

seconds, and assume that the flux from the desired target is negligible compared to the background flux. We note that for wavelengths longward of 2.3 μm the S/N ratios achieved for binning 50 mas lenslets to 100 mas scales is about 90% of that achived using actual 100 mas sampling, suggesting that for long wavelength observations it may be worthwhile to use small lenslets even for faint sources (although finer sampling will come at the cost of decreased field-of-view).

3.3.2 Observing Star-Forming Regions at Intermediate-to-High Redshifts

To assess the anticipated performance of OSIRIS we estimate the S/N ratios expected for observations of star-forming regions at redshifts $z = 0.5 - 2.5$, considering the cases of a spatially unresolved (i.e., pointlike), isolated star-forming region, and a spatially extended source with a physical diameter of 1 kpc. In each case it is assumed that the star-formation rate is 1 $M_\odot$ yr^{-1} (assuming a Salpeter IMF this corresponds to an Hα luminosity of 1.27×10^{41} erg s^{-1} from Kennicutt 1998a), and that the velocity dispersion is negligible within a single spatial sample. In each of these cases both simulated Hα and [O III] λ5007 emission lines (assuming [O III]/H$\alpha \sim 1$) are artificially observed to calculate the expected S/N ratio expected in the peak lenslet at sampling scales of 100, 50, 35, and 20 mas. These simulations take into account the redshift dependence of flux and angular diameter, and the wavelength dependence of the atmospheric seeing,[8] diffraction limit, sky brightness, and AO correction strehl (assuming a fixed wavefront error $\sigma_{\rm wfe} = 337$ nm).

Figure 3.4 plots the results as a function of redshift for each of the available OSIRIS lenslet scales. In general the shape of the curves reflects the adopted atmospheric and spectrograph transmission spectra, with gaps where atmospheric transmission is particularly poor (OSIRIS filters are designed to cut out these wavelength intervals). The monotonic decrease in the S/N ratio for observations of Hα at redshift $z > 2.1$ however is due to the rapidly rising thermal contribution to the background radiation in the K-band. We note that for point-like sources virtually the same signal level is obtained using both 100 mas and 50 mas sampling scales since nearly the same amount of integrated light is contained within the lenslet, while losses begin to occur on scales of 35 and 20 mas which are below the Keck diffraction limit. In contrast, for extended sources the signal obtained using smaller lenslets

[8] $\Theta_{\rm seeing} = \Theta_{\rm V} \times (\lambda/5500\ {\rm \AA})^{-0.2}$, where visual-band seeing $\Theta_{\rm V} = 0.7$ arcseconds.

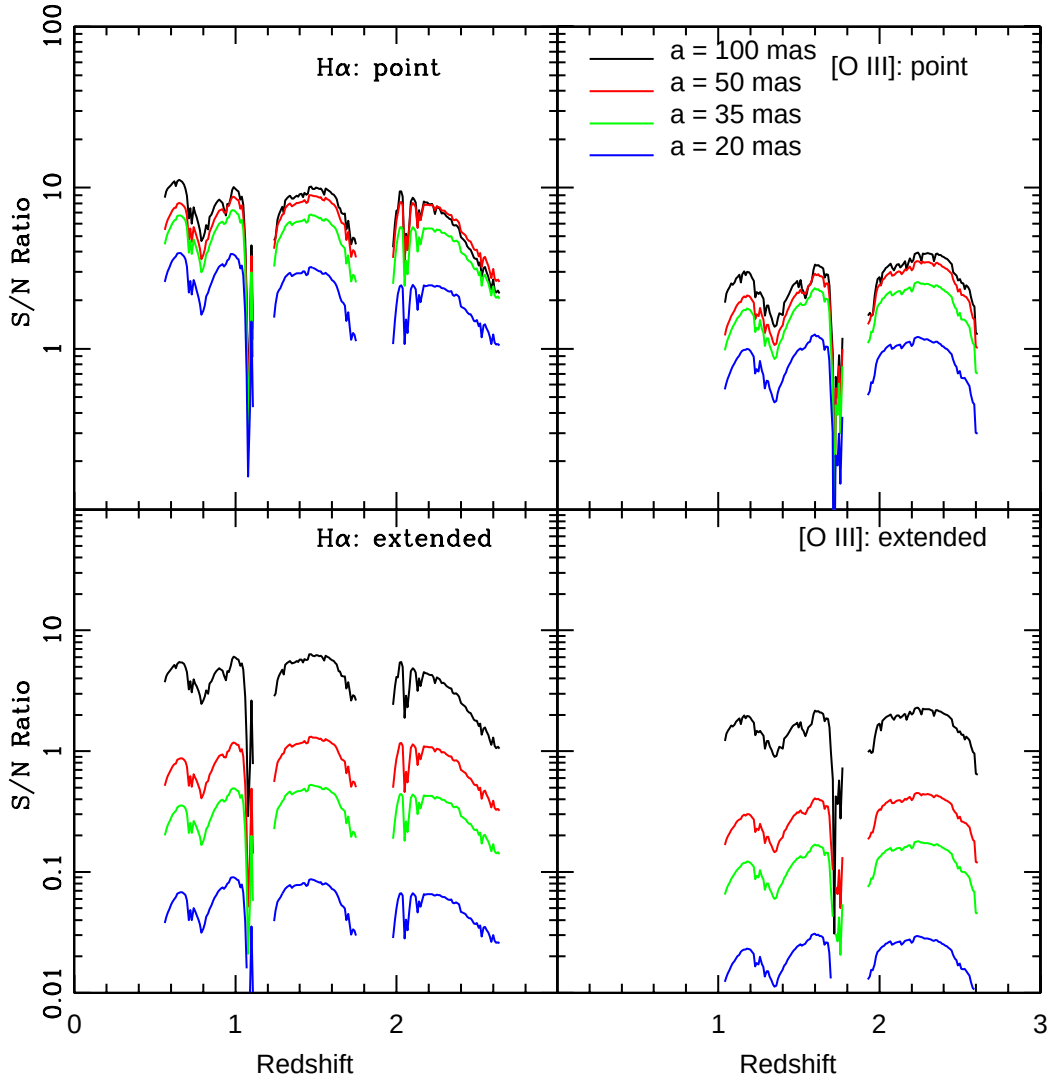

Figure 3.4 Expected signal-to-noise ratios for 1 hour observations of point and extended (1 kpc diameter) sources with a star formation rate of 1 $M_{\odot}$ yr^{-1} using different OSIRIS lenslet scales (a). The line flux ratio [O III] (λ5007)/Hα is taken to be unity, and the velocity dispersion in each spatial sample is assumed to be negligible.

is considerably reduced since the lenslets are gathering light from a smaller effective area.[9]

Observations of the rest-frame optical spectra of redshift $z \sim 2$ and $z \sim 3$ Lyman-Break Galaxies (LBGs, e.g., Pettini et al. 2001; Erb et al. 2003) have demonstrated that these galaxies have strong nebular emission lines, particularly [O III] λ5007, for which the line flux ratio [O III]/Hα can be close to unity[10] for relatively metal-poor (< 0.5 solar) sources. Since the thermal background rises rapidly in the K band (Fig. 3.1), this strong [O III] emission can present an appealing observational alternative to Hα since it falls in the H band (which has a lower thermal background) for redshifts $z \approx 1.9 - 2.6$. However the exponential decrease of strehl with shorter wavelengths, paired with the fact that detector dark current rather than thermal background radiation tends to dominate the error budget at most wavelengths and sampling scales, means that as shown in Figure 3.4 (right panels) it will still be most efficient to observe Hα emission for all except those sources at $z > 2.5$, or at redshifts for which Hα emission is severely attenuated by the atmosphere.

We conclude for redshift $z \sim 2-2.6$ star-forming galaxies (which have typical uncorrected Hα star-formation rates of $\sim 16\ M_{\odot}\ \mathrm{yr}^{-1}$, Erb et al. 2003) that 100 mas sampling of Hα emission with OSIRIS should in general yield fairly comprehensive spatial coverage with an integration time of a few hours (see also §3.3.3). However, background radiation and detector dark current will largely be prohibitive for obtaining spectroscopic data on scales of 50 mas or below. As described in §3.3.1.2 though, it may nonetheless be desirable to use such fine sampling scales since: (1) coarser sampling scales can be reconstructed by binning data, often with relatively little loss of signal strength, and (2) if emission regions visible in the ACS data resolve into point-like sources (e.g., giant H II regions or super-star clusters) on scales below the HST-ACS resolution limit, the signal on small scales may be larger than anticipated.

[9] Recall that spillover from surrounding lenslets is assumed to be a source of noise. In localized areas, across which the physical properties of the source change very little, this spillover light from neighboring lenslets may instead boost the observed signal (particularly for small lenslet scales), resulting in slightly higher S/N ratios than the conservative estimates given here.

[10] [O III]/Hα has not been directly measured, but the fluxes are often comparable.

3.3.3 Signal-to-Noise Ratio Maps

In order to reliably reconstruct the velocity profile of a galaxy it will be necessary to obtain spectra with high S/N ratios over many lenslets. Using the tools developed so far we generate theoretical S/N ratio maps for four of the $z \sim 2-2.6$ star-forming galaxies observed by Erb et al. (2004) to illustrate the spatial extent of the data which Keck/OSIRIS will be capable of providing.

Using the instrument parameters outlined previously in Table 3.2, we simulate observations of BX galaxies 1311, 1332, 1397, and 1479 drawn from the Steidel et al. (2004) catalog. These four sources were selected because they all have long-slit Hα spectra, two of them (BX 1332, 1397) with actual tilted velocity curves, and generally have elongated or multiple-component morphologies. Hα fluxes for these galaxies are estimated using lower limits to the fluxes measured by Erb et al. (2004); motivated by narrowband imaging and continuum spectroscopy of similar sources we estimate a factor of ~ 2 correction to the Erb et al. (2004) values to account for slit losses and non-photometric observing conditions (see Table 3.5 for a summary of these corrected flux values). The average Hα flux of the BX galaxy sample is roughly $\sim 6 \times 10^{-17}$ erg s^{-1} cm^{-2} (Erb et al. 2006b), and therefore while BX 1332 and 1397 are slightly brighter than average we note that BX 1479 may be taken as roughly representative of the typical flux of the sample. These Hα fluxes are used to scale the ACS B-band (F450W) images to generate Hα flux maps as described in §3.2.1.2. In each case we assume that the velocity dispersion is negligible within a single spatial sample.[11]

S/N ratio maps of these four galaxies are given in Figure 3.5, and show that in a four hour integration we expect to obtain numerous spectra with S/N ratios $\gtrsim 5$ (red pixels) across the source if a lenslet scale of 100 mas is used (as expected on the basis of Fig. 3.4). In comparison, Figure 3.6 illustrates the S/N ratios expected in the same integration time for BX 1332 using the four available lenslet scales of 20, 35, 50, and 100 mas (panels (a) – (d), respectively). Clearly, 20 and 35 mas sampling scales are unlikely to be of use for

[11] This assumption will be valid so long as the velocity dispersion σ_v within the sample is less than $c/\mathcal{R}/2.4$ (≈ 30 km s^{-1} for spectral resolution $\mathcal{R} = 3800$). This translates to a total velocity dispersion for a source of angular size 1 arcsecond (with a smoothly varying velocity field) of about 300 km s^{-1} using 100 mas sampling, and 1500 km s^{-1} using 20 mas sampling.

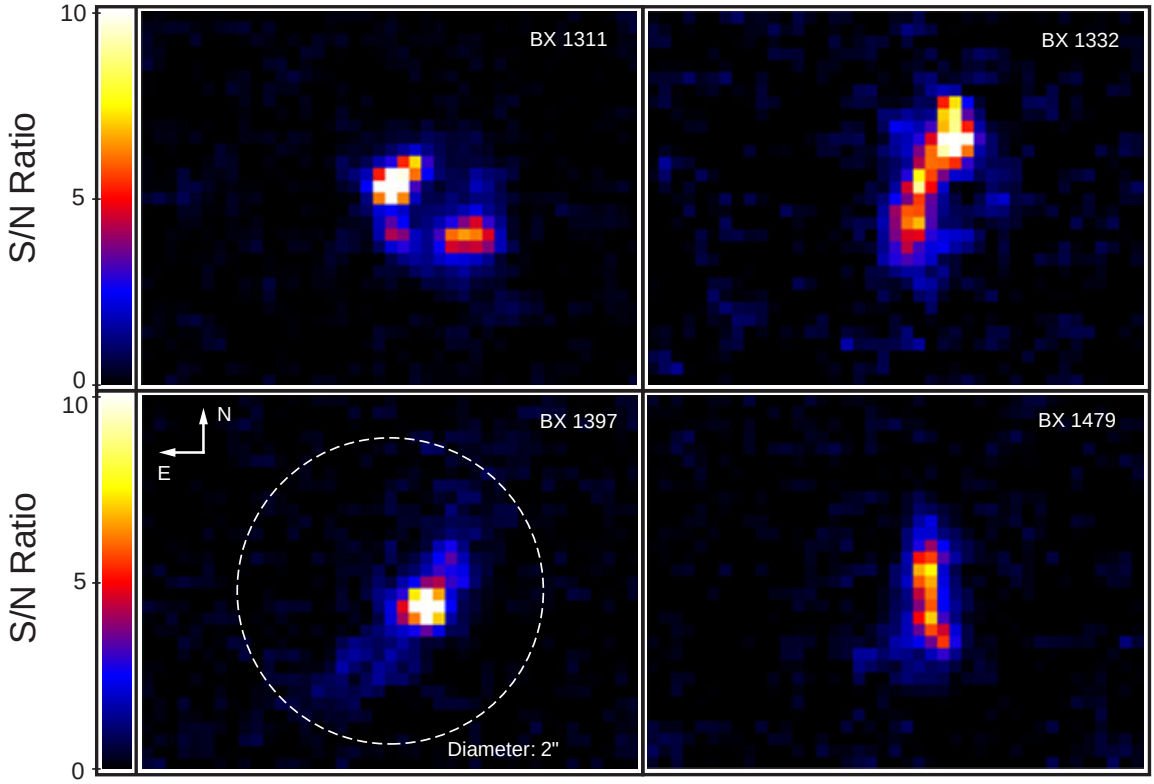

Figure 3.5 Estimated S/N ratio maps for $z \sim 2 - 2.6$ star forming galaxies BX 1311, 1332, 1397, and 1479. Simulated observations use 100 mas lenslets and image Hα emission for 4 hours of total integration time. The velocity dispersion in each spatial sample is assumed to be negligible.

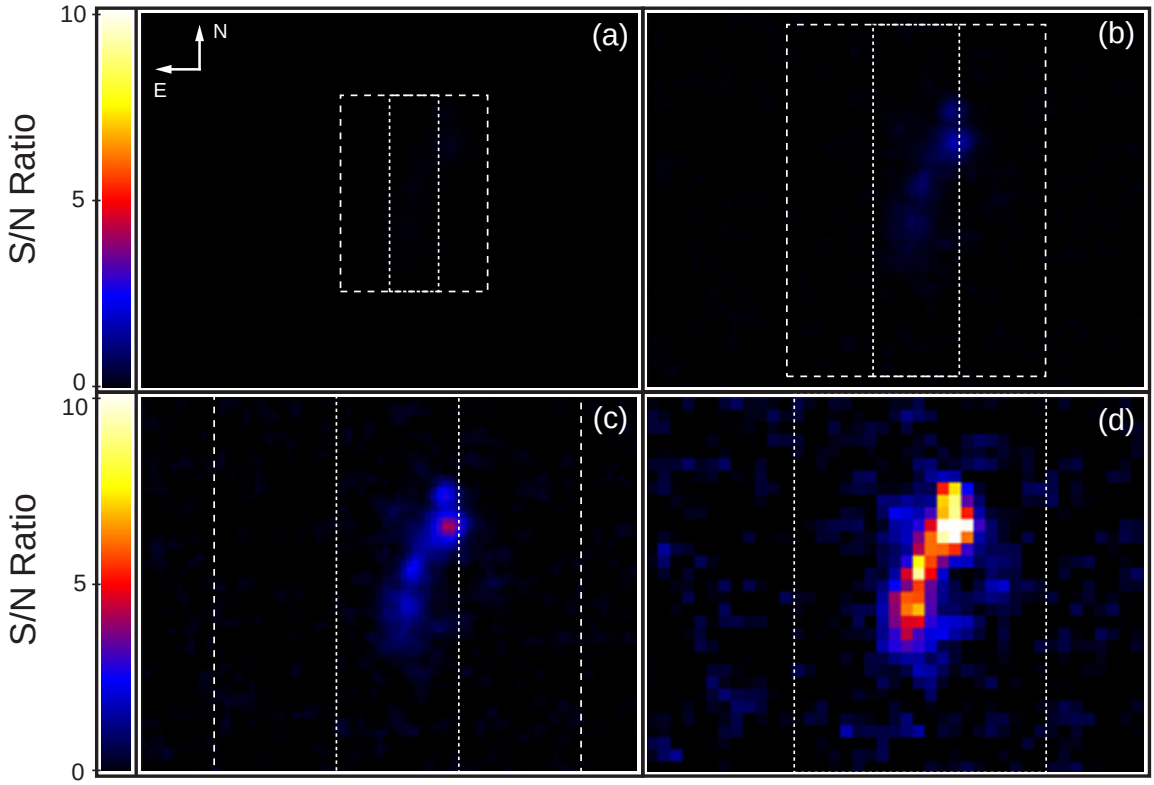

Figure 3.6 As Figure 3.5, but plots show S/N ratio maps for BX 1332 using lenslet scales of 20, 35, 50, and 100 mas (panels (a) – (d), respectively). OSIRIS broadband and narrowband fields of view (Table 3.4) for each lenslet scale are overplotted (dotted and dashed lines respectively) for comparison.

observations of $z \sim 2$ galaxies since peak S/N ratios for emission line detection are less than or of order unity in a four hour exposure, indicating that the integration times required to achieve detectable signals are prohibitively large. As demonstrated by panel (c), 50 mas sampling scales could nonetheless prove of use when spatially binned, for brighter sources, or for those sources in which emission regions resolve out into identifiable point sources.

In the event that the assumption of negligible velocity dispersion within a single lenslet were to break down (as when observing an AGN), the line emission would be spread over a greater number of detector pixels, increasing the noise in the detection and resulting in S/N ratios somewhat lower than found for unresolved line emission.

3.3.4 Recovery of Velocity Structure

As described in §3.2.2, detecting line emission in a given lenslet does not necessarily mean that it will be possible to measure a value of the velocity centroid to within an accuracy necessary for studying velocity substructure (i.e., tens of km s^{-1}) since severe contamination of the light in a given lenslet by spillover from a bright nearby component may mask the velocity signature. We therefore test how accurately we can expect to reconstruct the velocity field of BX 1332 given two possible kinematic models for the system.

In a previous study using long-slit Keck/NIRSPEC spectroscopy Erb et al. (2004) observed a tilted velocity curve along the major axis of BX 1332 (Fig. 3.7, filled squares), but the high degree of correlation among their data points due to atmospheric seeing (~ 0.8 arcsec) meant it was uncertain whether the tilted velocity curve was due to ordered disk rotation, or simply to two clumps merging or otherwise passing each other at some relative velocity. We therefore construct two kinematic models for this source: 1) a disk exhibiting solid-body rotation for which the size, inclination, and position angle[12] are chosen so that the projected ellipsoid roughly traces the contours where the S/N ratio is equal to 3 in Figure 3.6 (d), 2) a bimodal velocity distribution in which the velocities of the northwest and southeast regions are separated by the total observed velocity gradient ($\sim$ 100 km s^{-1}). In each case, the intrinsic velocity dispersion within a given spatial sample is assumed

[12]The model disk has a diameter of 1.4 arcseconds (as seen face-on, roughly corresponding to a linear size of 12 kpc), a position angle of -20°, and an inclination to the line of sight $i = 70°$. The projected radial velocity is set to be 50 km s^{-1} at the edge of the disk (Erb et al. 2004), corresponding to a disk of mass $M = 4 \times 10^9 M_\odot$.

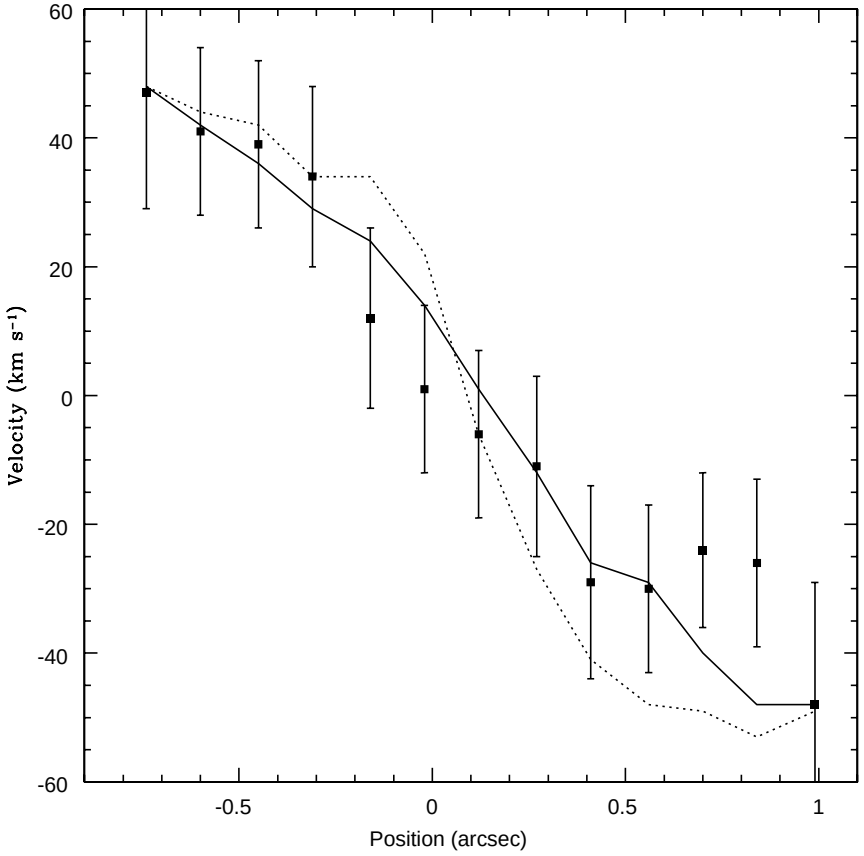

Figure 3.7 Observed Keck/NIRSPEC velocity curve of HDF-BX1332 (filled squares, from Erb et al. 2004) overplotted with simulated Keck/NIRSPEC observations assuming rotating disk kinematics (solid line) and a bimodal velocity distribution (dotted line). Model velocities have been uniformly scaled along the vertical axis to precisely match the dynamic range of the observational data.

to be negligible. These velocity maps are superimposed on the line flux map (generated as described in §3.3.3) on a pixel-to-pixel basis. While there are many uncertainties and degeneracies in this method the exact set of parameters used for the two models is of little consequence since we are primarily interested in how well we can distinguish between two fundamentally distinct kinematic models on the basis of velocity maps reconstructed from simulated observational data (§3.2.1.4 and 3.2.2). This is illustrated in Figure 3.8, which plots the HST-ACS B-band image of BX 1332 (panel (a)), the S/N ratio map for spectral line detection (panel (b)), and the velocity map recovered from a 4 hour exposure using the techniques described in §3.2.2 for both rotating disk and bimodal velocity models (panels (c) & (d) respectively).

Based on long-slit Keck/NIRSPEC observations, it would not be possible to distinguish these two kinematic models. Adopting a rough model of the NIRSPEC spectrograph with spectral resolution $\mathcal{R} = 1400$ in the K band, Figure 3.7 overplots the Erb et al. (2004) observational data with model velocity curves recovered from simulations assuming a rotating disk model (solid line) and a bimodal velocity model (dotted line). Although these two model velocity curves are generally quite similar, a chi-squared analysis prefers the disk model over the bimodal model with a chi-square probability function of 0.02 compared to 10^{-10}. However, this distinction is deceptive, since a bimodal velocity model with identical shape but 80% the dynamic range in velocity produces a chi-square fit as good as for the disk model. Since the velocity amplitude of the source is uncertain to within about 20%, we conclude that both rotating disk and bimodal velocity models are equally consistent with the NIRSPEC velocity curve.

In contrast, with IFS, adaptive optics, and increased spectral resolution, simulations of OSIRIS were able to clearly distinguish between the two models: in panel (c) of Figure 3.8 the velocity map shows a smooth transition from redshift to blueshift (relative to systemic) over the entirety of the source, while in panel (d) only a few pixels on the boundary between the two clumps give intermediate recovered velocities (since residual atmospheric seeing blurs the light from the two clumps into a slightly broader emission feature at close to the systemic redshift). We therefore conclude that OSIRIS will in some cases be capable of distinguishing between rotating disks and two-component mergers previously indistinguishable with long-slit spectrographs alone. However, BX 1332 is a particularly extended

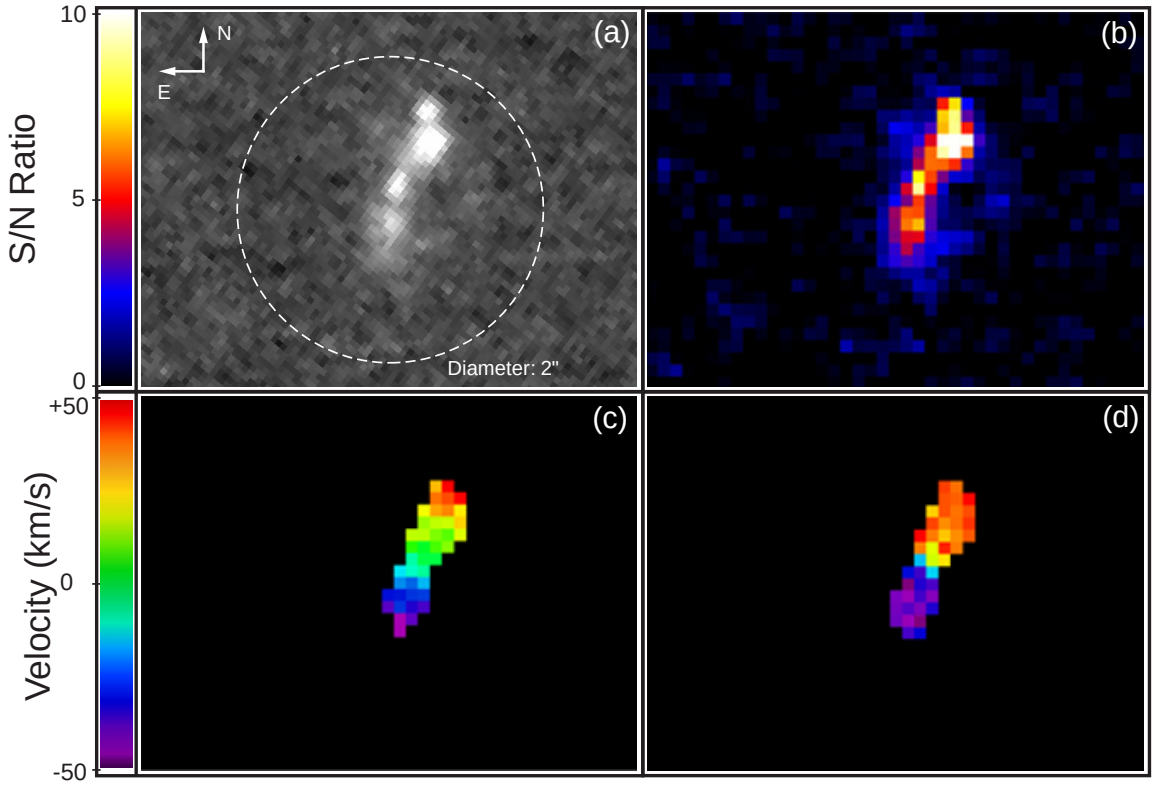

Figure 3.8 (a) HST-ACS B-band image of BX 1332 from the GOODS-N survey. Panel (b) reproduces the S/N ratio map for spectroscopic detection of the galaxy, and panels (c) & (d), respectively, show the velocity profiles reconstructed from simulated observational data for rotating disk and bimodal velocity structures. Panels (c) & (d) plot only data from those lenslets with greater than 3σ detections of emission line flux, and for which the recovered velocity is within 1000 km s^{-1} of the systemic redshift.

source, which makes it more amenable to study than most galaxies at similar redshifts; for faint, compact, or particularly disordered and chaotic systems obtaining accurate kinematic information for component features may prove challenging since residual atmospheric seeing may blur the combined emission lines into broader emission features.

A comprehensive study of velocity recovery from a wide variety of kinematic models using OSIRIS modeling is underway, and will hopefully determine general classes of galaxies which OSIRIS is capable of distinguishing between on the basis of observed 2-d velocity information. In future, the ability to draw such distinctions may allow us to test the predictions of heirarchical formation theory by quantifying the relative star formation rates in massive disks versus in proto-galactic mergers at high redshift.

3.3.5 Hα Morphologies and Photometry

In addition to providing valuable kinematic information, OSIRIS stands to provide high quality broad-band, narrow-band, and emission-line morphologies and photometry of galaxies both at high redshift and in the local universe. Since roughly 80% of the wavelength range covered by the instrument is free of atmospheric OH emission, it will be possible to sum only those spectral channels free of contamination to reach effective backgrounds up to 3 magnitudes fainter (in the H-band) than possible with standard photometry. Narrow-band photometry will thus in a sense come "free" with kinematic studies, and the observer will be free, post-observing, to use the data cube to create any of a number of desirable data products. Since for photometric purposes all emission in a given lenslet may be summed regardless of small velocity shifts, photometry of $z \sim 2 - 2.6$ star-forming galaxies will be possible on scales of at least 50 mas, and possibly below. Such photometric and morphological data will present complementary information to the kinematic data, and will likely be of use in interpreting kinematic results.

3.4 PHYSICAL LIMITATIONS

Having explored the scientific promise of OSIRIS for the $z \sim 2$ galaxy sample, we extend our discussion to consider basic design specifications for an arbitrary ground-based telescope and their impact on possible targets for integral-field spectroscopy. As the range of parameter

space is too broad to cover fully, we restrict ourselves to considering an OSIRIS-like IFS with mechanical and electrical specifications as detailed in §3.3.1. This study will therefore be specific to OSIRIS-type spectrographs and Mauna-Kea-like atmospheric conditions, but will indicate general trends.

3.4.1 Limiting Line Fluxes: Sampling Scales

We begin by considering the limiting line fluxes which Keck/OSIRIS will be able to detect at the 5σ level in one hour of integration. Were detector noise negligible, then for a "large" and uniformly bright extended source (i.e., a source for which strehl and PSF losses may be neglected) this line flux density would be roughly independent of lenslet sampling scale, since both sky background and line flux scale with the area a^2 of sky subtended by a lenslet. However, as demonstrated previously in Figure 3.2, detector noise dominates the noise budget at most wavelengths, so while line flux still decreases with the lenslet area the noise within a given lenslet remains approximately constant. As indicated in Figure 3.9, the limiting line flux therefore tends to increase dramatically as lenslet size shrinks. Unsurprisingly, this increase in limiting flux is less rapid for unresolved point sources.

3.4.2 Limiting Line Fluxes: Telescope Aperture

Increasing telescope aperture for an AO-enabled telescope affects the limiting line flux both by increasing the photon collection area and by concentrating the PSF of the diffraction-limited image, effectively increasing signal in proportion to the primary mirror diameter D^4. The net effect as a function of wavelength is shown in Figure 3.10 for telescopes with $D = 5$, 10, 30, and 50 meters. In addition to the improvements in limiting flux, 30 m and larger class telescopes will also permit spatially resolved studies at finer angular scales than possible with current generation instruments, since the diffraction limit of a 30 m telescope is ~ 18 mas in the K band (roughly one third that of the Keck telescope).

To illustrate this point we repeat our earlier calculations of the expected S/N ratios for detection of emission from star-forming regions using a simulated thirty-meter class telescope (TMT) in combination with an OSIRIS-like spectrograph. As shown in Figure 3.11, with this configuration even spatially extended sources observed with lenslet sampling scales of 35 mas (~ 300 pc at redshift $z = 2.5$) provide reasonable detections for spectroscopically

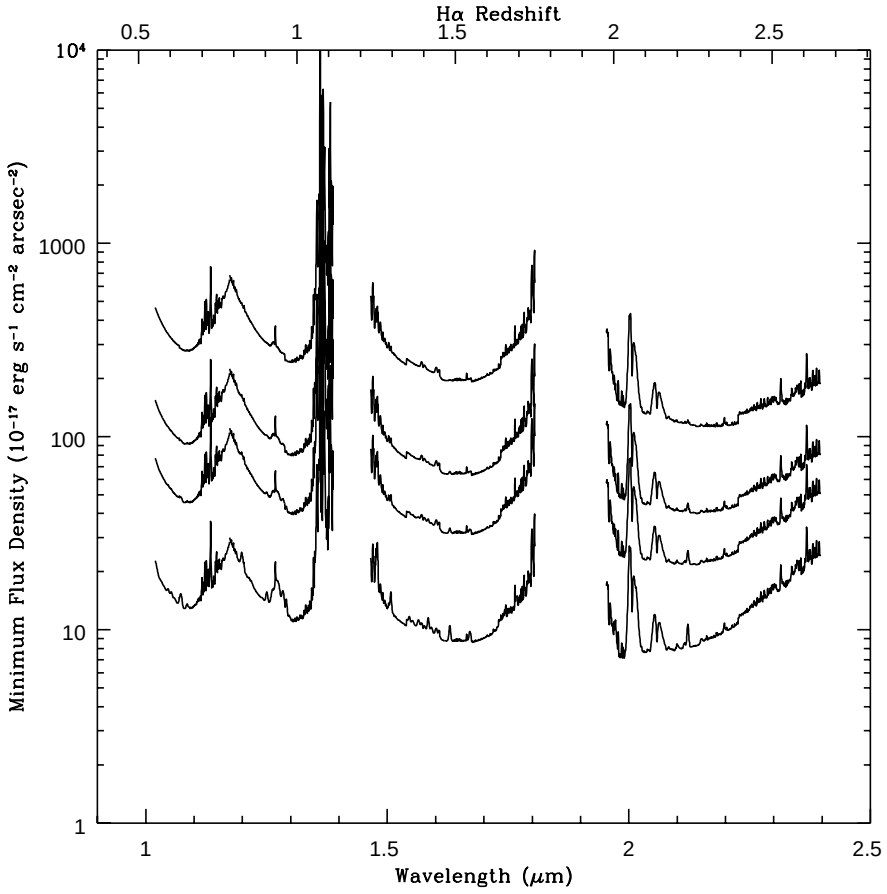

Figure 3.9 Limiting line flux density (surface brightness) for a 5 σ detection in one hour of integration using Keck/OSIRIS. Curves are for (top to bottom) lenslet scales of a = 20, 35, 50, and 100 mas, respectively. Line emission is assumed to be spectrally unresolved.

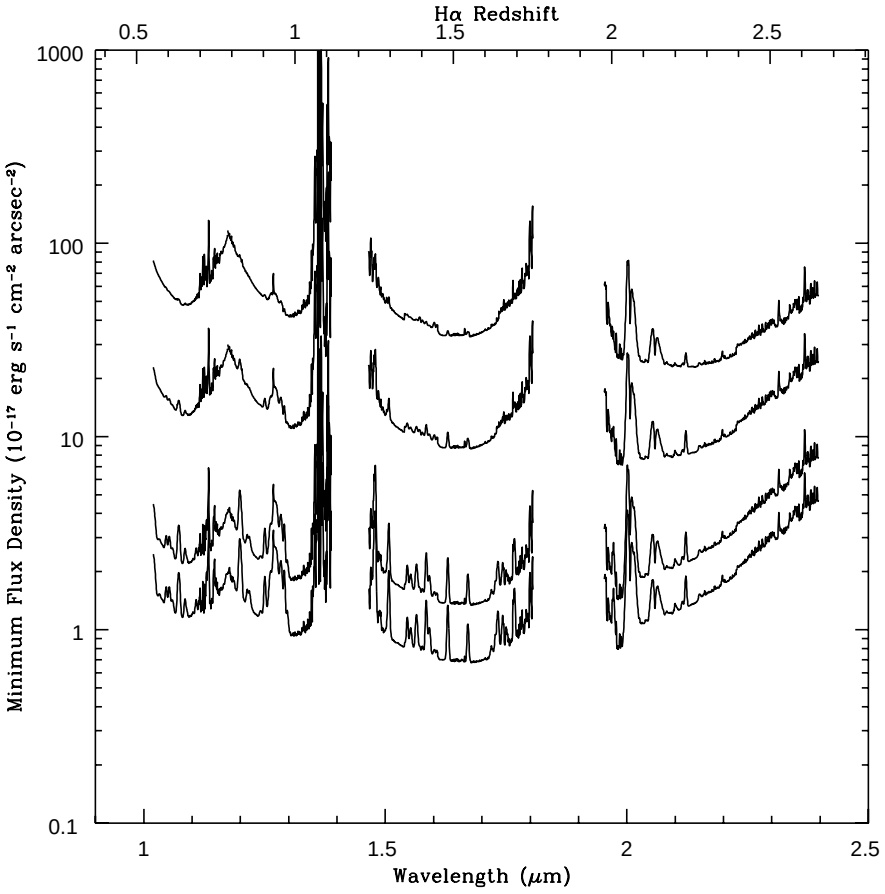

Figure 3.10 As Figure 3.9, but for $a = 100$ mas lenslets using an OSIRIS-like IFS on telescopes of assorted primary mirror diameters (D). Curves are for (top to bottom) telescopes with $D = 5$, 10, 30, and 50 meters.

unresolved emission lines at redshifts up to $z = 2.5$ in only an hour of integration. On scales of 100 mas, TMT is likely to provide Hα spectra for point-like regions forming stars at a rate of 1 $M_{\odot}$ yr^{-1} with a peak S/N ratio of 50+, permitting detailed study of even the fainter components of target galaxies.

3.4.3 Limiting Line Fluxes: Cryogenic Considerations

As discussed in §3.3.2, thermal emission dominates the K-band background (see Fig. 3.12), particularly for large aperture telescopes. This emission comes from telescope primary and secondary mirrors, re-imaging optics in the AO system light path, and atmospheric contributions. Although the latter is uncontrollable for ground-based instruments, it is of obvious interest to attempt to minimize the contribution from optical components.

In Figure 3.13 we plot the limiting line flux at K-band wavelengths for a 30 m class telescope operated under a range of thermal conditions. Assuming it were possible to cryogenically cool the AO bench to $T = -20°C$, the thermal emission from the AO system would become largely negligible compared to that from the telescope and atmosphere, pushing the limiting flux in the K-band a factor of three lower. If, in addition, it were possible to achieve near-perfect reflectivity from the telescope mirrors, then the combined reduction in background flux would reduce the limiting line flux by a factor of almost ten.

This improvement is most noticeable around wavelengths of 2.2 – 2.4 microns where the atmosphere is particularly transparent, and we therefore gain the most from suppressing emission from optical components. Longward of 2.4 microns however the improvement becomes less pronounced as atmospheric emission begins to increase rapidly.

It is therefore an attractive goal for next-generation telescopes to cryogenically cool their adaptive optics system since a temperature change of only 20 degrees (coupled with increased mirror reflectivity) may suffice to increase sensitivity in the K-band by almost an order of magnitude. This 20 degrees of cooling would reduce thermal emission from the AO system to the level of the background sky, so additional cooling (e.g., to liquid nitrogen temperatures $T = 77$ K) would not greatly decrease the background further. Such a cooling system should not pose a great technological challenge (C. Max, private communication), although it would somewhat increase the cost and complexity of such a telescope project.

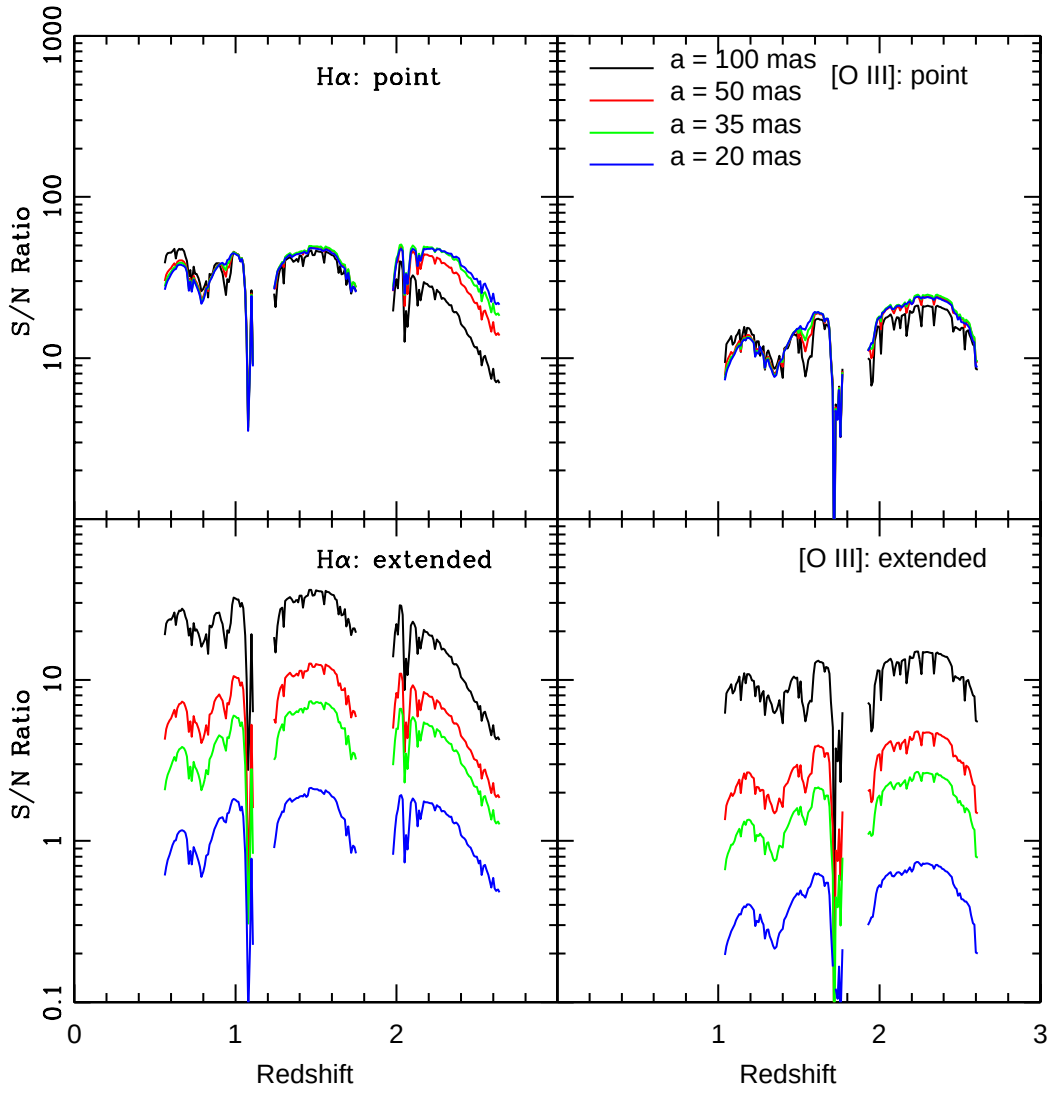

Figure 3.11 As Figure 3.4, but for a 30 m class telescope with an OSIRIS-like IFS.

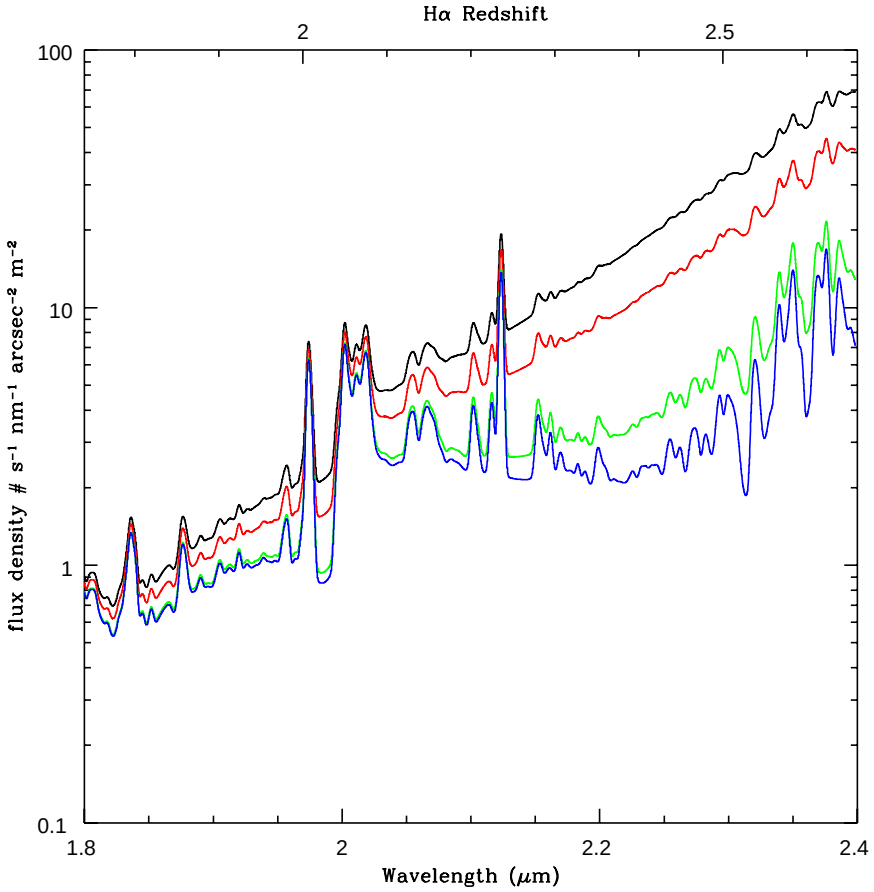

Figure 3.12 Model effective K-band background spectra for: (1) 35% emissivity in AO optics and 20% emissivity in telescope optics at temperature $T = 270K$ (black line, as Figure 3.1), (2) 35% emissivity in AO at $T = 270K$ and 0% telescope emissivity (red line), (3) 35% emissivity in AO cryogenically cooled to $T = 250K$ and 0% telescope emissivity (green line), (4) 35% emissivity in AO cryogenically cooled to $T = 77K$ and 0% telescope emissivity (blue line). All models incorporate the Gemini model for zodiacal light and atmospheric emission, for further commentary see Figure 3.1.

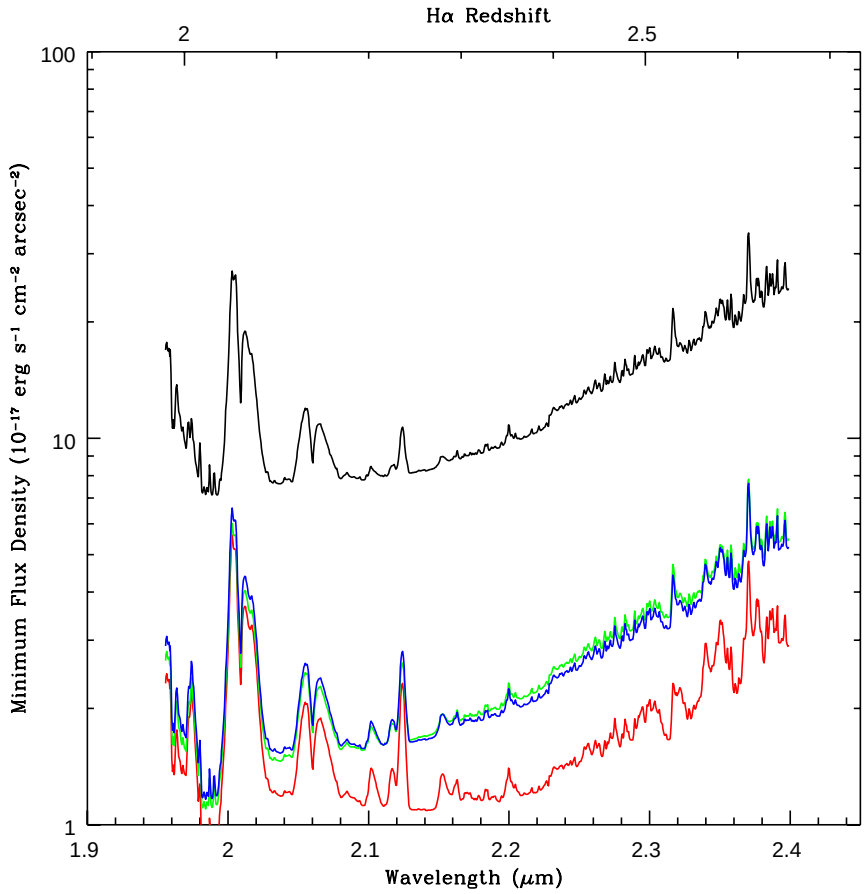

Figure 3.13 Limiting line flux density in the K-band for a 5 σ detection in one hour of integration using an OSIRIS-like IFS on a 30 m class telescope (100 mas sampling). Curves are for: (1) 35% emissivity in AO optics and 20% emissivity in telescope optics at temperature $T = 270K$ (black line), (2) 35% emissivity in AO at $T = 270K$ and 0% telescope emissivity (green line), (3) 35% emissivity in AO cryogenically cooled to $T = 250K$ and 20% telescope emissivity at temperature $T = 270K$ (blue line), (4) 35% emissivity in AO cryogenically cooled to $T = 250K$ and 0% telescope emissivity (red line). Line emission is assumed to be spectrally unresolved.

3.4.4 Spectral Resolution Requirements

Moderate spectral resolution ($\mathcal{R} \sim 3000$) is necessary for spectroscopic studies of high redshift galaxies, largely so that individual atmospheric OH emission lines may be suppressed, and in general the greater the resolution the greater the range of wavelengths for which it will be possible to achieve inter-line background levels. In addition, high spectral resolution aids in the successful recovery of velocity substructure, and spectrograph resolution must be great enough that it is possible to measure velocities to within tens of km s^{-1}. We note, however, that the benefits of increasing spectral resolution do not continue indefinitely, but peak when emission lines in a lenslet are just barely unresolved, beyond which detector noise begins to grow as the line emission is spread over a greater number of pixels.

3.4.5 Benefits of Adaptive Optics

Adaptive optics is a key component for integral-field observations of targets whose angular size is less than or comparable to the size of the seeing disk. Most importantly, AO correction concentrates an appreciable fraction of emitted light into the PSF core of the lenslet subtending the region from which that light was emitted, greatly increasing the signal strength from point sources and permitting improved imaging of structures blurred together in the seeing disk. We note however that for slightly larger sources ($\gtrsim 4$ arcsec^2) atmospheric seeing may also be partially corrected for using ground-layer adaptive optics (GLAO) techniques (e.g., Chun 2003) or post-processing wavelet decomposition methods (e.g., Puech et al. 2004; Flores et al. 2004) instead of a conventional adaptive optics system.

One particularly useful observation for which AO correction will be essential is the targeted observation of AGN with integral field spectrographs. In many sources the central AGN often outshines its host galaxy, which may be extremely difficult to study if the AGN emission is blurred over its host in an atmospheric seeing halo. With AO correction however, the AGN emission may be concentrated more fully in its PSF core, decreasing the contamination in the seeing halo and possibly enabling an IFS to probe the emission from, and kinematics of, the host galaxy.

3.5 SUMMARY

We have outlined an observing strategy for infrared integral-field spectroscopy of high-redshift galaxies, and presented a formalism for simulating observations with an arbitrary telescope plus lenslet spectrograph system. These calculations may be generalized to predict the integration times required to observe extended or compact sources both at high redshift and in the local universe.

We have determined 5 σ limiting line flux densities as a function of wavelength for typical AO-equipped integral-field spectrographs mounted on telescopes with primary mirror diameters ranging from 5 to 50 meters. Using 100 mas angular sampling, these limiting flux densities are typically $\sim 10^{-16}$ erg s^{-1} cm^{-2} arcsec^{-2} for 10 m class telescopes, and $\sim 10^{-17}$ erg s^{-1} cm^{-2} arcsec^{-2} for 50 m class telescopes. These limiting line fluxes increase by a factor of ~ 3 for each factor of ~ 2 that the angular lenslet scale is decreased. Realistic models of the infrared background flux are taken into account in these calculations, and include blackbody emission from both the atmosphere and telescope optics and atmospheric OH line emission. Warm adaptive optics systems contribute significantly to the K-band background flux, and cryogenic cooling to $T = 250$ K may reduce the effective background by as much as a factor of ten.

Using parameters characteristic of the Keck/OSIRIS spectrograph we have predicted S/N ratios for detection of line emission from star-forming regions at redshifts $z = 0.5 - 2.5$ with angular lenslet scales of 20, 35, 50, and 100 mas, and find that OSIRIS can observe Hα emission from regions forming stars at a rate of about 1 $M_\odot$ yr^{-1} per 100 mas angular grid square with a signal-to-noise ratio S/N ~ 10. Simulated integral-field spectroscopy of $z \sim 2 - 2.6$ star-forming galaxies in the GOODS-N field indicates that OSIRIS can observe Hα emission from these sources with an angular resolution of 100 mas (~ 1 kiloparsec at redshift $z \sim 2$) and signal-to-noise ratios between 3 and 20, and will be able to produce two-dimensional velocity maps for these galaxies relative to the systemic redshift. These simulated velocity maps suggest that OSIRIS will be able to distinguish between some disparate kinematic models permitted by ambiguous long-slit spectroscopic data alone, and may distinguish between mature disk kinematics and active mergers for spatially extended, bright galaxies at these redshifts.

Further observational constraints on the Hα morphologies of the $z \sim 2 - 2.6$ galaxies

from AO-corrected narrow-band photometry will help determine whether sources may resolve into individual star-forming regions on scales less than a kiloparsec, permitting more detailed simulations and kinematic studies. The morphological and velocity structure of these galaxies at such small scales may be observable with OSIRIS for particularly bright sources, and will certainly be accessible to future studies using next-generation 30 m and 50 m class telescopes.

The authors thank James Larkin for numerous helpful discussions regarding the OSIRIS spectrograph, and for kindly providing the results of early commissioning tests of the instrument. DRL also thanks D. LeMignant, K. Matthews, and K. Taylor for helpful discussions. CCS, DKE, and DRL have been supported by grant AST03-07263 from the US National Science Foundation, and AR grant HST-AR 10311 from the Space Telescope Science Institute.

Table 3.1. Current Optical/IR Integral-Field Spectrographs

Spectrograph	Telescope	Optical[a]	NIR[b]	AO[c]	Reference
GIRAFFE	VLT	yes	no	no	Hammer et al. (1999)
GMOS	Gemini	yes	no	NGS	Davies et al. (1997)
GNIRS	Gemini	no	yes	no	Allington-Smith et al. (2004)
INTEGRAL	WHT	yes	no	NGS	García-Lorenzo et al. (2000)
NIFS	Gemini	no	yes	NGS	McGregor et al. (2003)
OSIRIS	Keck II	no	yes	LGS	Larkin et al. (2003)
SAURON	WHT	yes	no	no	Bacon et al. (2001)
SINFONI/SPIFFI	VLT	no	yes	LGS	Tecza et al. (1998)
UIST	UKIRT	no	yes	no	Ramsay Howat et al. (1998)

[a]Wavelength coverage at least $\lambda\lambda$ 4000 – 7000 Å.

[b]Wavelength coverage at least $\lambda\lambda$ 1 – 2.5 μm.

[c]Present adaptive-optics capability; natural guide star (NGS) or laser guide star (LGS).

Table 3.2. Keck/OSIRIS System Characteristics

Parameter	Symbol	Value
Telescope/AO characteristics		
AO throughput[a]	$\eta_{\rm AO}$	65%
Collecting area	A	7.85×10^5 cm^2
K-band diffraction limit	$\theta_{\rm diff}$	55 mas
K-band seeing	$\theta_{\rm seeing}$	550 mas
Telescope throughput[a,b]	$\eta_{\rm tel}$	80%
Wavefront error[c]	$\sigma_{\rm wfe}$	337 nm
OSIRIS Characteristics[a]		
Average OSIRIS throughput	$\eta_{\rm spec}$	15% (z-H bands)
		20% (K band)
Average system throughput[d]	η	8% (z-H bands)
		10% (K band)
Dark current	$R_{\rm DK}$	.03 e$^-$ s^{-1} pixel^{-1}
Grating blaze	$\cdots$	6.5 μm
Read noise[e]	$N_{\rm RD}$	3 e$^-$ pixel^{-1}
Spectral length	$\mathcal{N}_2$	1600 pixels (broadband)
		400 pixels (narrowband)
Spectral resolution	$\mathcal{R}$	3900 (20, 35, 50 mas lenslets)
		3400 (100 mas lenslets)
Spectral width	$\mathcal{N}_1$	3 pixels

[a]Values based on OSIRIS pre-ship report and preliminary commissioning results (J. Larkin, private communication).

[b]Assumes 90% throughput of primary and secondary mirrors.

[c]Based on achieved K-band strehl of 0.36 (http://www2.keck.hawaii.edu/optics/lgsao/performance.html)

[d]Average system throughput $\eta = \eta_{\rm tel}\eta_{\rm AO}\eta_{\rm spec}$

[e]After multiple-correlated double samples.

Table 3.3. OSIRIS Broadband Filters and Effective Model Sky Surface Brightness

Band	Wavelength (μm)	$\eta_{\rm filter}$[a]	$\mu_{\rm AB}$[b]	$\mu_{\rm Vega}$[b]	f_λ[c]
z	.98 — 1.20	0.73	17.9	17.3	3.64044
J	1.18 — 1.44	0.81	17.8	16.8	3.33187
H	1.47 — 1.80	0.79	18.0	16.6	2.09761
K	1.96 — 2.40	0.81	14.1	12.2	20.5934

[a]Average narrowband filter throughput for filters within the indicated broadband wavelength range (J. Larkin, private communication).

[b]Effective sky brightness in units of AB and Vega magnitudes per arcsecond^2.

[c]Average effective background flux density in units of photons s^{-1} nm^{-1} arcsecond^{-2} m^{-2}.

Table 3.4. Available OSIRIS Angular Lenslet Scales and Fields of View

Lenslet Scale	Broadband FOV	Narrowband FOV
0.02	0.32 × 1.28	0.96 × 1.28
0.035	0.56 × 2.24	1.68 × 2.24
0.05	0.8 × 3.2	2.4 × 3.2
0.10	1.6 × 6.4	4.8 × 6.4

Note. — All data are given in arcseconds and are based on the OSIRIS pre-ship report (J. Larkin, private communication).

Table 3.5. Parameters of Selected Galaxies

Galaxy	$z_{\mathrm{H}\alpha}$ [a]	$F_{\mathrm{H}\alpha}$ [b]	σ_{v} [c]
BX 1311	2.4843	16.0	88
BX 1332	2.2136	8.8	54
BX 1397	2.1332	10.6	123
BX 1479	2.3745	5.0	46

[a]Vacuum heliocentric redshift of Hα emission line.

[b]Hα emission line flux in units of 10^{-17} erg s^{-1} cm^{-2}. Note these estimates have been corrected for slit aperture and non-photometric conditions.

[c]One-dimensional velocity dispersion of Hα emission in units of km s^{-1}

Note. — All data are from Erb et al. (2004).

Chapter 4

Integral Field Spectroscopy of High-Redshift Star-Forming Galaxies with Laser-Guided Adaptive Optics: Evidence for Dispersion-Dominated Kinematics*

David R. Law[a], Charles C. Steidel[a], Dawn K. Erb[b], James E. Larkin[c], Max Pettini[d], Alice E. Shapley[e], Shelley A. Wright[c]

[a]California Institute of Technology, MS 105–24, Pasadena, CA 91125

[b]Harvard-Smithsonian Center for Astrophysics, MS 20, 60 Garden St, Cambridge, MA 02138

[c]Department of Physics and Astronomy, University of California, Los Angeles, CA 90095

[d]Institute of Astronomy, Madingley Road, Cambridge CB3 0HA, UK

[e]Department of Astrophysical Sciences, Princeton University, Peyton Hall, Ivy Lane, Princeton, NJ 08544

Abstract

We present early results from an ongoing study of the kinematic structure of star-forming galaxies at redshift $z \sim 2-3$ using integral-field spectroscopy of rest-frame optical nebular

*A version of this chapter was published in *The Astrophysical Journal*, 2007, vol. 669, 929–946, and is reproduced by permission of the AAS.

emission lines in combination with Keck laser guide star adaptive optics (LGSAO). We show kinematic maps of 3 target galaxies Q1623-BX453, Q0449-BX93, and DSF2237a-C2 located at redshifts $z = 2.1820$, 2.0067, and 3.3172, respectively, each of which is well-resolved with a PSF measuring approximately 0.11 – 0.15 arcsec ($\sim$ 900 – 1200 pc at $z \sim 2 - 3$) after cosmetic smoothing. Neither galaxy at $z \sim 2$ exhibits substantial kinematic structure on scales $\gtrsim 30$ km s^{-1}; both are instead consistent with largely dispersion-dominated velocity fields with $\sigma \sim 80$ km s^{-1} along any given line of sight into the galaxy. While the primary emission component of Q0449-BX93 shows no spatially resolved kinematic structure, a faint, kinematically distinct emission region is superposed on the primary region at a relative velocity of ~ 180 km s^{-1}, suggesting the possible presence of a merging satellite galaxy. In contrast, DSF2237a-C2 presents a well-resolved gradient in velocity over a distance of ~ 4 kpc with peak-to-peak amplitude of 140 km s^{-1}. This velocity shear was previously undetected in seeing-limited long-slit observations despite serendipitous alignment of the slit with the kinematic major axis, highlighting the importance of LGSAO for understanding velocity structure on sub-arcsecond scales. It is unlikely that DSF2237a-C2 represents a dynamically cold rotating disk of ionized gas as the local velocity dispersion of the galaxy ($\sigma = 79$ km s^{-1}) is comparable to the observed shear. Using extant multi-wavelength spectroscopy and photometry we relate these kinematic data to physical properties such as stellar mass, gas fraction, star formation rate, and outflow kinematics, and consider the applicability of current galaxy formation models. While some gas cooling models reproduce the observed kinematics better than a simple rotating disk model, even these provide a poor overall description of the target galaxies, suggesting that our current understanding of gas cooling mechanisms in galaxies in the early universe is (at best) incomplete.

4.1 INTRODUCTION

At high redshifts $z \sim 2-3$ galaxies undergo strong and rapid evolution from highly irregular clumps of star-formation into the familiar Hubble sequence of the local universe (Giavalisco et al. 1996, Papovich et al. 2005), during which time they are thought to accumulate the majority of their stellar mass (Dickinson et al. 2003). The evolution of structure and ordered motion in galaxies at such redshifts is therefore of considerable interest in the attempt to understand the process of galaxy formation. As such, numerous authors (e.g., Steidel et al.

2004; Papovich et al. 2006; Reddy et al. 2006b; Erb et al. 2006c; and references therein) have used deep UV-IR photometry and spectroscopy to ascertain such global properties as stellar mass, population age, AGN fraction, star formation rate, and the strength of large-scale gaseous outflows expelled by rapid starbursts.

These studies have greatly increased our understanding of the physical nature of these galaxies, indicating (for instance) that the $z \sim 2$ universe contains galaxies in a wide variety of evolutionary states from young and actively star-forming to massive and passively evolving (Glazebrook et al. 2004; Daddi et al. 2005; Papovich et al. 2006; Reddy et al. 2006b; and references therein) and suggesting (based on clustering properties) that typical star-forming galaxies at $z \sim 2$ may evolve into the elliptical galaxy population of the local universe (Adelberger et al. 2005b). However, in general it is unknown whether the majority of star formation in these galaxies occurs in flattened disk-like systems (as anticipated by cosmological models, e.g., Mo, Mau, & White 1998) or disordered non-equilibrium configurations, and whether this star formation is due primarily to large-scale gravitational instabilities, tidal shocks induced by major mergers, or some other as-yet-undetermined physical mechanism. Similarly, it is unknown whether individual regions of star formation within a given galaxy follow a global abundance pattern or exhibit strong variations in chemical enrichment.

These questions are most readily investigated by means of optical nebular emission lines (redshifted into the near-IR at $z \gtrsim 1$) such as Hα, Hβ, [O III] λ5007, and [N II] λ6584, which predominantly trace ionized gas in active star-forming regions and can provide a kinematic probe of the gravitational potential. Such studies using slit spectroscopy (e.g., Erb et al. 2003, 2004, 2006b; Weiner et al. 2006) have met with moderate success, enabling the determination of dynamical masses for a large sample of galaxies at $z \gtrsim 1$, but are complicated by uncertainties resulting from slit placement, possible misalignment with the kinematic major axis, and the small angular size of the galaxies (typically less than an arcsecond; see Fig. 2 of Law et al. 2007b) relative to the size of the seeing disk. The twin complications of slit placement and alignment have recently been overcome using seeing-limited integral-field unit (IFU) spectroscopy to obtain two-dimensional maps of the ionized gas kinematics within these galaxies. A sample of the largest and brightest galaxies in the rest-frame UV-selected sample has recently been observed by Förster Schreiber et al. (2006),

who find (in 9 out of 14 cases) smoothly varying velocity shear generally consistent with rotation in a flattened disk-like configuration. However, it is unknown whether atmospheric seeing (typically $\sim$ half the size of the galaxy) masks more complex structure, and to what extent the prevalence of velocity shear in these sources is a product of the selection criteria of the study, which (for observational reasons) preferentially select bright, extended sources, many of which exhibited large velocity shear or dispersion in previous long-slit studies (Erb et al. 2003, 2006b).

With the aid of laser guide star adaptive optics (LGSAO) technology it is now possible to study high-redshift galaxies on sub-kiloparsec scales, permitting fruitful observation of galaxies either unresolved or barely resolved in previous ground-based observations. Wright et al. (2007) have demonstrated the utility of LGSAO in combination with integral-field spectroscopy for a galaxy at redshift $z \sim 1.5$; in this contribution we present early results from an ongoing study of galaxies in the redshift range $z \sim 2 - 3$. In §4.2 we describe our observational program and basic data reduction techniques. In §4.3 and 4.4 we describe the morphological properties, globally integrated spectra, and line ratio diagnostics of these galaxies as derived from the integral-field data. In §4.5 we use extant broadband photometry and UV spectroscopy of the target galaxies to model the stellar populations and baryonic masses of the galaxies. We present spatially resolved maps of the ionized gas kinematics in §4.6, discussing the velocity field of each of our targets in the context of theoretical models and the physical properties given in §4.3 – 4.5. Finally, in §4.7 we compare our results to those of Förster Schreiber et al. (2006) and other groups, and discuss what general conclusions can be drawn about galaxy formation in the early universe.

We assume a standard ΛCDM cosmology in which $H_0 = 71$ km s^{-1} Mpc^{-1}, $\Omega_{\rm m} = 0.27$, and $\Omega_\Lambda = 0.73$.

4.2 OBSERVING AND DATA REDUCTION

4.2.1 Sample Selection and Observational Strategy

Observations were performed using the OSIRIS (OH Suppressing InfraRed Imaging Spectrograph; Larkin et al. 2006) integral-field spectrograph in conjunction with the Keck II LGSAO system (Wizinowich et al. 2006, van Dam et al. 2006). As described in detail by

Larkin et al. (2006), OSIRIS is a lenslet-type spectrograph with a 2048 x 2048 Hawaii II detector array, spectral resolution $R \sim 3600$, and a complement of reimaging optics which permit sampling of the field with spectral pixels (spaxels) ranging in angular size from 20 – 100 milliarcseconds (mas).

We select star-forming galaxies at redshifts $z \sim 2 - 3$ (for which Hα and [O III] λ5007, hereafter simply [O III], respectively, fall into the observed-frame K-band) from the spectroscopic redshift catalog of Steidel et al. (2003, 2004). Based on the IFU simulations of Law et al. (2006), which explore the flux requirements necessary for reasonable detection within a few hours of integration using OSIRIS, we focus on those galaxies which are known to have either nebular line fluxes greater than $\sim 10^{-16}$ erg s^{-1} cm^{-2} based on previous long-slit observations (Erb et al. 2003, 2006b) or high star formation rates (SFR) as estimated from rest-frame UV photometry (for one galaxy [Q0449-BX93] not targeted with long-slit spectroscopy). Physical constraints also dictate that we preferentially select galaxies which are within 60 arcseconds of a suitably bright ($R \lesssim 17$ mag) tip-tilt reference star (as required by the LGSAO system), and which lie at spectroscopic redshifts such that nebular emission lines fall between the strong spectroscopically unresolved night-sky OH emission features which dominate the near-IR background.

At K-band wavelengths between the OH-emission features, thermal radiation from warm optical components in the light path is the dominant contributor to the total background flux (see Law et al. 2006). Since successful observation of our target galaxies requires performance at the limit of OSIRIS' capability, we use the second-largest spaxel scale[1] of 50 mas lenslet^{-1}, for which the balance between thermal background and detector noise is optimal for detection of extremely faint objects. Using narrow-band order sorting filters ($\Delta\lambda \sim 100$ nm), the OSIRIS field of view in this configuration is approximately 2 $\times$ 3 arcseconds.

Observations were performed on UT 2006 June 5 and 2006 October 4–5; the June data were obtained under exceptional photometric conditions with visual-band seeing estimates varying between 0.4 and 0.6" while the October data were obtained in moderate conditions with seeing varying between 0.7 and 1.0" over the duration of the observations. In Table 6.1 we list the three targets discussed herein as part of our pilot program. Each target was

[1]Note that 50 mas is approximately the Keck diffraction limit at $\lambda = 2\,\mu$m.

observed with the aid of the Keck LGSAO system, typically using a magnitude $R \sim 15-16$ tip-tilt (TT) reference star with an angular separation from the science target of less than an arcminute for a correction strehl of greater than 30% at $\lambda = 2\,\mu$m and an approximately circular PSF with FWHM $\sim 75/125$ mas for the June/October data, respectively.[2]

A typical observing sequence was established as follows. First, we obtained short (~ 1 minute) observations of the TT reference star for a given science target to refine the pointing model, provide an estimate of the PSF, and serve as an approximate check for later flux calibration. The telescope was then blind-offset to the science target using relative offsets calculated from deep ground-based optical imaging of the target fields. The position angle of OSIRIS for these observations was chosen to ensure that the tip-tilt reference star fell within the unvignetted field of view of the LGSAO system. Each target was observed in sets of two 15 minute[3] integrations with the target galaxy alternately placed 0.7 arcseconds above and below the center of the IFU (positions A and B). Small dithers were introduced around these positions on each successive set of exposures. This 30 minute exposure sequence was repeated for $\sim$ 2–4 hours as necessary to achieve a high-quality detection; typically it was possible to verify detection of target galaxies in the difference of two 15 minute exposures.

4.2.2 Reducing IFU Data

Data reduction was performed using a multi-step process consisting of both Keck/OSIRIS data reduction pipeline (DRP) routines and custom IDL scripts tailored for use with faint emission line spectra. Since OSIRIS is a relatively new scientific instrument and standard data reduction methods have yet to be generally accepted, we present our current data reduction method in detail.

We divide the exposures into two sets taken at positions A and B, and use DRP routines to median combine each set to produce a sky frame. These sky frames are then subtracted from each of the respective object frames (i.e., the sky produced by stacking observations

[2]The 75 mas measurement is strictly an upper limit since this PSF is undersampled using 50 mas spaxels. Since science observations are performed with the TT star off-axis the PSF of the science observations will not perfectly match that of the TT star; however, this generally does not greatly increase the effective PSF (see Liu et al. 2006).

[3]Due to the read noise characteristics of OSIRIS, long individual exposures are desirable in order to optimize the S/N ratio of the observations.

at position B is subtracted from the observations at position A and vice versa). After sky subtraction, individual exposures are extracted from the raw two-dimensional format into three-dimensional data cubes. This DRP extraction algorithm is complicated and non-intuitive since spectra from individual spaxels physically overlap on the detector; we refer the reader to the OSIRIS user manual for further information. Due to the highly time-variable nature of the IR background the residual flux pedestal in these sky-subtracted data cubes is often unsatisfactorily high and we therefore perform a second-pass background subtraction on each of these cubes as follows. Using custom IDL routines we calculate the median pixel value in each spectral channel and subtract this value from all pixels within the channel to ensure a zero-flux median in all spectral slices throughout the data cube. This effectively removes flux pedestals resulting from variable sky brightness, although small variations in the background persist across the spatial dimensions of each cube. As OSIRIS data reduction algorithms are progressively refined it may prove possible to further suppress background fluctuations, achieving effectively deeper integrations.

These sky-subtracted data cubes are spatially registered using the telescope steering system (TSS) offset coordinates contained within the image headers and combined using a 3 σ clipped mean algorithm. The resulting cube is spatially oversampled by a factor of two in each dimension (i.e., mapped to pixels 25 mas in size), rotated with flux-conserving resampling to a standard (North up, East left) orientation, and the image slice at each spectral channel convolved with a spatial Gaussian kernel of FWHM 3.2 oversampled pixels (80 mas, giving an effective PSF FWHM of 110/150 mas for June/October data, respectively) in order to increase the S/N ratio of each spectrum. Wavelength calibration is automatically performed by the OSIRIS DRP; we determine that this calibration is generally accurate to within $\sim 0.1\,\mathring{A}$ based on fits to the centroids of strong OH sky lines with regard to fiducial vacuum wavelengths given by Rousselot et al. (2000). Finally, all spectra are converted to the heliocentric rest frame using the relative motion solution given by the IRAF/*rvcorrect* package. Based on the measured FWHM of the (unresolved) OH lines, we conclude that the effective spectral resolution of our data is $R \sim 3600$.[4]

Since we do not dedicate time in each observing sequence to obtaining a clean "sky"

[4]This represents the narrowest OH line observed; many appear to be broader because the OH forest is typically composed of unresolved doublets separated by less than ~ 1 Å.

observation, negative residuals of the target galaxy are located about 1.4" above and below the positive image in the final stacked data cube, effectively halving our useful field of view. However, given the small size of the target galaxies (UV morphologies indicate that $\sim$ 90% are less than 1" in extent; Law et al. 2007b) we find this approach preferable for maximization of on-source integration time by eliminating the need to frequently nod off-target in order to adequately characterize the background flux (although c.f. discussion by Davies 2007).

4.3 NEBULAR MORPHOLOGIES

We produce maps of the ionized gas morphology of the three target galaxies by collapsing each data cube about the 4–5 spectral channels corresponding to the peak emission wavelength of the spectral line (Hα for Q1623-BX453 and Q0449-BX93, [O III] for DSF2237a-C2). As illustrated in Figure 4.1 (top left panel), Q1623-BX453 consists of an Hα bright nucleation[5] with a lower surface brightness region extending towards the southwest and an extremely faint feature on the western edge. This faint feature is only barely detected and may be an artifact of imperfect sky subtraction. While fairly centrally concentrated, the bright emission region is inconsistent with a point source, having a diameter of 200 mas (1.7 kpc) at the half peak-flux contour compared to (an upper limit of) 110 mas for the PSF of the tip-tilt reference star. Q0449-BX93 (Fig. 4.1; middle left panel) has a morphology quite similar to that of Q1623-BX453, consisting of a bright nucleated region with low surface brightness emission extending towards the northwest. Again, the bright region is inconsistent with a point source, having diameter 180 mas (1.5 kpc) at the half peak-flux contour. In contrast, DSF2237a-C2 (Fig. 4.1; bottom left panel) has a more elongated morphology than either Q1623-BX453 or Q0449-BX93, with flux distributed fairly evenly along the major axis.

Given the elongated morphology of DSF2237a-C2, one traditional assumption would be that emission in this galaxy is predominantly from an inclined disk of ionized gas, and that the apparent ellipticity is due to perspective foreshortening of a circularly symmetric disk. Under such an assumption, we fit a 2-d Gaussian to the Hα surface brightness map and

[5] We adopt the term "nucleation" to qualitatively describe a concentrated region of high surface brightness that might naively be described as the "nucleus" of a given galaxy (see discussion in Law et al. 2007b).

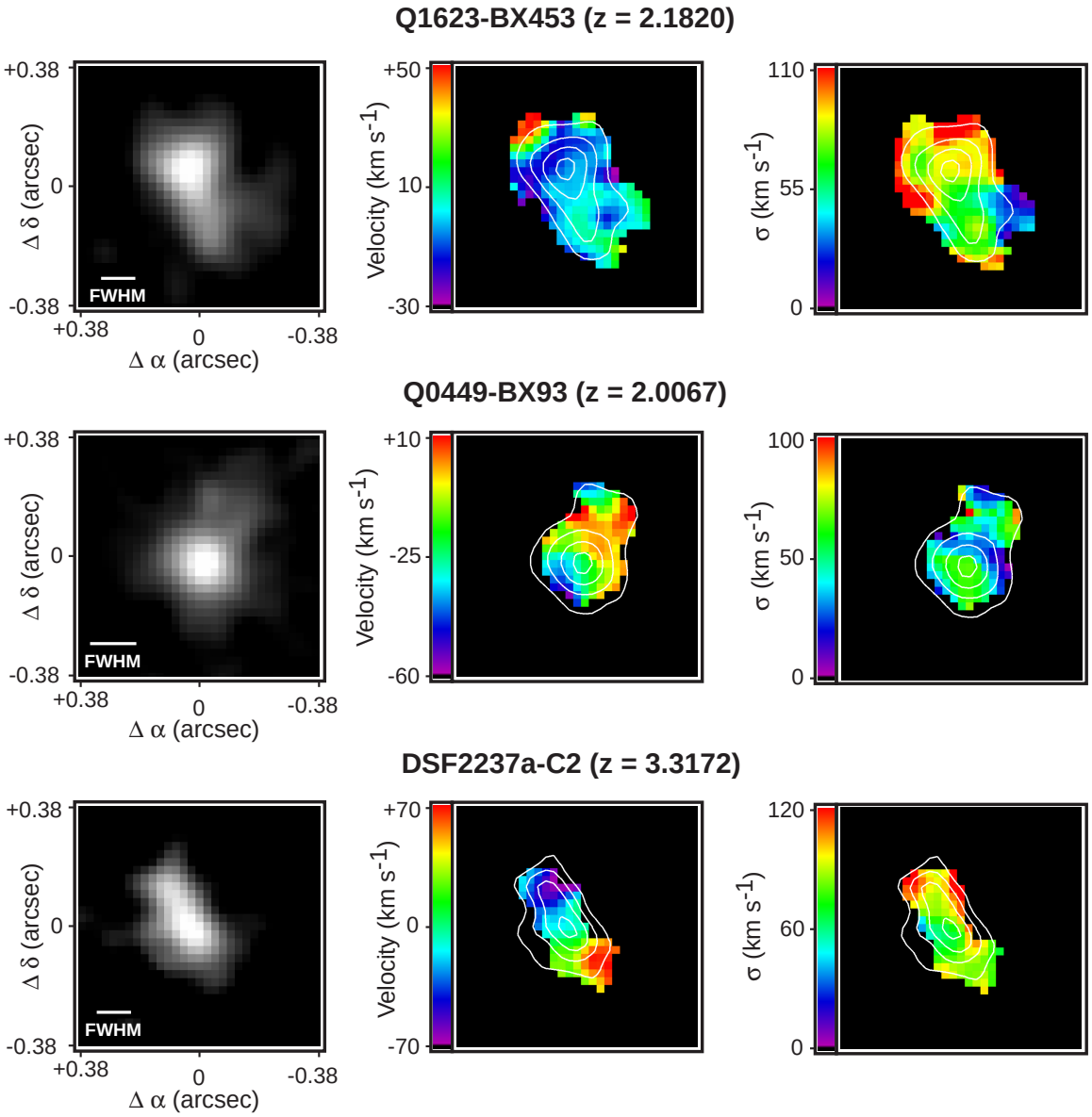

Figure 4.1 OSIRIS maps of (left to right) nebular emission line flux density (Hα for Q1623-BX453 and Q0449-BX93, [O III] for DSF2237a-C2), velocity, and velocity dispersion for the three target galaxies. Stretch on plots of emission line flux density is linear and runs from zero to the peak flux density of each galaxy; linear contours in flux density are overplotted on the velocity and dispersion maps. The FWHM of the PSF after smoothing is 110 mas in Q1623-BX453 and DSF2237a-C2 and 150 mas in Q0449-BX93, indicated by solid lines in the left-hand panels. Individual pixels measure 25 mas, the total field of view (0.75 $\times$ 0.75 arcseconds) is comparable to the seeing-limited spatial resolution of previous work. This field of view corresponds to 6.3, 6.4, and 5.7 physical kpc at the redshift of Q1623-BX453, Q0449-BX93, and DSF2237a-C2, respectively.

conclude that with a major/minor axis ratio of $r_{\rm maj}/r_{\rm min} = 1.53$, such a disk has a position angle of $\theta = 38^\circ$ East of North and an inclination of $i = 49^\circ$ away from the normal.

While it is tempting to draw such physical inferences from the ionized-gas morphologies, these inferences are not necessarily robust given the irregularity of typical star-forming galaxies at redshift $z \sim 2-3$, which typically consist of 1–3 nucleations connected by regions of low surface-brightness emission (as viewed in the rest-frame UV; see Fig. 2 of Law et al. 2007b). Since the UV and ionized gas morphologies are strongly correlated (at least in the local universe; Gordon et al. 2004, Kennicutt et al. 2004, Lee et al. 2004, although c.f. Conselice et al. 2000), and trace the brightest regions of star formation unobscured by dust they are therefore a complex product of the strength and distribution of star-forming regions, dust, viewing angle, and possible merger-induced irregularities, rendering them unreliable indicators of the galactic potential. Indeed, recent studies have found little to no correlation between morphology and major-axis velocity shear (Erb et al. 2004) or any of an assortment of other parameters such as stellar mass, star formation rate, or the strength of galactic-scale outflows (Law et al. 2007b). Even if the rotating gas disk hypothesis were correct, it is not obvious that estimates of the disk size and/or orientation based on the length of the major/minor axes are meaningful since the observed morphology of such a disk will be dominated by the clumpy distribution of star formation (see, e.g., theoretical models by Noguchi 1999 and Immeli et al. 2004b).

We quantify an average linear dimension of the nebular line emission region by adopting a segmentation map which includes all spaxels (i.e., lenslets) for which nebular emission can be fit with a Gaussian profile with S/N ratio (SNR) ~ 6, and which have a velocity of less than 300 km s^{-1} relative to systemic (see §4.6 for further explanation of these selection criteria). The effective size of this region is determined as follows: assuming that the N elements in the segmentation map are distributed in an approximately circular arrangement, the radius of this circle is given simply by $r' = \sqrt{N/\pi}$. The corrected radius r is then determined by subtracting off the radius of the stellar PSF in quadrature (Table 6.1; this is typically a small correction of less than $\sim$10%) and converting to physical kpc at the redshift of the source. The PSF-corrected emission area is defined as $I = \pi r^2$. Adopting the non-parametric gini–multiplicity ($G - \Psi$) classification scheme described by Law et al. (2007b), we note that the ionized-gas morphologies of our three target galaxies (Table 4.2)

closely resemble the typical rest-frame UV morphologies of $z \sim 2-3$ star-forming galaxies in the GOODS-N (Law et al. 2007b) and Q1700 (Peter et al. 2007) fields as seen by HST-ACS, albeit with limiting star formation rate density roughly five times higher than that of the HST data.

4.4 GLOBAL SPECTRA

4.4.1 Flux Calibration

Integrated spectra (shown in Fig. 4.2) were generated for each source by convolving the data cube during reduction with a broad 150 mas spatial Gaussian kernel, which considerably improves the S/N ratio (SNR) of each spaxel at the cost of suppressing spatial information. All spaxels with SNR > 6 were combined to produce a "clean" integrated spectrum, while all spaxels within a radius of about $2r$ were combined to produce a "total flux" integrated spectrum. The first of these is of higher quality and is used to determine the relative flux in individual emission lines, while the second spectrum better samples the faint flux distribution and is used to fix the absolute flux calibration. We eliminate any residual gradients as a function of wavelength by subtracting off a first-order spline fit to the integrated spectrum using standard IRAF techniques (with iterative rejection to exclude emission lines from the spline fit). We estimate the flux calibration of our integrated emission-line spectrum using detailed modeling of the OSIRIS + Keck LGSAO system + atmospheric throughput as a function of wavelength based on the simulations of Law et al. (2006) and refined to accomodate recent measurements of system throughput parameters. The results of this wavelength-dependent calibration method agree to within $\sim 25\%$ with those obtained using the broadband photometric zero-point calibrations published in the OSIRIS manual (roughly as close an agreement as may reasonably be expected since these zero-points average the transmission function throughout the bandpass). The greatest uncertainty in flux calibration arises however in the additional requirement that we correct for the unknown amount of flux lost to the seeing halo of the AO-corrected PSF. For a point source with a 35% strehl correction, approximately 35% of the total light is contained within the diffraction-limited core of FWHM ~ 50 mas while the remaining 65% is spread throughout a seeing-limited halo. The percentage of total flux measured for a given obser-

vation is therefore a complex function of the strehl of the AO correction (which depends in turn upon the magnitude/separation of the TT star and the wavelength of observation), the quality of the seeing, and the physical structure of the source. Based on simulations adopting quantities for these various parameters roughly representative of our observing conditions, we expect to recover $\sim 60\%$ of the light from a given target source. This percentage is roughly consistent with that estimated using measurements of the average flux density in narrow-band observations of our TT stars compared to K_s magnitudes drawn from the 2MASS database.

Given all of the uncertainties inherent in this bootstrapped flux calibration, we estimate that the systematic flux uncertainty for a given source is $\sim 30\%$. In contrast, the relative flux uncertainty between two emission lines (i.e., the uncertainty in the line flux ratio) is considerably lower and dominated simply by the root-mean square (RMS) deviation of the integrated spectrum. Formally, we adopt as the 1σ uncertainty in each emission line flux the error due to RMS fluctuations per spectral channel compounded over the measured width of the emission line. Similar estimates of the RMS uncertainty may be used to place 3σ upper limits on the strength of undetected emission lines using a reasonable guess at the likely intrinsic width of the undetected line.

Based on these calibrations and observations of the three target galaxies we determine that $f_{\rm lim} = 3 \times 10^{-16}$ erg s^{-1} cm^{-2} arcsec^{-2} represents the 6σ Hα surface brightness threshhold for our observations (i.e., the faintest believable feature for two hours of integration at $\lambda \sim 2\mu$). At redshift $z = 2.5$ this is equivalent to a detection threshhold of ${\rm SFR}_{\rm lim} = 1 M_\odot$ yr^{-1} kpc^{-2} (adopting the Hα flux to SFR calibration described in §4.5.2).[6] Given that a star formation rate density of ~ 0.1 $M_\odot$ yr^{-1} kpc^{-2} represents the threshhold between starburst galaxies and the centers of normal galactic disks in the local universe (Kennicutt 1998a), we do not expect to detect local-type disk galaxies in the course of our study even if such galaxies existed at high redshift.

In Table 4.3 we compile the systemic, UV absorption-line, and Lyα emission redshifts and nebular line fluxes of the target galaxies. In both cases for which previous NIRSPEC observations were obtained (Q1623-BX453 and DSF2237a-C2) the systemic redshifts agree

[6]Note that this is the threshhold for *detection*, the threshhold for deriving reliable kinematic information is approximately 4 $M_\odot$ yr^{-1} kpc^{-2}. For comparison, the limiting star formation rate density in the rest-UV morphological analysis presented by Law et al. (2007b) is ~ 0.2 $M_\odot$ yr^{-1} kpc^{-2}.

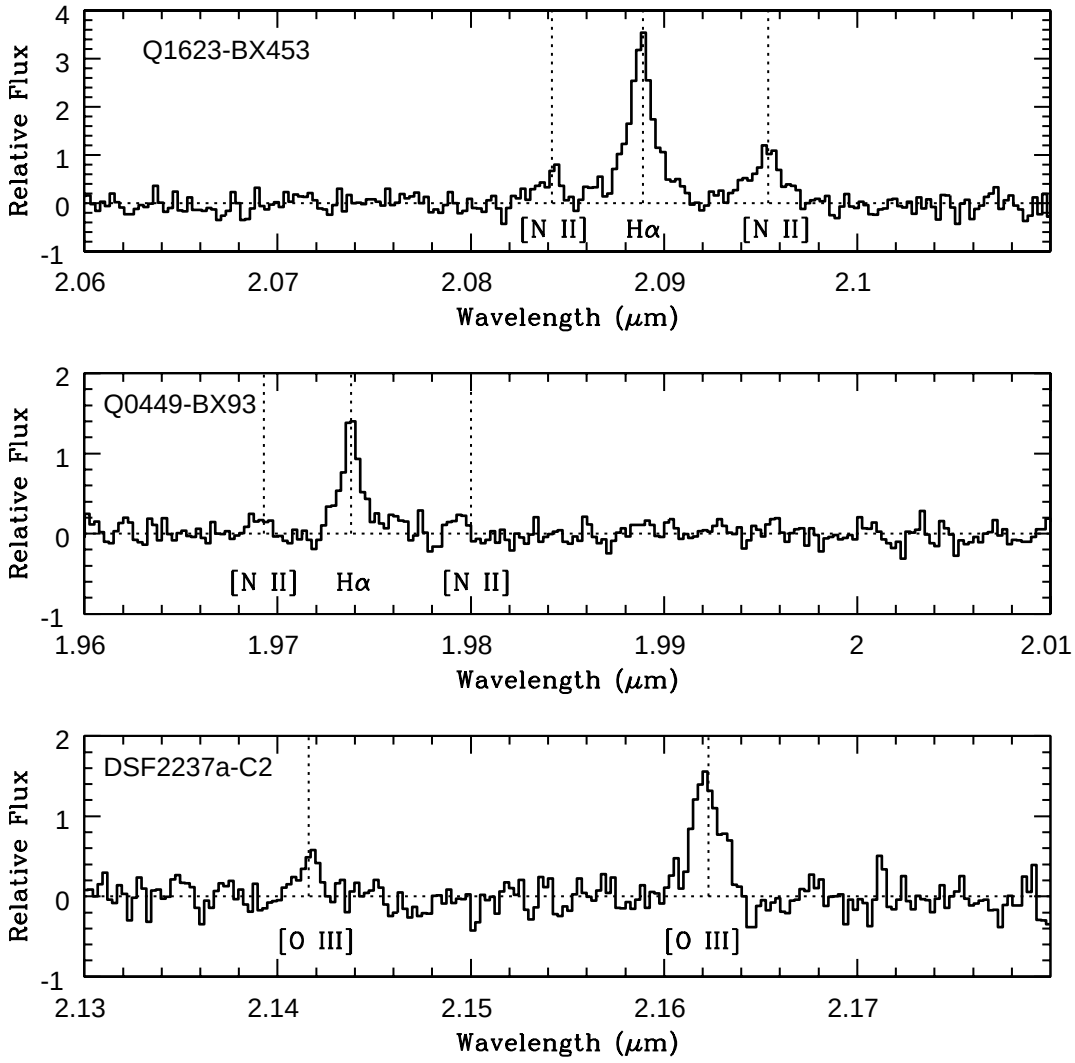

Figure 4.2 OSIRIS spectra of Q1623-BX453, Q0449-BX93, and DSF2237a-C2 collapsed over the spatial extent of each galaxy. Vertical dotted lines denote the wavelengths of [N II] λ6550, Hα, and [N II] λ6585 emission (for Q1623-BX453 and Q0449-BX 93) and [O III] λ4960 and λ5008 emission (for DSF2237a-C2). Lines for [N II] and [O III] λ4960 are drawn at the fiducial wavelengths expected based on the Hα and [O III] λ5008 emission redshifts.

to within $\Delta z = 0.0008$ or about 50 km s^{-1} (i.e., consistent to within roughly one fifth the velocity resolution of NIRSPEC [$R \sim 1400$]). The integrated Hα flux of Q1623-BX453 is 1.7 times greater in the OSIRIS data than the NIRSPEC, consistent with the approximately 50% slit-loss correction factor estimated by Erb et al. (2006b). However, the [O III] flux of DSF2237a-C2 appears to be a factor of ~ 2 weaker in the OSIRIS data than the NIRSPEC. The first, and perhaps most likely, explanation for this discrepancy is that the NIRSPEC flux observed is strongly sensitive to differential slit losses between the standard star and target galaxy observations, which can drive flux errors in both directions depending on atmospheric conditions and the quality of the background subtraction in each case. However, it is also possible that this galaxy contains a large fraction of its total flux in the form of extended low surface brightness emission undetected with OSIRIS but detected in the more sensitive long-slit observations.

4.4.2 Global Chemistry

In the case of Q1623-BX453, both [N II] λ6549 and λ6584 (the stronger λ6584 line is hereafter simply [N II]) are detected reliably in the integrated galaxy spectrum (see Figure 4.2), allowing us to estimate the average metallicity of the galaxy. Defining the flux ratio $N2 = \log([\mathrm{N\,II}]/\mathrm{H}\alpha)$, we follow Pettini & Pagel (2004), who estimate the oxygen abundance as

$$12 + \log(O/H) = 8.90 + 0.57 \times N2. \tag{4.1}$$

Adopting the [N II] flux tabulated in Table 4.4 we find $N2 = -0.48 \pm 0.03$, and therefore $12 + \log(\mathrm{O/H}) = 8.63 \pm 0.18$ (this uncertainty is dominated by the 0.18 dex systematic uncertainty in the calibration given in Equation 4.1), consistent with near-solar enrichment ($12 + \log(\mathrm{O/H})_\odot = 8.66$; Asplund et al. 2004). This is consistent with the results of Shapley et al. (2004), who find $12 + \log(\mathrm{O/H}) = 8.60 \pm 0.18$ based on long-slit spectroscopy. As noted previously by Shapley et al. (2004) however, the FWHM of the [N II] emission line is roughly 30% larger than that of Hα, which can be a signature of shock ionization (Lehnert & Heckman 1996a). Since Q1623-BX453 shows no evidence of AGN activity in either rest-frame UV spectra (§4.4.3) or long-wavelength deviations from simple stellar population models (§4.5.1), and the measured value of $N2$ is consistent with that observed for normal

star-forming galaxies (Shapley et al. 2004; Erb et al. 2006a) we see no concrete evidence that this high ratio is due to shock heating or physical processes other than simple enrichment. Erb et al. (2006a) have considered this question in greater detail using a [O III]/Hβ versus [N II]/Hα diagnostic diagram and find that while the [O III]/Hβ ratio is greater for a given [N II]/Hα ratio in Q1623-BX453 than in local galaxies, this offset may be explained by a harder ionizing spectrum or a higher electron density (see also discussion by Shapley et al. 2005a) and does not provide concrete evidence for a central AGN.

Although the spectra are too faint to determine the precise [N II] morphology, we note that [N II] appears to be coincident with the Hα peak and varies slightly in relative strength across the face of the galaxy. Figure 4.3 plots individual spectra of the northeastern and southwestern quadrants and illustrates the stronger [N II] lines present in the northeastern region. Taking careful measurements of the respective spectra we find (Table 4.5) that the flux ratio of the bright core is $N2 = -0.46 \pm 0.03$ (consistent with the overall spectrum; as expected since it dominates the total flux of the source) while the flux ratio of the fainter region is $N2 = -0.67 \pm 0.09$. This $\sim 2.3\sigma$ difference (~ 0.1 dex in log(O/H))offers mild evidence to suggest that the distribution of heavy elements in Q1623-BX453 is not perfectly well-mixed, suggesting either that heavy elements from the latest burst of star formation (produced primarily in the northeastern region) have not yet had time to be fully distributed throughout the galaxy, or that the two regions may have had distinct star formation histories (as might be expected for instance in a merger-type scenario).

Since Q0449-BX93 is considerably fainter than Q1623-BX453 it is not possible to detect [N II] emission confidently. We place a 3σ detection limit on $f_{[\mathrm{N\,II}]}$ (Table 4.3) and conclude that an upper bound on the metallicity is $12 + \log(\mathrm{O/H}) \lesssim 8.37$ (i.e., less than 1/2 solar). Given the monotonic relation between stellar mass and metallicity found by Erb et al. (2006a) for similar galaxies at $z \sim 2$, this metallicity limit implies that $M_\star \lesssim 10^{10} M_\odot$. Unfortunately, it is not possible to constrain the metallicity of DSF2237a-C2 as we have only observed the wavelength interval surrounding [O III] λ5007Å.

4.4.3 Outflow Properties: UV Spectroscopy

In Figure 4.4 we plot the Keck-LRIS UV spectra of the three target galaxies shifted into the rest-frame as defined by the OSIRIS nebular redshifts. The spectrum of DSF2237a-C2

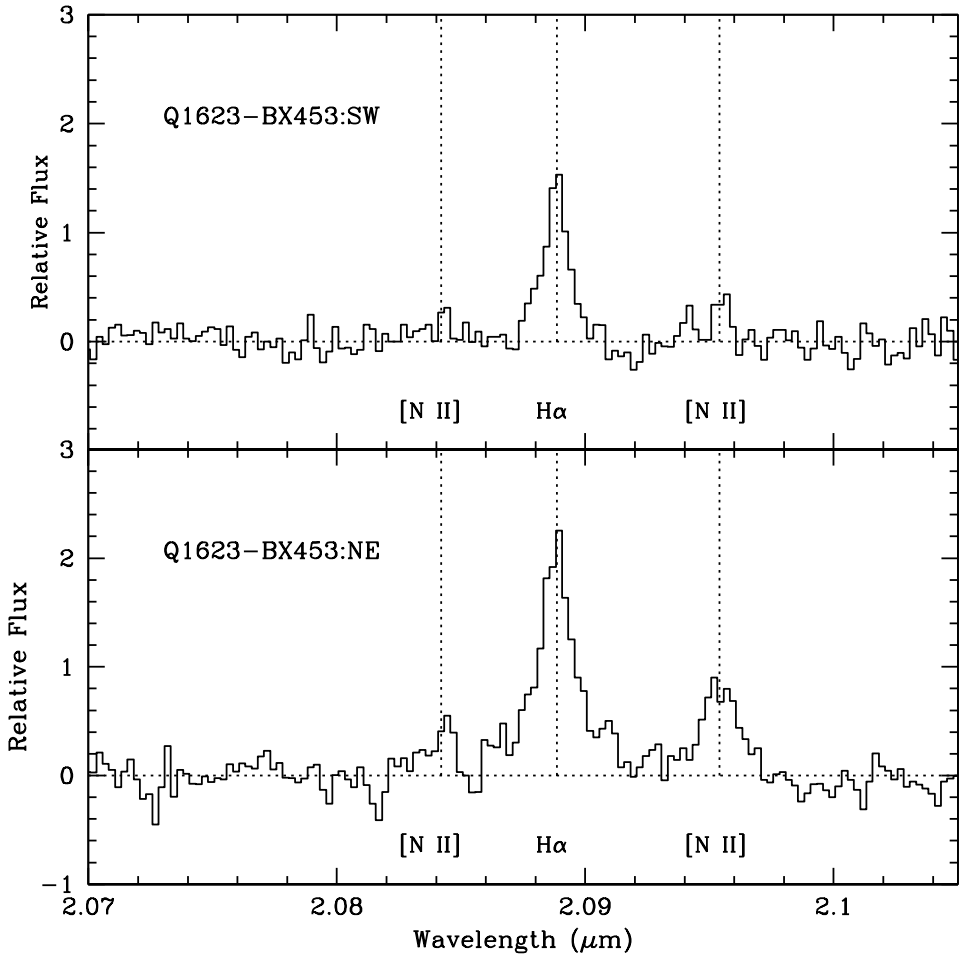

Figure 4.3 OSIRIS spectra of the northeastern (NE) and southwestern (SW) regions of Q1623-BX453. Vertical dotted lines denote the wavelengths of [N II] λ6550, Hα, and [N II] λ6585 emission.

was obtained as part of a survey of $z \sim 3$ LBGs (Steidel et al 2003; see also Giallongo et al 2002), while Q1623-BX453 and Q0449-BX93 were obtained more recently using LRIS-B, described by Steidel et al (2004). Q1623-BX453 was included on a slit mask receiving a total of 5.5 hours integration time, whereas the other spectra were obtained using shorter, survey-mode integration times of 1.5–2 hours.

The spectra of all three galaxies are broadly similar to high-quality composite spectra of the $z \sim 2-3$ star-forming galaxy sample (e.g., Shapley et al. 2003); these spectra exhibit strong interstellar absorption features (e.g., Si II, O I, C II, Si IV, C IV) and Lyman α that may appear in either emission or absorption. It is typical of star forming galaxies at these redshifts for the interstellar lines to be blue-shifted, and Lyα emission red-shifted (when present), by several hundred km s^{-1} with respect to the systemic redshift; these features are generally interpreted as scattered emission from the far-side and absorption in the near-side of an expanding shell of outflowing gas (see, e.g., Steidel et al. *in prep.*). The mean values for a sample of $\simeq 100$ galaxies in the redshift range $1.9 \leq z \leq 2.6$ are $\Delta v_{\rm abs} = -164$ km s^{-1} and $\Delta v_{\rm em} = +445$ km s^{-1} for the centroid of the interstellar lines and Lyα emission relative to Hα (which tends to trace gas at the systemic redshift), respectively (Steidel et al. *in prep.*).

The spectra of Q1623-BX453 and of Q0449-BX93 are typical with regard to the *sense* of the velocity offsets observed, as summarized in Table 4.3. The centroids of the interstellar lines of Q0449-BX93 are blue-shifted by $\simeq -270$ km s^{-1} with respect to the Hα redshift, placing it within the top $\sim 10-15\%$ in terms of this quantity, and making it very similar to the well-studied spectrum of cB58 (Pettini et al 2000, 2002). We note in passing that relatively strong Lyα, C IV, and Si IV absorption lines at $z_{\rm abs} = 2.0074$ are detected in the Keck/HIRES spectrum of the $z_{\rm em} = 2.677$ QSO Q0449−1645. The difference from the systemic redshift of Q0449-BX93 is only 70 km s^{-1}, even though the projected separation between the QSO and galaxy sightlines is 44", or 373 (proper) kpc.

The far-UV spectrum of Q1623-BX453 is more remarkable, in that the blue-shifted interstellar lines have a centroid offset of $\Delta v_{\rm abs} \simeq -900$ km s^{-1}, and a FWHM of $\simeq 1200$ km s^{-1}, both values being by far the largest observed in the sample of $\simeq 100$ mentioned above. The Lyα emission redshift exhibits a relatively modest shift of $\Delta v_{\rm em} = +170$ km s^{-1}. The spectrum of Q1623-BX453 also has unusually strong high-ionization interstellar absorption

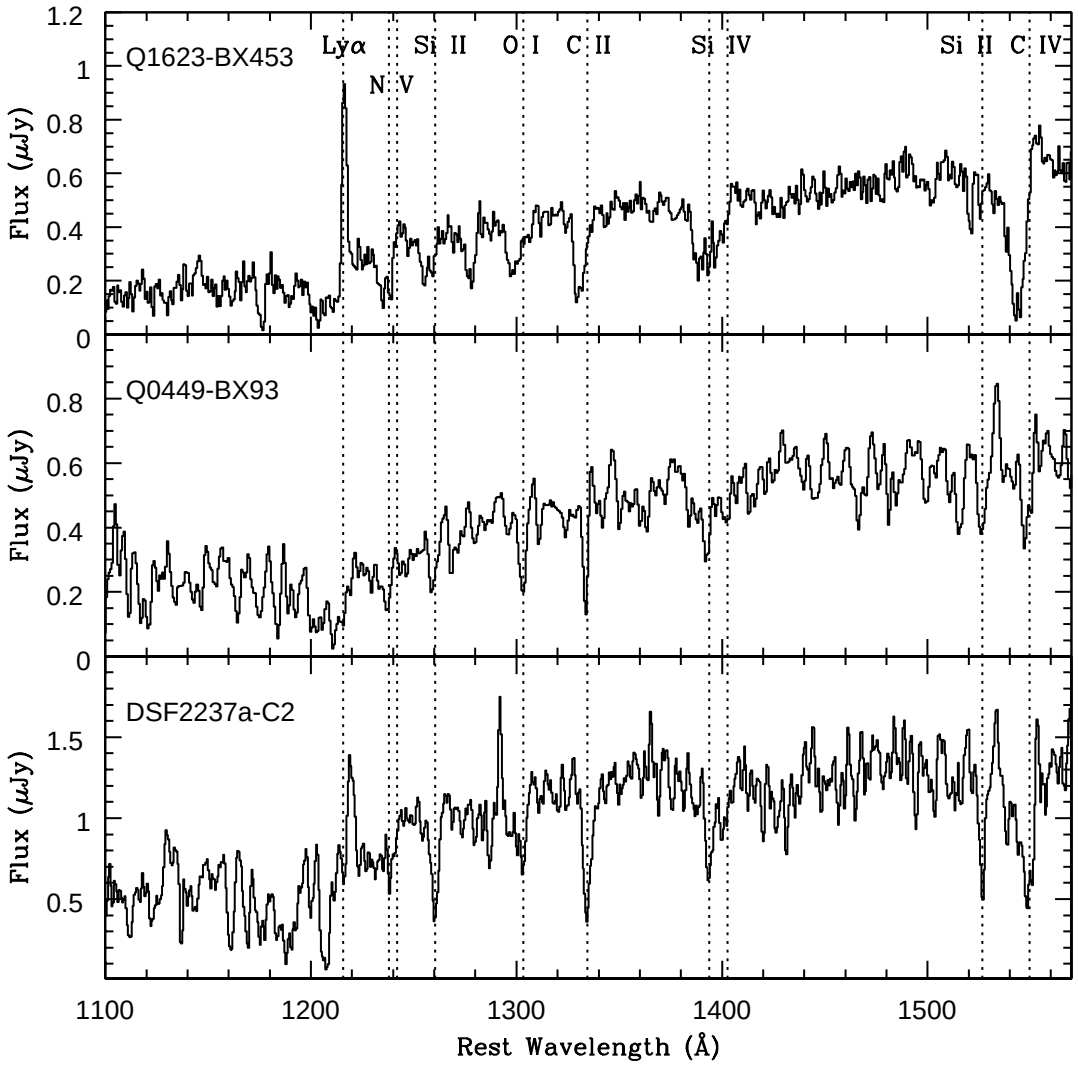

Figure 4.4 Flux-calibrated UV spectra of the three target galaxies. Spectra have been shifted to the systemic rest frame using the nebular line redshifts given in Table 4.3. The identifications and wavelengths of the strongest spectral features are indicated by vertical dotted lines. Spectra of Q0449-BX93 and DSF2237a-C2 have been smoothed with a 3-pixel boxcar filter.

features, including NV $\lambda\lambda$1238,1242, and many of the absorption features have complex velocity structure, with two dominant components at -600 and -1100 km s^{-1}. These unusual spectral features might lead one to suspect an AGN is involved, but there are no significant emission lines aside from Lyα in the high quality spectrum, and (as discussed further below) there is no evidence from the full spectral energy distribution to suggest the presence of anything but stellar energy. In spite of the rather violent kinematics of the outflowing interstellar gas, the Hα emission line kinematics show no hint of being affected, presumably because any Hα emission associated with the outflowing material is of much lower surface brightness than what we have detected with OSIRIS.

The spectrum of DSF2237a-C2 has typically strong interstellar absorption lines, but in this case close examination reveals that they are actually *redshifted* slightly with respect to the nebular redshift, with $\Delta v_{\rm abs} \simeq +100$ km s^{-1}, while the Lyα emission line is redshifted by an unusually large $\simeq 1100$ km s^{-1}. It turns out that such kinematics, where the interstellar line centroids are consistent with zero velocity with respect to the nebular systemic velocity, are observed in $\sim 15\%$ of $z \sim 2-3$ galaxies (Steidel et al. *in prep.*), and it is quite typical for such objects to have unusually large Lyα emission offsets. Of possible significance is that interstellar absorption line centroid velocities consistent with zero occur relatively frequently (5 out of 7) for galaxies in the Erb et al (2006a) sample having measured velocity shear from NIRSPEC Hα spectra. As discussed further by Steidel et al. (*in prep.*), these observations suggest a connection between the presence of velocity shear (as in the case of DSF2237a-C2; see §4.6.3) and increased absorption close to zero systemic velocity, though at present it is not possible to distinguish between orientation effects (e.g., outflows collimated along the rotation axis) and real differences in the dynamical structure of the galaxies. In any case, OSIRIS is much more sensitive to the measurement of velocity shear in the galaxies, and any correlation between the kinematics of gas associated with outflows and the kinematics of the H II regions should become clearer as the sample size increases.

4.5 STELLAR POPULATIONS, STAR FORMATION RATES AND GAS MASSES

4.5.1 Stellar Masses and Stellar Populations from SED Modeling

As part of an ongoing survey program we have obtained broadband photometry (Table 6.2) in each of our target fields. The wavelength coverage of these data varies from field to field: all fields (Q1623, Q0449, and DSF2237a) have ground-based optical $U_nG\mathcal{R}$ photometry which serves as the basis for the optically selected galaxy catalog (Steidel et al. 2003, 2004); Q1623 and DSF2237a have deep near-IR J and K_s photometry, described by Erb et al. (2006c) and Shapley et al. (2001), respectively; and Q1623 has also been imaged in the mid-IR by the *Spitzer Space Telescope*, with both IRAC at 3–8 μm and MIPS at 24 μm.

Wavelength coverage from the rest-frame UV to near-IR (in Q1623) or UV to optical (DSF2237a) enables us to model the spectral energy distributions of Q1623-BX453 and DSF2237a-C2 and obtain estimates of these galaxies' stellar masses, ages, reddening, and star formation rates (the Q0449 data are restricted to the rest-frame UV and are insufficient for such modeling). Previous modeling of the SEDs of these two galaxies has been presented by Erb et al. (2006c) and Shapley et al. (2001), respectively; we redo the modeling here to add the Spitzer IRAC data in the case of Q1623-BX453 and update the method for consistency in the case of DSF2237a-C2. In both cases the K_s magnitudes have been corrected for line emission according to the values determined in §4.4.1 (the corrections are ~ 0.2 mag in both cases).

The modeling procedure has been described in detail by Shapley et al. (2005b). Briefly, we use Bruzual & Charlot (2003) models with a constant star formation rate, solar metallicity, and a Chabrier (2003) IMF. The resulting stellar masses for Q1623-BX453 and DSF2237a-C2 are $M_\star = 3.1 \times 10^{10}$ M$_\odot$ and $M_\star = 2.9 \times 10^{10}$ M$_\odot$, respectively. The remaining stellar population parameters are given in Table 6.2, and the best-fit spectral energy distributions are shown in Figure 5.2.

4.5.2 Star Formation Rates

A direct estimate of the instantaneous star formation rate may be derived from the observed Hα luminosity since it traces the ionizing radiation produced by young, massive stars. We

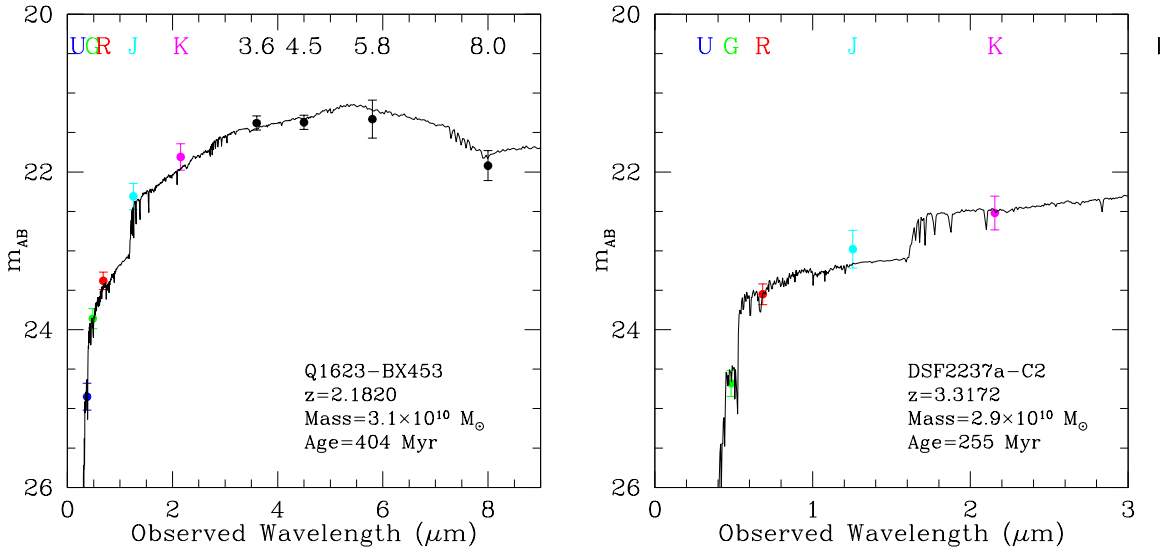

Figure 4.5 The best-fit constant star formation (CSF) model (solid black line) is overplotted against the observed spectral energy distribution for Q1623-BX453 and DSF2237a-C2. Colored points represent ground-based optical and near-IR photometry, black points are based on *Spitzer*-IRAC observations. The K-band photometry for both galaxies is shown corrected for nebular line emission (see discussion in §4.5.1). Values given for stellar mass and population age represent the values derived from the best-fit CSF model; typical uncertainties are given in Table 6.2.

adopt the calibration derived by Kennicutt et al. (1994; summarized in Kennicutt 1998a) whereby

$$\mathrm{SFR}\ (\mathrm{M}_\odot\ \mathrm{yr}^{-1}) = \frac{\mathrm{L(H}\alpha)}{1.26 \times 10^{41}\ \mathrm{erg\ s}^{-1}} \times 0.56, \tag{4.2}$$

where we have introduced the factor of 0.56 to convert to the Chabrier (2003) IMF.

This enables direct calculation of the star formation rate from our observed Hα fluxes for Q1623-BX453 and Q0449-BX93; we find $\mathrm{SFR}_{\mathrm{H}\alpha} = 36\ \mathrm{M}_\odot\ \mathrm{yr}^{-1}$ for Q1623-BX453 and $\mathrm{SFR}_{\mathrm{H}\alpha} = 12\ \mathrm{M}_\odot\ \mathrm{yr}^{-1}$ for Q0449-BX93. Although Hα is redshifted beyond the K-band for $z \gtrsim 2.6$, it is nonetheless possible to estimate a star formation rate for DSF2237a-C2 based on the observed [O III] flux. Using long-slit spectroscopy, Pettini et al. (2001) determined the Hβ flux to be $3.5 \pm 0.4 \times 10^{-17}$ erg s^{-1} cm^{-2}, and the ratio of the [O III] and Hβ fluxes to be $F_{\mathrm{H}\beta}/F_{[\mathrm{O\,III}]} = 0.19$ (their [O III]λ5007 flux of 18×10^{-17} erg s^{-1} cm^{-2} is in rough agreement with the OSIRIS value of $10.1 \pm 0.5 \times 10^{-17}$ erg s^{-1} cm^{-2}, given the significant uncertainties in the calibration of long-slit spectra). While Hβ falls outside the narrow wavelength range which we have observed with OSIRIS, we can use the $F_{\mathrm{H}\beta}/F_{[\mathrm{O\,III}]}$ ratio observed by Pettini et al. (2001) to infer an Hβ flux of 2.0×10^{-17} erg s^{-1} cm^{-2} from our observed [O III] value. We then assume a standard recombination ratio of $F_{\mathrm{H}\alpha}/F_{\mathrm{H}\beta} = 2.75$ (Osterbrock 1989) to find $F_{\mathrm{H}\alpha} = 5.4 \times 10^{-17}$ erg s^{-1} cm^{-2} and $\mathrm{SFR}_{\mathrm{H}\alpha} = 23\ \mathrm{M}_\odot\ \mathrm{yr}^{-1}$. These SFRs are uncorrected for dust extinction (which we discuss below) and have typical uncertainties $\sim 30\%$ (dominated by the uncertainty in the flux calibration described in §4.4.1).

We use the values of $E(B-V)$ determined by the SED modeling discussed in §4.5.1 to correct the observed Hα flux of Q1623-BX453 and the inferred Hβ flux of DSF2237a-C2 for extinction using a modified Calzetti et al. (2000) starburst attenuation law as described by Erb et al. (2006c). For Q1623-BX453 we find $E(B-V) = 0.245$ for a corrected SFR of 77 $\mathrm{M}_\odot\ \mathrm{yr}^{-1}$, in agreement with the value of 77 $\mathrm{M}_\odot\ \mathrm{yr}^{-1}$ we obtain from the SED modeling. For DSF2237a-C2 we use the best fit $E(B-V) = 0.175$ to correct the Hβ flux inferred above, and then assume $F_{\mathrm{H}\alpha}/F_{\mathrm{H}\beta} = 2.75$ to find $F_{\mathrm{H}\alpha} = 11.3 \times 10^{-17}$ erg s^{-1} cm^{-2} and $\mathrm{SFR}_{\mathrm{H}\alpha} = 49\ \mathrm{M}_\odot\ \mathrm{yr}^{-1}$. This is somewhat smaller than the value of 112 $\mathrm{M}_\odot\ \mathrm{yr}^{-1}$ we find from the SED modeling, but not inconsistent with the factor of ~ 2 RMS found by Erb et al. (2006c) for SFRs determined from SED modeling and Hα emission, especially given the

additional extrapolations needed to calculate the nebular line SFR.[7]

Because we lack the IR data to model the SED of Q0449-BX93, we estimate the extinction from the $G - \mathcal{R}$ color alone, assuming a constant star formation age of 570 Myr, the median age[8] of the $z \sim 2$ sample as found by Erb et al. (2006b). Assuming this median age we find $E(B-V) = 0.125$ and a corrected SFR of 18 $M_\odot$ yr^{-1}. The uncertainty in age has a negligible effect on the corrected SFR; for an age of 50 Myr, we find $SFR_{H\alpha} = 20$ $M_\odot$ yr^{-1}, while the maximum age of 3.2 Gyr leads to $SFR_{H\alpha} = 17$ $M_\odot$ yr^{-1}. The corrected and uncorrected SFRs for the three galaxies are summarized in Table 4.7, and for reference we note that the mean extinction-corrected SFR of the $z \sim 2$ sample, from both Hα and the UV continuum, is ~ 30 $M_\odot$ yr^{-1} (Erb et al. 2006b).

By way of comparison, we also include in Table 4.7 estimates of the star formation rate obtained using UV and mid-IR photometry. In the former case, we use the rest-frame monochromatic luminosity at 1500 Å (L_ν; based on linear interpolation of the broadband photometry given in Table 6.2) and the Kennicutt (1998b) conversion between L_ν and SFR:

$$\mathrm{SFR}\ (M_\odot\ \mathrm{yr}^{-1}) = \frac{L_\nu}{7.14 \times 10^{27}\ \mathrm{erg\ s^{-1}\ Hz^{-1}}} \times 0.56, \tag{4.3}$$

where the factor of 0.56 has again been introduced to convert to the Chabrier (2003) IMF. After correcting for extinction using the Calzetti et al. (2000) starburst attenuation law, we find $SFR_{UV} = 81$, 39, 95 $M_\odot$ yr^{-1} for Q1623-BX453, Q0449-BX93, and DSF2237a-C2, respectively. These values are in good agreement with $SFR_{H\alpha}$ for Q1623-BX453; the factor of ~ 2 difference between UV and Hα estimates for DSF2237a-C2 and Q0449-BX93 may be due (in the former case) to the uncertainties introduced in our conversion from [O III] flux to Hα and suggests (in the latter case) that Q0449-BX93 may be a particularly young, blue, dust-free galaxy for which the conversion from $(G-\mathcal{R})$ color to $E(B-V)$ is imperfect. Using *Spitzer*-MIPS 24 μ photometry, it is also possible to estimate the SFR for Q1623-BX453 using the rest-frame 8 μ flux given in Table 6.2. Adopting the calibrations discussed

[7]Curiously, the original Hβ flux measured by Pettini et al. (2001) gives a better match to SED star formation rate than the extrapolated flux measured using OSIRIS, highlighting the possibility that OSIRIS may sometimes "miss" low surface brightness flux.

[8]The values of $E(B-V)$ allowed by the $G - \mathcal{R}$ color are relatively insensitive to the age of the galaxy; for reasonable ages ranging from 50 Myr (approximately the dynamical timescale) to 3.2 Gyr (the age of the universe at the redshift of the galaxy), $E(B-V)$ varies from 0.164 to 0.113.

in Reddy et al. (2006b), we estimate $\mathrm{SFR_{IR}} = 96\ M_\odot\ \mathrm{yr}^{-1}$ under the Chabrier (2003) IMF, in good agreement with the UV, SED, and Hα estimates.

4.5.3 Gas Masses and Gas Fractions

We can also use the Hα luminosities in combination with the galaxy sizes measured in §4.3 to estimate the galaxies' gas masses and gas fractions. Such indirect techniques are required because emission from molecular gas is very difficult to detect in all but the most luminous high-redshift galaxies with current technology. We follow the procedure described by Erb et al. (2006b), benefitting here from the higher spatial resolution of the OSIRIS data, which provides better constraints on the galaxies' sizes. As described by Erb et al. (2006b), we use the empirical global Schmidt law (Kennicutt 1998a), which relates the surface density of star formation to the surface density of molecular gas (in the starburst regime in which our galaxies fall; more quiescent star-forming galaxies at low redshift also have significant amounts of atomic gas).

We determine the surface density of Hα luminosity ($\Sigma_{\mathrm{H}\alpha}$) by dividing the extinction-corrected observed (or inferred, in the case of DSF2237a-C2) Hα luminosity by the projected linear area I of the galaxy as determined in §4.3. The gas surface density Σ_{gas} is then given by the global Schmidt law, and the total gas mass by $M_{\mathrm{gas}} = \Sigma_{\mathrm{gas}} I$. Gas masses inferred in this way are subject to significant uncertainties beyond those associated with the measurements of fluxes and sizes and the ~ 0.3 dex uncertainty introduced by the scatter in the Schmidt law itself. It is not yet known whether the Schmidt law in this form holds at high redshift, although the one galaxy for which it has been tested, the gravationally lensed Lyman break galaxy MS1512-cB58, appears to be consistent with the local form (Baker et al. 2004). It is also likely that the Schmidt law, which applies to only the cold gas associated with star formation, does not account for all of the gas; in a typical local disk galaxy, $\sim 40\%$ of the total gas mass is not included by the Schmidt law (Martin & Kennicutt 2001).

The measured areas of Q1623-BX453, Q0449-BX93, and DSF2237a-C2 are $I = 9.5 \pm 0.3$, 4.7 ± 0.6, and 3.3 ± 0.3 kpc^2, respectively. The size of Q1623-BX453 derived here ($r = 1.74 \pm 0.03$ kpc) is considerably smaller than the value of $r = 4.4 \pm 0.4$ found by Erb et al. (2006c) from long-slit NIRSPEC observations, reflecting in part the slightly different definitions of r and the difficulty of estimating sizes from seeing-limited long-slit

data. However, it is also likely that the luminous area of a given galaxy is genuinely greater in the Erb et al. (2006c) data since NIRSPEC is more sensitive than OSIRIS, and may thus detect lower surface-brightness features at larger radii. Galaxy size r and I as defined here are only meaningful with regard to the detection threshhold of a particular study.

Combining these size estimates with the extinction-corrected Hα luminosities, we find gas masses of 2.4 $\times 10^{10}$, 6.9 $\times 10^{9}$, and 1.3 $\times 10^{10}$ $M_{\odot}$ (each with $\sim$ 20% statistical uncertainty, but note discussion of systematic uncertainties above) for Q1623-BX453, Q0449-BX93, and DSF2237a-C2, respectively. The stellar mass of Q1623-BX453 is 3.1×10^{10} $M_{\odot}$, for a gas fraction $\mu = 0.44$; for DSF2237a-C2 we find $M_{\star} = 1.6 \times 10^{10}$ $M_{\odot}$and $\mu = 0.32$. We are unable to determine a gas fraction for Q0449-BX93 because of the lack of near-IR imaging from which to derive a stellar mass, although the mass limit estimated from the mass-metallicity relation (Erb et al. 2006a) suggests that $\mu \gtrsim 0.41$. Combining the typical uncertainties of the stellar ($\sigma_{\mathrm{M}_{\star}}/\mathrm{M}_{\star} = 0.4$) and gas ($\sigma_{\mathrm{M}_{\mathrm{gas}}}/\mathrm{M}_{\mathrm{gas}} = 0.2$) masses, we estimate the uncertainty in the gas fraction $\sigma_{\mu}/\mu = 0.35$. The stellar mass and gas fraction of Q1623-BX453 are close to the mean values ($< M_{\star} >= 3.6 \pm 0.4 \times 10^{10} M_{\odot}$, $< \mu >= 0.37 \pm 0.03$) found for a larger sample of 114 galaxies at $z \sim 2$ by Erb et al. (2006c). While there is no similar determination of the mean gas fraction at $z \sim 3$, the stellar mass of DSF2237a-C2 is only slightly higher than the median of 1.4×10^{10} $M_{\odot}$found for $z \sim 3$ Lyman break galaxies by Shapley et al. (2001; we convert their reported median to our adopted IMF).

We also use the extinction-corrected SFRs determined above to estimate the average and peak star formation rate surface density Σ_{SFR} (Table 4.7). Dividing the SFRs by the total areas, we find an average Σ_{SFR} = 8, 4, and 15 $M_{\odot}$ yr^{-1} kpc^{-2} for Q1623-BX453, Q0449-BX93, and DSF2237a-C2, respectively. These values lie in the middle of the distribution of Σ_{SFR} found for local starbursts by Kennicutt 1998a (after accounting for the different IMF), and at the upper end of the range for $z \sim 2$ galaxies found by Erb et al. (2006c). Based on the peak flux densities observed in a given spaxel, we estimate the corresponding peak star formation rate surface densities to be roughly twice the mean, with Σ_{SFR} = 20, 7, and 25 $M_{\odot}$ yr^{-1} kpc^{-2}. These values are comparable to the maximal star-formation rate densities observed in the local universe by Lehnert & Heckman (1996b; $\Sigma_{\mathrm{lim}} = 11$ $M_{\odot}$ yr^{-1} kpc^{-2} in our adopted IMF) and Meurer et al. (1997; $\Sigma_{\mathrm{lim}} = 25$ $M_{\odot}$ yr^{-1} kpc^{-2} in our adopted IMF), implying that Q1623-BX453 and DSF2237a-C2 may be forming stars at close to the

maximal rate in their brightest regions. Given that (in the local universe) a SFR density of $\Sigma_* = 0.1 M_\odot$ yr^{-1} kpc^{-2} is sufficient for the resulting supernovae to drive a wind into the surrounding ISM (Heckman 2002), it is likely that rapidly star-forming galaxies similar to these are quite "leaky" systems, with a significant fraction of metal-enriched gas finding its way into the IGM (Erb et al. 2006a; Adelberger et al. 2003,2005a).

4.6 SPATIALLY RESOLVED KINEMATICS AND DYNAMICAL MASSES

Using the integrated spectra described in §4.4.1 we estimate the kinematic dispersion of the ionized gas by fitting a Gaussian profile (corrected for instrumental resolution) to the observed emission. We obtain values of $\sigma_{\rm v} = 92 \pm 8, 72 \pm 12, 101 \pm 15$ km s^{-1}, respectively, for Q1623-BX453, Q0449-BX93, and DSF2237a-C2.

Although our velocity dispersion for Q1623-BX453 is slightly higher than that obtained previously by Erb et al. (2006c; $\sigma_{\rm v} = 61 \pm 4$ km s^{-1})[9], the measured dispersion of DSF2237a-C2 agrees with the value $\sigma_{\rm v} = 100 \pm 4$ km s^{-1} observed by Pettini et al. (2001). However, as we demonstrate below in §4.6.3, the velocity shear of DSF2237a-C2 contributes to the line width of the integrated spectrum. Based on examination of the spatially resolved velocity map of the galaxy, we conclude that the central velocity dispersion $\sigma_{\rm v} = 79$ km s^{-1}, rising slightly to about 89 km s^{-1} at larger radii.

While the total amplitude of any velocity shear may be an unreliable probe of the dynamical mass of a system, the central velocity dispersion σ is predominantly driven by the gravitational potential of the system even in kinematically complex systems such as local ULIRGS (Colina et al. 2005). These σ may therefore be used to estimate the dynamical mass of the galaxies using the relation

$$M_{\rm dyn} = \frac{C\sigma^2 r}{G}, \tag{4.4}$$

where a relatively straight-forward derivation (e.g., Erb et al. 2006c) gives the constant

[9]This discrepancy appears to be due to the presence of a residual OH sky feature in the NIRSPEC Hα spectrum; the OSIRIS velocity dispersion is roughly in agreement with the NIRSPEC velocity dispersion of $\sigma_{\rm v} = 106 \pm 8$ km s^{-1} measured using the [O III] emission line.

geometric prefactors $C = 5$ appropriate for a uniform sphere and $C = 3.4$ for a thin disk with average inclination. Based on the kinematic data presented in §4.6.1 – 4.6.3, we adopt $C = 5$ for Q1623-BX453 and Q0449-BX93, and $C = 3.4$ for DSF2237a-C2.

While σ is reasonably well-determined, r is not and can affect the resulting dynamical mass calculated via Equation 4.4 significantly. Ideally, we might adopt the virial radius, for which the derived $M_{\rm dyn}$ should be a reasonable estimate of the total gravitational mass. However, the only observationally determined length scale is that of the much smaller region from which nebular line emission is detected (see Table 4.2). Adopting this nebular emission radius, we calculate dynamical masses of $M_{\rm dyn} = 17 \pm 2$, 7 ± 2, and $5 \pm 1 \times 10^9 M_\odot$ for Q1623-BX453, Q0449-BX93, and DSF2237a-C2 (using $\sigma_{\rm v} = 79$ km s^{-1}) within a radius $r = 1.74$, 1.23, and 1.03 kpc, respectively. Unsurprisingly (given that our dynamical masses probe only the central 1–2 kpc), these masses differ by $\sim$ a factor of 15 from the typical halo mass within the virial radius calculated for similar galaxies by Adelberger et al. (2005b) based on clustering statistics. A previous estimate of $M_{\rm dyn}$ has also been obtained for Q1623-BX453 by Erb et al. (2006c); their value $M_{\rm dyn} = 12 \times 10^9 M_\odot$ is similar to our own, with the predominant difference arising from the difference in observed $\sigma_{\rm v}$.

We construct kinematic maps of the three target galaxies by fitting Gaussian profiles to the spectra contained within each resampled spaxel. Generally, single-component models suffice to represent the emission line profiles (although see discussion in §4.6.2 for Q0449-BX93). Such maps of the relative radial velocity and velocity dispersion (Fig. 4.1, center and right panels, respectively) are intrinsically noisy; we reduce the contribution of noisy spaxels to the resulting maps by considering only those for which the derived velocity is within 300 km s^{-1} of the systemic redshift, the FWHM is greater than or equal to the instrumental width, and the SNR of the detection is greater than six. These criteria are not derived from theoretical limits, but rather represent empirical constraints which we have found (based on iterations with various parameters) to produce the cleanest kinematic maps. These velocity maps are generally robust to systematic uncertainties (since all spaxels are processed in a similar manner) and the largest source of uncertainty is from random errors arising from the difficulty in determining the accurate centroid for an emission line of given S/N ratio. Given the OSIRIS spectral resolution $R \sim 3600$, the velocity FWHM is about 80 km s^{-1}. We estimate that uncertainties in the velocity maps are $\sim$ 10 km s^{-1} for bright

central regions of a galaxy, tapering to ~ 20 km s^{-1} towards the edges.

4.6.1 Q1623-BX453

The 2-d velocity map of Q1623-BX453 (Fig. 4.1, top middle panel) is largely consistent with a flat velocity field across the entire galaxy (~ 4 kpc along the major axis) and does not present any evidence for spatially resolved shear. Typical deviations from zero relative velocity are within the uncertainty of our ability to accurately measure velocity centroids from individual spaxels (i.e., about 10–20 km s^{-1}). The only suggestion of kinematic substructure is a small ~ 100 mas (800 pc) feature at the northeastern edge of the galaxy which appears to be receding at ~ 50 km s^{-1} relative to systemic and has a sharp discontinuity with the bulk velocity field (i.e., it does not appear to "blend in" by means of a gradual velocity transition). Given the extremely low flux of this feature (which lies outside the faintest flux contour illustrated on Fig. 4.1) this may be simply a residual noise artifact.

Although the line-of-sight velocity of the ionized gas is roughly constant across the face of the galaxy, the dispersion of this gas (σ) varies slightly with position (Fig. 4.1; top right panel). In particular, σ peaks around 100 km s^{-1} in the northeastern region approximately coincident with the flux peak, decreases to ~ 70 km s^{-1} in the southwestern region, and drops to below 30 km s^{-1} in the extremely faint emission region to the west. While there appear to be peaks of $\sigma \sim 120$ km s^{-1} on the northern and eastern edges of the galaxy, it is uncertain whether these represent real features or are simply noise in the extremely faint surface brightness edges of the galaxy.

The flat velocity field of this galaxy is particularly intriguing in light of the semi-analytic picture of galaxy formation in the early universe (e.g., Mo, Mau, & White 1998; Baugh 2006) in which (in brief) cold gas falls into collapsed dark halos, shock heats, radiatively cools to form a disk supported by residual angular momentum, and proceeds to form stars within this gaseous disk. Unless Q1623-BX453 happens to be inclined almost perfectly face-on to our line-of-sight,[10] the absence of a velocity gradient across the galaxy indicates that the kinematics of the ionized gas are not dominated by ordered rotation. Clearly, the simplest description of galaxy formation is incomplete.

[10]In order to mask a 100 km s^{-1} circular velocity within a 20 km s^{-1} uncertainty a galaxy must have inclination $i \lesssim 10^{\circ}$. This occurs in less than 2% of cases for a randomly distributed set of inclinations.

One variant on the basic rotating disk model which provides a reasonable explanation of some of the observed characteristics is that described by Noguchi et al. (1999) and Immeli et al. (2004; their models A/B), in which highly efficient cooling mechanisms lead to early fragmentation of the gas disk into self-gravitating clouds. These clouds are sufficiently massive that they spiral to the center of the galaxy via dynamical friction within a few dynamical times, largely dragging the existing stellar population along with the gas. Immeli et al. (2004) find that an intense burst of star formation typically occurs in the nuclear region of the galaxy when these massive gas clouds collide, typically peaking at around 100 $M_{\odot}$ yr^{-1} (over twice that expected for "traditional" star formation histories in galaxies with less efficient gas cooling mechanisms) and leading to the rapid formation of a stellar bulge. Such a theory may provide a natural explanation for Q1623-BX453, which we infer to have a large cold gas fraction, near-peak star formation rate density, and a sizeable stellar population. Alternatively, such characteristics may also be explained by the merger of two massive, gas-rich galaxies whose cold gas reservoirs are undergoing rapid star formation in the center of the new gravitational potential.

While it might appear surprising that a system with such violent dynamics should show so little evidence for kinematic structure, such systems are well-known in the local universe. Local ULIRGS may often have gas masses constituting the bulk of their dynamical mass (Solomon et al. 1997), fueling intense starbursts from the dense molecular gas in their cores. The common presence of multiple nuclei and tidal features (e.g., Sanders et al. 1988; Bushouse et al. 2002) suggests that these starbursts may commonly arise from the major merger of two gas-rich systems, and the ionized gas kinematics typically show star formation in gas flows rapidly forming stars in the center of the gravitational potential. The velocity fields of ULIRGS are typically dominated by strong, asymmetric gas flows (Colina et al. 2005), although the specific properties of these flows vary considerably from case to case. The velocity structure of Q1623-BX453 resembles in particular the kinematics of Mrk 273 and IRAS 15250+3609 (see Fig. 1 of Colina et al. 2005); these galaxies show no strong kinematic substructure in the brightest regions of Hα emission within $\sim 2-3$ kpc of the peak Hα emission despite relatively strong (~ 200 km s^{-1}) kinematic features in regions with Hα surface brightness lower by a factor ~ 5. It is an interesting speculation therefore whether deeper observations of Q1623-BX453 will reveal similar kinematic structure in regions of

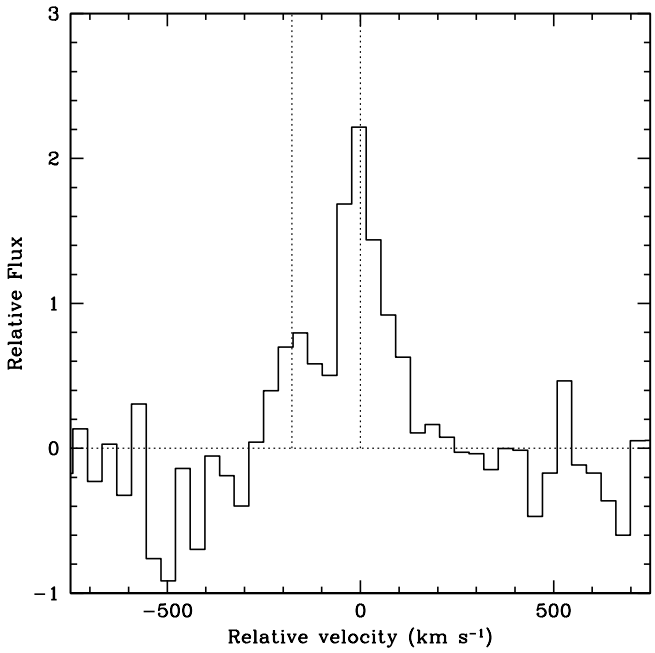

Figure 4.6 The spectrum of Q0449-BX93 is shown (in units of velocity relative to systemic) integrated over the region in which a secondary Hα emission component is observed blueward of the systemic emission. Vertical dashed lines denote the fiducial galaxy velocity (i.e., 0 km s^{-1}) and the location of the secondary emission peak after deblending. This peak occurs at a relative velocity of -177 $\pm$11 km s^{-1}.

lower surface brightness.

4.6.2 Q0449-BX93

While the integrated spectrum of Q0449-BX93 (Fig. 4.2) is dominated by a single emission spike defining the systemic redshift, the spectrum of the northwestern region of the galaxy shows a faint secondary emission peak blueshifted by $\sim$ 180 km s^{-1} from the systemic redshift (Fig. 4.6). Given that the FWHM of the primary emission component is $\sim$ 150 km s^{-1}, these two components in Figure 4.6 are blended, motivating the use of a 2-component Gaussian model in order to adequately characterize the emission line profile of the source.

Considering first the primary spectroscopic component, the velocity and dispersion structure of Q0449-BX93 (Fig. 4.1, middle-center and middle-right panels, respectively) are similar to those of Q1623-BX453, although there is mild evidence for velocity shear

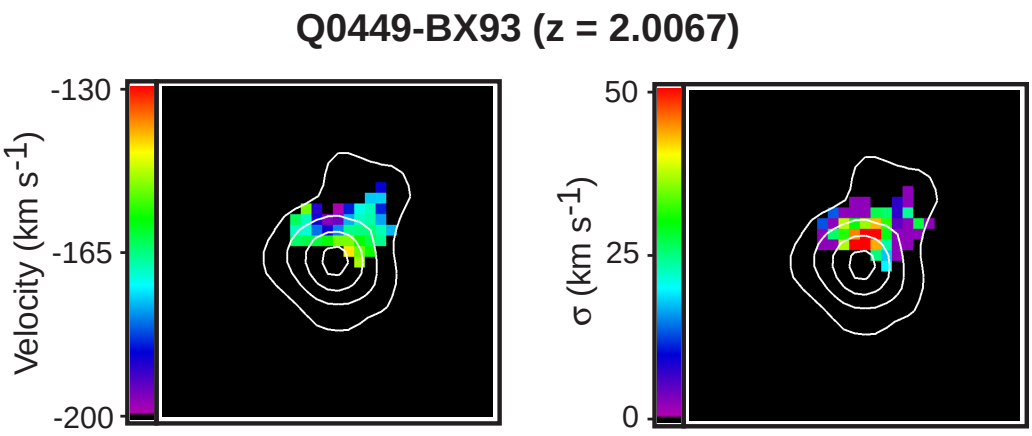

Figure 4.7 As Figure 4.1, shows the Hα emission line velocity and velocity dispersion maps for the faint blueshifted component of Q0449-BX93. Overlaid contours are Hα flux density.

along the northwest-southeast axis. The peak-to-peak amplitude of this velocity differential is only ~ 40 km s^{-1}, and therefore not highly significant with respect to our estimated velocity uncertainty of $10 - 20$ km s^{-1}. Even if this shear is genuine, it is not obvious that this implies a rotationally supported system. Assuming a simplistic model in which the circular velocity at the outer edge of the galaxy (1.23 kpc; see Table 4.2) is 40 km s^{-1} (i.e., with an extremely generous inclination correction to the observed 20 km s^{-1}), we obtain a dynamical mass of only $M_{\rm dyn} = 5 \times 10^8 M_\odot$, far less than the gas mass alone within the same region as derived from the Hα emission flux. That is, the observed shear is insufficient to provide dynamical support for the galaxy. As in the case of Q1623-BX453, the velocity dispersion is considerably larger ($\sigma = 72$ km s^{-1}) than the peak-to-peak velocity shear, suggesting the physical interpretation that Q0449-BX93 may also represent a merger-induced starburst or the bright central emission region of a gas-rich disk which has fragmented due to instability. While insufficient broadband data exist for Q0449-BX93 to be able to reliably fit stellar population models, estimates of the stellar mass using the mass-metallicity relation of Erb et al. (2006a) suggest that this galaxy is considerably less massive ($M_\star \lesssim 10^{10} M_\odot$) than Q1623-BX453. Coupled with its moderate extinction-corrected Hα star formation rate of 18 $M_\odot$ yr^{-1} (close to the average for the $z \sim 2$ galaxy sample, Erb et al. 2006b) Q0449-BX93 may be more representative of the general galaxy population.

Selecting next the Gaussian fits to the secondary emission line component, it is possible to create velocity and dispersion maps (Fig. 4.7) of this faint, kinematically distinct sub-

component (hereafter KDSC). To the limiting surface brightness of our study, the KDSC is marginally resolved over only a small ($\sim$ 200 $\times$ 150 mas, i.e., $\sim$ 1 kpc) part of the northwestern region of the galaxy comparable in size to the PSF ($\sim$ 150 mas). The kinematic offset of the KDSC from the systemic redshift is approximately constant across the region of emission and does not smoothly join to the kinematics of the primary component. While this may be simply due to the small size of the KDSC (across which we expect only $\sim 1-2$ spatially independent spectra), an additional interpretation (within the framework of a fragmenting disk model) may be that the KDSC represents one of multiple starbursting regions in the process of coalescing in the center of the galaxy for which we happen to see a kinematic differential. Alternatively, the KDSC may have initially begun star formation as a unit (i.e., satellite galaxy) distinct from the bright component of Q0449-BX93 which is only now merging with its host galaxy and is perhaps responsible for the observed burst of star formation. It is unfortunately beyond the scope of the current data to derive the parameters (e.g., relative mass) of such a scenario with any pretense of reliability.

4.6.3 DSF2237a-C2

The kinematic map of ionized gas in DSF2237a-C2 is notably different from those of Q1623-BX453 and Q0449-BX93, presenting clear evidence for resolved velocity shear along the morphological major axis at redshift $z > 3$. As illustrated in Figure 4.1 (bottom-center panel), the velocity of peak [O III] emission relative to the systemic redshift varies smoothly from about -70 to $+70$ km s^{-1} over a distance $\sim$ 2.5 kpc. An apparent ridge-line of high velocity (most evident in the southwest corner of the galaxy) presents some evidence for a flattening in the velocity curve, although this is far from robust. The velocity dispersion of individual regions within the galaxy is $\sigma \sim 79$ km s^{-1}; this is inflated by velocity shear in the integrated spectrum, giving $\sigma = 101$ km s^{-1}.

For comparison to previous studies we produce an "ideal" long-slit spectrum of DSF2237a-C2 by extracting spaxels along the major axis (PA 38°, see §4.3) using a 180 mas wide "slit" and plot the resulting velocity curve in Figure 4.8. The gradual trend of velocity across the galaxy is clear in this figure, along with the apparent flattening of the velocity curve in the outskirts of the galaxy. Although long-slit spectra were previously obtained with Keck-NIRSPEC observations (Pettini et al. 2001), no shear was observed by these authors,

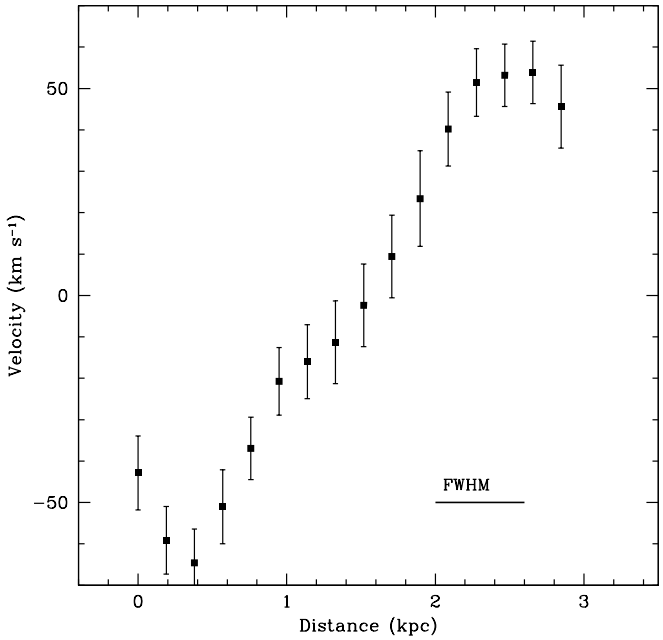

Figure 4.8 One-dimensional spectrum of DSF2237a-C2 (solid boxes) extracted from the OSIRIS data using an idealized "slit". Uncertainties are conservative estimates based on the number of spaxels (each with 20 km s^{-1} uncertainty) included in the spectrum at each position along the simulated slit. The solid line indicates the FWHM of the PSF. Note that this figure underestimates the turnover velocity apparent in 2-d data because spatial averaging across the simulated slit combines peak ridgeline velocities with lower velocities on either side of the "v"-shaped pattern (see Fig. 4.10).

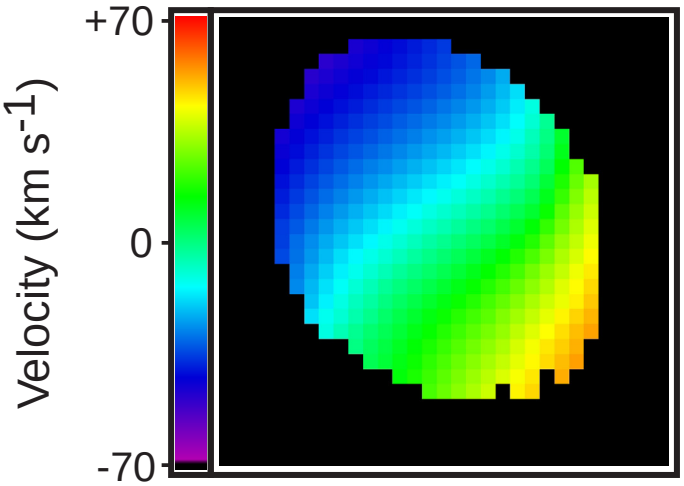

Figure 4.9 Velocity map recovered from OSIRIS observations of DSF2237a-C2 after convolution with a 0.5" PSF. The field of view is identical to that in Figure 4.1.

despite close alignment of the NIRSPEC slit (PA 55°) with the now-known shear axis (PA 38°). Given that the total peak-to-peak amplitude of the shear ($\sim$ 140 km s^{-1}) should be identifiable with the spectral resolution of NIRSPEC, we infer that DSF2237a-C2 represents a practical case-example of how seeing-limited studies may miss velocity structure on spatial scales smaller than that of the seeing halo. For comparison, in Figure 4.9 we plot the 2-d velocity map recovered from our OSIRIS observations of DSF2237a-C2 after introducing a 0.5" spatial Gaussian blur to roughly simulate the smearing effects of atmospheric seeing. While the overall semblance of shear is retained, the peak-to-peak observed amplitude of this shear is reduced by a factor ~ 2.[11] In concert with the lower spectral resolution of NIRSPEC (in the low-resolution mode used for the Pettini et al. 2001 observations) and slight offsets in slit placement and orientation from the optimal, it is easy to see why previous observations did not detect shear.

Adopting the inclination and position angle derived in §4.3 from the nebular morphology, we create an idealized thin-disk model (i.e., a rotating sheet) which reproduces the size and orientation of DSF2237a-C2 and adjust the asymptotic velocity and turnover radius as needed to match the observations shown in Figures 4.1 and 4.8. This model is characterized

[11] We note that Erb et al. (2004; their Fig. 3) reach a similar general conclusion based on observations of the galaxy Q1700-BX691, for which the apparent amplitude of velocity shear varied by at least a factor of ~ 2 depending on the quality of seeing.

by a radius of 0.21"=1.6 kpc and a deprojected asymptotic velocity of 93 km s^{-1}, implying a dynamical mass of $3.2 \times 10^9 M_\odot$ interior to 1.6 kpc.[12] We plot the velocity map of this model disk in Figure 4.10 (left panel), along with the velocity map recovered from this model using simulated OSIRIS observations which include convolution with the PSF and extraction of the high surface brightness pixels (right panel). We have not attempted to match every detail of the observed velocity map by fitting a more complex model, and some discrepancies remain (the blue-side velocities in particular are imperfectly matched by the simple model). While more complicated fitting routines could certainly be performed (and indeed have been for galaxies studied by Förster Schreiber et al. 2006 and other groups), the exacting fits of such models frequently belie the large uncertainties inherent to the observations. For example, the evidence for a turnover in the velocity curve of DSF2237a-C2 largely disappears with only slightly less careful data reduction, and the salient features of the model are almost indistinguishable from similar models for which the inclination of the disk to the line of sight differs by over 20°.

Given the uncertainties in such quantitative models, what may we conclude about this galaxy with some confidence? It is unlikely that the shear in DSF2237a-C2 is due primarily to a major merger because the velocity field shows a smooth, gradual transition rather than any sharp discontinuity as might be expected for two kinematically distinct components. In addition, the flux distribution is smooth and centrally concentrated; we do not detect multiple nuclei on scales more widely separated than $\sim$ 750 pc (the spatial resolution of the observation). Adopting the simplest interpretation — that the observed shear represents a rotating gaseous disk — it is worth asking whether the disk is stable against gravitational collapse. One traditional way of quantifying such stability is via the Toomre 'Q' parameter (Toomre 1964), which effectively assesses the mass of the disk with respect to the total gravitating mass of the system:

$$Q = \frac{V^2}{GM_{\rm disk}/r_{\rm disk}} = \frac{M_{\rm dyn}}{M_{\rm disk}}. \tag{4.5}$$

Typically, values of $Q < 1$ represent dynamically unstable systems for which the total

[12]This mass is slightly lower than that calculated on the basis of the velocity dispersion (and quoted in Table 4.3), reflecting in large part the uncertainty in the geometric prefactors used when converting from velocities to estimates of the dynamical mass.

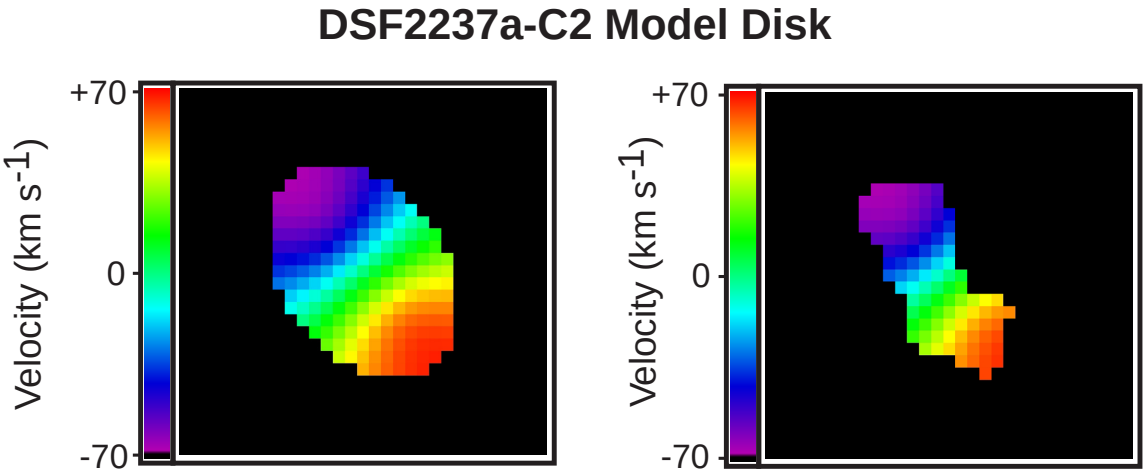

Figure 4.10 *Left panel:* Idealized rotating disk model for DSF2237a-C2. *Right panel:* Velocity field which might be observed with OSIRIS after convolution of the idealized disk model with the real PSF and selection of an appropriate distribution of bright "emission" regions. Compare to the actual recovered velocity map shown in Figure 4.1 (bottom center panel). The field of view is identical to that in Figure 4.1.

baryonic mass exceeds that which can be supported by the observed rotational velocity of the disk, indicating either that the disk itself is unstable or that non-rotational motions contribute a significant degree of support to the system. In contrast, values $Q > 1$ suggest that the observed baryonic component can be supported by the observed rotational motion alone, while $Q \sim 1$ represents the case of marginal stability.

Considering all of the uncertainties involved in determining the baryonic and dynamical masses, it is not possible to establish a single well-defined value for Q, although realistic estimates for various cases place a limit $Q < 1$. In the first case, we consider the ratio of masses within the radius probed by the OSIRIS detections ($r = 1.03$ kpc), for which $M_{\rm disk} = M_{\rm gas} + M_{\star} = 4.2 \times 10^{10} M_{\odot}$ in the limit that the entirety of the stellar mass lies within this radius, and $M_{\rm disk} = 1.3 \times 10^{10} M_{\odot}$ in the opposite limit for which there is negligible stellar mass within the central kpc. Similarly, we may elect to use estimates of the dynamical mass based on the central velocity dispersion ($M_{\rm dyn} = 5 \times 10^{9} M_{\odot}$) or the rotationally supported thin disk model ($M_{\rm dyn} = 3.2 \times 10^{9} M_{\odot}$). Combining these assorted estimates, we obtain a range of values $0.08 < Q < 0.38$. In the second case, we calculate the global Q value if we consider the mass within a much larger 10 kpc radius. At such

radii $M_{\rm disk} \geq 4.2 \times 10^{10} M_{\odot}$ (as the contribution of gas mass outside the central kiloparsec is unknown). The dynamical mass is even more uncertain:[13] inserting $r = 10$ kpc in Equation 4.4 we find $M_{\rm dyn} = 5 \times 10^{10} M_{\odot}$, while extending the disk model with asymptotic velocity 93 km s^{-1} out to such radii gives $M_{\rm dyn} = 2 \times 10^{10} M_{\odot}$. Adopting the highest physically motivated limit, we determine that $Q \leq 1.2$ within 10 kpc. In both cases (and most noticeably within the central kpc), the baryonic mass in the system outweighs what could be supported by a simple rotating disk model, highlighting the importance of the ionized gas velocity dispersion and indicating the improbability that star formation in DSF2237a-C2 occurs predominantly in a rotationally supported thin disk of gas (see also discussion by Förster Schreiber et al. 2006). Interestingly, the kinematics of this galaxy are quite similar to those of the $z = 1.4781$ galaxy Q2343-BM133 observed by Wright et al. (2007), which also had dispersion ($\sigma = 73 \pm 9$ km s^{-1}) comparable to its velocity shear (one-sided amplitude $v = 67$ km s^{-1}).

4.7 DISCUSSION

We have presented the results of a pilot study of the spatially resolved spectra of galaxies at redshift $z \sim 2 - 3$, demonstrating that the velocity structure of the ionized gas appears to be inconsistent with simple rotational support mechanisms. While there has been some effort to target galaxies with particularly high star formation rates to ensure detection in these early stages of the observational program, the Hα flux of one of our three galaxies (Q0449-BX93, whose star formation rate was predicted from UV photometry) is found to be quite close to the average (Erb et al. 2006b,c) of the $z \sim 2$ optically selected galaxy sample.

It is, nevertheless, more than a little challenging to attempt to draw general conclusions about the entire $z \sim 2 - 3$ galaxy population on the basis of only three galaxies, and therefore interesting to compare our results to integral-field velocity maps obtained recently by Förster Schreiber et al. (2006) for 14 rest-UV selected galaxies at redshift $z \sim 2$ drawn from the catalog of Erb et al. (2006b) and observed with SINFONI (Eisenhauer et al. 2003) on the VLT. While selection criteria varied, generally galaxies were known to be large and

[13] The dynamical mass may be particularly uncertain if the velocity curve continues rising out to larger radii instead of turning over at ~ 93 km s^{-1} as suggested by observations.

bright and (in many cases) known to exhibit considerable velocity shear or dispersion on the basis of previous long-slit observations (Erb et al. 2003, 2006b). Of these 14 galaxies, 9 show evidence of spatially resolved velocity gradients with peak-to-peak amplitude ranging from 40 to 410 km s^{-1} over $\sim$ 10 kpc. Certainly, systems with strong kinematic features appear to exist at $z \sim 2$, some of which may genuinely represent orbital velocities in massive rotating disks. Indeed, the mean stellar mass of the subsample with shear greater than 50 km s^{-1} is $9.4 \times 10^{10} M_{\odot}$ (based on the 6 galaxies for which $M_{\star}$ is given by Erb et al. 2006c), almost three times greater than the mean of the Erb et al. (2006c) sample ($< M_{\star} >= 3.6 \pm 0.4 \times 10^{10} M_{\odot}$). In contrast, the remaining galaxies in the Förster Schreiber et al. (2006) sample which do *not* show such large-scale shear have mean stellar mass $2.6 \times 10^{10} M_{\odot}$, similar to the masses of Q1623-BX453, Q0449-BX93, and DSF2237a-C2 ($M_{\star} = 3.1$, $\lesssim 1$, and $2.9 \times 10^{10} M_{\odot}$, respectively). Rather than representing rare cases (such as counter-rotating mergers; Förster Schreiber et al. 2006), the distribution of stellar masses suggests that these non-rotating galaxies may instead be quite common in the $z \sim 2$ population.

Unfortunately, it is difficult to directly compare the detailed kinematics of the Förster Schreiber et al. (2006) observations with our own since these data are seeing-limited with PSF FWHM $\sim$ 0.6" (therefore smearing kpc-scale kinematics like those discussed in this contribution beyond recognizability; see Fig. 4.9). A more detailed comparison may be made to the $z = 2.3834$ galaxy BzK-15504 observed by Genzel et al. (2006) using SINFONI in combination with natural guide-star adaptive optics for an angular resolution of 150 mas (i.e., comparable to the $\sim 110 - 150$ mas resolution of our target galaxies after smoothing). While this galaxy exhibits resolved velocity shear in the outer regions of the galaxy it is not well fit by a simple disk model within 3 kpc of the nucleus (i.e., approximately the region probed in our three target galaxies), which Genzel et al. (2006) postulate may be due to radial gas flows fueling the central AGN whose presence is inferred from rest-frame UV spectroscopy. One possibility may therefore be that disordered nuclear kinematics could generally join to more orderly shear at larger radii, although in our data we find evidence for neither AGN nor large-radius shear. Indeed, even in the circum-nuclear regions of BzK-15504 it is not obvious that a simple disk model provides an optimal description of the kinematics, since the line-of-sight velocity dispersion remains high at large radii

($\sigma \sim 60 - 100$ km s^{-1}, similar to the large values observed in DSF2237a-C2, and in Q2343-BM133 by Wright et al. 2007), and difference maps of the observed velocity field with the best-fitting exponential disk model show deviations of greater than 100 km s^{-1} (see discussion by Wright et al. 2007).

What, then, may we conclude about the kinematics of these early galaxies and their implications for galaxy formation? One common explanation for both the unusual kinematics and the high nuclear gas fraction is that these galaxies may represent major mergers of gas-rich galaxies. While this explanation may suffice for a few cases however (e.g., perhaps Q0449-BX93), it is unlikely (based on current cosmological models) that this is the general explanation for the $z \sim 2$ population, since the space density of such galaxies with similar physical properties is far too high. Alternatively, efficient gas cooling in the early universe could have led to high cold gas fractions in early-stage galactic disks which then fragmented due to self-gravity and collapsed to form a nuclear starburst (e.g., Immeli et al. 2004a). In both pictures, considerable kinematic structure should exist in these galaxies although (similar to local ULIRGS; Colina et al. 2005) the kinematics of the brightest nebular emission regions may be relatively featureless and quite variable in detail from system to system. However, it is unknown whether the lack of shear (or indeed any significant velocity structure beyond a high dispersion) persists to lower surface-brightness ionized gas at larger radii or if the kinematics of this gas are strong and disordered, ordered with dynamically cold orbital motion, or if indeed significant nebular line emission exists at all beyond the radii probed in this study. For one of the galaxies studied here (Q1623-BX453) previous deep long-slit spectroscopy (Erb et al. 2006c) could have detected any significant shear if it were present at larger radii (and the kinematic major axis was reasonably well-aligned with the slit), but found no evidence for such a trend.

What is perhaps most clear is that we do not yet understand the dynamical state of galaxies during this period in which they are forming the bulk of their stars. While traditional theories of galaxy formation posit that the majority of star formation should occur in rotationally supported gaseous disks, this does not appear to be in good agreement with the accumulating observational evidence, inviting the construction of new models of gas cooling which can explain the flat, dispersion-dominated kinematic features of galaxies in the young universe.

We would like to thank Andrew Benson and Juna Kollmeier for numerous helpful discussions, and Naveen Reddy for providing *Spitzer* photometry for Q1623-BX453. The authors also thank Randy Campbell, Al Conrad, David LeMignant, and Jim Lyke for their invaluable help obtaining the observations presented herein. D.R.L. and C.C.S. have been supported by grants AST-0606912 and AST-0307263 from the US National Science Foundation. Finally, we wish to extend thanks to those of Hawaiian ancestry on whose sacred mountain we are privileged to be guests.

Table 4.1. General Information

Name	RA (J2000)	DEC (J2000)	Observed	Time[a]	R_{TT}[b]	θ_{TT} [c]	θ_{seeing} [d]	θ_{PSF} [e]
Q1623-BX453	16:25:50.854	+26:49:31.28	Jun '06	2.5	15.1	32	0.4	75/110
Q0449-BX93	04:52:15.417	-16:40:56.88	Oct '06	4.5	15.8	51	0.6	125/150
DSF2237a-C2	22:40:08.298	+11:49:04.89	Jun '06	1.5	16.0	24	0.4	75/110

[a]Total observing time in hours.

[b]R-band magnitude of TT star for LGSAO correction.

[c]Angular separation (arcseconds) of TT star from target.

[d]Average K-band seeing (arcseconds) during observation.

[e]FWHM of the K-band PSF (mas) during on-axis TT star observation (before/after spatial smoothing respectively).

Table 4.2. OSIRIS Morphologies

Galaxy	I[a]	r[b]	G[c]	Ψ[d]
Q1623-BX453	9.5 ± 0.3	1.74 ± 0.03	0.33	1.48
Q0449-BX93	4.7 ± 0.6	1.23 ± 0.07	0.25	1.32
DSF2237a-C2	3.3 ± 0.3	1.03 ± 0.04	0.29	3.33

[a]Area of nebular emission (kpc^2). Uncertainty represents half the PSF correction.

[b]Radius of nebular emission (kpc). Uncertainty represents half the PSF correction.

[c]Gini.

[d]Multiplicity.

Table 4.3. Primary Spectroscopic Characteristics

Galaxy	$\lambda_{\rm neb}$[a]	$z_{\rm neb}$[b]	$z_{\rm abs}$[c]	$z_{{\rm Ly}\alpha}$[d]	$F_{{\rm H}\alpha}$[e]	$L_{{\rm H}\alpha}$[f]	$F_{[{\rm O\,III}]}$[e]	$L_{[{\rm O\,III}]}$[f]	$\sigma_{\rm v}$[g]	$v_{\rm c}$[h]	$M_{\rm dyn}$[i]
Q1623-BX453	20888.30	2.1820	2.1724	2.1838	23.1 ± 0.5	18.0 ± 0.4	...	...	92 ± 8	...	17 ± 2
Q0449-BX93	19737.80	2.0067	2.004	...	9.3 ± 0.3	4.1 ± 0.1	...	...	72 ± 12	...	7 ± 2
DSF2237a-C2	21621.80	3.3172	3.319	3.333	...	...	10.1 ± 0.5	22.0 ± 0.1	$101/79 \pm 15$	70 ± 10	5 ± 1

[a]Vacuum wavelength of peak emission in Angstroms.

[b]Vacuum redshift of nebular emission line: Hα for Q1623-BX453 and Q0449-BX93, [O III] λ5007 for DSF2237a-C2.

[c]Vacuum heliocentric redshift of rest-frame UV interstellar absorption lines.

[d]Vacuum heliocentric redshift of Lyα emission.

[e]Emission line flux in units of 10^{-17} erg s^{-1} cm^{-2}. Uncertainties quoted are based on random errors, global systematic uncertainty is $\sim 30\%$.

[f]Extinction-corrected emission line luminosity in units of 10^{42} erg s^{-1}. Uncertainties quoted are based on random errors, global systematic uncertainty is $\sim 30\%$.

[g]Velocity dispersion in units of km s^{-1}. Two values are given for DSF2237a-C2, the overall dispersion of the integrated spectrum and the median velocity dispersion in a given spaxel.

[h]Circular velocity in units of km s^{-1}.

[i]Dynamical mass in units of $10^9 M_\odot$.

Table 4.4. Secondary Spectroscopic Characteristics

Galaxy	$F_{[\mathrm{O\,III}]}(\lambda 4960)^{\mathrm{a}}$	$F_{[\mathrm{N\,II}]}(\lambda 6549)^{\mathrm{a}}$	$F_{[\mathrm{N\,II}]}(\lambda 6585)^{\mathrm{a}}$
Q1623-BX453	...	3.3 ± 0.4	7.7 ± 0.5
Q0449-BX93	...	< 1.1	< 1.1
DSF2237a-C2	2.5 ± 0.5	...	...

[a]Emission line flux in units of 10^{-17} erg s^{-1} cm^{-2}. Limits are 3σ limits. Uncertainties quoted are stochastic, global systematic uncertainty is $\sim 30\%$.

Table 4.5. Q1623-BX453 Regional Emission Line Characteristics

Region	$f_{\mathrm{H}\alpha}$	$f_{[\mathrm{NII}]\lambda 6549}$	$f_{[\mathrm{NII}]\lambda 6585}$	$N2^{\mathrm{a}}$
NE	14.8 ± 0.4	1.9 ± 0.4	5.1 ± 0.4	-0.46 ± 0.03
SW	6.6 ± 0.4	< 1.0	1.4 ± 0.4	-0.67 ± 0.09

[a]$N2 = \log([\mathrm{N\,II}]/\mathrm{H}\alpha)$.

Note. — Emission line flux in units of 10^{-17} erg s^{-1} cm^{-2}. Limits are 3 σ limits.

Table 4.6. Photometric Data and SED Model Parameters

Galaxy	U_n[a]	G[a]	$\mathcal{R}$[a]	J[b]	K_s[b]	$m_{3.6\mu}$[c]	$m_{4.5\mu}$[c]	$m_{5.8\mu}$[c]	$m_{8.0\mu}$[c]	$f_{24\mu}$[d]	M_*[e]	Age[f]	$E(B-V)$[g]
Q1623-BX453	24.85	23.86	23.38	21.41	19.76 [20.00]	21.38	21.37	21.33	21.92	195	3.1	404	0.245
Q0449-BX93	23.62	23.17	22.99	...	...	...	...	...	...	...	$\lesssim 1$[h]	...	0.125
DSF2237a-C2	...	24.68	23.55	22.08	20.53 [20.71]	...	...	...	...	...	2.9	255	0.175

[a] $U_n, G, \mathcal{R}$ magnitudes are AB.

[b] J, K_s magnitudes are Vega. Values in brackets for K_s magnitudes represent continuum magnitudes corrected for line emission.

[c] *Spitzer*-IRAC magnitudes (AB standard).

[d] *Spitzer*-MIPS 24 μ flux (μJy).

[e] Stellar mass ($10^{10} M_\odot$) from the best-fitting constant star formation model, using the Chabrier (2003) IMF. Typical uncertainty $< \sigma_{M_*}/M_* >= 0.4$.

[f] Stellar population age (Myr) from SED fitting, typical uncertainty $< \sigma_{\rm Age}/{\rm Age} >= 0.5$.

[g] $E(B-V)$ from the best-fit SED for Q1623-BX453 and DSF2237a-C2; $E(B-V)$ is estimated for Q0449-BX93 from the $G-\mathcal{R}$ color, assuming an age of 570 Myr.

[h] Estimated from the metallicity limit (§4.2) using the mass-metallicity relation of Erb et al. (2006c).

Table 4.7. Star Formation Rates and Gas Masses

Galaxy	$SFR_{H\alpha}$[a] Uncorrected	$SFR_{H\alpha}$[a] Corrected	SFR_{UV}[b] Uncorrected	SFR_{UV}[b] Corrected	SFR_{IR}[c]	SFR_{SED}[d]	Σ_{SFR}[e] Mean	Σ_{SFR}[e] Peak	M_{gas}[f]	μ[g]
Q1623-BX453	36	77	8	81	96	77	8	20	2.4	0.44
Q0449-BX93	12	18	12	39	...	...	4	7	0.7	$\gtrsim 0.41$
DSF2237a-C2	23	49	18	95	...	112	15	25	1.3	0.32

[a]Star formation rate ($M_\odot$ yr^{-1}) estimated from Hα flux. Typical uncertainty $< \sigma_{SFR}/SFR >= 0.3$.

[b]Star formation rate ($M_\odot$ yr^{-1}) estimated from rest-frame UV continuum flux.

[c]Star formation rate ($M_\odot$ yr^{-1}) estimated from rest-frame 8 μ flux.

[d]Star formation rate ($M_\odot$ yr^{-1}) derived from SED modeling. Typical uncertainty $< \sigma_{SFR}/SFR >= 0.6$.

[e]Star formation rate surface density ($M_\odot$ yr^{-1} kpc^{-2}).

[f]Molecular gas mass ($10^{10} M_\odot$). Typical uncertainty $< \sigma_M/M >= 0.2$.

[g]Gas fraction $\mu = M_{gas}/(M_{gas} + M_*)$. Typical uncertainty $< \sigma_\mu/\mu >= 0.35$.

Chapter 5

The Kiloparsec-Scale Kinematics of High-Redshift Star-Forming Galaxies*

David R. Law[a], Charles C. Steidel[a], Dawn K. Erb[b], James E. Larkin[c], Max Pettini[d], Alice E. Shapley[c], Shelley A. Wright[c]

[a]California Institute of Technology, MS 105–24, Pasadena, CA 91125

[b]Department of Physics, University of California, Santa Barbara, CA 93106-9530

[c]Department of Physics and Astronomy, University of California, Los Angeles, CA 90095

[d]Institute of Astronomy, Madingley Road, Cambridge CB3 0HA, UK

Abstract

We present the results of a spectroscopic survey of the kinematic structure of star-forming galaxies at redshift $z \sim 2-3$ using Keck/OSIRIS integral field spectroscopy. Our sample comprises 12 galaxies between redshifts $z = 2.0$ and 2.5 and one galaxy at $z \sim 3.3$ which are well detected in either Hα or [O III] emission, the morphology of which is consistent with *Hubble Space Telescope* rest-UV continuum images. Each of these observations was obtained in conjunction with the Keck laser guide star adaptive optics system, providing a typical angular resolution ~ 0.15" (approximately 1 kpc at the redshift of the target sample). All

*This chapter represents a preliminary draft of a manuscript currently being prepared for submission to *The Astrophysical Journal*.

of our target galaxies have high local velocity dispersions $\sim$ 70–80 km s^{-1}, while at most three show smoothly varying velocity gradients consistent with rotation. A strong case for merging can be made for two of the remaining ten galaxies. At least eight of our thirteen galaxies show negligible spatially resolved kinematic structure. Stellar population models suggest that galaxies with larger stellar mass are statistically more likely to show resolved velocity structure. We discuss these data in light of complementary kinematic surveys and postulate the importance of a massive stellar population in stabilizing gas-rich early galaxies against fragmentation.

5.1 INTRODUCTION

Galaxies are the discrete luminous building blocks of the visible universe, tracing the development of gravitational structures across cosmic ages. The earliest galaxies likely formed near the density peaks of the primordial power spectrum (e.g., Bardeen et al. 1986) which were able to decouple from the cosmic expansion at early times and form a burst of stars from the primordial gas. As time progressed however, these chaotic proto-galaxies gradually evolved, merging with their neighbors in newly collapsing dark matter halos, accreting greater quantities of gaseous fuel from a filamentary intergalactic medium, and polluting their environments with the metallic detritus of their early stellar generations. It is intermediate redshifts $z \sim 2-3$ at which these morphologically irregular, juvenile galaxies are thought to have formed the majority of the stellar mass which we observe in modern-day galaxies (Dickinson et al. 2003, Reddy et al. 2008). Through a combination of galaxy–galaxy mergers, rapid star formation, and secular evolution, these galaxies experienced a strong morphological transformation into the coherent structures of the Hubble sequence which have predominated since redshift $z \sim 1$ (Giavalisco et al. 1996; Papovich et al. 2005).

Despite our growing knowledge of the broad global characteristics of high redshift galaxies (e.g., Erb et al. 2006c; Reddy et al. 2006b; Papovich et al. 2006; Cowie et al. 2008; and references therein), our knowledge of their internal structure and dynamical evolution has been limited by their small angular size, typically $\lesssim$ 1 arcsecond. Such objects are generally not well resolved in the ground-based imaging and spectroscopy which form the backbone of our observational data, precluding us from determining (for instance) the triggering and regulation mechanisms of these starbursts, whether this star formation occurs in nuclear

or circum-nuclear regions of dynamically relaxed systems or as a result of tidal shocks induced by major mergers, and whether individual regions of star formation follow a global abundance pattern or exhibit strong variations in chemical enrichment. Each of these distinctions has appreciable implications for the evolution and development of structure and stellar populations within a given galaxy.

One of the most promising means to investigate these questions is studying the ionized gaseous structure surrounding bright star-forming regions produced by the flood of energetic photons from these young stars. Excited atoms in this gas lose energy predominantly by emission of strong rest-frame optical nebular emission lines (redshifted into the NIR for galaxies at $z \sim 2-3$) such as Hα, [O III], and [N II]. The relative strengths of these lines encodes information about the chemical composition of the gas and the shape of the ionizing spectrum, permitting deduction of the metallicity and star formation rates of the emission regions. These emission features are also intrinsically narrow and good kinematic tracers of the ionized gas.

Such efforts using slit (e.g., Erb et al. 2004, 2006b, 2006c at $z \sim 2$; Weiner et al. 2006 at $z \sim 1$) spectroscopy have met with qualified success and demonstrated that the kinematics of these galaxies are frequently inconsistent with rotation and simple rotationally supported gas disk models (although c.f. discussion by Förster-Schreiber et al. 2006). However, these studies are still limited by the small angular size of typical galaxies relative to the atmospheric seeing halo. Often there might be only 1–2 spatially independent samples across the face of a given galaxy, and additional uncertainty may be introduced by misalignment of the slit with the (*a priori*) unknown kinematic axis. It is usually unclear whether the observed dispersion is genuine or caused by the smearing out of unresolved kinematic structure.

The recent advent of adaptive optics (AO) on 10 m class telescopes has offered the opportunity to overcome the limitations previously imposed by atmospheric turbulence by rapidly correcting the distorted wavefront using deformable mirrors. Paired with integral-field spectroscopy, it is possible to obtain diagnostic spectra of spatial regions resolved on scales of order 100 milliarcseconds (mas), corresponding to roughly 1 kpc at redshift $z \sim 2-3$. The data provide an empirical answer to whether the velocity fields of galaxies in the early universe are predominantly represented by virialized disk-like systems, major mergers, or some other dynamical structure, and whether the resulting star formation is

uniform in its properties across a given galaxy or exhibits regional variation on kiloparsec scales. Early results from such programs have recently been presented by (for example) Genzel et al. (2006), Law et al. (2007a), and Wright et al. (2007), although the total number of individual galaxies observed remains extremely small. In this contribution we quadruple the 3-galaxy sample of Law et al. (2007a), presenting spatially resolved laser guide star adaptive optics (LGSAO) spectroscopy of an additional 10 galaxies located between at $2.0 \lesssim z \lesssim 2.5$ which permits us to draw broader conclusions about the typical characteristics of the galaxy population.

This paper is structured as follows. In §5.2 we describe our sample selection, observational technique, and data reduction algorithms. We describe the ionized gas morphologies of the target galaxies in §5.3 and the integrated source spectra in §5.4. We review stellar populations models of these galaxies in §5.5, and *Hubble Space Telescope* (*HST*) continuum morphologies in §5.6. We describe kinematic results for the overall galaxy sample and for individual galaxies in §5.7 – 5.7.13. In §5.8 we discuss our ability to fit kinematic models to these data, concluding with a discussion of our results in the context of the larger galaxy population in §5.9. Readers interested in the broader implications of the results rather than the specific details may be most interested in §5.9. We assume a standard ΛCDM cosmology based on 3-year WMAP data (Spergel et al. 2007) in which $H_0 = 73.2$ km s^{-1} Mpc^{-1}, $\Omega_{\rm m} = 0.238$, and $\Omega_\Lambda = 0.762$.

5.2 OBSERVATIONS

5.2.1 Target Selection

Recent years have witnessed a veritable explosion of methods for locating galaxies in the redshift range $z \sim 2-3$. These methods include optical ($U_nG\mathcal{R}$) color selection (e.g., Steidel et al. 2003, 2004), near-IR BzK (Daddi et al. 2004) and $J-K$ (Franx et al. 2003) color selection, and selection by sub-mm flux density (Smail et al. 1997). Of these samples, those arising from the optical color selection are perhaps the most well studied. As described in detail by Adelberger et al. (2004), the $U_nG\mathcal{R}$ selection technique represents a generalized version of the Lyman-break technique employed by Steidel et al. (2003) to identify rapidly star-forming galaxies at redshift $z \sim 3$ on the basis of their strong 912 Å Lyman break as it

is redshifted into the U_n bandpass. In this paper, we focus primarily on this $U_nG\mathcal{R}$ sample, and particularly on those galaxies in the redshift range $z = 1.8 - 2.6$ (i.e., the "BX" galaxy sample of Steidel et al. 2004). As detailed by Adelberger et al. (2004), this redshift range is dictated by the selection function of the color selection criteria. While initial identification of these galaxies was based upon photometric preselection, extensive rest-UV spectroscopic follow-up work has derived precise redshifts for all galaxies in our primary target sample.

The galaxies selected in this manner are typically bright and actively forming stars, with mean extinction-corrected star formation rates (SFR) $\sim 30\,M_\odot$ yr^{-1} (see discussion by Erb et al. 2006b), and SFR surface densities similar to those observed in local starburst galaxies (e.g., Kennicutt et al. 1998b). The resulting winds from supernovae and massive stars drive energetic (~ 500 km s^{-1}; Steidel et al. *in prep.*) large-scale outflows into the IGM surrounding these galaxies, creating the ubiquitous blueshifted interstellar absorption features observed in rest-frame UV spectra (e.g., Shapley et al. 2003). With the aid of deep near-IR (e.g., Erb et al. 2006c) and mid-IR (e.g., Shapley et al. 2005b; Papovich et al. 2006; Reddy et al. 2006b; and references therein) photometry, stellar population modeling suggests that galaxies at $z \sim 2 - 3$ span a broad range of stellar masses and evolutionary states.

Individual galaxies selected for study were drawn from this pool of available targets subject to a variety of criteria. Some targets were deliberately selected for their young stellar population ages and correspondingly small stellar masses, some for their old ages and large stellar masses, and some for other reasons including interesting rest-UV morphologies, strong detections in Hα narrowband surveys (Q1700-BX710 and Q1700-BX763), unusual spectral features, or previous acquisition of long-slit kinematic data. Given the relatively shallow OSIRIS sensitivity limit (SFR$_{\rm lim} \sim 0.1\,M_\odot$ yr^{-1} kpc^{-2} in 2 hours of integration; Law et al. 2007a) however, the most general criterion applied is preferential selection of those galaxies which previous long-slit spectroscopy (Erb et al. 2006b) indicate have nebular line fluxes (Hα or [O III]) $\gtrsim 5 \times 10^{-17}$ erg s^{-1} cm^{-2}. We discuss the nature of our final target sample further in §5.9.1.

Additional physical constraints require that there be a suitably bright ($R \lesssim 17$) star within ~ 60" of each galaxy to use as a tip-tilt (TT) reference for the LGSAO system (this constraint is particularly stringent in the Hubble Deep Field), and that the wavelength of

peak line emission falls between the strong spectroscopically unresolved night-sky OH emission features that dominate the near-IR background, and avoids wavelengths of extremely strong telluric absorption bands. The first of these constraints will not systematically bias the resulting sample given its reliance only on the distribution of nearby stars, while the second imposes blackout "windows" in redshift space, the most significant of which spans $z \sim 2.6 - 2.9$. The final target sample is listed in Table 6.1 (in order of field RA and catalog name) and includes 23 galaxies in 9 distinct fields selected for their proximity to high-redshift QSOs and international survey fields and distributed widely across the sky. Table 6.1 includes a complete list of all galaxies observed with OSIRIS, both successfully and unsuccessfully, in order to better characterize our final sample selection. Of the 23 galaxies observed, we have obtained significant detections of 13 galaxies distributed among 7 fields.

5.2.2 Observational Technique

Observations were performed using the OSIRIS (Larkin et al. 2006) integral-field unit (IFU) in combination with the Keck II LGSAO system during 5 observing runs between June 2006 and June 2008. The majority of these sessions followed the basic observing scheme described in §2.1 of Law et al. (2007a, Chp. 4), to which we refer the reader for a detailed description of our approach. In brief, we observed the target galaxies in narrowband filters (bandwidth ~ 0.1 μm) corresponding to the wavelength of either Hα or [O III] nebular line emission using the 50 mas lenslet sampling scale with 900 second individual exposures. Given the redshift range of most of our target galaxies ($z \sim 2 - 2.5$), Hα is redshifted into the K-band and we opt to observe this emission line for most cases since the quality of the LGSAO correction increases towards longer wavelengths. At wavelengths longer than ~ 2.26 μm, however, the thermal continuum background seen by OSIRIS becomes comparable to that of individual OH lines, significantly degrading the quality of the observational data. We therefore observe [O III] emission in either the H or K bands as necessary for some galaxies (e.g., Q1623-BX543 and DSF2237a-C2). The observational configuration for each of our target galaxies is detailed in Table 6.1.

During a typical observing sequence we first acquire a brief (~ 60 second) IFU observation of our TT reference star in order to center our pointing and provide both a point-spread

function (PSF) and flux calibration reference. We then offset to the target galaxy using precise offsets measured from deep ($\sim$ 10 hour) ground-based optical and/or *HST* Advanced Camera for Surveys (ACS) imaging data (where available). Each galaxy was observed in pairs of 900 second exposures dithered on-IFU, typically by $\sim 1.4''$ along the long axis of the IFU. This on-IFU dithering maximizes our on-source integration time but effectively halves our useful field of view to $\sim$ 1" $\times$ 1.5" (still significantly larger than the typical galaxy, see discussion by Law et al. 2007b). Each exposure pair was then repeated with small $\sim$ 50 mas dithers for a total of between 1800 and 12600 seconds of integration. These total integration times were dictated by both observational availability and a desire to obtain sufficient integration to ensure a high-quality detection of the target galaxies. It was typically possible to detect a given galaxy in the difference of two 900 second exposures, allowing us to determine in real-time the targets which were likely to produce the best detections given sufficient integration. With some notable exceptions (e.g., Q2343-BX389) deeper integrations were not performed if a given galaxy was undetected within 1–2 hours. When possible, we obtained another observation of the TT reference star at the end of our integration on a given galaxy in order to bracket the science observations and measure any changes in the PSF.

5.2.3 Data Reduction

Data reduction was performed using a combination of OSIRIS pipeline and custom IDL routines described in §2.2 of Law et al. (2007a) which were used to produce a composite, three-dimensional data cube (consisting of two image dimensions and one spectral dimension) for each target galaxy. Given the multi-year baseline over which our observations were obtained, the reduction algorithms have evolved slightly over time to reflect the changing performance characteristics of OSIRIS. The most significant modification was introduced for data obtained in June 2007 (i.e., for our observation of galaxies HDF-BX1564 and Q1623-BX502) which were affected by an imperfect focus within OSIRIS resulting in a PSF which was slightly elongated along an axis oriented at roughly 45 degrees to the lenslets. This was corrected by implementing a CLEAN-type algorithm (e.g., Högbom et al. 1974) to deconvolve the elongated PSF and replace it with a typical circular PSF.

As described by Law et al. (2007a) the composite data cube for each galaxy is sub-

sampled by a factor of two in each spatial dimension and convolved with a Gaussian kernel in order to increase the signal-to-noise ratio (SNR) of the spectrum in each spatial pixel (spaxel). The width of this Gaussian is chosen as required to produce the highest quality smoothed data cube without significantly inflating the PSF delivered by the LGSAO system. We typically choose a FWHM of 80 mas, although for some extremely low surface brightness galaxies (e.g., HDF-BX1564) we increase this smoothing to $\sim$ 200 mas in order to boost the spectral emission signature at the cost of spatial resolution. The effective width of the PSF before and after this smoothing is given for all galaxies in Table 6.1. For one galaxy (HDF-BX1564) we also smooth the spectrum of each lenslet in the wavelength domain by a kernel of FWHM 5 Å to better pick the faint emission feature from the surrounding noise. We note that while these algorithms may be largely automated, it can nonetheless be time-consuming to carefully optimize the individual reductions to produce the highest-possible quality final products. A significant fraction of our galaxies have therefore not yet been reduced to their final form, given that the data were obtained very recently (June 2008). Preliminary analyses for these galaxies have been provided where possible, although these should be regarded as subject to future revision.

5.3 IONIZED GAS MORPHOLOGIES

We produce maps of the ionized gas morphology of the target galaxies by collapsing the data cube about the spectral channels corresponding to the nebular emission wavelength. We adopt the formalism of Law et al. (2007b) to describe the parameters G (gini, a measure of the curve of growth of the light distribution) and Ψ (multiplicity, a measure of the number of components of the light distribution) using a segmentation map composed of those spaxels whose spectra fulfill the criteria described in §5.7. We also measure the luminous area I, the radius r corrected for the PSF as described in Law et al. (2007a), and the distance d_{2c} between individual components for galaxies which have spatially separated pieces. These measurements are given in Table 5.2, although we note that these are subject to change by adopting a significantly revised formalism in the near future. We therefore defer comprehensive analysis of these morphological data to a later date.

5.4 GLOBAL SPECTRA

Raw composite spectra of each galaxy (shown in Fig. 5.1) were obtained by summing the data from all spaxels in a box encompassing the nebular emission morphology into a single spectrum, thereby sampling both bright and faint emission regions. This raw spectrum is calibrated using a telluric transmission spectrum of the night sky to normalize the throughput as a function of wavelength. This calibration spectrum is determined directly from observations of bright telluric standard stars for data obtained in June 2008, and from the OSIRIS + Keck LGSAO system + atmospheric models of Law et al. (2006) for all previous data (see detailed discussion in Law et al. *in prep* [Ch. 6]). The absolute flux calibration of this corrected spectrum is determined by matching our TT star observations to IR photometry given in the 2MASS Point-Source-Catalog. We note that this method differs from that adopted by Law et al. (2007a), and slight differences from their calibration are to be expected.

The largest single uncertainty in the flux calibration of these data arises from the nature of the LGSAO PSF, which can vary both with isoplanatic angle and (rapidly) with time, resulting in significant fluctuations in the percentage of total light residing in the AO-corrected core of the PSF. These fluctuations are poorly understood, and correlated primarily with mid-level atmospheric turbulence not well corrected by the AO system. Given the uncertainties in our bootstrapped flux calibration, we estimate that the systematic flux uncertainty for any given source is $\sim 30\%$ (see also discussions in Law et al. 2007a and *in prep* [Ch. 6]).

In Table 5.3 we list the [O III], Hα, and [N II] emission line fluxes of each galaxy, with uncertainties based on the noise present in the underlying spectra after subtraction of Gaussian models for the identifiable emission components.[1] Total nebular emission line luminosity is calculated from these fluxes assuming a standard cosmological model and correcting for extinction derived from stellar population models (§5.5). We also list the central wavelength of the primary emission feature in each spectrum (i.e., Hα or [O III]). Systemic redshifts are determined by dividing these wavelengths by the rest-frame vacuum wavelengths of Hα and [O III] (i.e., 6564.614 Å and 5008.239 Å, respectively) and correcting for the heliocentric motion of the Earth at the date, time, and direction of observation

[1] Residual features at the emission line wavelength (after subtraction of the Gaussian model profile) are generally indistinguishable from the noise in the rest of the spectrum.

(calculated using the IRAF *rvcorrect* algorithm). We do not include fainter [N II] or [O III] λ4960 in our systemic redshift calculations as these features are generally too weak to improve the redshift fit.

5.5 STELLAR POPULATION MODELING

Using our extensive ground-based $U_n G\mathcal{R}JK_s$ and *Spitzer* IRAC and MIPS photometry in the selected survey fields it is possible to construct stellar population models for the spectral energy distributions of the target galaxies. The modeling procedure is described in detail by Shapley et al. (2005a). In brief, we use Bruzual and Charlot (2003) models with a constant star formation rate (unless otherwise specified), solar metallicity, and a Chabrier (2003) initial mass function (IMF). These models are overplotted on our photometric data in Figure 5.2 and the individual values for SFR, stellar mass (M_*), population age, and extinction are tabulated in Table 5.4. As discussed by previous authors (e.g., Shapley et al. 2001, 2005a; Papovich et al. 2001) the stellar mass is the best constrained of these parameters as it relies primarily on the normalization of the model fit rather than its precise shape. We note that previous modeling of many of these galaxies has been presented by Erb et al. (2006c) and Shapley et al. (2001); the previous models are updated here for consistency and to add *Spitzer* IRAC data where available.

5.6 REST-UV CONTINUUM MORPHOLOGIES

Four of our target galaxies (HDF-BX1564, Q1700-BX490, Q1700-BX710, and Q1700-BX763) lie in fields for which deep optical imaging data has been obtained with *HST*-ACS. These data in the HDF and Q1700 fields have been described by Law et al. (2007b) and Peter et al. (2007), respectively. The comparative morphologies of *HST*-ACS (i.e., tracing the rest-UV continuum) and OSIRIS Hα emission are shown in Figure 5.3. There is generally a good correspondence between the respective morphologies, subject to the roughly 5 times shallower limiting SFR surface density probed by the OSIRIS data (Law et al. 2007a). Given the extremely narrow field of view of OSIRIS however, there are no absolute reference points to which we can calibrate the coordinate solution as our offsets from the TT acquisition star are only reliable to within $\sim$ 100 mas (i.e., comparable to our PSF)

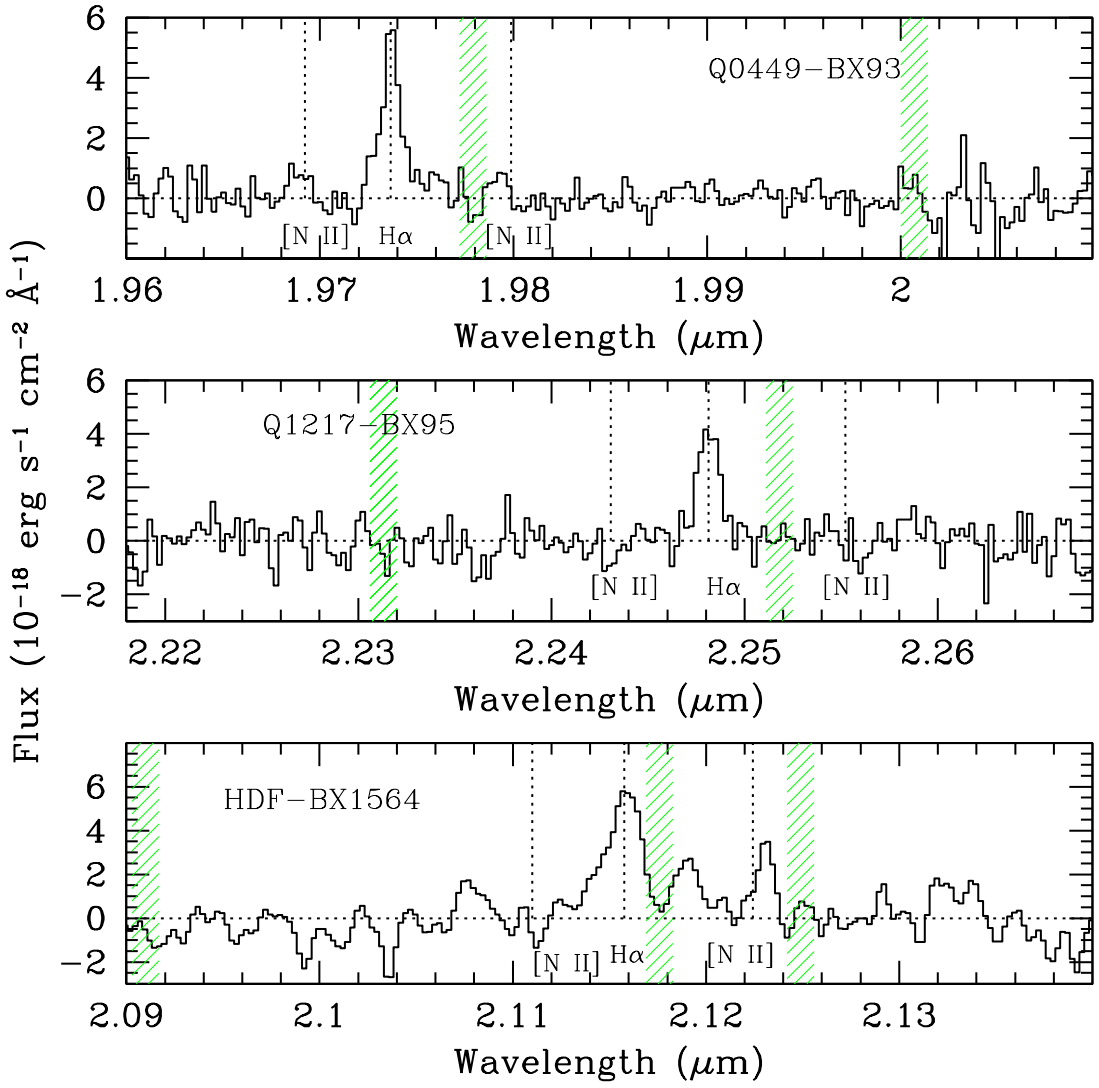

Figure 5.1 OSIRIS spectra integrated over the spatial extent of each galaxy. Vertical dashed lines indicate the fiducial locations of nebular emission lines based on the systemic redshift. Hashed green regions indicate the locations of strong atmospheric OH emission features which can give rise to strong residuals in the spectra.

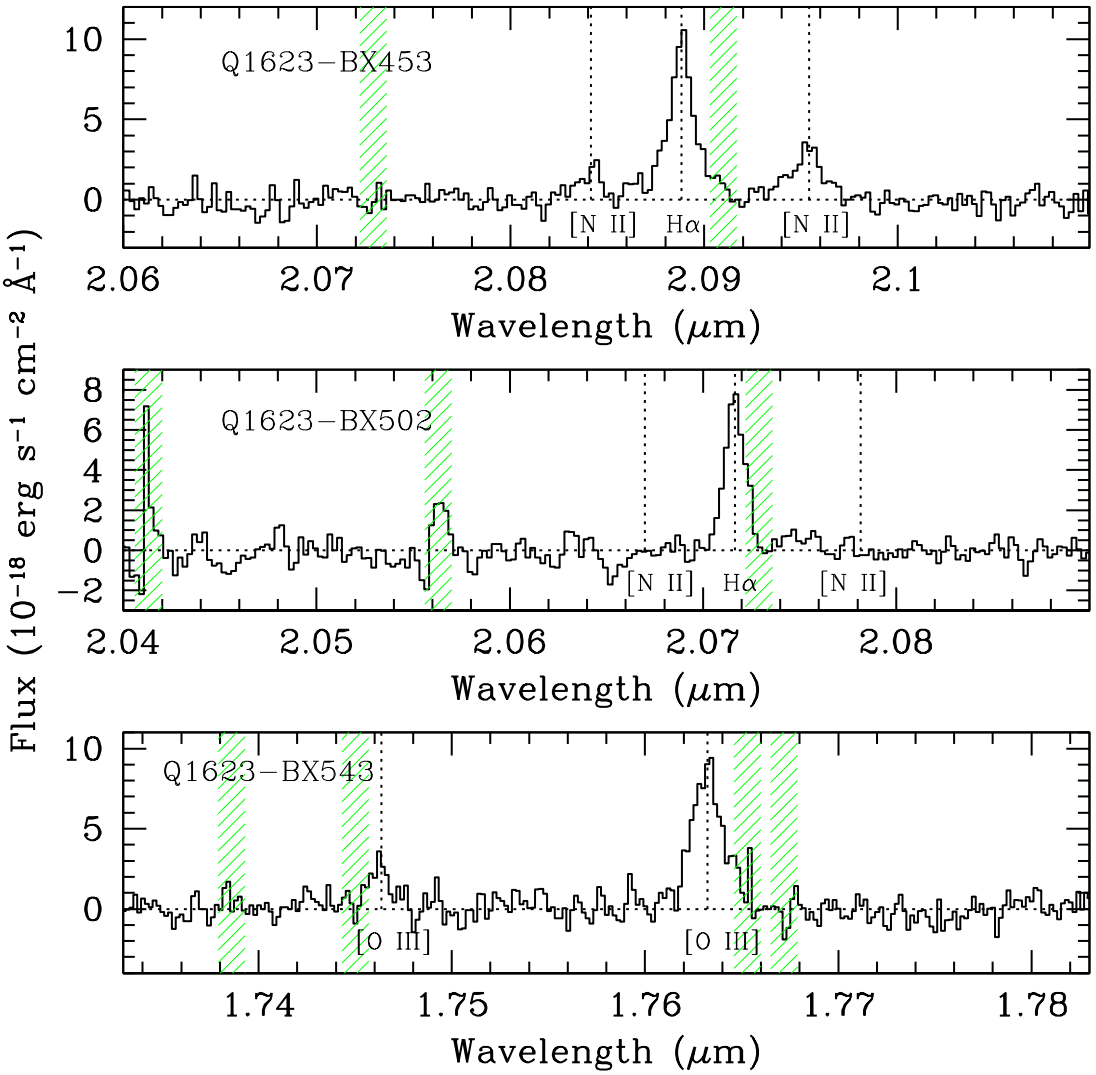

Figure 5.1 (continued)

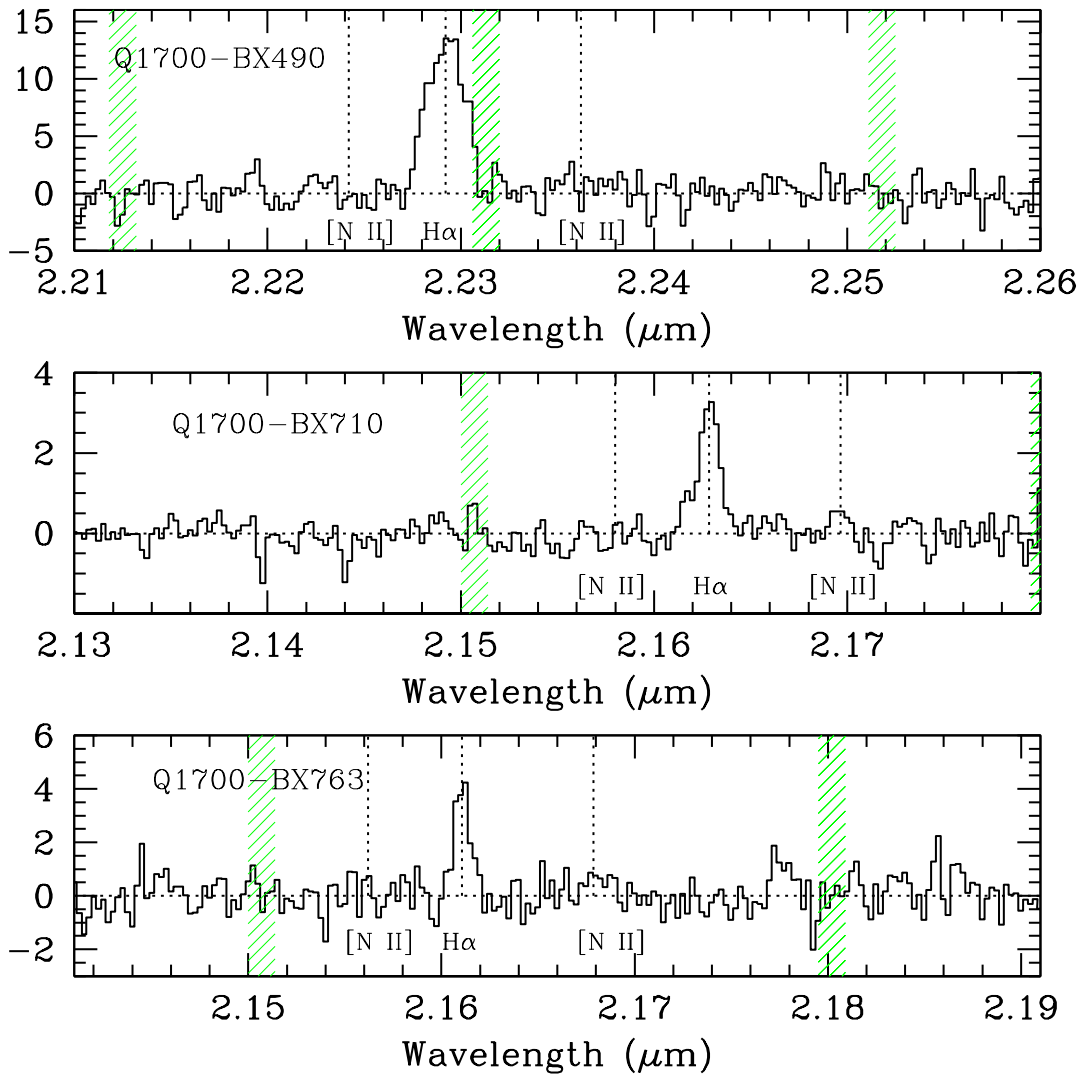

Figure 5.1 (continued)

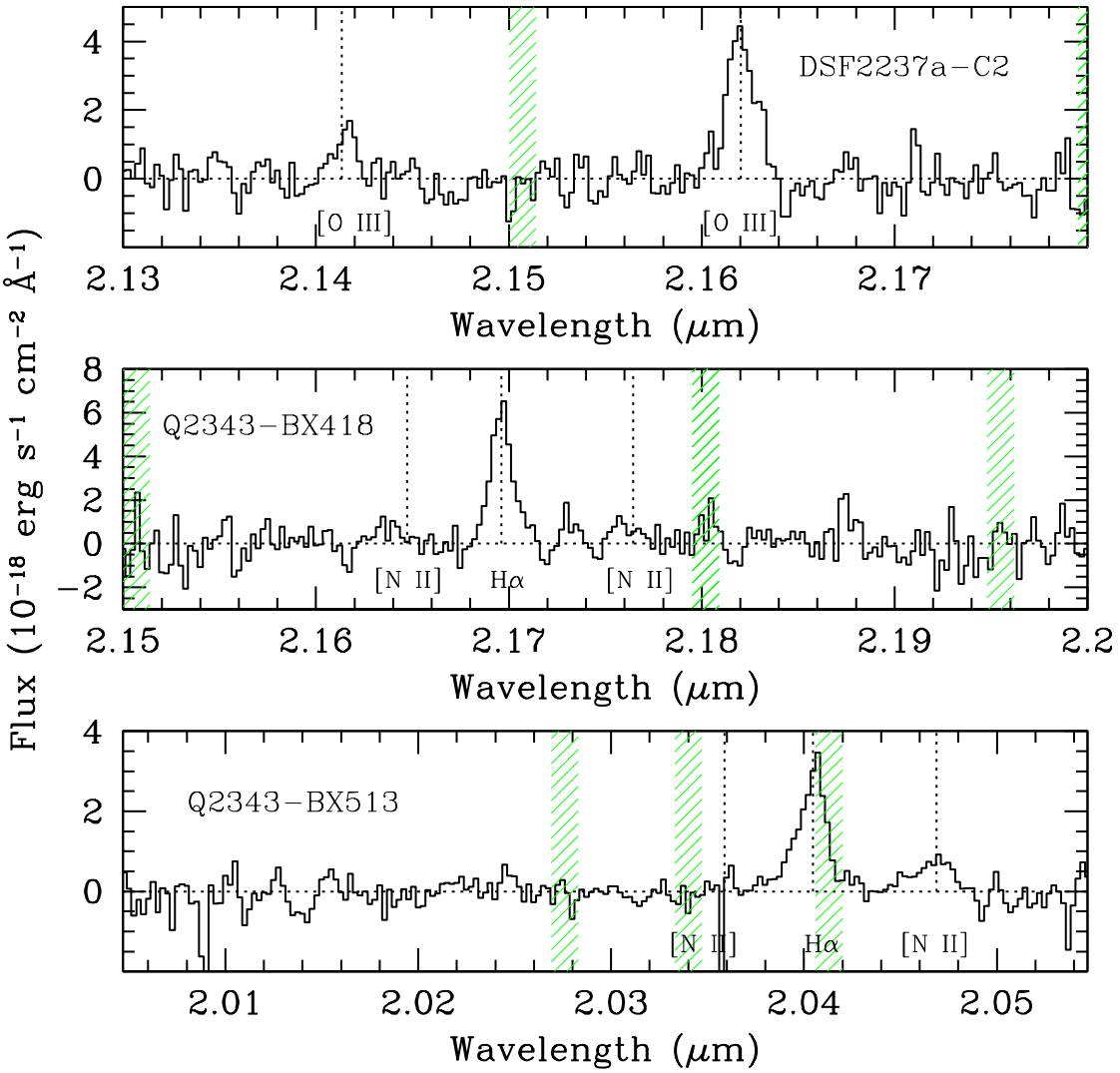

Figure 5.1 (continued)

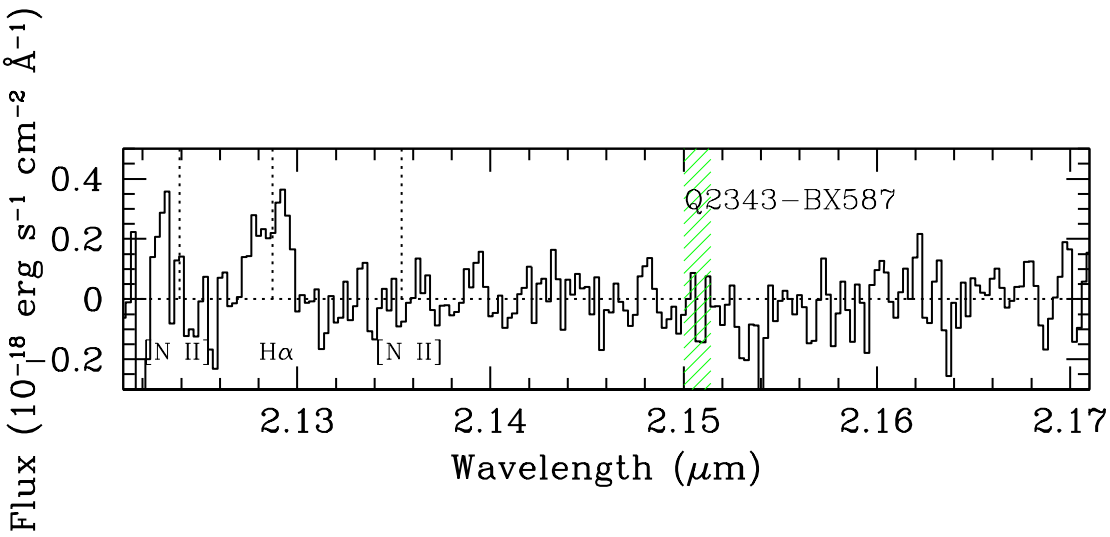

Figure 5.1 (continued)

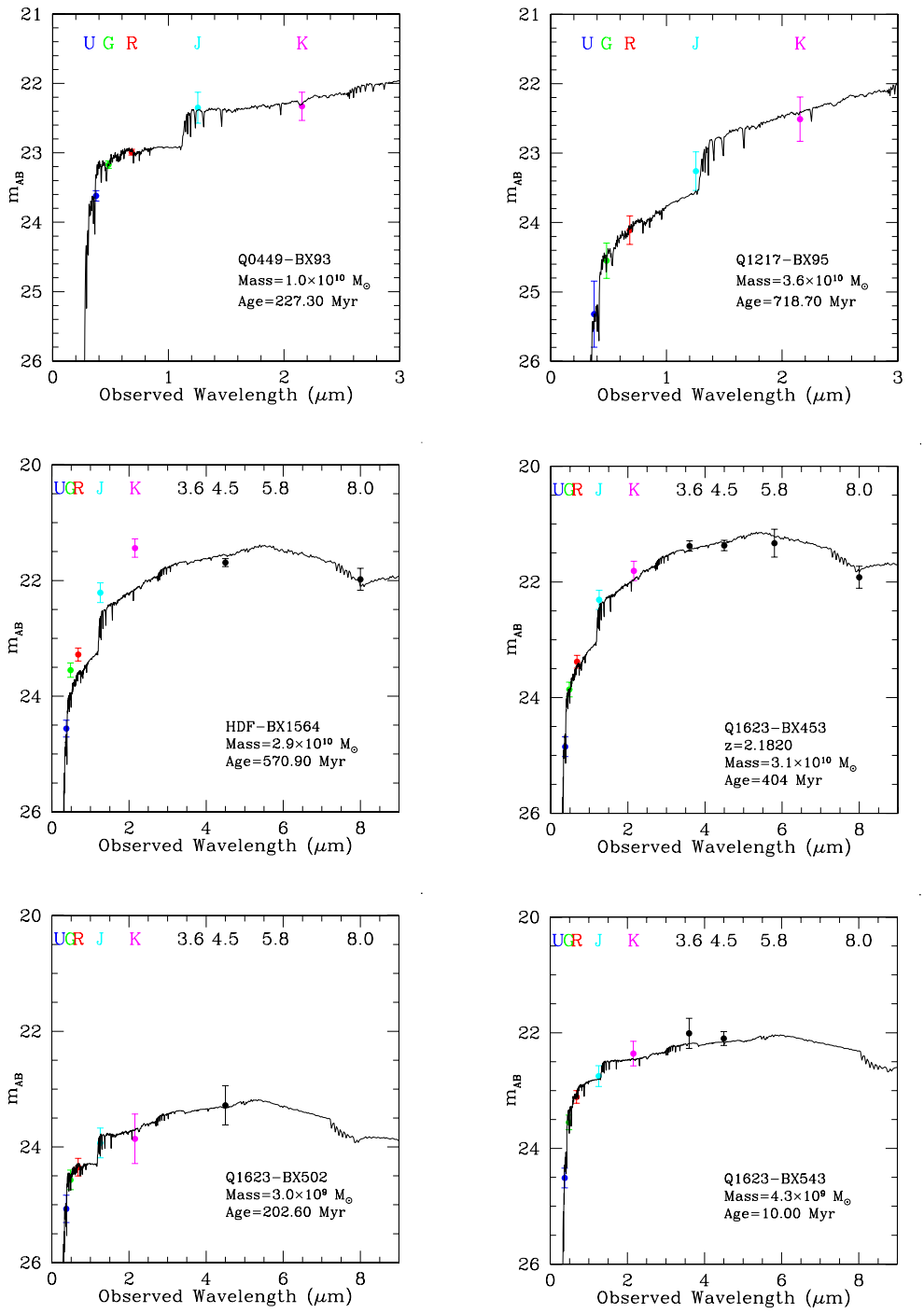

Figure 5.2 The best-fit constant star formation (CSF) model (solid black line) is overplotted against the observed spectral energy distribution for our target galaxies. Colored points represent ground-based optical and near-IR photometry; black points are based on *Spitzer*-IRAC observations. Values given for stellar mass and population age represent the values derived from the best-fit CSF model using a Chabrier (2003) IMF; typical uncertainties are given in Table 5.4.

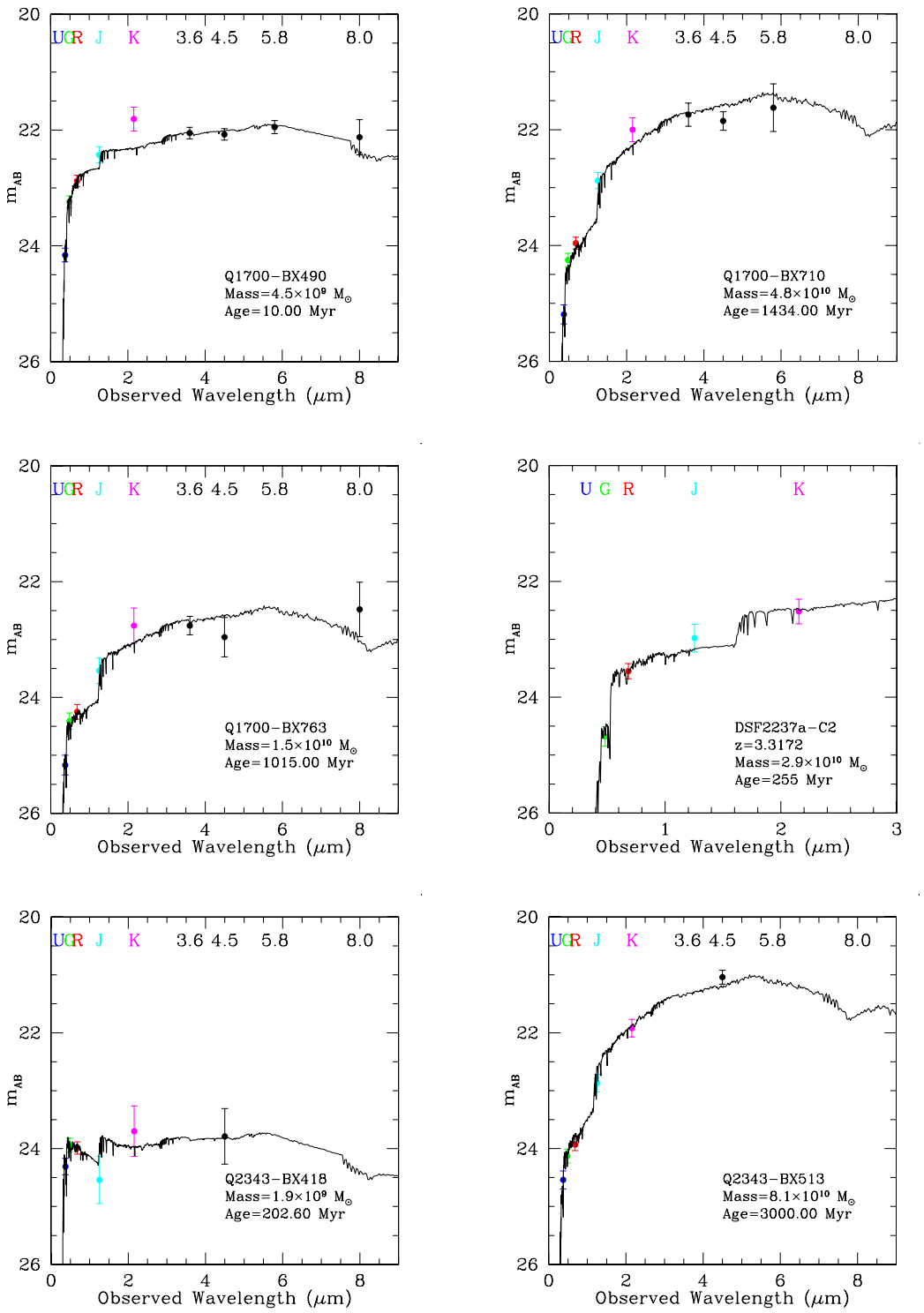

Figure 5.2 (continued)

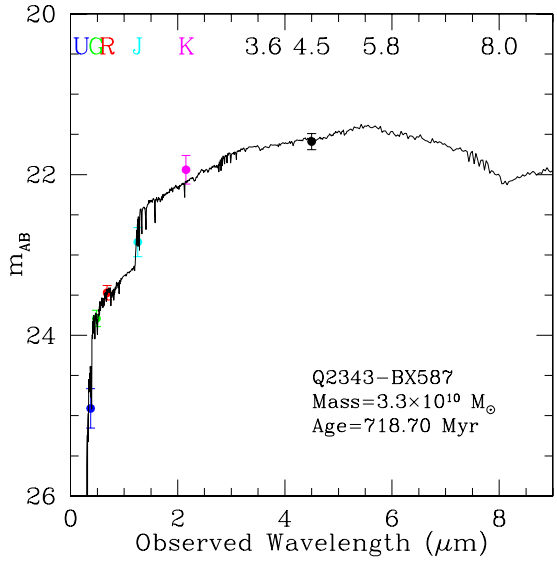

Figure 5.2 (continued)

due to various uncertainties resulting from (for example) measuring the coordinates of the TT star, global uncertainties in the coordinate solution of the ground based imaging data, and the unknown proper motion of the TT stars. It is not possible therefore to reliably align the *HST*-ACS and OSIRIS images to high precision using absolute coordinates alone. Instead, we align the *HST*-ACS contours shown in Figure 5.3 with the OSIRIS maps "by-eye", sliding the contours freely until they appear to best overlap the Hα flux data. While this prohibits us from investigating small discrepancies between the locations of peak emission in isolated single sources, we are still able to compare spatial differences for sources with multiple emission features and the relative shapes of the various emission profiles. We discuss the specific features of individual galaxies in §5.7.1 – 5.7.13 below.

5.7 KINEMATIC DATA

Kinematic data were extracted from the oversampled composite data cubes using custom IDL routines to fit Gaussian profiles to the spectrum in each spaxel, thereby obtaining spatial "maps" of the emission line flux, wavelength centroid, and spectral FWHM across each galaxy. This information is converted to maps of the emission line SNR, velocity relative to the systemic redshift, and velocity dispersion (with the instrumental $R \sim 3600$

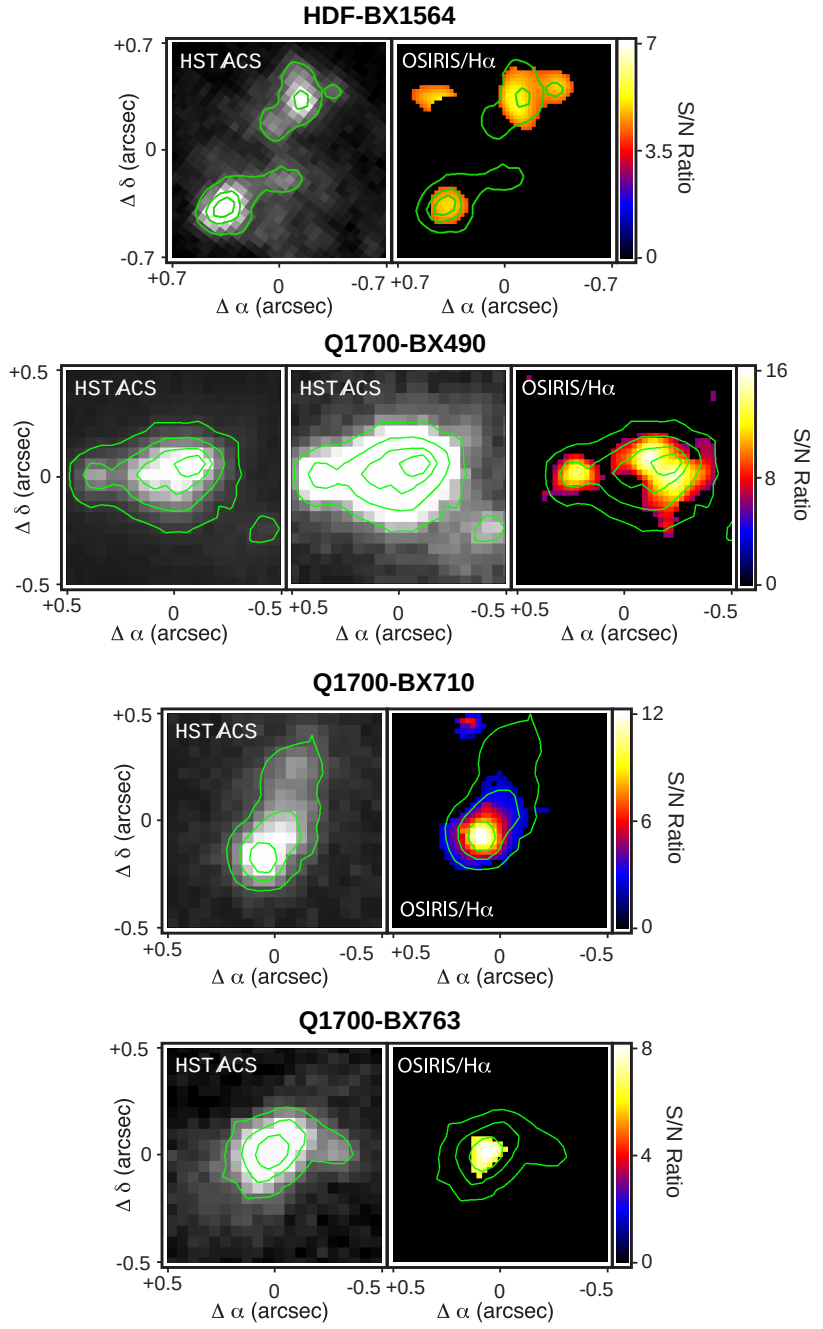

Figure 5.3 Comparison between HST/ACS rest-UV continuum morphologies and OSIRIS Hα morphologies. In each panel the contours are linear in rest-UV flux density. Two copies of the HST/ACS map for Q1700-BX490 are included with different greyscale stretches to best emphasize both bright and extended faint structure. Note that the field of view for Q1700-BX710 is slightly larger than that in Figure 5.3 in order to completely encompass the extended *HST*-ACS morphology.

profile subtracted off in quadrature), as shown in Figure 5.4. As discussed by Law et al. (2007a), the quality of these maps is improved considerably by the spatial convolution described in §5.2.3, and by applying additional constraints on the fitted profiles. These specific constraints vary for each galaxy, but generally force the algorithm to mask out any fits deviating from the systemic redshift by over 300 km s^{-1}, for which the velocity dispersion σ is either less than instrumental or greater than 300 km s^{-1}, or for which the SNR of the fit is < 6. These rejection criteria were individually verified by direct inspection to ensure that no genuine, significant structures were omitted from the final maps.

The velocity dispersion may be quantified in two ways. An estimate of the *overall* velocity dispersion of a galaxy may be obtained by simply fitting a single Gaussian profile to the spatially integrated spectrum of the entire galaxy (i.e., those spectra shown in Fig. 5.1). We call this quantity $\sigma_{\rm net}$, values for which are tabulated in Table 5.5. This measurement does not distinguish between spatially resolved velocity gradients and small-scale motions within a given resolution element. While $\sigma_{\rm net}$ can provide a reasonable estimate of the dynamical mass, it is not an optimal means of determining the intrinsic local dispersion of the ionized gas. In the case of HDF-BX1564 for instance (which has two components well separated in both physical space and velocity), stacking the spectra of components at two slightly different redshifts inflates the apparent velocity dispersion of the gas in the system. We therefore also calculate $\sigma_{\rm mean}$ which is the flux-weighted mean of the velocity dispersions measured in each individual spaxel (i.e., as shown in the right-hand panels of Figure 5.4). This quantity effectively suppresses spatially resolved velocity gradients, and provides a more accurate probe of the local velocity dispersion at an average point within the galaxy, albeit with residual uncertainty introduced by the finite PSF and sampling of the observational data. In the three cases where the galaxy is composed of distinct pieces (HDF-BX1564, Q1623-BX543, Q1700-BX490) we calculate values for $\sigma_{\rm mean}$ in each of the pieces in Table 5.5 and also measure the kinematic offset $v_{\rm 2c}$ between the pieces. As expected, values of $\sigma_{\rm mean}$ given in Table 5.5 are generally consistent with or slightly less than $\sigma_{\rm net}$.

As illustrated by Figure 5.4, the majority of galaxies are dominated by galaxy-wide velocity dispersions ($< \sigma_{\rm mean} >= 78 \pm 17$ km s^{-1}, $< \sigma_{\rm net} >= 91 \pm 20$ km s^{-1}) rather than by large scale, spatially resolved velocity structures. Indeed, while four of our 13 galaxies

show some evidence for velocity shear, only three of these may be consistent with rotation, while an additional three are composed of kinematically and spatially distinct fragments. We note that, given the absence of resolved velocity structure in the majority of our galaxies, the globally high velocity dispersions cannot be explained by the convolution of resolved features with the observational PSF (as, for instance, in the $z \sim 1.5$ sample of Wright et al. 2008). We discuss the velocity maps and characteristics of each galaxy individually below, noting that three of these galaxies obtained early in our survey (Q0449-BX93, Q1623-BX453, and DSF2237a-C2) were previously presented by Law et al. (2007a). These are included here for completeness and comparison to the rest of the sample, although we refer the reader to this earlier contribution for a more thorough discussion of these sources.

5.7.1 Q0449-BX93

As detailed in Law et al. (2007a) this galaxy is dominated by a single emission component at the systemic redshift with a faint secondary component offset by ~ 150 km s^{-1} ~ 1 kpc to the NE. This faint secondary feature may represent a kinematically distinct star-forming region or small galaxy in the process of merging with the the brighter system. The central peak shows mild evidence for a velocity gradient (~ 20 km s^{-1} peak amplitude) which is only marginally significant compared to our estimated velocity uncertainty of $\sim$ 10–20 km s^{-1}. The possible shear is substantially smaller than the mean local velocity dispersion ($\sigma_{\rm mean} = 56 \pm 20$ km s^{-1}) and, if genuine, is unlikely to represent the primary means of dynamical support of the system. We refer the reader to Law et al. (2007a) for further discussion.

5.7.2 Q1217-BX95

This galaxy was observed recently in June 2008 and appears to be qualitatively similar to Q0449-BX93. Similar mild evidence exists for coherent velocity shear across the source, again with peak amplitude ~ 20 km s^{-1} that is significantly smaller than the local velocity dispersion ($\sigma \sim 60$ km s^{-1}). This compact source has a FWHM only slightly larger than the TT reference star PSF and shows no evidence of extended structure.

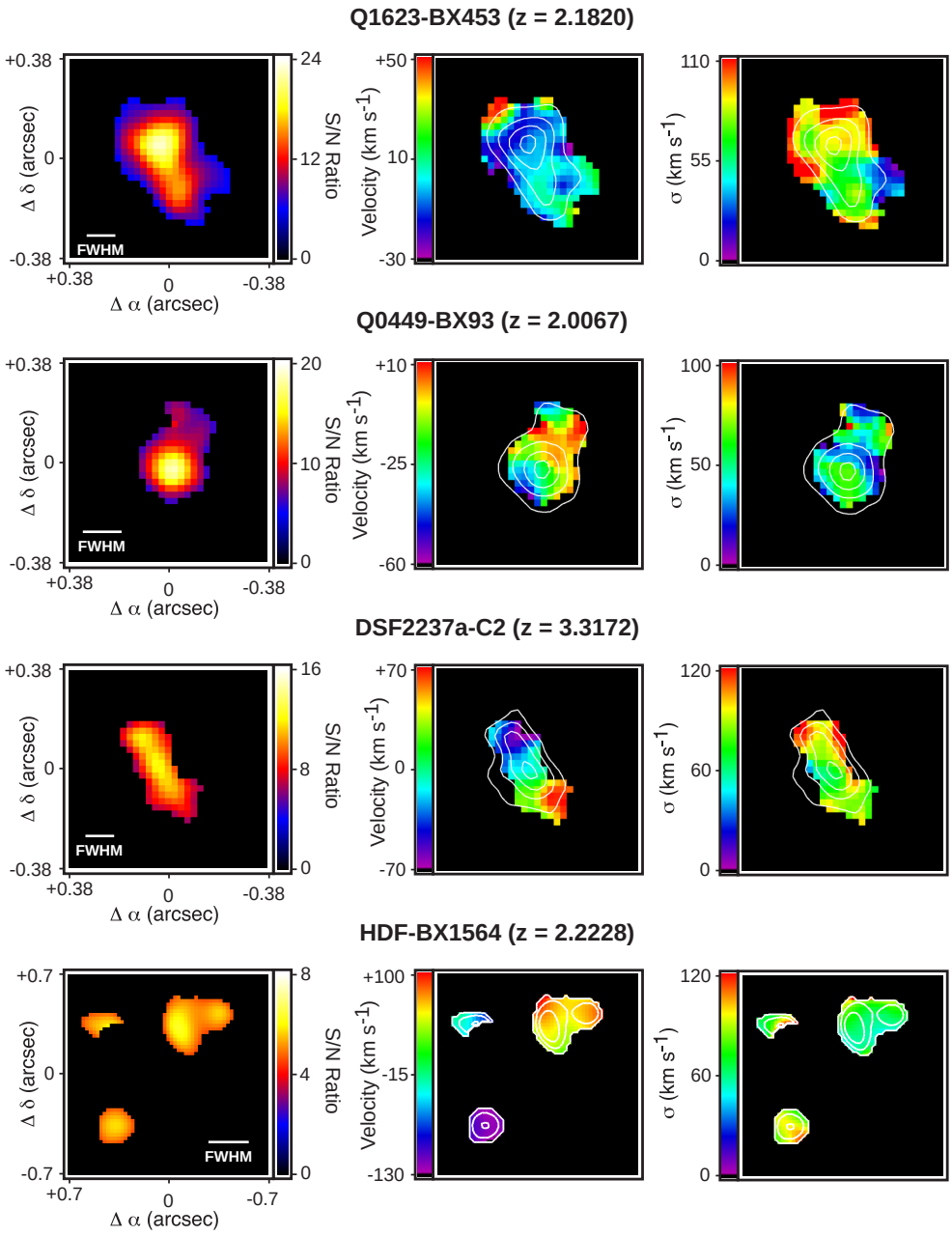

Figure 5.4 OSIRIS maps of nebular emission ([O III] for Q1623-BX543 and DSF2237a-C2, Hα for all others). Panels represent (left to right) S/N ratio, relative velocity, and velocity dispersion maps. Individual pixels measure 25 mas, the total field of view varies from target to target as needed to contain the emission line regions. The FWHM of the PSF (after smoothing described in §5.2.3) is indicated in the left-hand panel for each galaxy. Contours represent linear intervals in line flux density. All images are presented in a standard orientation with North up, and East left.

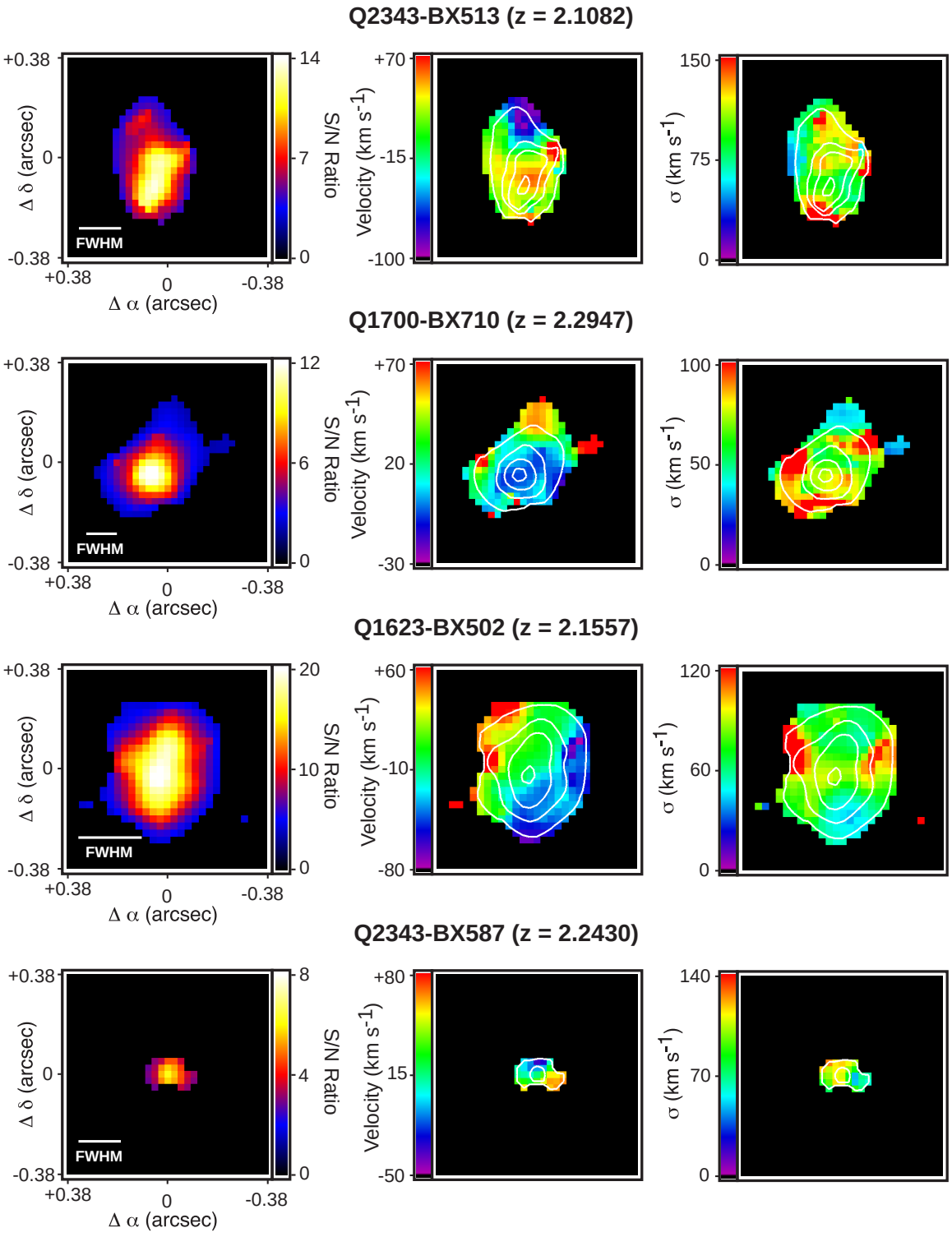

Figure 5.4 (continued)

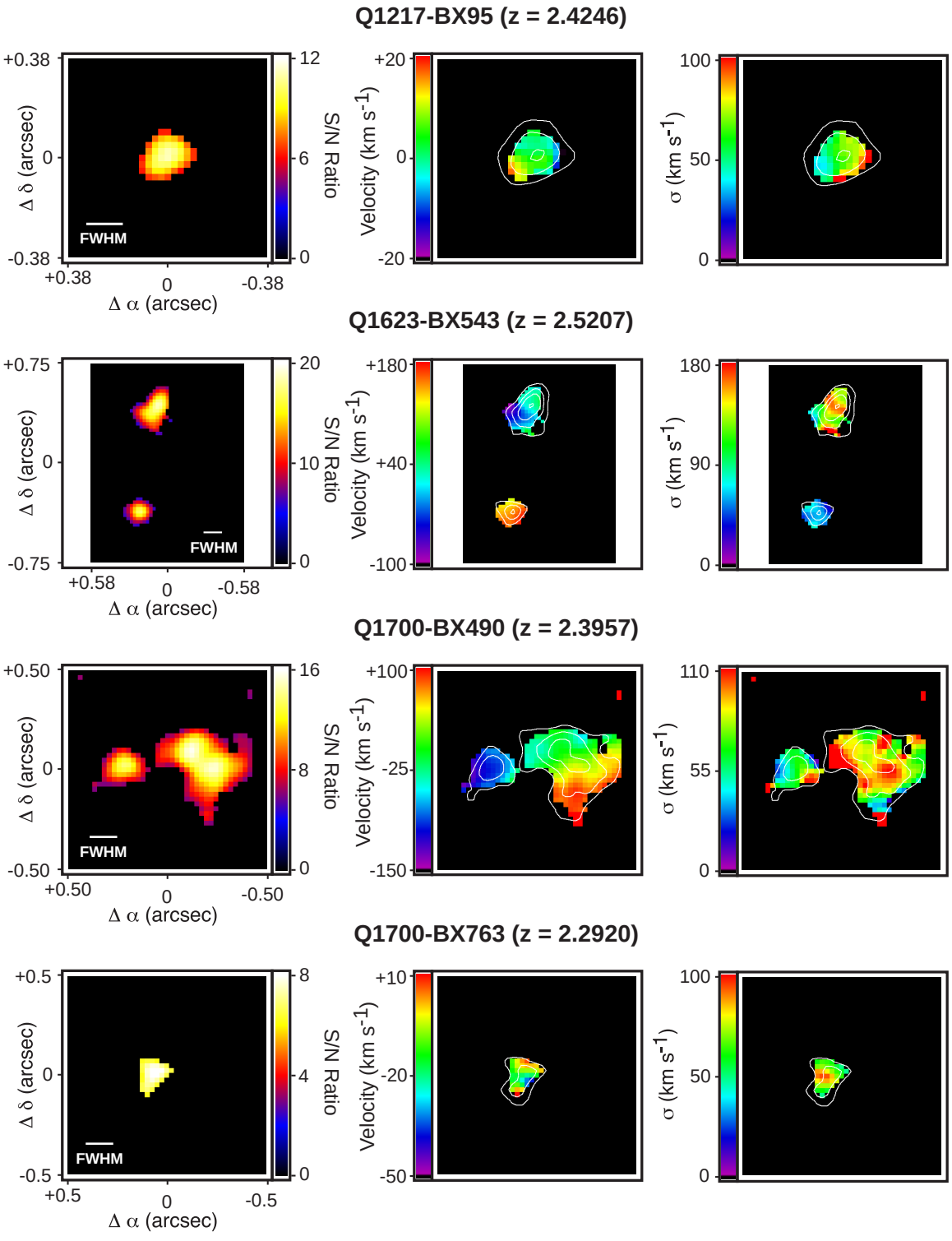

Figure 5.4 (continued)

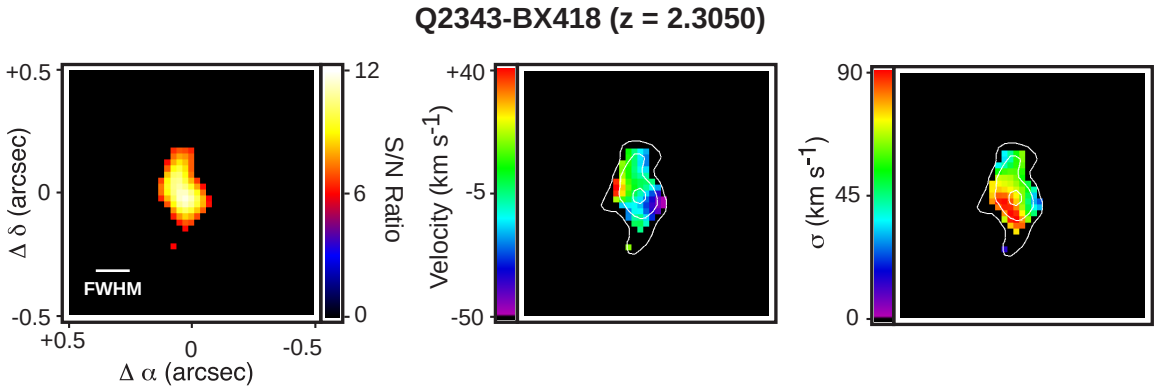

Figure 5.4 (continued)

5.7.3 HDF-BX1564

HDF-BX1564 is among the least well detected of our galaxies, and required heavy spatial and spectral smoothing of the composite data cube in order to successfully discern emission features. This extensive processing has the unfortunate consequence of increasing our effective PSF to ~ 0.3", comparable in size to the two primary emission regions (NW and SE) comprising the source. While we are therefore unable to reliably determine the kinematics *within* these regions, it is possible to determine that the NW and SE features are separated by $v_{2c} \sim 171$ km s^{-1} and $d_{2c} = 7$ kpc. Assuming an average inclination of $i = 57°$ (see 5.A.1) this implies a dynamical mass $M_{\rm dyn} \sim 1.2 \times 10^{11} M_{\odot}$. The local velocity dispersion of the NW and SE features is 60 ± 13 and 86 ± 8 km s^{-1}, respectively, consistent with the typical values observed for the rest of the galaxy sample. We note that the larger, NW feature has the smaller $\sigma_{\rm mean}$ of the two, contrary to what might be expected if both possessed velocity structure with a similar gradient.

While a third component is apparent in Figure 5.4, based on analysis of typical noise patterns within the composite data cube we believe that this feature is probably not real. Supporting this explanation is the rest-UV morphology, which we show for comparison in Figure 5.3. Both the NW and SE features have counterparts in the ACS imaging data, while the questionable NE feature does not. The *HST*-ACS imaging data also suggests an overall level of faint diffuse emission in the field of view, particularly in the form of spurs reaching between the bright knots. Given that the bright knots themselves are only barely detected (i.e., at a S/N ratio of ~ 5) in the OSIRIS data, it is not surprising that we do

not detect these spurs, even if they have Hα counterparts.

Such a multiple component morphology with emission "tails" and a large kinematic offset is immediately suggestive of a major merger, in which we may be viewing these two galaxies shortly before their coalescence. Should this be the case, it is perhaps slightly surprising that this galaxy is not forming stars particularly rapidly ($\mathrm{SFR}_{\mathrm{H}\alpha} = 20 M_{\odot}$ yr^{-1}), suggesting that there has not been a significant quantity of tidally triggered star formation.

In this case, additional insight may be gained from previous Keck/NIRSPEC long-slit spectroscopy obtained in June 2004 (see Erb et al. 2006b) with a 0.76" wide slit aligned along the axis between the two major components to within 5°. As illustrated in Figure 5.5, both primary components are well detected in the spectrum with similar kinematic and spatial separation as in the OSIRIS data. In this considerably deeper observation there is evidence for nebular emission extending between the two components, the SE feature has a spatial FWHM of 1.1" and reaches all of the way to the NW component, whose 0.6" FWHM is more closely matched to the PSF of these seeing-limited data. Notably, there is no gradual shift in wavelength along the axis connecting the two, but instead a sharp transition upon reaching the NW feature, suggesting that the emitting material between the two components does not partake in a smoothly varying velocity curve and bolstering the case for a major merger interpretation of this galaxy.

5.7.4 Q1623-BX453

As discussed in Law et al. (2007a) this galaxy is one of the best examples of the "typical" kinematics observed in our sample, with spatially well-resolved nebular emission exhibiting negligible velocity differentials across the entirety of the galaxy and kinematically dominated by a local velocity dispersion $\sigma_{\mathrm{mean}} = 78 \pm 23$ km s^{-1}. While there is a single region of slightly higher velocity at the NE end of the galaxy, it is unclear if this feature is genuine given its small size ($\sim$ 3 pixels) and extremely low SNR $\sim$ 4. Q1623-BX453 is inferred to have a large cold gas fraction, a sizeable stellar population, and high SFR surface density with a correspondingly large outflow velocity $\sim$ 900 km s^{-1} as traced by rest-UV spectroscopy of interstellar absorption lines. Given the large quantity of cold gas in this galaxy, it is particularly intriguing that there is no evidence for the rotational structure in which such gas is traditionally supposed to reside.

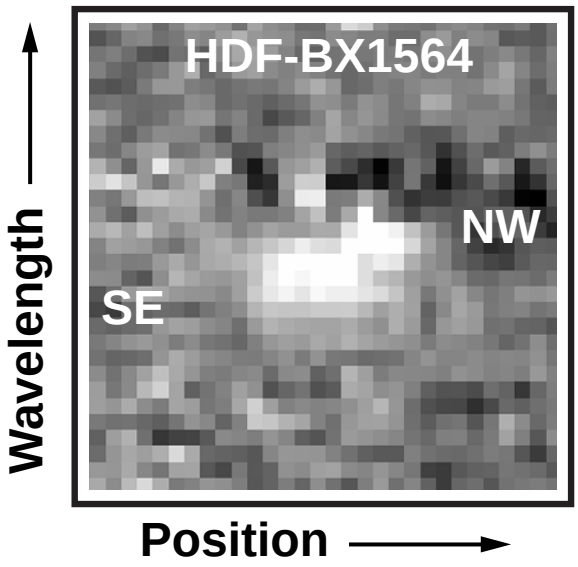

Figure 5.5 Two-dimensional NIRSPEC long-slit spectrum of HDF-BX1564. Each pixel corresponds to 0.143" along the spatial and 4.2 Å along the spectral axes. Note the abrupt wavelength transition between SE and NW components.

5.7.5 Q1623-BX502

Q1623-BX502 is one of the lowest stellar mass objects observed with OSIRIS ($M_* = 3 \times 10^9 M_\odot$) and is the only galaxy to be successfully detected under poor observing conditions with high humidity and V-band seeing $\gtrsim$ 1". These sub-optimal observing conditions are reflected in the relatively broad PSF (240 mas) compared to the other galaxies in Figure 5.4. In addition, BX502 was one of the two galaxies which required correction for a spatially distorted PSF as described in §5.2.3. While there is mild evidence for resolved velocity structure with peak amplitude $\sim$ 50 km s^{-1}, this shear is not aligned with the apparent N-S morphological major axis. Given that the entire luminous area of this object is approximately twice the size of our PSF, it is unclear whether this structure is significant.

5.7.6 Q1623-BX543

Unexpectedly, this galaxy was found to consist of two spatially distinct components separated by $v_{2c} = 125$ km s^{-1} and $d_{2c} = 6.7$ kpc in projection (with one almost due north of the other) implying a dynamical mass $M_{\rm dyn} \sim 6.3 \times 10^{10} M_\odot$. We note, however, that in retrospect deep ground-based $\mathcal{R}$-band imaging suggests a slight elongation along the N–S

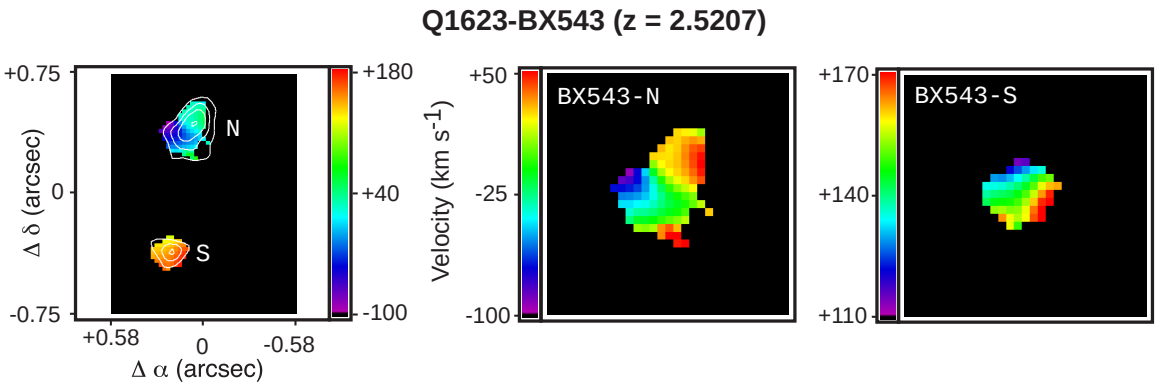

Figure 5.6 The velocity map of Q1623-BX543 (left panel, see also Fig. 5.4) is expanded about each of the two components labelled North ('N') and South ('S'). The color scale represents line-of-sight velocity relative to the systemic redshift in all three panels, the limits of this velocity scale vary as indicated to best illustrate the velocity features of each component.

axis, indicating that both components correspond to rest-UV continuum emission regions. Given the typical $\sim 1''$ PSF of the seeing-limited data however, it is not possible to determine whether the continuum image is a single elongated central feature, or two separate features similar to those shown in Figure 5.4.

While not apparent in Figure 5.4 due to the limitations imposed by the dynamic range of the velocity scale, there is significant velocity structure within the northernmost (N) component. In Figure 5.6 we show an expanded view of each of the components which demonstrates this structure and shows that there is no particular axis along which the velocity in Q1623-BX543-N varies smoothly. The NW section is relatively flat around +20 km s^{-1} with a mild E – W gradient, this velocity falls off rapidly to the SE reaching $\sim$ -20 km s^{-1} within 3 pixels (75 mas, or 0.6 kpc), where it again plateaus with a separate mild velocity gradient along a NE – SW axis. It is currently unknown how best to interpret these complex kinematic data (these data were collected only recently in 2008 June), but the observed patterns in Q1623-BX543-N do not presently appear to be consistent with rotational models.

5.7.7 Q1700-BX490

As in the case of Q1623-BX543, this galaxy also unexpectedly proved to have a complex, multiple-component structure. In the larger western component there is a smoothly varying velocity gradient along the NE – SW axis from which emission line flux appears to be concentrated in two closely separated knots. The smaller eastern component is blueshifted from the main body by ~ 60 km s^{-1}. As demonstrated by Figure 5.3, the overall location and size of these components is broadly consistent with *HST*-ACS rest-UV imaging, although the western component appears in the UV image to consist of a single central concentration located mid-way between the Hα peaks (see contours in Fig. 5.3). Analysis of this complex system is ongoing.

5.7.8 Q1700-BX710

As for Q1623-BX453, this galaxy exhibits no strong evidence for spatially resolved velocity structure, and has a local velocity dispersion $\sigma_{\rm mean} = 68 \pm 25$ km s^{-1}. There is a slightly redshifted extension of flux to the NW of the galaxy core which has a lower velocity dispersion and is coincident with the low surface brightness emission tail seen in *HST*-ACS imaging data (Fig. 5.3). We note that Q1700-BX711 is located ~ 5" (41 kpc) to the northwest of Q1700-BX710 (i.e., approximately along the direction of the 'tail' indicated by the *HST*-ACS data) and at the same redshift to within 10 km s^{-1}. However, a long-slit NIRSPEC spectrum obtained along the line connecting the two galaxies shows no evidence for star formation occuring in the region between the two galaxies.

5.7.9 Q1700-BX763

Q1700-BX763 is reasonably well-detected by OSIRIS, but exemplifies the case for which significant additional processing of our recent observational data is required before significant conclusions regarding galaxy kinematics can be made. In particular, the automated fitting routines have been unable to distinguish nebular emission from the noise for all but the very highest surface brightness pixels. While the emission from this galaxy may genuinely be consistent with a point source, further analysis is required before we may be confident in this interpretation.

5.7.10 DSF2237a-C2

DSF2237a-C2 is located at a significantly higher redshift than any other galaxies in the target sample ($z \sim 3.3$), and is drawn from the "LBG" galaxy catalog of Steidel et al. (2003). Given the current fascination with locating rotating galaxies at high redshifts, it is a curious (if statistically meaningless) coincidence that this is also the galaxy which presents the strongest case for an isolated rotating system in the entirety of our sample, with a relatively strong (peak amplitude ~ 70 km s^{-1}) velocity gradient aligned with the morphological major axis. Despite this velocity gradient, the local velocity dispersion of DSF2237a-C2 is comparable to that of the rest of the galaxy sample with $\sigma_{\rm mean} = 89 \pm 20$ km s^{-1} . While some aspects of this galaxy are discussed in §5.8 below, we refer the reader to Law et al. (2007a) for a detailed treatment. We note in passing that the value of $L_{[\rm O\,III]}$ in Table 3 of Law et al. (2007a) was incorrectly given as 2.2×10^{42} erg s^{-1}, while it should instead have been given as 22×10^{42} erg s^{-1}. The revised number is consistent with the estimate of 16.8×10^{42} erg s^{-1} derived using our new flux calibration routine.

5.7.11 Q2343-BX418

As for Q1217-BX95 and Q1700-BX763, Q2343-BX418 is well detected in the composite OSIRIS data cube but appears to be spatially compact, perhaps with a slight elongation along the N–S axis. There is no evidence for spatially resolved velocity structure, and preliminary analyses suggest that $\sigma_{\rm mean}$ is consistent with values typically observed for the rest of the galaxy sample. We expect further details to become available as our recent observational data are more thoroughly analyzed.

5.7.12 Q2343-BX513

Q2343-BX513 is elongated along the N–S axis and exhibits a complex multi-component velocity structure. The northernmost region of the galaxy is blueshifted by -80 km s^{-1} relative to the systemic redshift and shifts to a maximum velocity of +50 km s^{-1} located near the flux peak of the galaxy before falling off again to ~ 0 km s^{-1} on the southern edge of the galaxy. Indeed, if the Hα emission line is divided into redshifted and blueshifted components, the redshifted component peaks in the center of the system while the blueshifted component peaks to the north and south of this. Such behaviour is clearly inconsistent

with simple rotational models, and suggests that the redshifted component may be (for instance) a kinematically distinct star-forming region which we are viewing superimposed on the larger background system.

We note that this galaxy is the oldest in the OSIRIS sample (among both detected and undetected targets) with an estimated stellar population age of ~ 3 Gyr and a large stellar mass $M_* = 5.9 \times 10^{10} M_\odot$. It is possible that this larger, blueshifted background source could represent the more "mature" galaxy which contains the majority of the stellar mass traced by long-wavelength continuum emission, while a smaller redshifted star-forming region is responsible for the majority of the (relatively) small 20 $M_\odot$ yr^{-1} of current star formation. Such an explanation is beyond the scope of this work to verify at present, but we note that the local velocity dispersion of Q2343-BX513 is consistent with such an interpretation: $\sigma_{\rm mean} = 100 \pm 25$ km s^{-1}, greater than that observed for the majority of galaxies in our sample, as might be expected for a higher-mass galaxy or if there are kinematically distinct components superimposed along the line of sight.

5.7.13 Q2343-BX587

This galaxy is poorly detected in the OSIRIS data cube. The FWHM of Q2343-BX587 is apparently less (~ 140 mas) than that of the PSF reference star (160 mas), and therefore consistent with being unresolved so that it is not possible to determine the spatially resolved kinematics of this galaxy. We note, however, that our net velocity dispersion measurement $\sigma_{\rm mean} = 101 \pm 18$ km s^{-1} is consistent with the previous long-slit measurement (Erb et al. 2006c), while our flux estimate is ~ 8 times lower. This discrepant flux measurement is highly uncertain and likely biased by our extremely poor detection, which may in part fail to account for low surface brightness flux detected in the long-slit data.

5.8 KINEMATIC MODELING

As discussed above, four galaxies (Q1623-BX502, Q1623-BX543N, Q1700-BX490, and DSF2237a-C2) exhibit spatially resolved velocity gradients. Given the theoretical expectation that the cold, star-forming gas in these galaxies might be distributed in a thin, rotationally supported disk, it is worthwhile investigating whether such a model suffices to

explain the observed kinematics. We therefore construct idealized thin-disk models which match the overall size and orientation of the kinematic maps shown in Figure 5.4, adjusting the asymptotic velocities and turnover radii as necessary to produce the best match to these observations. We note that many of the parameters involved in constructing such models are degenerate, particularly the inclination i between our line of sight and the vector normal to the putative disks. At low redshifts, the morphological regularity of most disk-like systems may be used to derive i directly from the observed minor-axis foreshortening of the galaxy. At redshift $z \sim 2$ however, morphology appears to be poorly indicative of such physical properties (see, e.g., Law et al. 2007b) and cannot reliably be used to obtain the inclination. We therefore adopt the mean inclination $< i >= 57.3^{\circ}$ expected for an isotropically distributed ensemble of galaxies (see discussion in §5.A.1).

The results of this disk modeling for DSF2237a-C2 have already been presented by Law et al. (2007a), and we refer the reader to this paper (Chp. 4) for a full discussion of the modeling process. In brief, the model is characterized by a turn-over radius of 1.6 kpc and a deprojected asymptotic velocity of 93 km s^{-1}, matching the observational velocity map with relatively small residuals. Assuming that the disk is supported primarily by its rotational velocity, this implies a dynamical mass of $3.2 \times 10^9 M_{\odot}$ in the solid-body region of this galaxy. Given that the stellar mass of this galaxy is almost a factor of 10 larger ($M_* = 2.9 \times 10^{10} M_{\odot}$) we conclude that either the stellar population of this galaxy must extend to considerably larger radii than the present star formation, that the majority of the dynamical support of the system is not provided by the rotational motion, or that one of the mass estimates is incorrect. Indeed, even accounting for the blurring of the velocity field of the fiducial cold disk model by the observational PSF it is not possible to reproduce the high local velocity dispersion $\sigma_{\rm mean} = 89 \pm 20$ km s^{-1} with a thin disk model alone.

Similarly, preliminary analyses of the three other galaxies (for which it has not yet been possible to fit detailed models) suggest that while models can be constructed which approximately reproduce the line-of-sight velocity fields, these models are unable to match the observed local velocity dispersions without introducing an intrinsic dispersion to the disk models comparable to or greater than the rotational velocity. As a result, it is not apparent that a flattened rotating "disk" is necessarily the best theoretical model given the disk thicknesses implied by the large dispersion.

We note that much more detailed modeling (e.g., using Fourier decomposition of concentric ellipsoids) than that described in this contribution is possible, and for such detailed kinemetric analyses we refer the reader to Shapiro et al. (2008). In the majority of cases presented here, however, the observational data do not justify such detailed analyses. The results of such detailed modeling for galaxies at similar redshifts by Genzel et al. (2008) also indicate the importance of local velocity dispersions in the dynamical structure of these galaxies (see also discussion in §5.9.3).

5.9 DISCUSSION

5.9.1 Selection Effects and the Global Population

As outlined in §5.2.1, targets were selected for a wide variety of reasons (high/low stellar mass, extended/compact morphology, presence/absence of kinematic shear in long-slit spectra, etc.) subject to the general constraint that we believed the galaxy to be detectable based on total emission line flux observed in previous long-slit observations (Erb et al. 2006b) or narrowband Hα imaging. An additional bias is introduced by those galaxies which we were unable to detect despite the investment of significant observing time. This bias is difficult to quantify since the probability of detecting a given galaxy is a strong function of observing conditions; indeed, 11 of the 15 failed observations (some of which represent multiple attempts to observe the same galaxy) listed in Table 6.1 were performed under sub-optimal conditions typically characterized by poor seeing $\gtrsim 1''$ (resulting in poorer AO correction), high humidity (exacerbating telluric absorption), and attenuation by cirrus ($\gtrsim 1$ mag). In contrast, only one of our successfully detected galaxies (Q1623-BX502) was observed under similarly poor conditions. The contribution of observing conditions to the nature of the final galaxy sample is therefore impossible to quantify precisely.

The long-slit observations of Erb et al. (2006c) provide a larger sample against which we may compare our target galaxies. In Figure 5.7 we plot the stellar mass and extinction-corrected Hα SFR for both the detected and undetected sample of galaxies in comparison to the larger NIRSPEC sample of Erb et al. (2006c). The galaxies detected with OSIRIS have a mean stellar mass $<\log(M_*/M_\odot) >= 10.2 \pm 0.2$[2] and SFR $<\log(\mathrm{SFR}_{\mathrm{H}\alpha}/(M_\odot$

[2]Value represents the uncertainty in the mean rather than the standard deviation among individual values

$\mathrm{yr}^{-1}))>= 1.3 \pm 0.2$, both consistent with the mean properties of the NIRSPEC sample ($<\log(M_*/M_\odot)>= 10.2 \pm 0.1$ and $<\log(\mathrm{SFR}_{\mathrm{H}\alpha}/(M_\odot\ \mathrm{yr}^{-1}))>= 1.4 \pm 0.1$). In contrast, the galaxies undetected with OSIRIS have a slightly higher mean stellar mass $<\log(M_*/M_\odot)>$ $= 10.5 \pm 0.2$. While the total number of galaxies observed with OSIRIS is relatively low and there is considerable overlap between the three populations, it nonetheless suggests a slight bias in the sense that we are more likely to detect low stellar mass, gas-rich galaxies with a high SFR surface density.

This detection bias may be partly responsible for the relative incidence of various kinematic signatures; for example, galaxies which were known on the basis of long-slit spectroscopy to exhibit velocity shear are almost uniformly undetected in our OSIRIS observations. In particular, we note that there is a propensity for galaxies with the highest stellar masses (or similarly, lowest gas fraction) to be those that demonstrate evidence for velocity shear in the Erb et al. (2006c) survey. In Figure 5.8 we plot the fraction of galaxies with velocity shear as a function of stellar mass, demonstrating both that the *fraction* of galaxies with shear and the *magnitude* of that shear increases towards greater M_*. Indeed, the mean stellar mass of galaxies with velocity shear in the Erb et al. (2006c) sample is $<\log(M_*/M_\odot)>= 10.5 \pm 0.2$ compared to $<\log(M_*/M_\odot)>= 10.2 \pm 0.1$ for the overall sample. If velocity shear is indicative of systematic rotation, this suggests that stable rotation may be more prevalent (or at least more observable) among galaxies which have already accumulated a sizeable stellar population. While this trend might hold in a *statistical* sense, however, the individual galaxies which exhibit shear in our OSIRIS observations span a wide range in stellar mass from $M_* = 0.3 - 2.9 \times 10^{10} M_\odot$, and one of our targets with the highest stellar mass (Q2343-BX453) is perhaps the single best example of a galaxy without *any* resolved large-scale kinematic structure.

5.9.2 Relation to Complementary Surveys

In order to best construct a picture of the overall $z \sim 2$ galaxy population it is necessary to combine these results with similar studies of overlapping samples recently undertaken by a variety of authors. The largest single sample of IFU observations of galaxies at redshift $z \sim 2$ to date has been provided by the "SINS" survey using SINFONI on the VLT, a

in the population.

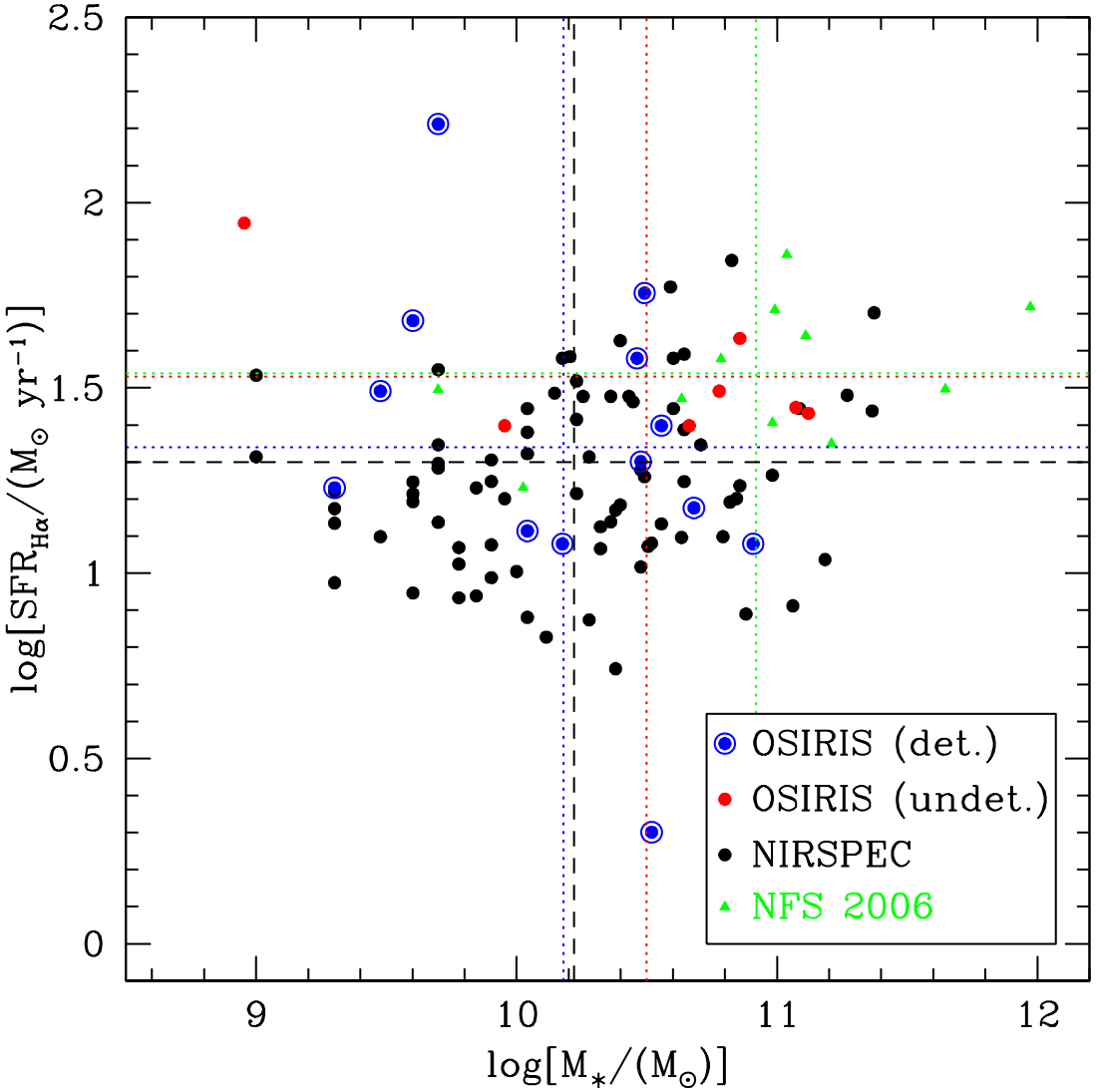

Figure 5.7 Plot of stellar mass versus extinction-corrected Hα star formation rate for galaxies successfully (blue circled points) and unsuccessfully (red points) observed with OSIRIS in comparison to the larger NIRSPEC sample of Erb et al. (2006c, black points) and the SINS sample of Förster Schreiber et al. (2006, green triangles). The dashed blue, red, black, and green lines represent the mean values of each of the populations respectively. Note that the average OSIRIS detection has a lower stellar mass than the SINS sample, although individual members populate a wide range of the available parameter space.

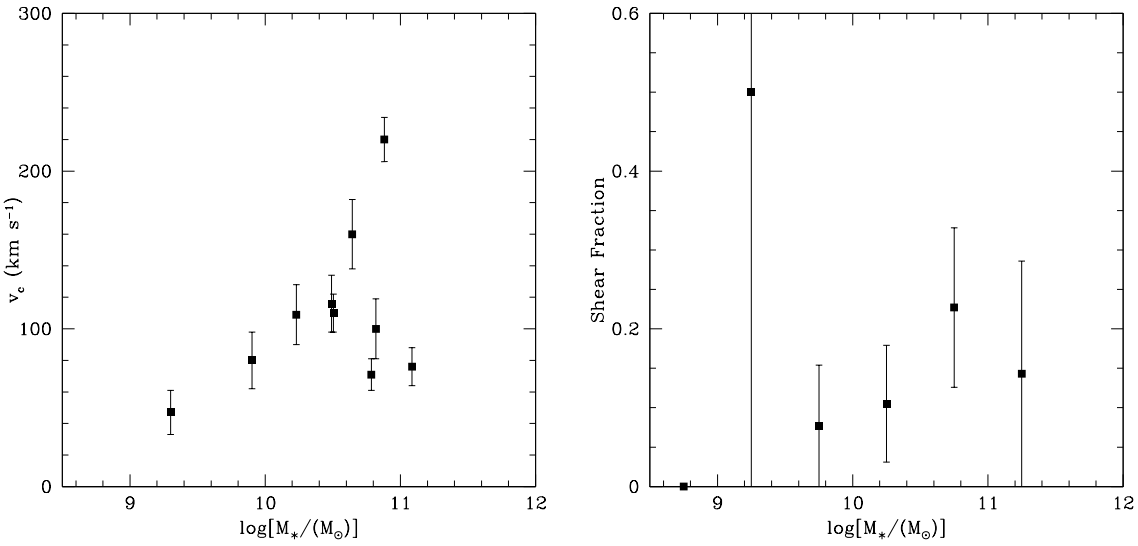

Figure 5.8 *Left:* Velocity shear as a function of stellar mass. *Right:* Fraction of galaxies which exhibit velocity shear when binned according to stellar mass. Error bars in the left panel represent 1σ uncertainties, and in the right panel Poisson noise for the number of galaxies with observable shear in a given stellar mass bin. Both panels are based on the large NIRSPEC-based galaxy sample presented by Erb et al. (2006c).

selection of results from which have been variously presented by Förster Schreiber et al. (2006), Genzel et al. (2006), Bouché et al. (2007), and more recently by Shapiro et al. (2008) and Genzel et al. (2008). While this survey similarly finds high velocity dispersions, a larger fraction of their galaxies also exhibit spatial velocity shear (over 50% in the Shapiro et al. 2008 sample) which may be consistent with rotation. Given the implications of such kinematic features for galaxy formation models, it is particularly important to understand the source of the survey discrepancy giving rise to a high incidence of detected shear in the SINS sample and the general absence of shear in our OSIRIS sample.

One important distinction is the respective galaxy populations traced by each of the two studies. As discussed in §5.9.1, the OSIRIS targets are drawn from optically selected "BX" star-forming galaxy catalogs, within which our successful observations are slightly biased towards lower-mass, rapidly star-forming galaxies with higher Hα surface brightness. In contrast, the SINFONI sample incorporates some optically selected galaxies in addition to a large number of near-IR BzK galaxies (see, e.g., Daddi et al. 2004), and a selection of sub-millimeter galaxies (SMGs; see Chapman et al. 2005). These latter may be fundamentally distinct from the BX galaxy population (see, e.g., discussions by Bouché et al. 2007 and Menéndez-Delmestre et al. *in prep.*) with large dust contents and significantly larger velocity widths which Bouché et al. (2007) interpret as evidence for major mergers. As detailed by numerous authors however, there is a large overlap between the BX and BzK samples, and many galaxies simultaneously satisfy both selection criteria. However, the BzK sample is brighter in the K band than the deeper BX sample (see discussion by Reddy et al. 2006), and therefore of higher average stellar mass. Indeed, the average stellar mass of those galaxies presented by Förster Schreiber et al. (2006) is $<\log(M_*)> = 10.9 \pm 0.1$, much larger than the values of 10.2 ± 0.2 and 10.2 ± 0.1 given in §5.9.1 for the OSIRIS and NIRSPEC samples, respectively.

One conceivable explanation for the discrepant kinematic results may therefore simply be that the two surveys trace distinct, complementary populations. It may be that the lowest mass galaxies tend to display negligible velocity shear and extremely high Hα surface brightness, while star formation in more massive galaxies with appreciable old stellar populations tends to trace the kinematics of any underlying disks with greater fidelity. While the morphologies of the BX and BzK galaxies are qualitatively similar, we note that BzK

sources which do not also fulfill the BX selection criteria tend to be slightly less strongly nucleated with fewer spatial irregularities (see discussion by Law et al. 2007b), consistent with the interpretation that they might more accurately be described as evolved stellar "disks" than the BX sample.

Another explanation for the discrepancy may lie in the difference in optical performance of the two surveys. With the sensitivity advantage of a slicer-type spectrograph, SINFONI is roughly twice as sensitive as OSIRIS and therefore able to probe fainter surface brightness features to larger radii. Indeed, there are some galaxies (e.g., Q1623-BX389) for which SINFONI has revealed large scale velocity shear which remains undetected with OSIRIS despite our best efforts and successful NIRSPEC observations. In contrast, the image quality of the OSIRIS data is generally superior, with LGSAO image correction for all of the target galaxies and a typical PSF $\sim$ 100 mas, compared to the large fraction of the SINS sample (13 of the 14 galaxies discussed by Förster Schreiber et al. 2006) which was obtained in seeing-limited mode with a PSF $\sim$ 500 mas (with some notable exceptions, e.g., Genzel et al. 2006). This difference suggests the possibility that velocity shear may simply be less prevalent in the inner few kpc of $z \sim 2$ star-forming galaxies in which we are most sensitive, and is only observable at larger radii and fainter surface brightnesses than we are able to detect. However, this simple 2-component explanation seems unlikely given that low-surface brightness shear occured in at most 10% of the sensitive NIRSPEC survey of Erb et al. (2006c), and the NIRSPEC spectra of the galaxies observed with OSIRIS generally show little evidence for significant nebular emission beyond that detected with OSIRIS.

Additional examples at similar redshifts have recently been given by van Starkenburg et al. (2008) and Nesvadba et al. (2008). The former used VLT/SINFONI to study the $z = 2.03$ galaxy HDFS-F257 (selected from a sample of large disk galaxy candidates) in an effort to constrain the high redshift Tully-Fisher relation (Tully & Fisher 1977). As for Förster Schreiber et al. (2006) and Genzel et al. (2008), van Starkenburg et al. (2008) are able to model HDFS-F257 with a regular disk velocity field but find that the massive gaseous component has a larger kinematic dispersion than local galaxies. Nesvadba et al. (2008) presented VLT/SINFONI integral-field spectroscopy of the Lyman Break Galaxy Q0347-383 C5, the second unlensed galaxy studied at redshift $z \sim 3$. Similarly to Q1623-BX543-N,

the velocity shear in this galaxy is inconsistent with rotation, transitioning rapidly from a plateau of ~ 60 km s^{-1} to ~ -80 km s^{-1} within a negligible physical distance, leading the authors to favor a merger interpretation for the galaxy.

5.9.3 Physical Mechanisms

As outlined by White & Rees (1978), the basic model of galaxy formation suggests that shocked gas falling through the halo virial radius should radiatively cool and contract to form a rotationally supported disk in which star formation can occur. Given the overall lack of evidence for such disks in the observational data, it is of particular interest to test whether alternate pictures of galaxy formation can better explain the dispersion-dominated kinematics and lack of rotational motions. In particular, we consider the possibility of gravitional instability in gas-rich early disks and the influence of cold flows and major mergers on the global kinematic signatures. Given the global importance of such a discussion beyond the data presented in this chapter alone, we postpone this discussion to Chapter 7, and now turn instead to our final observational chapter (Ch. 6) describing the structure of a QSO host galaxy at redshift $z \sim 2.6$.

The authors thank Randy Campbell, Al Conrad, and Jim Lyke for their invaluable assistance obtaining the observations presented herein. DRL also thanks Andrew Benson for helpful discussions. DRL and CCS have been supported by grants AST-0606912 and AST-0307263 from the US National Science Foundation. Finally, we wish to extend thanks to those of Hawaiian ancestry on whose sacred mountain we are privileged to be guests.

5.A.1 QUANTIFYING THE MEAN PROPERTIES OF INCLINED SYSTEMS

Given a collection of disks oriented isotropically in space, we wish to determine the mean expected inclination i between our line of sight to a given disk and the normal vector to the disk (where $i = 0^\circ$ represents a disk viewed face-on). It is simplest to reduce the problem to a single disk and consider it from the reference frame of the disk itself. Assuming that the viewing location is chosen completely at random, the distribution of possible lines of sight will uniformly cover the sky as seen from the reference frame of the disk. The probability

dP that the viewer is located within a given patch of sky is therefore proportional to the differential solid angle $d\Omega$ subtended by that patch of sky. Adopting a spherical polar coordinate system θ, ϕ centered on the disk where ϕ is the azimuthal angle and theta (ranging from $-\frac{\pi}{2}$ to $\frac{\pi}{2}$) is the polar angle the differential solid angle is given by

$$d\Omega = \cos\theta \, d\theta \, d\phi. \tag{A.1}$$

It is therefore possible to calculate the expectation value $< i >$ by integrating over the entire sky. Noting the symmetry present in the problem, we may omit the integral over the azimuthal coordinate ϕ and collapse the polar integral to consider only the range $\theta = 0$ to $\frac{\pi}{2}$, reducing the differential solid angle to $d\Omega = \cos\theta \, d\theta$. In this range, the inclination is related to the polar angle by $\theta = \frac{\pi}{2} - i$. Therefore,

$$< i >= \frac{\int_0^{\frac{\pi}{2}} i \cos\theta \, d\theta}{\int_0^{\frac{\pi}{2}} \cos\theta \, d\theta}. \tag{A.2}$$

Substituting the identities $\cos\theta = \sin i$ and $d\theta = -di$ we obtain

$$< i >= \frac{\int_0^{\frac{\pi}{2}} i \sin i \, di}{\int_0^{\frac{\pi}{2}} \sin i \, di} = \frac{[\sin i - i \cos i]_0^{\frac{\pi}{2}}}{[-\cos i]_0^{\frac{\pi}{2}}} = 57.3^\circ. \tag{A.3}$$

Since the observed radial velocities are effectively "foreshortened" by a factor $\sin i$, it is also often of interest to calculate the mean expected value of this correction factor. Similarly to those calculations performed above,

$$< \sin i >= \frac{\int_0^{\frac{\pi}{2}} \sin i \cos\theta \, d\theta}{\int_0^{\frac{\pi}{2}} \cos\theta \, d\theta} = \frac{\int_0^{\frac{\pi}{2}} \sin^2 i \, di}{\int_0^{\frac{\pi}{2}} \sin i \, di} = \frac{\pi}{4}. \tag{A.4}$$

Table 5.1. General Target Information

Galaxy	$z_{\rm neb}$[a]	R.A. (J2000.0)	Decl. (J2000.0)	Observed	Time[b] (seconds)	Filter	Em. Line[c]	Scale (mas)	$\theta_{\rm PSF}$[d] (mas)
				Detections					
Q0449-BX93	2.0067	04:52:15.417	-16:40:56.88	2006 Oct	16200	Kn1	Hα	50	125/150
Q1217-BX95	2.4246[e]	12:19:28.281	+49:41:25.9	2008 Jun	6300	Kn4	Hα	50	79/140
HDF-BX1564	2.2228	12:37:23.470	+62:17:20.00	2007 Jun	3600	Kn2	Hα	50	160/280
Q1623-BX453	2.1820	16:25:50.854	+26:49:31.28	2006 Jun	9000	Kn2	Hα	50	75/110
Q1623-BX502	2.1557	16:25:54.385	+26:44:09.30	2007 Jun	9900[f]	Kn2	Hα	50	220/240
Q1623-BX543	2.5207[e]	16:25:57.707	+26:50:08.60	2008 Jun	11700	Hn5	[O III]	50	79/140
Q1700-BX490	2.3957[e]	17:01:14.83	+64:09:51.69	2008 Jun	11700	Kn4	Hα	50	79/140
Q1700-BX710	2.2947	17:01:22.128	+64:12:19.21	2006 Jun	5400	Kn3	Hα	50	75/110
Q1700-BX763	2.2920[d]	17:01:31.463	+64:12:57.67	2008 Jun	12600	Kn3	Hα	50	79/140
DSF2237a-C2	3.3172	22:40:08.298	+11:49:04.89	2006 Jun	5400	Kn3	[O III]	50	75/110
Q2343-BX418	2.3050[e]	23:46:18.582	+12:47:47.77	2008 Jun	6300	Kn3	Hα	50	79/140
Q2343-BX513	2.1082	23:46:11.133	+12:48:32.54	2006 Oct	12600	Kn1	Hα	50	130/160
Q2343-BX587	2.2430	23:46:29.192	+12:49:03.71	2006 Oct	5400	Kn3	Hα	50	140/160
				Non-Detections					
Q0100-BX210	2.279[g]	01:03:11.996	+13:16:18.32	2006 Oct	1800[f]	Kn3	Hα	50	...
				2007 Sep	3600[f]	Hn3	[O III]	50	...
				2007 Sep	5400[f]	Kn3	Hα	50	...
HDF-BX1311	2.4843[g]	12:36:30.514	+62:16:26.0	2007 Jun	4500[f]	Kn4	Hα	50	...
HDF-BX1439	2.1865[g]	12:36:53.660	+62:17:24.0	2008 Jun	2700	Kn2	Hα	50	...
				2007 Sep	7200[f]	Kn2	Hα	100	...
Q1623-BX455	2.4074[g]	16:25:51.664	+26:46:54.6	2007 Sep	3600	Hn4	[O III]	50	...
				2008 Jun	5400	Kn4	Hα	50	...
Q1623-BX663	2.4333[g]	16:26:04.586	+26:47:59.8	2007 Jun	5400[f]	Kn4	Hα	50	...
Q1700-BX563	2.292[h]	17:01:15.875	+64:10:26.15	2007 Jun	1800[f]	Kn3	Hα	50	...
Q1700-BX691	2.1895[g]	17:01:06.117	+64:12:09.7	2006 Jun	10800[i]	Kn2	Hα	50	...
				2007 Jun	5400[f]	Kn2	Hα	50	...
Q2206-BX102	2.2104[g]	22:08:50.751	-19:44:08.24	2007 Sep	5400	Kn2	Hα	50	...
Q2343-BX389	2.1716[g]	23:46:28.911	+12:47:33.9	2007 Jun	8100[f]	Kn2	Hα	50	...
Q2343-BX442	2.1760[g]	23:46:19.362	+12:48:00.1	2007 Sep	9000[f]	Kn2	Hα	50	...

[a]Vacuum heliocentric redshift of primary nebular emission line.

[b]Total observing time.

[c]Primary targeted emission line (Hα or [O III] λ5007).

[d]FWHM of the K-band PSF (mas) during on-axis TT star observation (before/after spatial smoothing respectively).

[e]Redshifts are approximate and uncorrected for barycentric motion.

[f]Poor observing conditions.

[g]Redshifts estimated from NIRSPEC spectra.

[h]Redshifts estimated from rest-UV spectra.

[i]Individual exposures were each 300 seconds.

Table 5.2. OSIRIS Morphologies

Galaxy	I[a] (kpc^2)	r[b] (kpc)	d_{2c}[c] (kpc)	G[d]	Ψ[e]
Q0449-BX93	4.7 ± 0.6	1.2 ± 0.1	...	0.25	1.3
Q1217-BX95	1.1 ± 0.5	0.6 ± 0.1	...	0.11	0.4
HDF-BX1564	11.4 ± 2.1	1.9 ± 0.2	7.0	0.15	12.2
Q1623-BX453	9.5 ± 0.3	1.7 ± 0.1	...	0.33	1.5
Q1623-BX502	8.2 ± 1.5	1.6 ± 0.1	...	0.31	0.6
Q1623-BX543	6.0 ± 0.5	1.4 ± 0.1	6.7	0.22	11.3
Q1700-BX490	11.6 ± 0.5	1.9 ± 0.1	3.4	0.19	6.0
Q1700-BX710	8.2 ± 0.3	1.6 ± 0.1	...	0.43	0.4
Q1700-BX763	0.5 ± 0.5	0.4 ± 0.2	...	0.06	1.5
DSF2237a-C2	3.3 ± 0.3	1.0 ± 0.1	...	0.25	3.4
Q2343-BX418	2.4 ± 0.5	0.9 ± 0.1	...	0.10	1.8
Q2343-BX513	6.9 ± 0.7	1.5 ± 0.1	...	0.20	1.2
Q2343-BX587	< 1.4	< 0.7	...	0.16	1.8

[a]Area of nebular emission. Uncertainty represents half the PSF correction.

[b]Radius of nebular emission. Uncertainty represents half the PSF correction. Values in parentheses denote separation between individual blobs.

[c]Distance between the two morphological components.

[d]Gini.

[e]Multiplicity.

Table 5.3. Nebular Line Fluxes

Galaxy	$\lambda_{\rm neb}$[a] (Å)	$z_{\rm neb}$[b]	$F_{\rm H\alpha}$[c]	$F_{\rm [O\,III]}$[c] (λ5007)	$L_{\rm neb}$[d] (10^{42} erg s^{-1})	$F_{\rm [O\,III]}$[c] (λ4960)	$F_{\rm [N\,II]}$[c] (λ6549)	$F_{\rm [N\,II]}$[c] (λ6585)
Q0449-BX93	19737.8	2.0067	6.8 ± 0.2	...	3.0 ± 0.1	...	1.3 ± 0.4	0.8 ± 0.3
Q1217-BX95	22481.3	2.4246	5.9 ± 0.4	...	5.7 ± 0.4	...	< 1.2	< 1.2
HDF-BX1564	21156.7	2.2228	9.7 ± 0.8	...	4.6 ± 0.4	...	< 1.5	3.9 ± 0.5
Q1623-BX453	20888.3	2.1820	16.4 ± 0.4	...	12.8 ± 0.3	...	3.0 ± 0.4	6.5 ± 0.4
Q1623-BX502	20715.8	2.1557	10.0 ± 0.2	...	7.0 ± 0.1	...	< 0.7	< 0.7
Q1623-BX543	17632.4	2.5207	...	17.9 ± 0.5	30.2 ± 0.8	3.8 ± 0.5	...	...
Q1700-BX490	22292.1	2.3958	33.1 ± 0.8	...	36.7 ± 0.9	...	< 2.4	< 2.4
Q1700-BX710	21628.4	2.2947	4.5 ± 0.2	...	3.4 ± 0.2	...	< 0.6	0.6 ± 0.2
Q1700-BX763	21610.67	2.2920	4.3 ± 0.3	...	2.6 ± 0.2	...	< 0.9	1.1 ± 0.3
DSF2237a-C2	21621.8	3.3172	...	7.9 ± 0.4	16.8 ± 0.9	2.0 ± 0.3	...	...
Q2343-BX418	21696.1	2.3050	8.5 ± 0.4	...	3.8 ± 0.2	...	< 1.2	< 1.2
Q2343-BX513	20404.3	2.1082	5.4 ± 0.2	...	2.8 ± 0.1	...	< 0.6	1.8 ± 0.2
Q2343-BX587	21288.9	2.2430	0.7 ± 0.1	...	0.5 ± 0.1	...	< 0.3	< 0.3

[a]Vacuum heliocentric wavelength of peak emission.
[b]Heliocentric redshift of primary nebular emission line: [O III] λ5007 for DSF2237a-C2 and Q2343-BX415, Hα for all others.
[c]Emission line flux in units of 10^{-17} erg s^{-1} cm^{-2}. Uncertainties quoted are 1σ and based on random errors, global systematic uncertainty is $\sim 30\%$. Limits represent 3 σ limits.
[d]Extinction-corrected primary nebular emission line luminosity. Uncertainties quoted are based on random errors, global systematic uncertainty is $\sim 30\%$.

Table 5.4. Stellar Population Parameters

Galaxy	M_*[a] $10^{10} M_\odot$	Age[b] (Myr)	$\mathrm{SFR_{SED}}$[c] ($M_\odot$ yr^{-1})	$\mathrm{SFR_{H\alpha}}$[d] ($M_\odot$ yr^{-1})	$E(B-V)$[e]
		Detections			
Q0449-BX93	1.1	227	46	13	0.135
Q1217-BX95	3.6	719	50	25	0.230
HDF-BX1564	3.0	571	53	20	0.210
Q1623-BX453	3.1	404	77	57	0.245
Q1623-BX502	0.3	203	15	31	0.130
Q1623-BX543	0.4	10	435	48	0.285
Q1700-BX490	0.5	10	451	163	0.285
Q1700-BX710	4.8	1434	34	15	0.195
Q1700-BX763	1.5	1015	15	12	0.120
DSF2237a-C2	2.9	255	112	38	0.175
Q2343-BX418	0.2	203	9	17	0.015
Q2343-BX513	8.1	3000	27	12	0.160
Q2343-BX587	3.3	719	46	2	0.175
		Non-Detections			
Q0100-BX210	0.8	102	74	...	0.215
HDF-BX1311	0.9	255	35	25	0.110
HDF-BX1439	4.6	2200	21	25	0.175
Q1623-BX455	0.09	15	58	88	0.265
Q1623-BX663[f]	13.2	2000	21	27	0.135
Q1700-BX563	3.3	641	51	...	0.220
Q1700-BX691	6.0	2750	22	31	0.285
Q2206-BX102	11.8	2750	43	...	0.335
Q2343-BX389	7.2	2750	26	43	0.265
Q2343-BX442	11.8	2750	43	28	0.285

[a]Typical uncertainty $< \sigma_{M_*}/M_* >= 0.4$.

[b]Typical uncertainty $< \sigma_{\mathrm{Age}}/\mathrm{Age} >= 0.5$.

[c]SFR derived from stellar population model. Typical uncertainty $< \sigma_{\mathrm{SFR}}/\mathrm{SFR} >= 0.6$.

[d]Extinction-corrected Hα SFR. Values for non-detected sources based on previous long-slit observations (where available).

[e]Typical uncertainty $< \sigma_{E(B-V)}/E(B-V) >= 0.7$.

[f]AGN

Table 5.5. Kinematic Properties

Galaxy	$\sigma_{\rm mean}$[a] (km s^{-1})	$\sigma_{\rm net}$[b] (km s^{-1})	$v_{\rm shear}$[c] (km s^{-1})	$v_{\rm 2c}$[d] (km s^{-1})
Q0449-BX93	56 ± 20	71 ± 5	...	...
Q1217-BX95	67 ± 20	67 ± 5	...	...
HDF-BX1564	60 ± 13(NW)	103 ± 14	...	171
	86 ± 8(SE)			
Q1623-BX453	78 ± 23	94 ± 5	...	...
Q1623-BX502	67 ± 20	68 ± 3	40 ± 10	...
Q1623-BX543	139 ± 32 (N)	146 ± 7	43 ± 10	125
	60 ± 10 (S)			
Q1700-BX490	89 ± 25 (W)	123 ± 6	55 ± 10	109
	65 ± 29 (E)			
Q1700-BX710	68 ± 25	67 ± 7	...	...
Q1700-BX763	71 ± 13	45 ± 5	...	...
DSF2237a-C2	89 ± 20	99 ± 10	70 ± 10	...
Q2343-BX418	65 ± 17	68 ± 5	...	...
Q2343-BX513	100 ± 25	102 ± 6	...	...
Q2343-BX587	101 ± 18	121 ± 27	...	...

[a]Flux-weighted mean and standard deviation of velocity dispersions in individual spaxels in the OSIRIS map.

[b]Velocity dispersion of the spatially collapsed object spectrum. Uncertainty quoted is based on Monte Carlo analysis of synthetic spectra.

[c]Shear velocity $v_{\rm shear} = \frac{1}{2}(v_1 - v_2)$.

[d]Velocity difference between two discrete components.

Chapter 6

Kpc-Scale Structure in the Nebular Emission of $z \sim 2.6$ QSO Q2343-BX415*

David R. Law[a], Charles C. Steidel[a], Max Pettini[b], Dawn K. Erb[c], James E. Larkin[d], Naveen A. Reddy[e], Alice E. Shapley[d], Shelley A. Wright[d]

[a]California Institute of Technology, MS 105–24, Pasadena, CA 91125

[b]Institute of Astronomy, Madingley Road, Cambridge CB3 0HA, UK

[c]Harvard-Smithsonian Center for Astrophysics, MS 20, 60 Garden St, Cambridge, MA 02138

[d]Department of Physics and Astronomy, University of California, Los Angeles, CA 90095

[e]National Optical Astronomy Observatory, 950 North Cherry Avenue, Tucson, AZ 85719

Abstract

We present laser-assisted adaptive optics integral field spectroscopy of nebular line emission from Q2343-BX415, a QSO at $z = 2.57426$ which exhibits a proximate damped Lyα (PDLA) system at the emission redshift. The spatial resolution is 140 mas, equating to 1.1 kpc at the redshift of the QSO. We detect spatially resolved nebular [O III] emission from two nearby sources whose redshifts lie within 50 km s^{-1} of the QSO. The first of these we identify as narrow-line region (NLR) emission from gas ionized by near Eddington-rate radiation from the central QSO whose spatial and kinematic structure is consistent with low-redshift

*A version of this chapter is currently in preparation for submission to *The Astrophysical Journal*.

systems. The second emission region is consistent with star formation in a metal-poor ($Z \lesssim \frac{1}{5} Z_{\odot}$) region separated from the QSO by ~ 1 kpc in projection. This star-forming region has a kinematic dispersion $\sigma_{\rm v} = 146 \pm 11$ km s^{-1}, star formation rate SFR$_{H\alpha} \gtrsim 25 M_{\odot}$ yr^{-1} (uncorrected for extinction), and an estimated stellar mass $M_* \lesssim 10^9 M_{\odot}$. These properties overlap those observed for particularly metal-poor galaxies with little previous star formation within the $z \sim 2-3$ star forming galaxy sample. The physical interpretation of this star formation is uncertain, but may represent either the host galaxy of the QSO or a secondary galaxy in the final stages of merging with it. The redshift of this star formation is consistent with producing the the observed PDLA in relatively quiet ($\lesssim 300$ km s^{-1}) starburst-driven winds.

6.1 INTRODUCTION

Q2343-BX415 is a moderately faint ($\mathcal{R} = 20.22$) QSO at $z \sim 2.57$, discovered in the course of a spectroscopic survey of rest-UV color-selected galaxies (Steidel et al. 2003, 2004; Adelberger et al. 2004) in the field surrounding the bright quasar Q2343+1225. Such AGN[1] represent about 3% of the spectroscopic sample whose characteristic continuum magnitudes overlap those of the LBGs and may represent an evolutionary phase in the lifetimes of ordinary star-forming galaxies in the young universe ($z \sim 2-3$).

Q2343-BX415 is particularly notable for the presence in its spectrum of a metal-poor ($Z \sim \frac{1}{5} Z_{\odot}$) proximate damped Ly$\alpha$ absorption system (PDLA) coincident in redshift with the quasar (Rix et al. 2007; hereafter R07). The kinematics of this PDLA, as traced by rich rest-UV spectral features, show a complex combination of both blueshifted low-ionization gas (+20 to -355 km s^{-1})[2] and a redshifted highly ionized gas component (+120 to +570 km s^{-1} relative to the QSO systemic redshift) which only partially covers the continuum source. As suggested by these authors, the blueshifted gas (the bulk of which lies at -130 km s^{-1}) may represent the wind-driven outflowing ISM of an as-yet undetected QSO host galaxy.

[1] We adopt the conventional usage whereby AGN which show a broad emission line component are referred to as "QSO".

[2] We convert the original values from R07 into our systemic rest frame $z = 2.57426$, which differs by +30 km s^{-1} from the value adopted by R07.

Such an interpretation is perhaps consistent with observations in the low-redshift universe, which suggest a strong correlation between AGN activity and tidal merger signatures (e.g., Canalizo et al. 2000; Miller & Sheinis 2003; Bennert et al. 2008), with many QSO host galaxies exhibiting spectral signatures indicative of post-starburst stellar populations (see, e.g., Canalizo et al. 2006 and references therein). At high redshifts corresponding to the peak epoch of QSO activity ($z \sim 2-3$; Schmidt et al. 1995), however, the small angular scales of individual galaxies make it challenging for ground-based observations to reliably distinguish emission from the central AGN embedded within a host galaxy. While some morphological work has been done with the aid of HST imaging (e.g., Ridgway et al. 2001) our knowledge of the detailed properties of these systems is nevertheless lacking. With the aid of integral-field spectrographs equipped with laser-guided adaptive optics (LGSAO) however, it is possible to suppress the light from the central point source and measure the kinematics and spectral properties of previously unresolvable kpc-scale structures.

In this contribution, we present Keck/OSIRIS observations of rest-frame optical nebular line emission (redshifted into the near-IR) surrounding Q2343-BX415. In §6.2 we describe our observation and calibration techniques, discussing the resulting QSO spectrum in §6.3. In §6.4 we describe the properties of the spatially resolved emission line substructure surrounding the QSO, discussing its physical interpretation and relation to the PDLA in §6.5. §6.6 summarizes our conclusions regarding the state of the Q2343-BX415 system. We assume a standard ΛCDM cosmology based on year 3 WMAP data (Spergel et al. 2007) in which $H_0 = 73.2$ km s^{-1} Mpc^{-1}, $\Omega_{\rm m} = 0.238$, and $\Omega_\Lambda = 0.762$.

6.2 OBSERVING AND DATA REDUCTION

6.2.1 Observational Strategy

Observations were obtained in the Q2343 field (Table 6.1) using Keck/OSIRIS (Larkin et al. 2006) in conjunction with the LGSAO system on UT September 20 2007. We refer the reader to Law et al. (2007a) for a complete description of our typical observing strategy. In brief, we obtained 4 complete exposure sequences consisting of two 15 minute integrations dithered by $\sim$ 1.4" along the long axis of the IFU and 0.1" along the short axis. Using the Hn5 narrowband filter (half-peak transmission wavelength range 1.721 – 1.808 μm) and

50 mas lenslet scale, our field of view was 1.5 × 3.2" for a single pointing. Each exposure sequence was bracketed by 60 second observations of our tip-tilt (TT) reference star to provide a constant measure of the image quality. This image quality was variable with average Hn5 seeing ∼ 0.7", resulting in a FWHM of the LGSAO-corrected PSF of 140 mas (1.1 kpc at $z \sim 2.574$) after cosmetic smoothing with a Gaussian kernel (FWHM 50 mas).

Earlier survey-mode observations of Q2343-BX415 were obtained on 2007 June 20 and August 23 using the 100 mas lenslet scale in disparate conditions (Hn5 seeing ∼ 1.2" and 0.5" for June/August, respectively). While these earlier observations employed a similar observing strategy to that described above, the total integration times of each were relatively short (45 and 30 minutes for June/August, respectively).

6.2.2 Data Reduction and Flux Calibration

Each of the exposure sequences was reduced and stacked in accordance with the methods described by Law et al. (2007a). Since observing conditions deteriorated during the fourth exposure sequence, we included in this stack only the first 3 sequences for which the median seeing was ∼ 0.65" in Hn5, giving a total of 1.5 hours of integration. The common area of overlap in our final stacked data cube is 1.3" × 1.4" centered on Q2343-BX415. The raw spectrum of Q2343-BX415 was extracted from this cube by summing the contributions from all lenslets within a 0.3" radius of the QSO as theoretical modeling indicates that this generally incorporates over 80% of the flux from the LGSAO PSF (see §6.4.1).

These data were obtained as part of a larger program (Law et al. 2007a and *in prep.*) to map the kinematics of star-forming galaxies at redshift $z \sim 2$ (for which precise flux and telluric calibration is largely unimportant in the immediate vicinity of strong narrow emission features) and therefore we did not acquire traditional calibration standards. In order to best study the faint, broad features of Q2343-BX415 we adopt a bootstrapped calibration technique as follows. Using the equations given by Butler (1998) we estimate the atmospheric water column (∼ 1mm) from archived temperature and relative humidity data. We then adopt an atmospheric throughput model (Lord 1992) calculated for Mauna Kea using the water column and air mass (∼ 1.0) appropriate for our observations[3]. This model

[3]Available at http://www.gemini.edu/sciops/ObsProcess/obsConstraints/ocTransSpectra.html

atmospheric transmission spectrum is then multiplied by the Hn5 filter transmission curve[4] and a model of the Keck/OSIRIS grating blaze function and other instrumental/facility throughput characteristics (see discussion in Law et al. 2006) to produce a net transmission function. The raw QSO spectrum is divided by this transmission function and converted to standard flux density (erg s^{-1} cm^{-2} $Å^{-1}$; see, e.g., Eqn. 3 of Law et al. 2006).

The absolute flux calibration is fixed using observations of our TT reference star: while this $R \sim 16.8$ star is too faint to be used as a traditional telluric standard, it is possible to estimate an overall flux correction factor by extracting a TT spectrum in a similar manner to that of the QSO and calculating the AB magnitude of the observed continuum.[5] In this manner we estimate the H-band magnitude of our TT star as $m_{\rm H} = 15.36$. Adopting the true value as $m_{\rm H} = 14.98$ from the 2MASS point-source catalog, we determine a correction factor of 1.4 that should be applied to obtain the final flux calibrated spectrum.

As discussed in Law et al. (2007a), we estimate a global systematic uncertainty $\sim 30\%$ in our absolute flux calibration (although the relative flux ratios within a given spectrum are much more precisely constrained) predominantly caused by two factors. The first, and largest, uncertainty arises from the structure of the LGSAO PSF, which can vary considerably from on-axis TT star observations to off-axis science observations, and on the timescale of minutes or less even in a fixed field. Second, due to the unique characteristics of the OSIRIS spectrograph and matrix inversion algorithms involved in the rectification of raw data, the reduction process leaves an appreciable footprint on the observational data which is not easily incorporated into theoretical throughput models.

6.3 GLOBAL PROPERTIES OF Q2343-BX415

6.3.1 Photometric Properties

Using a variety of ground-based photometry and *Spitzer* IR observations, the SED of Q2343-BX415 has been mapped from the UV to the mid-IR (Table 6.2). This QSO is more luminous

[4] Available at http://www2.keck.hawaii.edu/inst/osiris/technical/filters/filter_index.html

[5] This methodology will necessarily be best for stars without strong spectral features in the Hn5 window from 1.72 to 1.8 μm. Based on the observed proper motion (~ 10 mas yr^{-1}) and color ($(V-J) = 2.45$) of the star as given by the NOMAD database, we surmise that the TT star is a dwarf of either late K or early M type, which are relatively featureless in this wavelength regime (Cushing et al. 2005).

for its redshift at 24 μm than any of the obscured AGN or optically selected galaxies in the GOODS-N field (Reddy et al. 2006a), and is comparable to SMGs at similar redshifts (Reddy et al. 2006b). Using this broadband photometry we estimate the rest-frame optical (5100Å) luminosity $L_\lambda(5100)$ by interpolation of the data given in Table 6.2. Following the prescription of Kaspi et al. (2000), we then estimate the total bolometric luminosity of Q2343-BX415 as $L_{\rm Bol} = 9\lambda L_\lambda(5100) = 8 \times 10^{12} L_\odot$. Based on photometric estimates of the UV spectral slope ($\beta = -1.65$) we determine that the QSO is consistent with only moderate reddening.

6.3.2 Spectral Properties

In the local universe, Seyfert and other galaxies hosting AGN typically show a mix of broad (FWHM ~ 2000 km s^{-1}) permitted and narrow (FWHM ~ 500 km s^{-1}) forbidden emission lines due to transitions arising in photoionized gas stratified by density. In Figure 6.1 we plot the continuum-subtracted spectrum of Q2343-BX415, which shows narrow [O III] λ5007 and λ4959 Å forbidden emission lines typical of the narrow-line region (NLR). While previous Keck/NIRSPEC long-slit observations by R07 spectrum also detect broad Hβ emission as well (Fig. 6.2), our OSIRIS spectra are too shallow to detect such faint, broad spectral features.

We measure the systemic redshift of the QSO by calculating the flux-weighted mean of the top 50% of the [O III] λ5007 emission profile in order to mitigate the effects of line asymmetry. This peak lies at $\lambda_{\rm mean} = 17900.7 \pm 0.2$ Å, resulting in a heliocentric QSO redshift $z = 2.57426 \pm 0.00014$ (after a 2 km s^{-1} solar motion correction).[6] This redshift is consistent with the value previously determined by R07 (2.57393 ± 0.00005) to within the systematic uncertainty resulting from our adoption of the flux weighted mean.

The [O III] λ5007 emission profile of Q2343-BX415 is asymmetric and contains a 6σ detection of excess flux blueward of the primary emission peak (Fig. 6.1). Despite the physical motivation for such features in local Seyfert galaxies (e.g., Heckman et al. 1981; Green & Ho 2005; Rice et al. 2006) we believe this to be an artifact of imperfect telluric

[6] This 0.00014 stochastic uncertainty in redshift is based on Monte Carlo modeling of the rms scatter in the spectrum. Comparison with flux-weighted mode measurements (e.g., Lupton 1993; Vanden Berk et al. 2001) gives a systematic uncertainty ~ 0.00028.

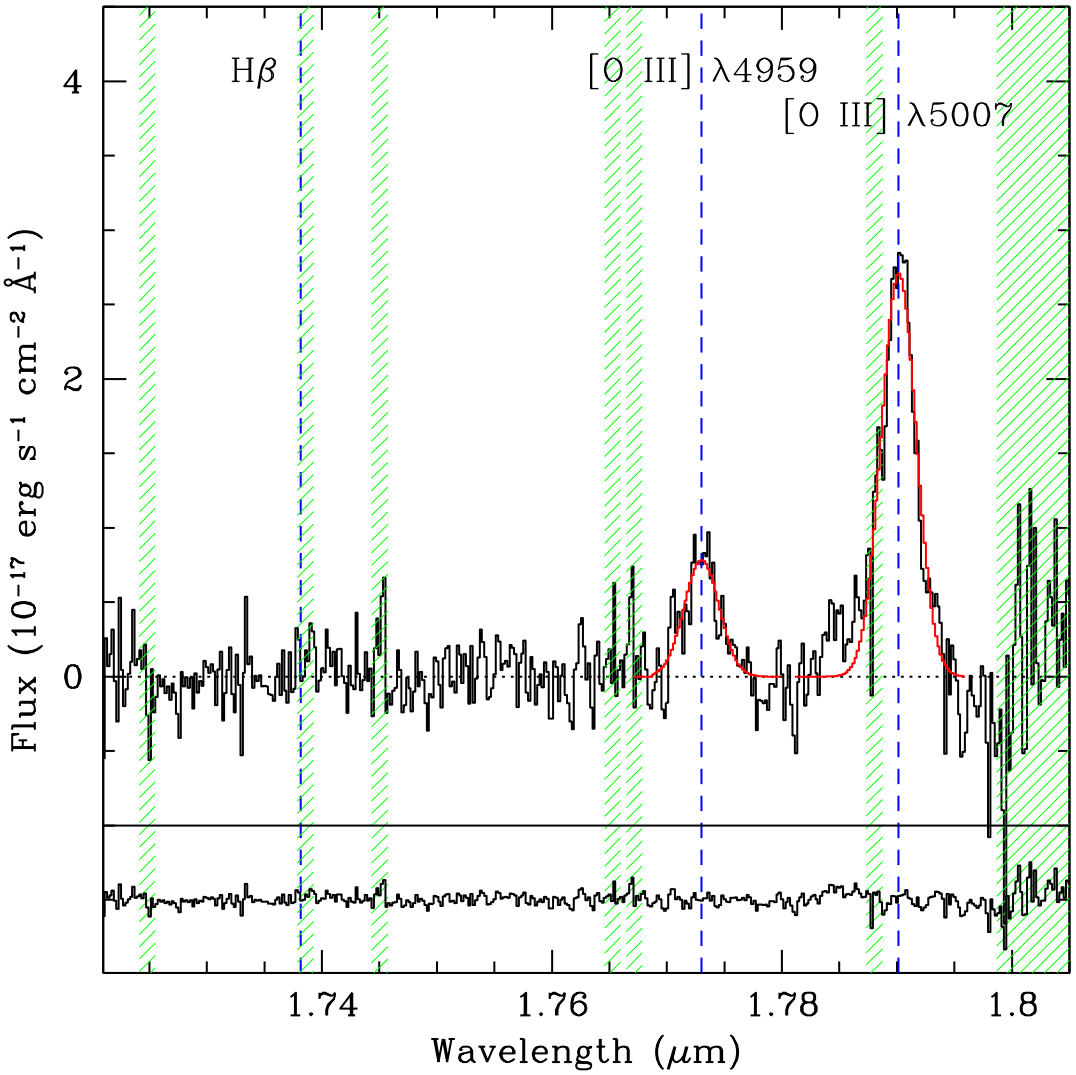

Figure 6.1 Emission-line spectrum of Q2343-BX415 (black line) across the OSIRIS bandpass after subtraction of a second-order polynomial fit to the continuum. Red lines represent Gaussian fits to the [O III] λ5007 and λ4959 Å emission lines (see discussion in §6.3.2), whose fiducial peak wavelengths (and that of Hβ) based on the systemic redshift $z = 2.57426$ are indicated by vertical dashed blue lines. Green hashed regions indicate wavelengths contaminated by particularly strong atmospheric OH emission features . The region redward of 1.8 μm is entirely hashed as the atmospheric transparency drops below 80% at these wavelengths and consists of multiple strong absorption features. The residual noise spectrum after subtraction of the model emission line profiles is shown in the lower panel (reduced by a factor of 5 in stretch).

and/or continuum correction as no similar bump is observed in the [O III] λ4959 line (which traces an identical ionization state).[7] In addition, this excess blue flux is not detected in either the previous long-slit spectrum of R07 (Fig. 6.2) or our previous OSIRIS observations (Fig. 6.3). While such a feature might conceivably vary on time scales $\sim$ 3 years such as elapsed between the R07 observations and our own if the emission arose in an intermediate density region located at the boundary between the BLR and the NLR (see, e.g., Sergeev et al. 1997; Wang et al. 2005), it is highly unlikely that similar variability could exist in the month between our August and September OSIRIS observations. We therefore focus only on the strong, central [O III] λ5007 feature.

Adopting a Gaussian fitting routine which simultaneously fits both [O III] λ5007 and λ4959 emission features we obtain line fluxes and widths (after correction for the 5 Å FWHM of the instrumental profile; see Law et al. 2007a) as given in Table 6.3. The residual spectrum after subtraction of the λ5007 and λ4959 models is plotted in the lower panel of Figure 6.1, and has RMS 2.7×10^{-18} erg s^{-1} cm^{-2} Å^{-1}. We estimate the uncertainty in line fluxes, peak wavelengths, and σ_v by Monte-Carlo bootstraps from these pixel-to-pixel RMS uncertainties. Both the total [O III] λ5007 flux ($f_{5007} = 9.6 \pm 2.9 \times 10^{16}$ erg s^{-1} cm^{-2}) and velocity width ($\sigma_v = 252 \pm 10$ km s^{-1}) are broadly consistent with the values determined by R07 ($5.86 \pm 0.05 \times 10^{16}$ erg s^{-1} cm^{-2} and 243 ± 3 km s^{-1}, respectively). The factor of $\sim$ 1.6 difference in the total flux between these two measurements may be explained by systematic uncertainties— the quoted uncertainty in the R07 flux measurement belies a factor of $\sim$ 2 systematic uncertainty (see discussion in Erb et al. 2006b) due to possible slit losses.

It is also possible to estimate the continuum flux of Q2343-BX415 from our flux calibrated spectra as an internal consistency check. The Hn5 continuum is 4.7×10^{-18} erg s^{-1} cm^{-2} $\mathring{A}^{-1}$, giving $m_{\rm AB}(1.76\,\mu{\rm m}) = 19.7$. Similar analyses of the spectra obtained using OSIRIS in 2007 June and August give $m_{\rm AB}(1.76\,\mu{\rm m}) = 19.8$ and 20.0, respectively. These values are consistent with each other and with that expected based on linear interpolation from broadband photometry ($m_{\rm AB} \sim 20.0$, see Table 6.2) to within 0.3 mag, in agreement with our estimate of the 30% uncertainty in flux calibration of the LGSAO data.

[7] It is conceivable, however, that such emission may simply be missed since we might expect to detect it at at a confidence level of only 2σ.

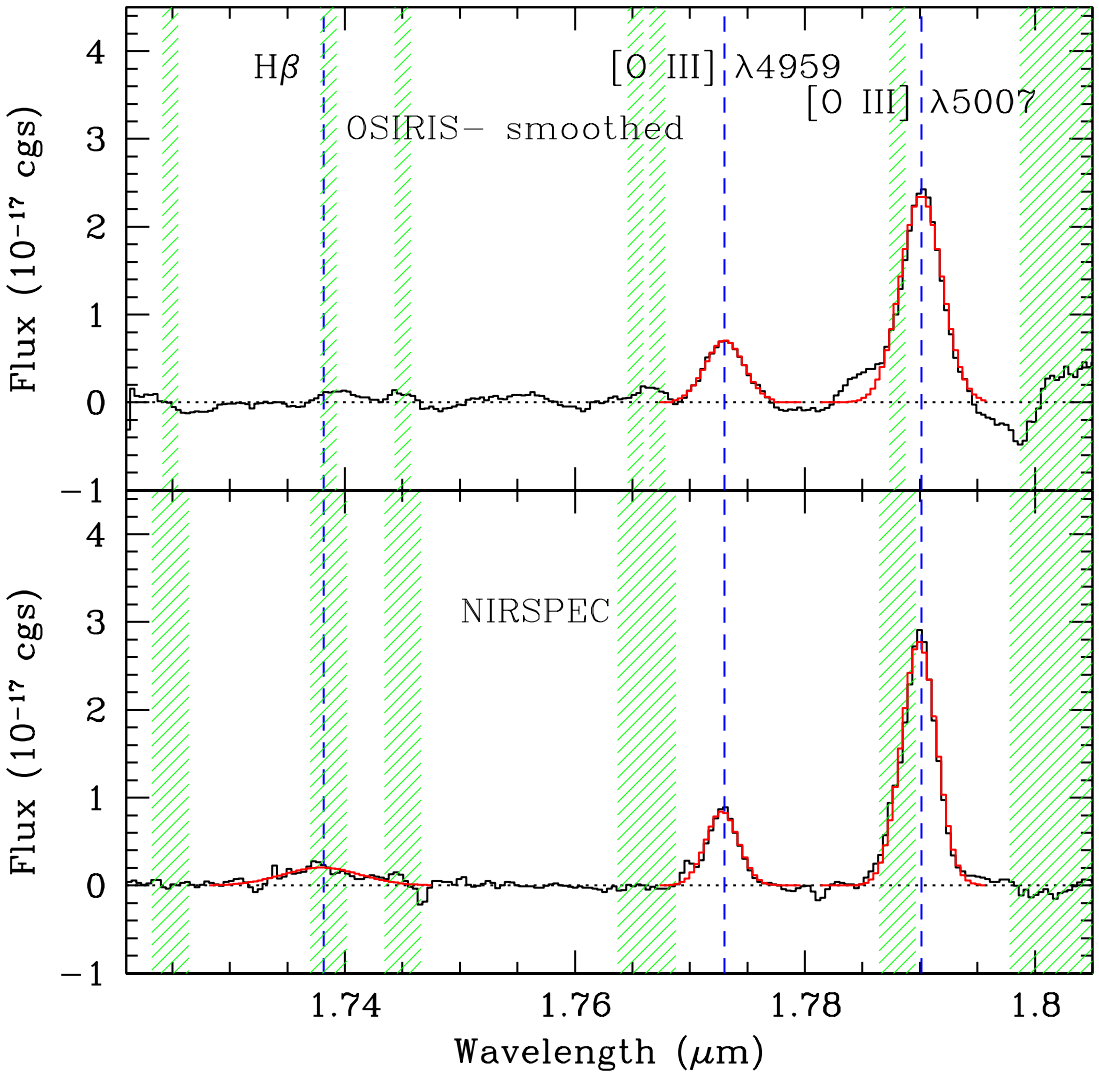

Figure 6.2 Plot of the long-slit NIRSPEC spectrum of Q2343-BX415 from R07 (lower panel), compared to the OSIRIS spectrum smoothed to match the NIRSPEC instrumental profile ($R \sim 1400$, FWHM 12.8 Å) and resampled to 4 Å pixel^{-1} (upper panel). Red lines represent Gaussian fits to the [O III] and Hβ emission lines. As in Figure 6.1, blue dashed lines indicate the fiducial [O III]and Hβ emission wavelengths at the systemic redshift of the QSO, while green hashed regions denote the wavelengths of particularly strong OH features (these contaminated wavelength ranges are broader in the NIRSPEC spectrum because of the lower instrumental resolution).

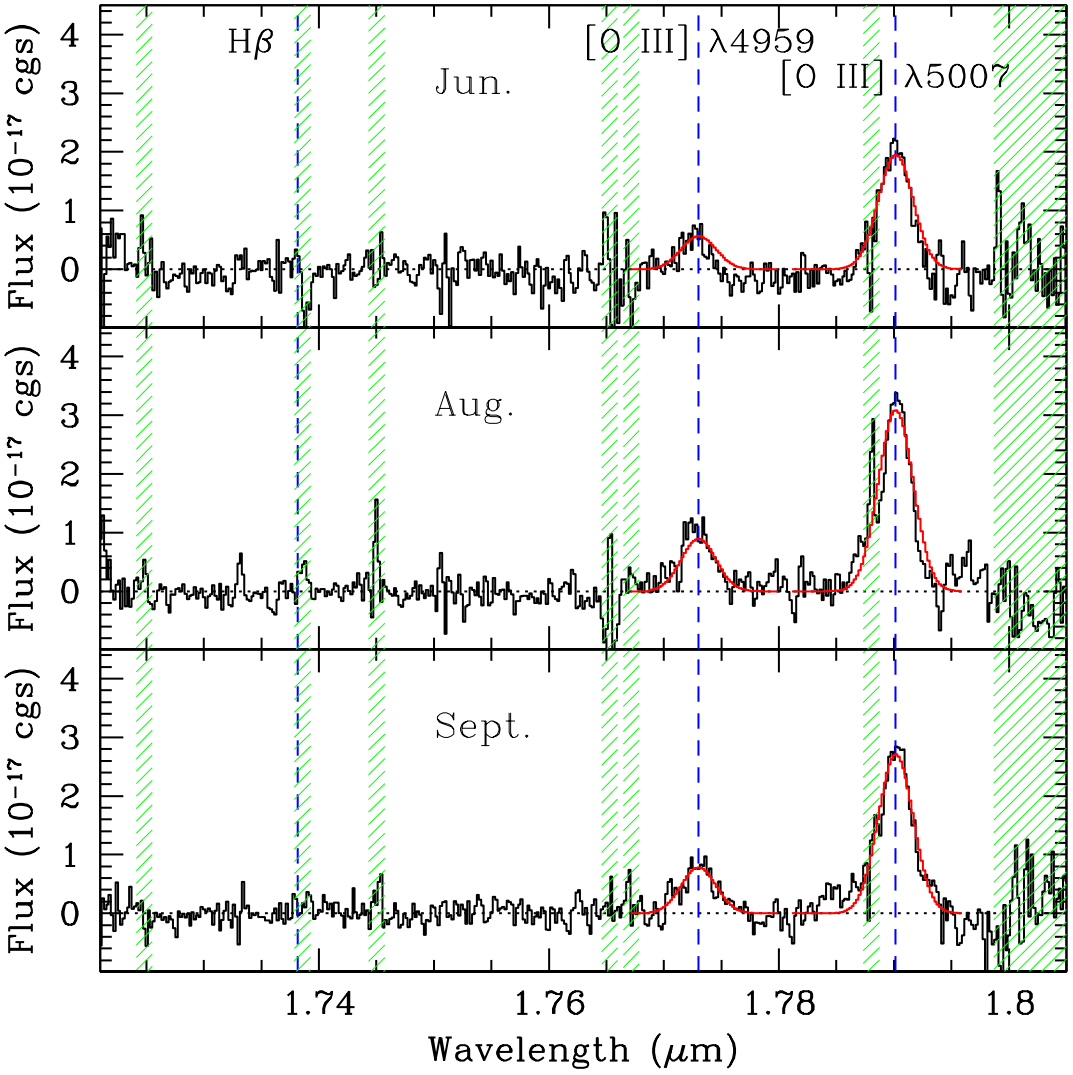

Figure 6.3 OSIRIS spectra of Q2343-BX415 obtained in 2007 June, August, and September. Colored lines are as in Figure 6.1, the model fit to the September data has been overplotted (red lines) for comparison on the June and August spectra and scaled to reflect the apparent [O III] flux in these spectra. A blue wing to the [O III] λ5007 emission is only apparent in the September spectrum. Note that stronger OH residuals (such as at 1.788 μm) are present in the June and August data as these data have poorer sky subtraction.

6.4 SPATIALLY RESOLVED STRUCTURE

In Figure 6.4 we show the spatial structure of [O III] emission in Q2343-BX415 by collapsing the data cube along the spectral axis within the 30 Å surrounding [O III] λ5007Å emission. While this structure is relatively circular, there is a pronounced extension towards the northwest of the QSO. In this section, we quantify the LGSAO PSF and subtract it from our data in order to best discern faint residual features.

6.4.1 Subtracting the LGSAO PSF

PSF characterization for LGSAO data is challenging, as the PSF is both pointing dependent and time variable. It has often been assumed (e.g., Law et al. 2006) that the general form of this PSF can be approximated by a 2-component profile composed of a diffraction-limited Airy core and a seeing-limited Gaussian halo with the relative fluxes of the two components dictated by the strehl ratio. However, we find (Fig. 6.5) that such a model has both too peaky a central flux and too much power at large radii to satisfactorily match our TT star observations. Instead, a Moffat model

$$I(r) = I_0(1 + (r/\alpha)^2)^{-\beta}, \tag{6.1}$$

with central FWHM scaling roughly as $\lambda^{-1/5}$ provides a better overall description of the LGSAO PSF. Nonetheless, for precise point-source subtraction it is preferable to use the observational PSF directly, as any idealized theoretical model will fail to account for distortions in the PSF.

Since the TT star was observed both at a different time (albeit by only minutes) and with a different instrumental configuration (on-axis versus off-axis TT correction to the wavefront), its FWHM is an imperfect match to that of the QSO and efforts to use the TT star for PSF subtraction result in a ring of residual flux around the central QSO resulting from this mismatch in the width of the respective PSFs (Fig. 6.5). Instead, the continuum image of the QSO itself is the ideal reference source because it is likely dominated by emission from the (effectively point-like) central accretion disk, and traces identical atmospheric and instrumental conditions as the [O III] emission. We therefore use the QSO continuum PSF to remove the central [O III] point source and search for residual extended [O III] emission.

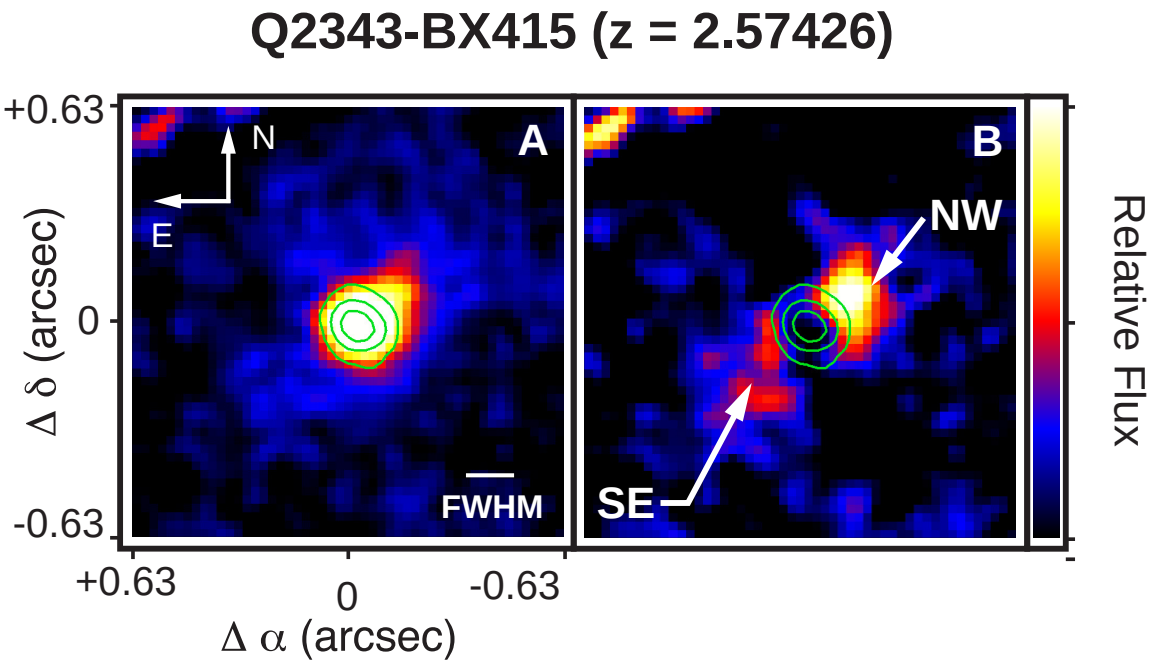

Figure 6.4 OSIRIS map of [O III] λ5007 Å nebular emission from Q2343-BX415. (A) Flux map (arbitrary linear scaling), (B) flux map after removal of the QSO continuum PSF (residual northwestern [NW] and southeastern [SE] features are labeled). Overlaid contours are derived from the continuum image as described in §6.4.1 and are linear in flux density. Individual pixels measure 25 mas, the total field of view in each frame is 1.25" × 1.25" (corresponding to 10.2 kpc at the redshift of Q2343-BX415). The FWHM of the continuum PSF after smoothing is 140 mas, indicated by the solid line in panel A. Note that the feature in the far NE corner is a noise artifact due to poor overlap in the dither sequence on the edge of the detector.

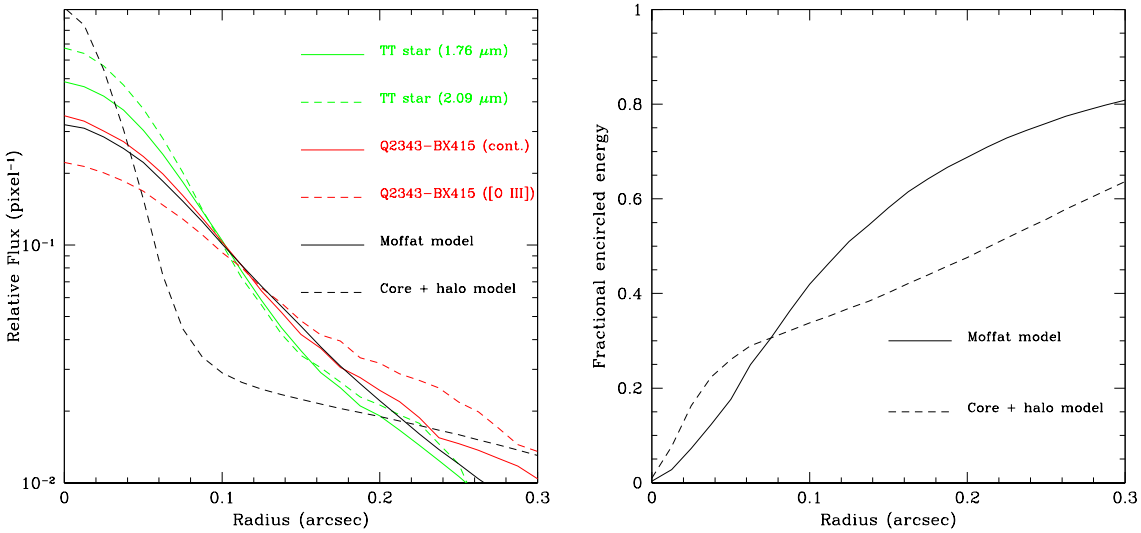

Figure 6.5 Left panel: Radial profiles for various theoretical and observational data. Solid and dashed green lines represent on-axis TT star observations at 1.76 μm and 2.09 μm, respectively (this latter observation is included to illustrate the wavelength dependence of the PSF). The Q2343-BX415 continuum and [O III] profiles are plotted as solid and dashed red lines, respectively, note the mismatch between the two indicating the existence of extended [O III] substructure. These four observations were obtained in similar atmospheric conditions. Black lines represent a Moffat PSF model (solid black line, $\alpha = 92$ mas and $\beta = 1.6$) fit to the Q2343-BX415 continuum profile and a 2-component core+halo model (dashed black line, assuming 30% strehl). All curves have been normalized by total flux, note also that both the Moffat and core+halo models have been convolved with a Gaussian kernel (50 mas FWHM) to match the processing of the observational data. Right panel: Fractional energy encircled as a function of radius for the two theoretical models.

Interpolating the data to a 4x oversampled "supercube" (in order to improve sampling of the psf) we create a continuum map of the QSO by median stacking the $\sim 50\%$ of spectral channels which are well separated in wavelength from both QSO emission lines and strong atmospheric OH features. We set all negative values in this continuum map to zero in order to guarantee that no artificial positive signals are introduced into the residual map via subtraction. At each spectral channel, we then subtract this continuum map scaled by a factor α_2/α_1, where α_1 is the sum of all pixels in the continuum image which fall within a 5 by 5 pixel box centered on the quasar, and α_2 is the sum of all corresponding pixels in the spectral channel. In the unlikely event that α_2 is ever negative (i.e., due to pixel noise far from the emission lines), no subtraction is performed. This residual supercube is then interpolated back to the original pixel size to create the residual data cube.

6.4.2 Extended Emission Regions

The dominant feature in this residual [O III] map after subtraction of the central QSO PSF (Fig. 6.4b) is a compact, high surface-brightness flux peak located 160 mas (1.3 kpc at $z = 2.57$) in projection to the northwest (NW) of the central QSO. This source is marginally resolved with a FWHM $\lesssim$ 200 mas, implying a physical diameter of $\lesssim$ 140 mas (1 kpc) after quadrature deconvolution of the 140 mas PSF. There is also a lower surface brightness feature centered 230 mas (1.9 kpc) to the southeast (SE) of the QSO. In contrast to the NW feature, this SE emission is diffuse and extended, with a major axis of 0.41" (3.3 physical kpc) after deconvolution of the PSF. Unfortunately, it is not possible to compare this spatial structure to those data obtained in 2007 June/August as these earlier observations used the 100mas lenslet sampling scale, which is insufficient to comparably characterize and subtract the central QSO PSF. Similarly, we do not expect to have detected either of these features in previous NIRSPEC spectroscopy (such as that of R07) since both are within 0.25" of the QSO, while the typical seeing-limited resolution of NIRSPEC is $\sim$ 0.6".

Summing all of the spectral data within boxes (0.25" $\times$ 0.25" for the NW feature and 0.35" $\times$ 0.35" for the SE) placed around these emission features, we construct integrated spectra (Fig. 6.6) of the subregions. Gaussian fitting to the emission lines (detailed in Table 6.3) indicates that both features are nearly coincident in redshift with the central QSO; the NW feature is redshifted by 53 ± 7 km s^{-1} while the SW is blueshifted by 51 ± 16

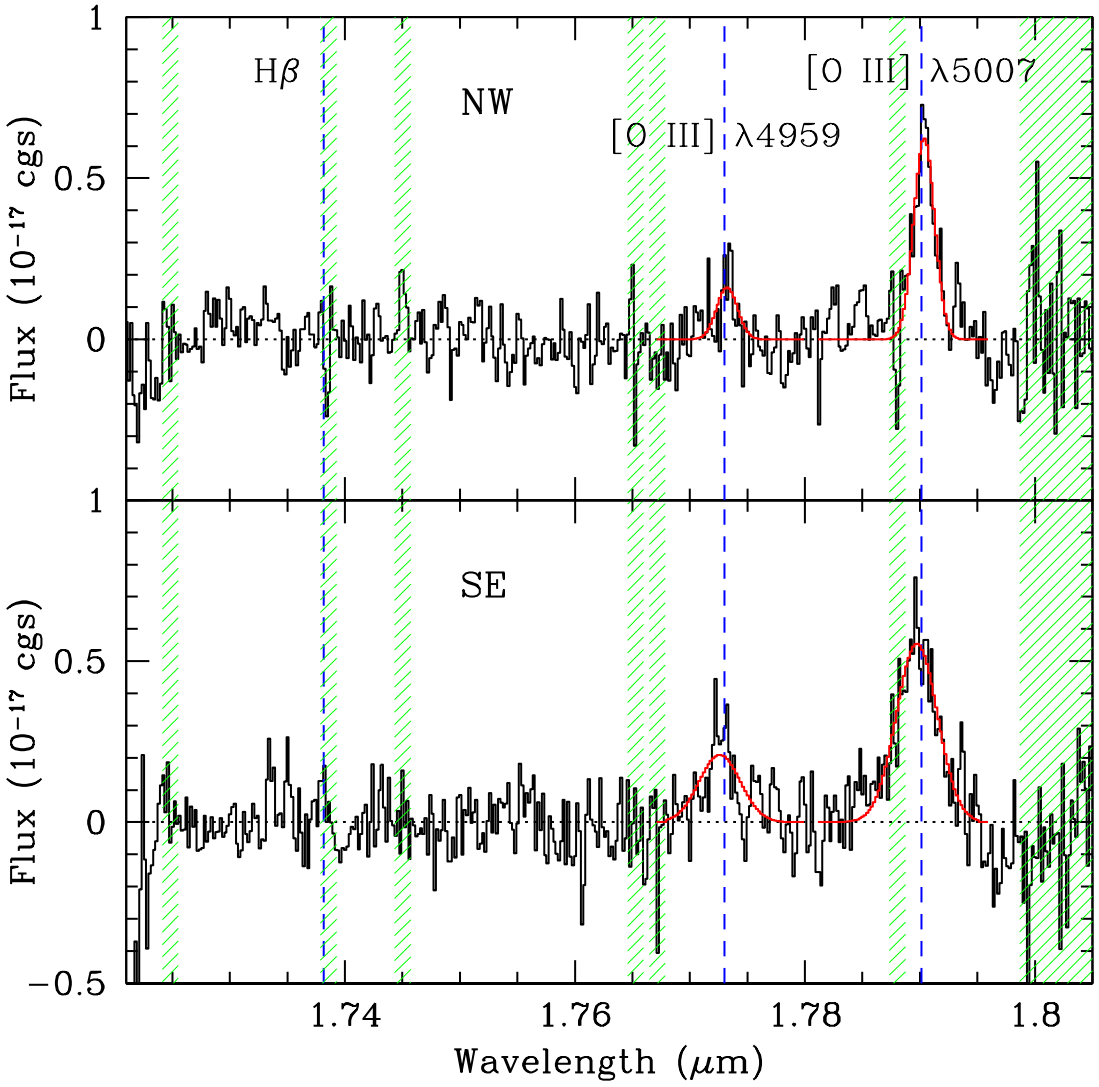

Figure 6.6 Spectra of the residual NW and SE regions shown in the PSF-subtracted [O III] map (Fig. 6.4b). Colored lines are as in Figure 6.1.

km s^{-1} relative to systemic. The SE feature is broad with $\sigma_{\rm v} = 297 \pm 22$ km s^{-1}, i.e. comparable to that of the central QSO. In contrast, the NW emission profile is significantly narrower with an intrinsic width $\sigma_{\rm v} = 148 \pm 11$ km s^{-1}, 10σ less than the gas probed by the central QSO line of sight.

Precise flux calibration for these features is at least as challenging as for the primary QSO spectrum, and the global flux calibration is bootstrapped relative to the flux of the central QSO spectrum. Within the global systematic uncertainty of $\sim 30\%$, we conclude that the [O III] λ5007 flux of the NW and SE features is $f_{5007} = 1.4 \pm 0.1 \times 10^{-16}$ and $2.4 \pm 0.1 \times 10^{-16}$ erg s^{-1} cm^{-2}, corresponding to luminosities $L_{5007} = 7.7 \times 10^{42}$ and 1.3×10^{43} erg s^{-1}, respectively. Based on the RMS of the spectra (1.14×10^{-18} erg s^{-1} cm^{-2} Å^{-1}) it is also possible to constrain the strength of narrow-line Hβ emission. While this is somewhat complicated by the presence of a strong atmospheric OH feature at the Hβ wavelength, we estimate a 3σ limit $\log([\mathrm{O\,III}]/H\beta) \gtrsim 1.0$. Finally, while continuum emission is detected in neither of the spectra of these residual emission features, we use the RMS to determine the 3σ constraint that $m_{\rm AB}(1.76\,\mu\mathrm{m}) \gtrsim 23.5$.

6.4.3 Detection Limits

Bootstrapping from the RMS of the residual data cube, we estimate that the residual map shown in Figure 6.4 is sensitive to narrow-line emission features brighter than $\sim 4 \times 10^{-15}$ erg s^{-1} cm^{-2} arcsec^{-2} located between ~ 0.5 and 10 kpc in projection from the central QSO. Interior to this radius any features will be indistinguishable from the central point source, while exterior to this radius we are limited by our effective field of view. Subject to these constraints, we may therefore conclude that no other emission features are present in the Hn5 spectral window.

6.5 DISCUSSION

6.5.1 SE Feature

The spectrum of the diffuse SE emission feature is similar to that of the central QSO (although with peak emission wavelength blueshifted by 51 ± 16 km s^{-1}), with velocity dispersion $\sigma_{\rm v} = 297 \pm 22$ km s^{-1}. Indeed, we cannot categorically reject the possibility

that this feature is simply a residual artifact of an imperfect subtraction of the PSF of the central QSO. However, we feel that this explanation is unlikely as the velocity offset has greater than 3σ significance, and Monte Carlo tests indicate that such a large shift is expected to occur in less than 1% of cases for a spectrum with the observed RMS and line flux. Instead, the SE feature likely traces ambient gaseous substructure within the NLR which is ionized by the strong radiation field of the central QSO. Indeed, the derived line ratio limit $\log([\mathrm{O\,III}]/\mathrm{H}\beta) \gtrsim 1$ is consistent with photoionization by a power-law spectral energy distribution similar to that expected from a central AGN (Baldwin et al. 1981, their Fig. 5).

The overall spatial structure of the NLR is consistent with expectations, with the centroid of the SE feature located 230 mas (1.9 kpc) in projection from the QSO. As discussed by Bennert et al. (2002, and references therein) the radius of the NLR,[8] as traced by *HST* imaging in nearby ($z \lesssim 0.3$) QSOs, is typically $r_{\mathrm{NLR}} \sim 2 - 5$ kpc, scaling roughly with the square root of the [O III] luminosity and with evidence for filamentary structure. I.e.,

$$\log R_{\mathrm{NLR}} = (0.52 \pm 0.06) \log L_{5007} - (21.5 \pm 2.6) \tag{6.2}$$

where R_{NLR} and L_{5007} are in units of kpc and erg s^{-1}, respectively. Given that $L_{5007} = 5.3 \times 10^{43}$ erg s^{-1} for Q2343-BX415 (Table 6.3), if this local scaling relation holds we might expect $R_{\mathrm{NLR}} = 17.2 \pm 3.7$ kpc. If we instead adopt the flatter relation of Schmitt et al. (2003) we expect $R_{\mathrm{NLR}} = 4.4 \pm 1.3$ kpc. While we do not expect to detect flux out to such faint surface brighnesses as probed by these HST data (limiting surface brightness $\sim 10^{-15}$ erg s^{-1} cm^{-2} arcsec^{-2}; Bennert et al. 2002), the overall scale and filamentary structures are comparable to the local relation.

The kinematic structure of the NLR (and hence the observed FWHM of [O III] emission) is dictated by the velocity distribution among its component unresolved clouds. The overall velocity width along a given line of sight can (in the low redshift universe) increase, decrease, or remain approximately constant with increasing radius from the central AGN, depending on the detailed structure of the NLR and degree of anisotropy of the velocity dispersion tensor (see, e.g., McCarthy et al. 1996, Leipski & Bennert 2006, Rice et al. 2006), the

[8] Defined by Bennert et al. (2002) as roughly the distance at which surface brightness declines to 0.3% of the central value.

detailed modeling of which is beyond the scope of this work. The similarity of $\sigma_{\rm v}$ for the off-nuclear SE feature and the central NLR (i.e., within 2 σ) is therefore consistent with observations of low redshift counterparts. Given the similarity between NLR emission and radio outflow morphology for local Seyfert galaxies (Capetti et al. 1996, Falcke et al. 1998) and for the $z = 0.163$ QSO PG0157+001 (Bennert et al. 2002), future radio wavelength observations could help to constrain the geometry of this system. Cursory inspection of the NVSS catalog (Condon et al. 1998) reveals no sources within 60" however, implying a (unresolved) radio flux density limit of 0.3 mJy at 1.4 GHz for any such outflows.

In typical Seyfert galaxies, the NLR is suffiently compact to be illuminated by the central AGN, yet sufficiently large that its kinematics are predominantly governed by the gravitational forces of the stellar bulge (Greene & Ho 2005). Using simple virial arguments, it is therefore possible to combine our analyses of the spatial and kinematic structure of the NLR to estimate the dynamical mass of Q2343-BX415 as

$$M_{\rm dyn} = \frac{C\sigma_{\rm v}^2 r}{G} = 1.4 \times 10^{11} M_{\odot}, \tag{6.3}$$

taking $r = 1.9$ kpc, the central velocity dispersion $\sigma_{\rm v} = 252$ km s^{-1}, and a constant geometric prefactor $C = 5$ appropriate for a uniform sphere. Adopting the $M_{\rm BH} - \sigma_{\rm v}$ relation of Tremaine et al. (2002, see also discussion by Shields et al. 2003), this also suggests that the central QSO has a mass $M_{\rm BH} \approx 3 \times 10^8 M_{\odot}$. The bolometric luminosity of Q2343-BX415 ($L_{\rm Bol} = 8 \times 10^{12} L_{\odot}$, §6.3.1) is consistent with approximately Eddington-rate accretion ($L_{\rm Edd} = 1.1 \times 10^{13} L_{\odot}$) onto such a supermassive black hole.

6.5.2 NW Feature

The narrow-lined NW feature has a velocity width ($\sigma_{\rm v} = 148 \pm 11$ km s^{-1}) roughly half that of the central QSO and comparable to that observed in typical star-forming galaxies at similar redshifts ($\sigma_{\rm v} \sim 110$ km s^{-1}, Erb et al. 2006c). Since we detect neither Hβ nor continuum emission from this feature and do not have a measurement of the [N II]/Hα diagnostic ratio, it is not possible for us to determine whether this emission traces gas ionized predominantly by star formation (with a velocity distribution tracing the gravitational potential thereof) or by the central AGN. While we cannot conclusively distinguish between

these possibilities at present, it is worthwhile to explore the consequences of associating this feature with a star-forming region. Indeed, we note both the spatial compactness of this structure and the striking similarity of the Q2343-BX415 system to PG1307+085 which shows similar evidence for kinematically broad NLR emission along one direction of a long-slit from the central QSO paired with kinematically narrow emission from an active star formation region in the other direction (Leipski & Bennert 2006).

The emission line luminosity of the source is consistent with such an interpretation; the [O III] luminosity overlaps with that of the $z \sim 3$ LBGs studied by Pettini et al. (2001), although it is slightly higher than the average of their sources. Despite our limited coverage of diagnostic emission lines, we can still obtain a rough estimate of the metallicity of the H II region, under the assumption that it is ionised predominantly by a stellar radiation field. Our data provide a firm lower limit to the $R23 = ([\mathrm{O\,II}] + [\mathrm{O\,III}])/\mathrm{H}\beta$ index of Pagel et al. (1979), given that Hβ is undetected and [O II] λ3727 is not covered by our observations. We find $\log R23 \gtrsim 1.1$, a value that is in the turn-over region in plots of the oxygen abundance versus $\log R23$ (see, for example, Figure 6 of Pettini et al. 2001). With the calibration of the $R23$ index by Pagel et al. (1979), we deduce 12+log(O/H)=8.0; higher *and* lower oxygen abundances would result in smaller values of R23. For comparison, the current estimate of the solar abundance of oxygen is $(12 + \log(\mathrm{O/H})_\odot = 8.66$ (Asplund et al. 2004), from which we conclude that the metallicity of the NW feature is $Z \sim \frac{1}{5} - \frac{1}{7}\, Z_\odot$.

Such low metallicity systems are poorly represented in current samples of $z \sim 2$ galaxies. For example, the median metallicity of the star-forming galaxies studied by Erb et al. (2006a) is $Z \sim 0.6 Z_\odot$. Although the relation between stellar mass and metallicity is not well defined in the low mass bin (for which metallicity estimates are particularly challenging), a simple extrapolation of the Erb et al. (2006a) mass-metallicity relation implies that *statistically* this object probably has a very low stellar mass $M_\star < 10^9 M_\odot$. Our non-detection of the stellar continuum ($m_{\mathrm{AB}}(1.76\mu\mathrm{m}) \gtrsim 23.5$, §6.3.2) is consistent with such a low stellar mass as similarly low-mass galaxies frequently have K-band continuum magnitudes $m_{\mathrm{AB}} \gtrsim 23.5$, in contrast to their more massive counterparts which typically have $m_{\mathrm{AB}} \lesssim 23.0$ (Erb et al. 2006c).

Using the Moustakas et al. (2006) survey of nebular emission lines in a large sample of $z \sim 0.1$ SDSS galaxies, it is possible to estimate a limiting star formation rate based on the

observed [O III] luminosity. Adopting the most pessimistic conversion $\log(10^{-41}\, L_{[\mathrm{O\,III}]}\ /\ \mathrm{SFR}_{H\alpha}) = 0.5$ (Fig. 13 of Moustakas et al. 2006), we determine a lower limit $\mathrm{SFR}_{H\alpha} \gtrsim 25 M_{\odot}\ \mathrm{yr}^{-1}$ and a SFR surface density $\Sigma \gtrsim 32 M_{\odot}\ \mathrm{yr}^{-1}\ \mathrm{kpc}^{-2}$. Given our complete absence of knowledge regarding the continuum (or indeed, more than a single spectral line) properties of the NW feature separate from the central QSO, it is not possible to make a realistic attempt to correct this ballpark estimate for extinction. This uncorrected, limiting star formation rate is nevertheless similar to the average uncorrected value $<\mathrm{SFR}_{H\alpha}>= 22 \pm 14 M_{\odot}\ \mathrm{yr}^{-1}$ observed for bright $z \sim 2$ galaxies by Erb et al. (2006b).

Such a high surface density of star formation is consistent with producing the PDLA observed by R07 in its resulting starburst driven outflows. As seen from the rest frame of the star formation, the gas in the PDLA (as traced by low-ionization absorption lines) is outflowing at speeds up to ~ 300 km s^{-1} , somewhat slower than values frequently observed for $z \sim 2-3$ star forming galaxies with such star formation rates (~ 700 km s^{-1} ; Steidel et al. *in prep*). The metallicity of the PDLA gas ($\frac{1}{5}\, Z_{\odot}$) and the current star formation regions ($\frac{1}{5} - \frac{1}{7}\, Z_{\odot}$) is also comparable. While the comparative metallicities of the stars and the gas in $z \sim 2-3$ galaxies has not been well studied in many cases, we note the case of MS1512-cB58 (Pettini et al. 2000), for which stellar and gas metallicities are also observed to be comparable. Although the physical relation between the NW feature and the PDLA (and the relation of both to the QSO environment) cannot be categorically proven, we note that we have not detected any alternative source within our field of view capable of both producing and ionizing the PDLA. As discussed by R07, the presence of excited fine structure lines such as C II* in the PDLA spectrum implies ionization of the PDLA by an intense radiation field shortward of the Lyman limit and close physical proximity to the QSO (8 – 37 kpc).

Our mass and star formation rate estimates however contain considerable uncertainties due to progressively bootstrapped estimates from local relations of uncertain applicability. In addition, the star-forming region may cover the central QSO. While the light from such regions would represent a correspondingly higher line flux and net star formation rate, we are insensitive to such an additional component as this light would be indistinguishable from the central QSO and therefore subtracted off from our final spectrum. Indeed, our present estimates of the stellar and gaseous masses of this star-forming region are insufficient to

explain the dynamical mass of the NW feature alone ($M_{\rm dyn} \sim 1.3 \times 10^{10} M_{\odot}$) implied by $\sigma_{\rm v} = 148$ km s^{-1}. This mismatch may itself be evidence for a greater stellar and/or gas mass than we have inferred, or may suggest that the dynamics of the gas illuminated by star formation are driven more by the gravitational potential of the entire QSO system than by just the local star-forming mass.

Despite these uncertainties, the comprehensive picture emerging is that we may be witnessing moderate star formation in a metal-poor gas whose dynamics are more chaotic than implied by the inferred stellar mass. In combination with the extremely small separation between the star-forming region and the QSO in both projected distance and redshift space, this suggests the probability this star formation is occuring either in the QSO host galaxy itself or in the nucleus of a gas-rich galaxy in the final stages of merging with the (unseen) QSO host galaxy. Indeed, by analogy with the low-redshift QSO population such a scenario may provide a natural explanation of both the currently observed burst of star formation and the triggering of QSO-mode instability.

6.6 CONCLUSIONS

We have presented spatially resolved observations of Q2343-BX415 which show extended NLR emission ionized by near-Eddington rate radiation from the central QSO ($M_{\rm BH} \approx 3 \times 10^8 M_{\odot}$) and possible evidence for star formation in a region close to the QSO in both redshift (~ 50 km s^{-1}) and projection (~ 1 kpc). If genuine, this star formation is occurring in a low metallicity ($Z \lesssim \frac{1}{5} Z_{\odot}$) gas with a (uncorrected) star formation rate of $\gtrsim 25$ $M_{\odot}$ yr^{-1} and a kinematic dispersion of 146 km s^{-1}. These properties are broadly consistent with observations of low stellar mass galaxies ($M_* \lesssim 10^9 M_{\odot}$) at redshift $z \sim 2-3$. While appreciable uncertainties remain (e.g., concerning the non-detection of Hβ, the blending of the star forming feature with the PSF of the central QSO, etc.), and we cannot categorically eliminate the possibility of chance superposition of the QSO/PDLA/star-formation features, we favor the interpretation that this star formation is physically related to the QSO and produces the PDLA observed in the QSO spectrum in relatively quiescent (~ 300 km s^{-1}) starburst-driven outflows. Assuming that (analogously to local counterparts) the QSO was produced by a gas-rich merger, the star formation may either be occuring in the QSO host galaxy itself or in shocked gas contributed by the merging galaxy. In either case it is doubtful

that the currently observed star formation traces the entirety of the stellar mass, and future observations of this complex system will doubtless continue to provide new insights.

D.R.L. appreciates helpful discussions with Mara Salvato, Brad Peterson, and Matthew Britton. The authors also thank Randy Campbell, Al Conrad, David LeMignant, and Jim Lyke for their invaluable help obtaining the OSIRIS observations presented herein. D.R.L. and C.C.S. have been supported by grant AST-0606912 from the US National Science Foundation. Finally, we wish to extend thanks to those of Hawaiian ancestry on whose sacred mountain we are privileged to be guests.

Table 6.1. General Information

Name	RA (J2000)	DEC (J2000)	Observed	Time[a]	$R_{\rm TT}$[b]	$\theta_{\rm TT}$ [c]	$\theta_{\rm seeing}$ [d]	PA [e]
Q2343-BX415	23 46 25.425	+12 47 44.25	Sep '07	1.5	16.8	17	0.7	120

[a]Total observing time in hours.

[b]R-band magnitude of TT star for LGSAO correction.

[c]Angular separation (arcseconds) of TT star from target.

[d]Average K-band seeing (arcseconds) during observation.

[e]Position angle (degrees) of the OSIRIS IFU.

Table 6.2. Q2343-BX415 Photometry

Band	$\lambda_{\rm rest}$	$m_{\rm AB}$
$U_{\rm n}$	993 Å	21.22 ± 0.05
G	1337 Å	20.32 ± 0.05
$\mathcal{R}$	1911 Å	20.22 ± 0.05
J	3525 Å	20.2 ± 0.1
Hn5	4938 Å	19.8 ± 0.2[a]
$K_{\rm s}$	6211 Å	19.9 ± 0.1
4.5μm	1.26μm	19.66 ± 0.07
8.0μm	2.24μm	18.86 ± 0.07
24μm	6.72μm	17.46 ± 0.06[b]

[a]Average of values derived from the June/Aug/Sept OSIRIS spectra.

[b]$f_{24\mu{\rm m}} = 375 \pm 21$ μJy.

Table 6.3. Emission Lines

Region	Wavelength[a]	z[b]	Δv[c]	σ_v[d]	f[e]	L[f]
QSO	17900.7 ± 0.7	2.57426 ± 0.00014	—	252 ± 10	9.6 ± 0.3	53.3 ± 1.7
NW	17904.1 ± 0.4	2.57494 ± 0.00008	+53 ± 7	148 ± 11	1.4 ± 0.1	7.8 ± 0.6
SE	17897.7 ± 0.9	2.57365 ± 0.00018	-51 ± 16	297 ± 22	2.4 ± 0.1	13.3 ± 0.6

[a]Gaussian 5008.4 Å emission line peak in the observed, vacuum frame (Å).

[b]Vacuum heliocentric redshift, quoted uncertainty is stochastic. Systematic uncertainty is 0.00032.

[c]Rest-frame offset from QSO systemic redshift (km s^{-1}).

[d]Velocity dispersion (corrected for instrumental broadening) in units of km s^{-1}.

[e]Total line flux in units of 10^{-16} erg s^{-1} cm^{-2}. Uncertainties quoted are based on random uncertainties, global systematic uncertainty is $\sim 30\%$.

[f]Total line luminosity in units of 10^{42} erg s^{-1}. Uncertainties quoted are based on random uncertainties, global systematic uncertainty is $\sim 30\%$.

Chapter 7

Epilogue

7.1 TOWARDS A PHYSICAL MODEL OF GALAXY FORMATION

According to basic theories of galaxy formation (e.g., White & Rees 1978; Mo, Mau, & White 1998; see also a lucid review by Baugh 2006), hot-mode accretion dominates the gas accretion history of galaxies. Once a sufficiently massive dark matter halo has virialized, gas collapses through the virial radius of the potential well, heating via shocks to the virial temperature of the host halo. As this gas cools over time (largely by collisionally excited line radiation for haloes with 10^4 K $< T < 10^6$ K, and bremsstrahlung radition for haloes with $T \sim 10^7$ K; White 1994) it collapses to form a rotating disk supported by angular momentum which the cooled gas has been unable to shed. This gaseous disk gradually grows over time as gas at progressively greater radii is able to cool and collapse, and is posited to be the home of the bulk of active star formation.

How, then, should we interpret the high local velocity dispersion and lack of rotating structures in recent observations of the ionized gas? While some relatively convincing candidates for massive rotating systems can be found (e.g., Genzel et al. 2006; van Starkenburg et al. 2008) such systems appear to be the exception rather than the norm. Is the rotationally supported disk theory incorrect, or are we merely unable to distinguish the rotational signature for many galaxies?

One possibility suggested by the early simulations of Noguchi et al. (1999) may be that efficient cooling mechanisms could lead to early fragmentation of gas-dominated disks

into self-gravitating clouds $\sim 10^9 M_\odot$ which can sink to the center of the galaxy in a few hundred Myr through dynamical friction. In gas-rich galaxies such as those of our target sample, these massive gaseous clumps may actually drive the dynamical evolution of the entire baryonic component. Star formation occurring in such self-gravitating, sinking clouds might naturally give rise to the morphologically irregular, multiple component morphologies observed for typical star forming galaxies at $z \sim 2$, and provide a mechanism for bulge formation in the massive starburst (SFR $\sim 100\ M_\odot\ \mathrm{yr}^{-1}$) predicted to occur (e.g., Immeli et al. 2004ab) when these gas-rich clouds merge in the galactic center. Despite the cold nature of the original disk, shocks and heating from supernovae in these gaseous clumps may heat the ionized gas to the point that it no longer retains the original rotational signature.

In a more recent series of simulations, Bournaud et al. (2007) similarly claim that "clump-cluster" galaxies (their name for the multi-component morphologies which we described in Chp. 2) are consistent with resulting from the fragmentation of unstable primordial disks, finding that simulated clumps constitute roughly 40% of the baryonic mass of the galaxy and last for ~ 400 Myr. As discussed by Erb et al. (2006c) such timescales are similar to the inferred ages of typical $z \sim 2-3$ star forming galaxies (see also Table 5.4), as are the characteristic gas fractions. The velocity fields of these simulated galaxies are highly disturbed with large local velocity dispersions and rotational signatures which can frequently be difficult to detect. Contrary to the central collapse model of Noguchi et al. (1999) and Immeli et al. (2004ab), however, Bournaud et al. (2007) find less overall clump migration and propose that a significant fraction of the mass of the clumps is released gradually into the disk itself over their dynamical lifetimes. Given the importance of gas-mode instabilities in clump formation, we suggest that the stellar mass may play a role in regulating the stability of these early disks when a suitably massive population has formed such that the gas disk no longer dominates the baryonic mass of the system. Such a stabilizing role provides a natural explanation for the increased prevalence of observable velocity shear in systems with a greater stellar mass, and the overall buildup of such mass over cosmological time may in turn explain how star-forming galaxies evolve out of this dispersion-dominated phase by redshifts $z \sim 1-1.5$ (see, e.g., Wright et al. *in prep*) and come to resemble the local Hubble sequence.

Alternatively, the multiple clumps of high-dispersion star-forming regions could be ob-

servational evidence for gas accretion via cold flows (e.g., Kereš et al. 2005; Dekel & Birnboim et al. 2006; Birnboim et al. 2007). In this scenario, cold gas can be funneled at variable rates from inhomogenous cosmological filaments directly into the center of the galaxy, where a high collision probability with gas packets from other filaments can dissipate their kinetic energy. The physical structure which might result from such an accretion mechanism is unclear, especially given the limited ability for numerical models to resolve the relevant spatial scales. Given the asymmetric nature of such flows, radial motions might be damped less efficiently than for hot spherical accretion, resulting in a higher velocity dispersion. Such an accretion model would be necessarily complex, with shocked gas both promoting star formation in some locations and the heating of the cold gas inhibiting star formation in others. If there were a central gas reservoir then newly accreting gas falling along these filaments may cause irregular "hot spots" of star formation where they collide with the central gas supply.

As discussed by Dekel & Birnboim (2006), there is a characteristic halo mass $\sim 10^{12} M_{\odot}$ below which gas is accreted predominantly through cold flows, and above which the formation of a stable virial shock permits hot-mode gas accretion to contribute a larger percentage of the total accretion rate. Intriguingly, we note that this mass is comparable to the $10^{11.8} - 10^{12.2} M_{\odot}$ haloes in which $z \sim 2$ BX galaxy sample reside, as derived from clustering statistics by Adelberger et al. (2005a). Our mass-dependent kinematics may therefore be probing the transition between cold-flow and hot spherical-mode accretion, with the mechanism of how gas is accreted dictating whether or not a rotating disk can be formed.

Of course, the observed multiple-clump morphologies and unusual kinematics could simply be a result of prevalent merger activity which prevents the formation of a stable thin disk at early times (e.g., Ostriker 1990). In the local universe, ULIRGS (whose multiple nuclei and tidal features may signify major gas-rich mergers; e.g., Sanders et al. 1988; Bushouse et al. 2002) such as Mrk 273 and IRAS 15250+3609 show large velocity dispersions with little resolved kinematic substructure in the regions of brightest Hα emission, despite relatively strong (~ 200 km s^{-1}) and highly disturbed features in lower surface brightness regions (Colina et al. 2005). Indeed, numerous morphological studies (e.g., Conselice et al. 2003a) have interpreted the irregular morphologies of $z \sim 2$ galaxies as evidence for such major mergers, and some of our own kinematic data may further bolster this case in specific

instances (e.g., HDF-BX1564). However, it seems perhaps improbable that major mergers can provide the explanation for the high velocity dispersion of *every single galaxy* at redshift $z \sim 2$ observed by ourselves, Erb et al. (2006c), Genzel et al. (2008, and references therein), van Starkenburg et al. (2008), and other groups. Since we might expect merging galaxies to spend the majority of their time at large separations from each other, it would also be curious that almost the entire $z \sim 2$ star-forming galaxy population consists of *close* major mergers. Alternatively, the heating element might be provided by merging lumps of dark matter with no observable baryonic tracer. Such lumps can inflate the velocity dispersion of disk galaxies in the local universe (e.g., Benson et al. 2004), and their effects would likely be stronger at higher redshifts when dark matter haloes were merging more rapidly (e.g., Zentner & Bullock 2003; Fakhouri & Ma 2008). By inflating the velocity dispersion of putative disks in all directions (and not simply perpendicular to the disk), such mergers may help mask weak rotational signatures, but it is not obvious how to interpret the observed relation between velocity shear and stellar mass. While disks may be more resilient to disruption in larger galaxies, these larger galaxies (residing in larger halos) may also be merging with larger dark matter clumps.

Given these numerous possibilities for the physical state and accretion history of galaxies at $z \sim 2$, it may be advisable to avoid classifying galaxies into the broad categories of either "disks" or "mergers" which have recently prevailed in the literature under the assumption that we *ought* to see one or the other. Instead, high-dispersion systems may simply be a natural consequence of the physics of gas-dominated systems during early phases of galaxy formation and as such provide intriguing constraints on theoretical models.

7.2 CONCLUDING REMARKS

In closing, we note that the work presented here naturally suggests numerous future avenues of investigation. Most immediately, the OSIRIS LGSAO data presented in Chp. 5 are still being analyzed and are expected to yield significantly expanded and substantive discussions of kinematic models than have been presented here. Similarly, Chp. 6 leaves open the nature of the nebular emission surrounding QSO Q2343-BX415. Whether this emission arises as a result of star formation (possibly in the QSO host galaxy) or in a clumpy NLR may be determined directly via measurement of the spectroscopic [N II]/Hα emission line ratio.

These measurements were obtained in June 2008 and await only the time to analyze them.

In the longer term, we have demonstrated that current theoretical models of galaxy formation may fail to explain the observed properties of galaxies at redshift $z \sim 2$, and further effort is necessary to characterize what model *is* the best description of their kpc-scale structure and kinematics. In particular, what is the *general* reason for the observed kinematic properties? Is this feature common to all $z \sim 2$ galaxies or is it a byproduct of our selection of rapidly star-forming sources? How do extremely faint and/or dusty galaxies fit into this picture? Is there a discrete property (e.g., baryonic mass, dark matter distribution, prevalence of cold versus hot mode accretion) which produces a strong stabilizing effect on the distribution and kinematics of star forming regions?

Some of these questions will be addressed in the near future by using *HST*-WFC3 to map the distribution of the stellar mass in hundreds of similar galaxies as a part of our upcoming Cycle 17 program HST-11694 (PI: Law). To a degree however, our experience has demonstrated the limitations of current technology for probing the spatially resolved features of high-redshift galaxies, and the tremendous demands of LGSAO observing time required to adequately detect and characterize the kinematics of redshift $z \sim 2$ galaxies may preclude significant additions to the sample presented herein (for which 18 allocated nights of observing were required) in the immediate future. Instead, such questions are some of the primary science drivers for next-generation facilities such as the Thirty Meter Telescope (TMT). Building on the knowledge acquired from our preliminary work, instruments such as IRIS and IRMOS (benefiting from greatly increased collecting area, improved adaptive optics technology, and multiplexing capabilities) will be well-equipped to pursue answers to the questions which we have just begun to frame.

Bibliography

Abraham, R. G., Tanvir, N. R., Santiago, B. X., Ellis, R. S., Glazebrook, K., & van den Bergh, S. 1996, MNRAS, 279, L47

Abraham, R. G., Valdes, F., Yee, H. K. C., & van den Bergh, S. 1994, ApJ, 432, 75

Abraham, R. G., van den Bergh, S., & Nair, P. 2003, ApJ, 588, 218

Adelberger, K. L., Shapley, A. E., Steidel, C. C., Pettini, M., Erb, D. K., & Reddy, N. A. 2005a, ApJ, 629, 636

Adelberger, K. L. & Steidel, C. C. 2005, ApJ, 630, 50

Adelberger, K. L., Steidel, C. C., Pettini, M., Shapley, A. E., Reddy, N. A., & Erb, D. K. 2005b, ApJ, 619, 697

Adelberger, K. L., Steidel, C. C., Shapley, A. E., Hunt, M. P., Erb, D. K., Reddy, N. A., & Pettini, M. 2004, ApJ, 607, 226

Adelberger, K. L., Steidel, C. C., Shapley, A. E., & Pettini, M. 2003, ApJ, 584, 45

Akiyama, M. 2005, ApJ, 629, 72

Alexander, D. M., Bauer, F. E., Brandt, W. N., Schneider, D. P., Hornschemeier, A. E., Vignali, C., Barger, A. J., Broos, P. S., Cowie, L. L., Garmire, G. P., Townsley, L. K., Bautz, M. W., Chartas, G., & Sargent, W. L. W. 2003, AJ, 126, 539

Allington-Smith, J. R. et al. 2004, in Ground-based Instrumentation for Astronomy, presented at the Society of Photo-Optical Instrumentation Engineers (SPIE) Conference (A. F. M. Moorwood & M. Iye, eds.), 5492, 701

Asplund, M., Grevesse, N., Sauval, A. J., Allende Prieto, C., & Kiselman, D. 2004, A&A, 417, 751

Babcock, H. W. 1953, PASP, 65, 229

Bacon, R., Adam, G., Baranne, A., Courtes, G., Dubet, D., Dubois, J. P., Emsellem, E., Ferruit, P., Georgelin, Y., Monnet, G., Pecontal, E., Rousset, A., & Say, F. 1995, A&AS, 113, 347

Bacon, R., Copin, Y., Monnet, G., Miller, B. W., Allington-Smith, J. R., Bureau, M., Carollo, C. M., Davies, R. L., Emsellem, E., Kuntschner, H., Peletier, R. F., Verolme, E. K., & de Zeeuw, P. T. 2001, MNRAS, 326, 23

Baker, A. J., Tacconi, L. J., Genzel, R., Lehnert, M. D., & Lutz, D. 2004, ApJ, 604, 125

Baldwin, J. A., Phillips, M. M., & Terlevich, R. 1981, PASP, 93, 5

Bardeen, J. M., Bond, J. R., Kaiser, N., & Szalay, A. S. 1986, ApJ, 304, 15

Baugh, C. M. 2006, Reports of Progress in Physics, 69, 3101

Bell, E. F., McIntosh, D. H., Katz, N., & Weinberg, M. D. 2003, ApJS, 149, 289

Bennert, N., Canalizo, G., Jungwiert, B., Stockton, A., Schweizer, F., Peng, C. Y., & Lacy, M. 2008, ApJ, 677, 846

Bennert, N., Falcke, H., Schulz, H., Wilson, A. S., & Wills, B. J. 2002, ApJL, 574, L105

Benson, A. J., Lacey, C. G., Frenk, C. S., Baugh, C. M., & Cole, S. 2004, MNRAS, 351, 1215

Bershady, M. A., Jangren, A., & Conselice, C. J. 2000, AJ, 119, 2645

Birnboim, Y., Dekel, A., & Neistein, E. 2007, MNRAS, 380, 339

Bouché, N. et al. 2007, ApJ, 671, 303

Bournaud, F., Elmegreen, B. G., & Elmegreen, D. M. 2007, ApJ, 670, 237

Bruzual, G. & Charlot, S. 2003, MNRAS, 344, 1000

Bushouse, H. A., Borne, K. D., Colina, L., Lucas, R. A., Rowan-Robinson, M., Baker, A. C., Clements, D. L., Lawrence, A., & Oliver, S. 2002, ApJS, 138, 1

Butler, B. 1998, in MMA Memo No. 238

Calzetti, D., Armus, L., Bohlin, R. C., Kinney, A. L., Koornneef, J., & Storchi-Bergmann, T. 2000, ApJ, 533, 682

Canalizo, G. & Stockton, A. 2000, AJ, 120, 1750

Canalizo, G., Stockton, A., Brotherton, M. S., & Lacy, M. 2006, New Astronomy Review, 50, 650

Capetti, A., Axon, D. J., Macchetto, F., Sparks, W. B., & Boksenberg, A. 1996, ApJ, 469, 554

Chabrier, G. 2003, PASP, 115, 763

Chandar, R., Leitherer, C., Tremonti, C. A., Calzetti, D., Aloisi, A., Meurer, G. R., & de Mello, D. 2005, ApJ, 628, 210

Chapman, S. C., Blain, A. W., Smail, I., & Ivison, R. J. 2005, ApJ, 622, 772

Chapman, S. C., Windhorst, R., Odewahn, S., Yan, H., & Conselice, C. 2003, ApJ, 599, 92

Chun, M. R. 2003, in Adaptive Optical System Technologies II., presented at the Society of Photo-Optical Instrumentation Engineers (SPIE) Conference (P. L. Wizonowich & D. Bonaccini, eds.), 4839, 94

Colina, L., Arribas, S., & Monreal-Ibero, A. 2005, ApJ, 621, 725

Condon, J. J., Cotton, W. D., Greisen, E. W., Yin, Q. F., Perley, R. A., Taylor, G. B., & Broderick, J. J. 1998, AJ, 115, 1693

Conselice, C. J. 2003, ApJS, 147, 1

Conselice, C. J., Bershady, M. A., Dickinson, M., & Papovich, C. 2003a, AJ, 126, 1183

Conselice, C. J., Bershady, M. A., & Jangren, A. 2000a, ApJ, 529, 886

Conselice, C. J., Blackburne, J. A., & Papovich, C. 2005, ApJ, 620, 564

Conselice, C. J., Chapman, S. C., & Windhorst, R. A. 2003b, ApJL, 596, L5

Conselice, C. J., Gallagher, J. S., Calzetti, D., Homeier, N., & Kinney, A. 2000b, AJ, 119, 79

Cowie, L. L. & Barger, A. J. 2008, ArXiv e-prints, 806

Cushing, M. C., Rayner, J. T., & Vacca, W. D. 2005, ApJ, 623, 1115

Daddi, E., Cimatti, A., Renzini, A., Fontana, A., Mignoli, M., Pozzetti, L., Tozzi, P., & Zamorani, G. 2004, ApJ, 617, 746

Daddi, E. et al. 2005, ApJL, 631, L13

Davies, R. I. 2007, MNRAS, 375, 1099

Davies, R. L. et al. 1997, in Optical Telescopes of Today and Tomorrow, presented at the Society of Photo-Optical Instrumentation Engineers (SPIE) Conference (A. L. Ardeberg, ed.), 2871, 1099

Dawson, S., McCrady, N., Stern, D., Eckart, M. E., Spinrad, H., Liu, M. C., & Graham, J. R. 2003, AJ, 125, 1236

Dekel, A. & Birnboim, Y. 2006, MNRAS, 368, 2

Dickinson, M. 2000, in Astronomy, physics and chemistry of H_3^+, Royal Society of London Philosophical Transactions Series A, 358, 2001

Dickinson, M., Papovich, C., Ferguson, H. C., & Budavári, T. 2003, ApJ, 587, 25

Eisenhauer, F. et al. 2003, in Instrument Design and Performance for Optical/Infrared Ground-based Telescopes, presented at the Society of Photo-Optical Instrumentation Engineers (SPIE) Conference (M. Iye & A. F. M. Moorwood, eds.), 4841, 1548

Erb, D. K., Shapley, A. E., Pettini, M., Steidel, C. C., Reddy, N. A., & Adelberger, K. L. 2006a, ApJ, 644, 813

Erb, D. K., Shapley, A. E., Steidel, C. C., Pettini, M., Adelberger, K. L., Hunt, M. P., Moorwood, A. F. M., & Cuby, J.-G. 2003, ApJ, 591, 101

Erb, D. K., Steidel, C. C., Shapley, A. E., Pettini, M., & Adelberger, K. L. 2004, ApJ, 612, 122

Erb, D. K., Steidel, C. C., Shapley, A. E., Pettini, M., Reddy, N. A., & Adelberger, K. L. 2006b, ApJ, 647, 128

—. 2006c, ApJ, 646, 107

Fakhouri, O. & Ma, C.-P. 2008, MNRAS, 386, 577

Falcke, H., Wilson, A. S., & Simpson, C. 1998, ApJ, 502, 199

Ferguson, H. C. et al. 2004, ApJL, 600, L107

Flores, H., Puech, M., Hammer, F., Garrido, O., & Hernandez, O. 2004, A&A, 420, L31

Förster Schreiber et al. 2006, ApJ, 645, 1062

Franx, M. et al. 2003, ApJL, 587, L79

García-Lorenzo, B., Arribas, S., & Mediavilla, E. 2000, The Newsletter of the Isaac Newton Group of Telescopes (ING Newsl.), 3, 25

Genzel, R., Tacconi, L. J., Rigopoulou, D., Lutz, D., & Tecza, M. 2001, ApJ, 563, 527

Genzel, R. et al. 2006, Nature, 442, 786

—. 2008, ArXiv e-prints, 807

Giallongo, E., Cristiani, S., D'Odorico, S., & Fontana, A. 2002, ApJL, 568, L9

Giavalisco, M., Steidel, C. C., & Macchetto, F. D. 1996, ApJ, 470, 189

Giavalisco, M. et al. 2004, ApJL, 600, L93

Gini, C. 1955, Memorie di Metodologia Statistica (E. Pizetti & T. Salvemini, eds.) (Rome: Libreria Eredi Virgilio Veschi)

Girardi, L., Bertelli, G., Bressan, A., Chiosi, C., Groenewegen, M. A. T., Marigo, P., Salasnich, B., & Weiss, A. 2002, A&A, 391, 195

Glasser, G. J. 1962, J. Am. Stat. Assoc.

Glazebrook, K. et al. 2004, Nature, 430, 181

Goldader, J. D., Meurer, G., Heckman, T. M., Seibert, M., Sanders, D. B., Calzetti, D., & Steidel, C. C. 2002, ApJ, 568, 651

Gordon, K. D. et al. 2004, ApJs, 154, 215

Greene, J. E. & Ho, L. C. 2005, ApJ, 627, 721

Grimes, J. P., Heckman, T., Hoopes, C., Strickland, D., Aloisi, A., Meurer, G., & Ptak, A. 2006, ApJ, 648, 310

Grogin, N. A. et al. 2005, ApJL, 627, L97

Hammer, F., Hill, V., & Cayatte, V. 1999, Journal des Astronomes Francais, 60, 19

Heckman, T. M. 2002, in Extragalactic Gas at Low Redshift, Astronomical Society of the Pacific Conference Series (J. S. Mulchaey & J. Stocke, eds.), 254, 292

Heckman, T. M., Miley, G. K., van Breugel, W. J. M., & Butcher, H. R. 1981, ApJ, 247, 403

Högbom, J. A. 1974, A&AS, 15, 417

Immeli, A., Samland, M., Gerhard, O., & Westera, P. 2004a, A&A, 413, 547

Immeli, A., Samland, M., Westera, P., & Gerhard, O. 2004b, ApJ, 611, 20

Kajisawa, M. & Yamada, T. 2001, PASJ, 53, 833

Kaspi, S., Smith, P. S., Netzer, H., Maoz, D., Jannuzi, B. T., & Giveon, U. 2000, ApJ, 533, 631

Kennicutt, R. C., Lee, J. C., Akiyama, S., Funes, J. G., & Sakai, S. 2004, in Bulletin of the American Astronomical Society, 36, 1442

Kennicutt, Jr., R. C. 1998a, ARAA, 36, 189

—. 1998b, ApJ, 498, 541

Kennicutt, Jr., R. C., Tamblyn, P., & Congdon, C. E. 1994, ApJ, 435, 22

Kent, S. M. 1985, ApJs, 59, 115

Kereš, D., Katz, N., Weinberg, D. H., & Davé, R. 2005, MNRAS, 363, 2

Larkin, J. et al. 2006, in Ground-based and Airborne Instrumentation for Astronomy, presented at the Society of Photo-Optical Instrumentation Engineers (SPIE) Conference, 6269

Larkin, J. E. et al. 2003, in Instrument Design and Performance for Optical/Infrared Ground-based Telescopes, presented at the Society of Photo-Optical Instrumentation Engineers (SPIE) Conference (M. Iye & A. F. M. Moorwood, eds.), 4841, 1600

Law, D. R., Steidel, C. C., & Erb, D. K. 2006, AJ, 131, 70

Law, D. R., Steidel, C. C., Erb, D. K., Larkin, J. E., Pettini, M., Shapley, A. E., & Wright, S. A. 2007a, ApJ, 669, 929

Law, D. R., Steidel, C. C., Erb, D. K., Pettini, M., Reddy, N. A., Shapley, A. E., Adelberger, K. L., & Simenc, D. J. 2007b, ApJ, 656, 1

Lee, J. C., Kennicutt, R. C., Funes, J. G., Sakai, S., Tremonti, C. A., & van Zee, L. 2004, in Bulletin of the American Astronomical Society, 36, 1442

Lehnert, M. D. & Heckman, T. M. 1996a, ApJ, 462, 651

—. 1996b, ApJ, 472, 546

Leipski, C. & Bennert, N. 2006, A&A, 448, 165

Lemoine-Busserolle, M., Contini, T., Pelló, R., Le Borgne, J.-F., Kneib, J.-P., & Lidman, C. 2003, A&A, 397, 839

Liu, M. C. 2006, in Advances in Adaptive Optics II, presented at the Society of Photo-Optical Instrumentation Engineers (SPIE) Conference, 6272

Lord, S. D. 1992, NASA Tech. Rep. 103957 (Moffett Field: NASA Ames Research Center)

Lotz, J. M., Madau, P., Giavalisco, M., Primack, J., & Ferguson, H. C. 2006, ApJ, 636, 592

Lotz, J. M., Primack, J., & Madau, P. 2004, AJ, 128, 163

Lupton, R. 1993, Statistics in theory and practice, Princeton, N.J.: Princeton University Press.

Majewski, S. R., Skrutskie, M. F., Weinberg, M. D., & Ostheimer, J. C. 2003, ApJ, 599, 1082

Martin, C. L. & Kennicutt, Jr., R. C. 2001, ApJ, 555, 301

McCarthy, P. J., Baum, S. A., & Spinrad, H. 1996, ApJS, 106, 281

McGregor, P. J. et al. 2003, in Instrument Design and Performance for Optical/Infrared Ground-based Telescopes, presented at the Society of Photo-Optical Instrumentation Engineers (SPIE) Conference (M. Iye & A. F. M. Moorwood, eds.), 4841, 1581

Meurer, G. R., Heckman, T. M., Lehnert, M. D., Leitherer, C., & Lowenthal, J. 1997, AJ, 114, 54

Miller, J. S. & Sheinis, A. I. 2003, ApJL, 588, L9

Mo, H. J., Mao, S., & White, S. D. M. 1998, MNRAS, 295, 319

Moorwood, A., van der Werf, P., Cuby, J. G., & Oliva, T. 2003, in The Mass of Galaxies at Low and High Redshift (R. Bender & A. Renzini, eds.), 302

Moustakas, J., Kennicutt, Jr., R. C., & Tremonti, C. A. 2006, ApJ, 642, 775

Newberg, H. J. et al. 2002, ApJ, 569, 245

Noguchi, M. 1999, ApJ, 514, 77

Oke, J. B. 1964, ApJ, 140, 689

Osterbrock, D. E. 1989, Astrophysics of gaseous nebulae and active galactic nuclei, Mill Valley, CA: University Science Books, 422.

Ostriker, J. P. 1990, in Evolution of the Universe of Galaxies, Astronomical Society of the Pacific Conference Series (R. G. Kron, ed.), 10, 25

Pagel, B. E. J., Edmunds, M. G., Blackwell, D. E., Chun, M. S., & Smith, G. 1979, MNRAS, 189, 95

Papovich, C., Dickinson, M., Giavalisco, M., Conselice, C. J., & Ferguson, H. C. 2005, ApJ, 631, 101

Papovich, C., Giavalisco, M., Dickinson, M., Conselice, C. J., & Ferguson, H. C. 2003, ApJ, 598, 827

Papovich, C. et al. 2006, ApJ, 640, 92

Peter, A. H. G., Shapley, A. E., Law, D. R., Steidel, C. C., Erb, D. K., Reddy, N. A., & Pettini, M. 2007, ApJ, 668, 23

Petrosian, V. 1976, ApJL, 209, L1

Pettini, M., Kellogg, M., Steidel, C. C., Dickinson, M., Adelberger, K. L., & Giavalisco, M. 1998, ApJ, 508, 539

Pettini, M. & Pagel, B. E. J. 2004, MNRAS, 348, L59

Pettini, M., Rix, S. A., Steidel, C. C., Adelberger, K. L., Hunt, M. P., & Shapley, A. E. 2002, ApJ, 569, 742

Pettini, M., Shapley, A. E., Steidel, C. C., Cuby, J.-G., Dickinson, M., Moorwood, A. F. M., Adelberger, K. L., & Giavalisco, M. 2001, ApJ, 554, 981

Pettini, M., Steidel, C. C., Adelberger, K. L., Dickinson, M., & Giavalisco, M. 2000, ApJ, 528, 96

Pierce, C. M. et al. 2007, ApJL, 660, L19

Puech, M., Flores, H., & Hammer, F. 2004, in SF2A-2004: Semaine de l'Astrophysique Francaise (F. Combes, D. Barret, T. Contini, & F. Meynadier, eds.), 633

Quirrenbach, A., Larkin, J. E., Krabbe, A., Barczys, M., & LaFreniere, D. 2003, in Instrument Design and Performance for Optical/Infrared Ground-based Telescopes, presented at the Society of Photo-Optical Instrumentation Engineers (SPIE) Conference (M. Iye & A. F. M. Moorwood, eds.), 4841, 1493

Ramsay Howat, S. K., Ettedgui-Atad, E., Bennett, R. J., Bridger, A., Content, R., Ellis, M. A., Hastings, P. R., Strachan, M., Wall, R., & Wells, M. 1998, in Infrared Astronomical Instrumentation, Proc. SPIE (A. M. Fowler, ed.), 3354, p. 456-467

Ravindranath, S., Giavalisco, M., Ferguson, H. C., Conselice, C., Katz, N., Weinberg, M., Lotz, J., Dickinson, M., Fall, S. M., Mobasher, B., & Papovich, C. 2006, ApJ, 652, 963

Reddy, N. A., Erb, D. K., Steidel, C. C., Shapley, A. E., Adelberger, K. L., & Pettini, M. 2005, ApJ, 633, 748

Reddy, N. A., Steidel, C. C., Erb, D. K., Shapley, A. E., & Pettini, M. 2006a, ApJ, 653, 1004

Reddy, N. A., Steidel, C. C., Fadda, D., Yan, L., Pettini, M., Shapley, A. E., Erb, D. K., & Adelberger, K. L. 2006b, ApJ, 644, 792

Reddy, N. A., Steidel, C. C., Pettini, M., Adelberger, K. L., Shapley, A. E., Erb, D. K., & Dickinson, M. 2008, ApJS, 175, 48

Renzini, A. 2005, in The Initial Mass Function 50 Years Later, Astrophysics and Space Science Library (E. Corbelli, F. Palla, H. Zinnecker, eds.), 327, 221

Rice, M. S., Martini, P., Greene, J. E., Pogge, R. W., Shields, J. C., Mulchaey, J. S., & Regan, M. W. 2006, ApJ, 636, 654

Ridgway, S. E., Heckman, T. M., Calzetti, D., & Lehnert, M. 2001, ApJ, 550, 122

Rix, S. A., Pettini, M., Leitherer, C., Bresolin, F., Kudritzki, R.-P., & Steidel, C. C. 2004, ApJ, 615, 98

Rix, S. A., Pettini, M., Steidel, C. C., Reddy, N. A., Adelberger, K. L., Erb, D. K., & Shapley, A. E. 2007, ApJ, 670, 15

Salpeter, E. E. 1955, ApJ, 121, 161

Sanders, D. B., Soifer, B. T., Elias, J. H., Madore, B. F., Matthews, K., Neugebauer, G., & Scoville, N. Z. 1988, ApJ, 325, 74

Schade, D., Lilly, S. J., Crampton, D., Hammer, F., Le Fevre, O., & Tresse, L. 1995, ApJL, 451, L1+

Schmidt, M., Schneider, D. P., & Gunn, J. E. 1995, AJ, 110, 68

Schmitt, H. R., Donley, J. L., Antonucci, R. R. J., Hutchings, J. B., Kinney, A. L., & Pringle, J. E. 2003, ApJ, 597, 768

Sergeev, S. G., Pronik, V. I., Malkov, Y. F., & Chuvaev, K. K. 1997, A&A, 320, 405

Shapiro, K. L. et al. 2008, ArXiv e-prints, 802

Shapley, A. E., Coil, A. L., Ma, C.-P., & Bundy, K. 2005a, ApJ, 635, 1006

Shapley, A. E., Erb, D. K., Pettini, M., Steidel, C. C., & Adelberger, K. L. 2004, ApJ, 612, 108

Shapley, A. E., Steidel, C. C., Adelberger, K. L., Dickinson, M., Giavalisco, M., & Pettini, M. 2001, ApJ, 562, 95

Shapley, A. E., Steidel, C. C., Erb, D. K., Reddy, N. A., Adelberger, K. L., Pettini, M., Barmby, P., & Huang, J. 2005b, ApJ, 626, 698

Shapley, A. E., Steidel, C. C., Pettini, M., & Adelberger, K. L. 2003, ApJ, 588, 65

Shields, G. A., Gebhardt, K., Salviander, S., Wills, B. J., Xie, B., Brotherton, M. S., Yuan, J., & Dietrich, M. 2003, ApJ, 583, 124

Smail, I., Ivison, R. J., & Blain, A. W. 1997, ApJL, 490, L5

Solomon, P. M., Downes, D., Radford, S. J. E., & Barrett, J. W. 1997, ApJ, 478, 144

Spergel, D. N. et al. 2007, ApJS, 170, 377

Stark, D. P., Ellis, R. S., Richard, J., Kneib, J.-P., Smith, G. P., & Santos, M. R. 2007, ApJ, 663, 10

Steidel, C. C., Adelberger, K. L., Shapley, A. E., Pettini, M., Dickinson, M., & Giavalisco, M. 2003, ApJ, 592, 728

Steidel, C. C., Hunt, M. P., Shapley, A. E., Adelberger, K. L., Pettini, M., Dickinson, M., & Giavalisco, M. 2002, ApJ, 576, 653

Steidel, C. C., Shapley, A. E., Pettini, M., Adelberger, K. L., Erb, D. K., Reddy, N. A., & Hunt, M. P. 2004, ApJ, 604, 534

Swinbank, A. M., Balogh, M. L., Bower, R. G., Hau, G. K. T., Allington-Smith, J. R., Nichol, R. C., & Miller, C. J. 2005a, ApJ, 622, 260

Swinbank, A. M., Smail, I., Bower, R. G., Borys, C., Chapman, S. C., Blain, A. W., Ivison, R. J., Howat, S. R., Keel, W. C., & Bunker, A. J. 2005b, MNRAS, 359, 401

Tacconi, L. J., Genzel, R., Lutz, D., Rigopoulou, D., Baker, A. J., Iserlohe, C., & Tecza, M. 2002, ApJ, 580, 73

Tecza, M., Thatte, N. A., Krabbe, A., & Tacconi-Garman, L. E. 1998, in Infrared Astronomical Instrumentation, Proc. SPIE (A. M. Fowler, ed.), 3354, 394

Toft, S., van Dokkum, P., Franx, M., Thompson, R. I., Illingworth, G. D., Bouwens, R. J., & Kriek, M. 2005, ApJL, 624, L9

Toomre, A. 1964, ApJ, 139, 1217

Tremaine, S., Gebhardt, K., Bender, R., Bower, G., Dressler, A., Faber, S. M., Filippenko, A. V., Green, R., Grillmair, C., Ho, L. C., Kormendy, J., Lauer, T. R., Magorrian, J., Pinkney, J., & Richstone, D. 2002, ApJ, 574, 740

Tremonti, C. A., Moustakas, J., & Diamond-Stanic, A. M. 2007, ApJL, 663, L77

van Dam, M. A., Bouchez, A. H., Le Mignant, D., Johansson, E. M., Wizinowich, P. L., Campbell, R. D., Chin, J. C. Y., Hartman, S. K., Lafon, R. E., Stomski, Jr., P. J., & Summers, D. M. 2006, PASP, 118, 310

Vanden Berk, D. E. et al. 2001, AJ, 122, 549

Wang, J., Wei, J. Y., & He, X. T. 2005, New Astronomy, 10, 353

Weinberg, M. D. & Blitz, L. 2006, ApJL, 641, L33

Weiner, B. J., Willmer, C. N. A., Faber, S. M., Melbourne, J., Kassin, S. A., Phillips, A. C., Harker, J., Metevier, A. J., Vogt, N. P., & Koo, D. C. 2006, ApJ, 653, 1027

White, S. D. M. 1994, ArXiv Astrophysics e-prints

White, S. D. M. & Rees, M. J. 1978, MNRAS, 183, 341

Wizinowich, P. L. et al. 2006, PASP, 118, 297

Wright, S. A., Larkin, J. E., Barczys, M., Erb, D. K., Iserlohe, C., Krabbe, A., Law, D. R., McElwain, M. W., Quirrenbach, A., Steidel, C. C., & Weiss, J. 2007, ApJ, 658, 78

Zentner, A. R. & Bullock, J. S. 2003, ApJ, 598, 49